Investigation, Manipulation, and Coupling of Single Nanoscopic and Quantum Emitters

DISSERTATION

zur Erlangung des akademischen Grades
d o c t o r r e r u m n a t u r a l i u m
(Dr. rer. nat.)
im Fach Physik

eingereicht an der
Mathematisch-Naturwissenschaftlichen Fakultät I
Humboldt-Universität zu Berlin

von
Dipl.-Phys. Stefan Schietinger
geboren in Neustadt an der Weinstraße am 23.6.1976

Präsident der Humboldt-Universität zu Berlin:
Prof. Dr. Jan-Hendrik Olbertz

Dekan der Mathematisch-Naturwissenschaftlichen Fakultät I:
Prof. Dr. Andreas Herrmann

Gutachter:
1. Prof. Dr. Oliver Benson
2. Prof. Dr. Beate Röder
3. Prof. D.Sc. Leonardo de Souza Menezes

Tag der mündlichen Prüfung: 1.3.2012

Er verspann sich..., länger, als er gewollt hatte. Es ließ ihn nicht los, und das Geschaute, unter den Linsen des Mikroskops etwa, war noch größer als das Gedachte.

Ernst Wiechert, aus *Das einfache Leben*

Abstract

The topic of the dissertation presented here is the investigation of nanoscopic emitters and the possibilities to influence their fluorescence behavior by controlled coupling to photonic and plasmonic structures. Thereby, the new, hybrid composites of nanoparticles and the appropriate dielectric environment can not only improve the performance in already existing applications, but are fundamental building blocks of future, integrated all-optical systems, e.g., chips for data processing. For the experiments displayed optical methods, especially confocal microscopy, are expanded by scanning probe techniques. This allows for investigation below the optical diffraction limit as well as for manipulation, enabling to assemble and couple individual optical entities to more complex systems.

$NaYF_4$ nanocrystals codoped with ytterbium and erbium are investigated since they provide excellent properties in upconverting of low-energetic photons to photons with higher energy. The fluorescence light that is generated in this process of a small cluster of nanocrystals is investigated on its dependence on the excitation intensity. With the help of an atomic force microscope (AFM) a dependence of the spectral composition of the fluorescence light from single nanocrystals on their size ranging between a few to 50 nm is demonstrated. By selective manipulation with the AFM, individual nanocrystals are coupled to gold nanospheres and the mechanisms of the observed plasmonic amplification of the emission is analyzed with time-resolved measurements.

Single nitrogen–vacancy centers in nanodiamonds are employed as single-photon sources in a second subject area. A near-field probe is employed to attach these single quantum systems to microspherical resonators, by which their emission features the typical peaks in the spectrum due to the coupling to the whispering gallery modes of the spheres. This method can not only be applied to couple two or more single-photon emitters to the very same modes of a microsphere, but the resonators themselves can be pre-characterized to match one of the modes with the emitter. Furthermore, it will be demonstrated how the efficiency of a single-photon source can be enhanced by coupling the nitrogen-vacancy center to a plasmonic antenna made of gold nanospheres.

Zusammenfassung

Die hier vorgelegte Dissertation beschäftigt sich mit Untersuchungen an nanoskopischen Emittern und den Möglichkeiten, deren Fluoreszenzverhalten durch kontrollierte Ankopplung an photonische und plasmonische Strukturen zu beeinflussen. Die neuen, hybriden Komposite aus Nanopartikeln und angepasster dielektrischer Umgebung können dabei nicht nur zur Leistungssteigerung bereits bestehender Anwendungen beitragen. Vielmehr stellen sie fundamentale Bausteine für zukünftige, integrierte optische Systemlösungen dar, z.B. von Chips zur Datenverarbeitung. Für die vorgestellten Experimente werden optische Methoden, insbesondere die der konfokalen Mikroskopie, um Rastersondentechniken erweitert, die sowohl Untersuchungen unterhalb des optischen Beugungslimits erlauben als auch zur Manipulation für die Anordnung und Kopplung einzelner Bestandteile zu komplexeren Systemen eingesetzt werden können.

Zum einen werden mit Ytterbium- und Erbium-Ionen kodotierte $NaYF_4$-Nanokristalle untersucht, die hervorragende Eigenschaften bei der Umwandlung von niederenergetischen Photonen in solche höherer Energie besitzen. Das so entstehende Fluoreszenzlicht einer Ansammlung von Nanokristallen wird auf seine Abhängigkeit von der Anregungsintensität untersucht. Mit der Hilfe eines Rasterkraftmikroskops (AFM) wird eine Abhängigkeit der spektralen Zusammensetzung des Fluoreszenzlichts einzelner Nanokristalle von deren Größe im Bereich von wenigen bis 50 nm aufgezeigt. Durch gezielte Manipulation mit dem AFM werden ebenfalls einzelne Nanokristalle an Goldnanokügelchen gekoppelt und die Mechanismen der beobachteten plasmonischen Verstärkung der Emission durch zeitaufgelöste Messungen analysiert.

Einzelne Stickstoff-Fehlstellen-Zentren in Nanodiamanten werden in einem zweiten Themenkomplex als Einzelphotonenquellen eigesetzt. Diese werden durch den Einsatz einer Nahfeld-Sonde auf Mikrokugel-Resonatoren aufgebracht, wodurch die Emission aufgrund der Ankopplung an die Flüstergalerie-Moden der Kugeln die typischen, scharfen Überhöhungen im Spektrum aufweist. Diese Methode lässt sich nicht nur verwenden, um zwei oder mehr Emitter an die selben Resonanzen einer Kugel zu koppeln. Es ist auch möglich, die Kugeln in einem Vorbereitungsschritt zu charakterisieren, und so kann insbesondere eine spektrale Übereinstimmung zwischen einer der Resonanzen und dem Emitter erreicht werden. Desweiterne wird demonstriert, wie durch die Kopplung an eine plasmonische Antenne aus Goldnanokugeln mittels AFM auch die Effizienz der Einzelphotonenquelle gesteigert werden kann.

Contents

CHAPTER 1

Introduction

It is spectacular how nanotechnology has found its way into virtually all areas of our lives during the last two decades. These areas are as diverse as the reasons for this impressive success story. In electronics, for example, smaller elements are equivalent to faster devices and higher storage densities [1]. Macroscopic properties like the adhesion to surfaces are governed by forces like the van der Waals interaction which establish on the nanometer scale [2]. For common use, various nanostructured coatings hold back bacteria on keyboards or prevent food from sticking in pans. The usage of nanocrystals as markers in life sciences gave a boost in understanding of inter- and intracellular processes. Finally, the miniaturization of electronic components is a prerequisite for ever smaller and powerful mobile devices that changed our way to communicate. These are just a few examples unimaginable without today's accomplishments on a scale below the millionth part of a meter.

Optics with visible light, however, faces one of its fundamental limitations below one micrometer: The resolution of microscopy with standard techniques is limited to around one half of the wavelength of the employed light [3], and microscopy is often not capable to give an appropriate insight when dimensions shrink below that critical value.

This however, did not prevent nanotechnology to conquer the field of photonics, writing a success story itself. The last decades saw great advances in fabrication techniques like chemical synthesis [4–6], epitaxy [7], lithography [8–10], or focused ion beam [11, 12]. They are accompanied by high-resolution characterization methods like electron microscopy, X-ray scattering, or scanning probe microscopy to overcome the optical far-

field limitations, with astonishing results for both optical active, i.e., light emitting, and passive components (see for example [13–16]): The preparation, fabrication, and optical investigation of ever smaller physical systems, down to the level of single atoms [17–19], single quantum dots [20–23], or single molecules [24–26] are done almost routinely. Structures like photonic crystal cavities with mode volumes on the order of the cube [27] of the modes wavelength or single plasmonic scatterers [28, 29] with a few tens of nanometer are the subject of intense studies.

A leitmotif in photonic research has been and still is the investigation and the intentional utilization of the interplay of emitters with their dielectric environment. The combination of different active and passive entities like nanoscopic emitters coupled to cavities, nanoantennas, or waveguides have been demonstrated. The next steps that lie in front of us are to build up more complex photonic structures featuring improved or even new functionalities with the promise of a wide range of possible applications. Though, for a full exploration of the interactions of light and matter on the nanoscale, all relevant factors have to be determined, and ideally, can be altered *in situ* during optical experiments.

In this thesis, the combination of a confocal microscope with scanning probe techniques (more precisely, an atomic force and a scanning near-field optical microscope) provides this exceptional degree of control on the micro- and nanoscale. This establishes the basis for the study of different fundamental optical entities and their interaction that is presented in this work: It allows not only to collect detailed information hidden below the diffraction limit, but also to actively intervene and manipulate on a scale from a few nanometers up to several micrometers.

As active elements two different kinds of nanocrystals are employed: $NaYF_4$ nanocrystals doped with rare-earth ions and nanodiamonds with color centers. Besides the sole examination on a single nanocrystal level, both these nanoscopic particles are coupled to resonant structures – passive counterparts – to affect their emission, namely plasmonic nanoantennas and microsphere resonators. Before going into the details in the chapters to follow, the different entities that are employed in this work shall be introduced briefly.

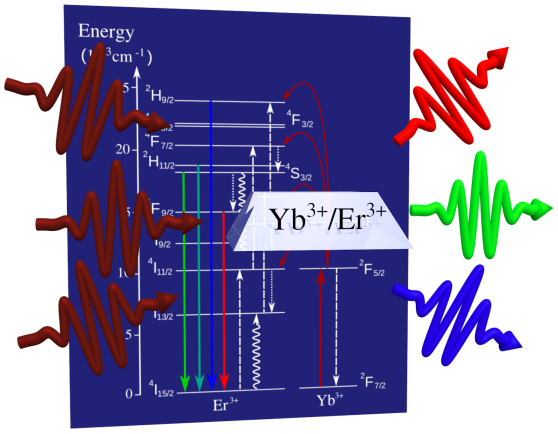

Upconversion nanocrystals consisting of $NaYF_4$ codoped with Ytterbium and Erbium ions are highly efficient in converting near-infrared into visible light [6]. The optical active constituents, the ions, are enclosed in the crystal's matrix and protected from outer influences which is the explanation for stable emission even from single nanocrystals. A step-wise absorption of photons followed by energy transfer processes including real electronic excitation levels [30] is the reason for their outstanding converting performance compared to other systems, e.g., making use of non-linearities in the polarization or two-photon absorption. This superior efficiency and the possibility to functionalize these nanocrystals make them excellent candidates to play a key role in technologically relevant fields from bio-labeling to improvement of solar-cell performance [31, 32].

Single photons are the most fundamental excitation of the electromagnetic field. Their reliable, deterministic generation for both fundamental and application-driven research in quantum optics and quantum communication is a major subject in photonics [33]. Imperfections in the crystal matrix of diamonds, so-called defect centers, are exceptional sources for single photons: They can provide high rates of single photons at ambient condition without degradation over time [34]. Similar to the ions in the aforementioned crystals, the optical active center is embedded in the diamond matrix and therefore protected against negative impact. Among the defects in diamonds, **nitrogen–vacancy centers** are most popular due to their emission at the edge between visible and near-infrared and their electronic structure, bearing great potential for the realization of single qubits in spin excitation [35]. Especially when located in nanodiamonds, they are perfectly suited to be incorporated as single-photon emitters

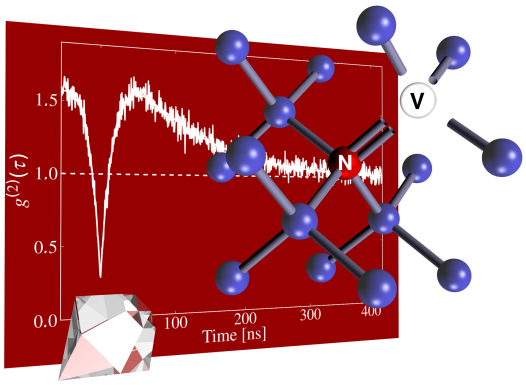

in photonic micro- or nanostructures.

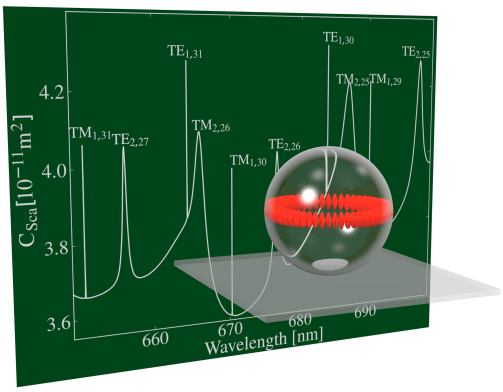

One prominent possibility to alter the dynamics of an emitter is to place it in an optical resonator, which results in the well-known possibility of enhanced or suppressed emission due to the mode structure of the cavity [36]. **Microspherical resonators**, optically transparent spheres with diameters starting from a few micrometers, support the so-called whispering gallery modes [37]. They combine extremely narrow optical resonances with small mode volumes producing a strongly enhanced field inside the mode. This increases the interaction between the electromagnetic field and matter and makes microsphere resonators ideal for quantum optical experiments [38–40] as well as for sensing applications [41–43].

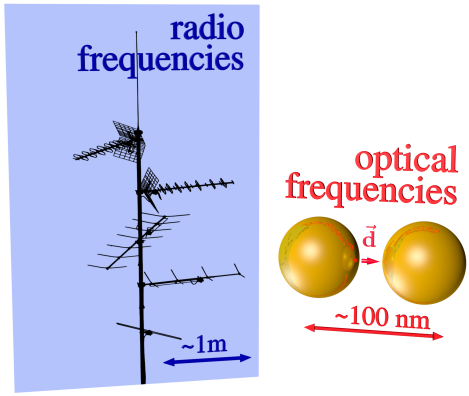

Gold nanospheres with diameters of several tens of nanometers are basic but nonetheless effective realization of an antenna for optical frequencies [44, 45]. The concept of antennas for electromagnetic radiation is known merely since the first observation of the propagation of electromagnetic waves by Heinrich Hertz in the late 19$^{\text{th}}$ century. Antennas build the connection between the localized energy of a dipole and the spread-out wave. A critical parameter is hereby the size with respect to the wavelength of the electromagnetic wave to develop a resonance: Therefore, with higher frequencies the antennas have to shrink. For optical frequencies, the typical extension of the antenna has to be below 100 nm.

Upconversion nanocrystals, nanodiamonds with single nitrogen–vacancies centers, microsphere resonators, and gold nanospheres are the physical systems studied and utilized in this work: It has to be highlighted that each of them can be considered as a fundamental building block for more complex optical systems. With the potential of

the experimental setup providing optical and scanning-probe access on the investigated samples, it will be the goal of this work to provide new insights in the physics on the nanoscale and give a taste of the bright prospects for photonics on the nanoscale.

The thesis starts in **Chapter 2** with a theoretical introduction to the concepts of microspherical resonators and optical antennas, particularly with regard to their potential to modify the spontaneous decay of an emitter.

In **Chapter 3** all components of the experimental setup and their combination to a multifunctional tool for the nanoscale are presented.

After that, the thesis addresses the two different emitters used in the experiment.

Chapter 4 starts with an introduction to the upconversion material $NaYF_4$ codoped with Yb^{3+} and Er^{3+}. Then, the investigation of the size-dependence of the emission from single nanocrystals is presented, before the coupling of single nanocrystals to nanoantennas consisting of gold nanospheres is demonstrated.

In **Chapter 5**, nanodiamonds with single nitrogen-vacancy centers are the active emitters. After single nitrogen-vacancy centers have been characterized, their coupling to the whispering gallery modes of a microsphere and to nanoantennas is shown.

The thesis concludes in **Chapter 6** with a short summary of the results and an outlook on the on-going and future development.

CHAPTER 2

Controlling Spontaneous Emission

The photophysical properties of an emitter such as absorption and fluorescence are not intrinsic features, since the dielectric environment plays a key role for determining them. Even for simple configurations like planar interfaces, the dielectric surrounding of an emitter can not be neglected and Drexhage and colleagues were the first to study these effects in the optical range. They investigated the dependence on the lifetime and the radial distribution pattern of the fluorescence from dye molecules as a function of their distance to a metal surface [46]. In the 1980s, the experiments by Goy et al. [47] and De Martini et al. [48] on spontaneous emission of atoms in a cavity were another impressive demonstration for the modification of the lifetime due to a change of the environment.

Nowadays, a major challenge is to design and realize new structures that allow for tailoring the absorption and fluorescence properties of emitters. For larger ensembles of emitters, this is motivated by possible technical applications, e.g., as it is possible to positively influence the performance of light-emitting diodes or solar cells. Moreover, also investigations on much smaller entities like single nanocrystals or even single quantum emitters allow a deeper physical understanding of the fundamental interactions of emitters and their surrounding.

In this chapter, the basic concepts to describe these interactions of emitters and their dielectric environment are introduced. In more detail, the optical properties of microspheres and metal nanoparticles are discussed, as they will be employed as microcavities and plasmonic nanoantennas in this work.

2.1. Photonic Mode Density

The photon emission rate accompanied by a transition of an excited quantum system from an initial state $|i\rangle$ to a final state $|f\rangle$ is described by Fermi's golden rule [49]

$$\Gamma_{if} \propto |M_{if}|^2 \, \rho(\nu_{if}), \tag{2.1}$$

where Γ_{if} is the transition rate and M_{if} is the dipole matrix element that connects the initial and final states. The transition frequency ν_{if} is given by the energy difference $\Delta E_{if} = h\nu_{if}$ between the two states and $\rho(\nu_{if})$ is the density of optical modes at this frequency, also known as the *photonic mode density* or *photonic density of states*. This term is responsible for the fact that the optical properties of an emitter can not be treated as an isolated system, but the dielectric surrounding has to be considered.

There are two ways to interpret the photonic mode density [50]: in the quantum-field picture as vacuum fluctuations of the electromagnetic field, and in the classical electrodynamics picture, as the ability of the structure to support the emitted electromagnetic mode. The classical treatment is often sufficient or even quantitatively equivalent for a large number of phenomena, including the change of spontaneous emission of a dipole by the dielectric environment. The difference often arises in the statistical nature, i.e., the temporal behavior of the field.

2.1.1. Emission of a Classical Dipole

In the classical picture, a point-like, harmonic dipole at a point $\mathbf{r_0}$ can be expressed by a current density [14]

$$\mathbf{j}(\mathbf{r}, t) = \frac{\mathrm{d}}{\mathrm{d}t}\boldsymbol{\mu}\delta(\mathbf{r} - \mathbf{r_0}) \tag{2.2}$$

with a harmonic dipole moment $\boldsymbol{\mu}(t) = \boldsymbol{\mu}\ e^{-i\omega t}$. The equation of motion in a homogeneous and isotropic environment for the dipole is given by

$$\frac{\mathrm{d}^2}{\mathrm{d}t^2}\boldsymbol{\mu}(t) + \gamma_0 \frac{\mathrm{d}}{\mathrm{d}t}\boldsymbol{\mu}(t) + \omega_0^2 \boldsymbol{\mu}(t) = 0, \tag{2.3}$$

with its natural frequency ω_0 and where a damping of the oscillation was introduced via a damping constant γ_0. The solution for $\boldsymbol{\mu}$ is

$$\boldsymbol{\mu}(t) = \mathrm{Re}\{\boldsymbol{\mu}_0\ e^{-i\omega_0\sqrt{1-(\gamma_0^2/4\omega_0^2)}t} e^{-\gamma_0\ t/2}\} \tag{2.4}$$

Classically, the damping γ_0 is caused by the loss of energy by radiation and can be evaluated with the Poynting's theorem and considering the energy conversation [14]

$$\gamma_0 = \frac{1}{4\pi\varepsilon_0}\frac{2q^2\omega_0^2}{3mc^3}. \tag{2.5}$$

q and m are the charge and mass of the dipole, ε_0 is the vacuum permeability. The time after which the energy stored in the dipole has decreased to a fraction of $1/e$ from its initial value at $t = 0$ is defined as the lifetime τ_0 of the dipole oscillator, obviously given by

$$\tau_0 = 1/\gamma_0. \tag{2.6}$$

For the more general case that also nonradiative processes are present, $1/\gamma_0$ can not be interpreted as the radiative lifetime of the system directly. However, it is possible to introduce the so-called *intrinsic quantum yield* q_i, defined by the ratio between energy dissipated radiatively and the total energy released. Then, Eq. 2.5 can be replaced by

$$\gamma_0 = q_i\frac{1}{4\pi\varepsilon_0}\frac{2q^2\omega_0^2}{3mc^3}, \tag{2.7}$$

which maintains the interpretation of γ_0 and $\tau_0 = 1/\gamma_0$ as radiative decay time and radiative lifetime, respectively.

The situation changes if scattering is present due to inhomogeneity in the dielectric environment. In this case the scattered field $\mathbf{E}_\mathrm{s}$ may act back on the dipole. The equation of motion Eq. 2.3 has to be supplemented by $\mathbf{E}_\mathrm{s}$ (which is also denoted as *local* or *self-field*) as a driving term [14]:

$$\frac{\mathrm{d}^2}{\mathrm{d}t^2}\boldsymbol{\mu}(t) + \gamma_0\frac{\mathrm{d}}{\mathrm{d}t}\boldsymbol{\mu}(t) + \omega_0^2\boldsymbol{\mu}(t) = \frac{q^2}{m}\mathbf{E}_\mathrm{s}. \tag{2.8}$$

With the ansatz $\boldsymbol{\mu}(t) = \mathrm{Re}\{\boldsymbol{\mu}_0 e^{-i\omega t}e^{-\gamma\ t/2}\}$ and $\mathbf{E}_\mathrm{s}(t) = \mathrm{Re}\{\mathbf{E}_0 e^{-i\omega t}e^{-\gamma\ t/2}\}$ for the dipole and the scattered field, respectively, one finds the new decay rate γ and resonance frequency ω. Under the assumption that γ is much smaller than ω, the ratio between the decay rates of the driven and the free dipole γ and γ_0 is

$$\frac{\gamma}{\gamma_0} = 1 + q_i\frac{6\pi\varepsilon_0}{|\boldsymbol{\mu}_0|^2}\frac{1}{k^3}\mathrm{Im}\{\boldsymbol{\mu}_0^* \cdot \mathbf{E}_\mathrm{s}(\mathbf{r}_0)\}. \tag{2.9}$$

The strength of the local field $\mathbf{E}_\mathrm{s}$ is directly proportional to $\boldsymbol{\mu}_0$ and the dependence on the initial strength of the dipole $|\boldsymbol{\mu}_0|$ cancels out.

The exact constitution of the scattering environment defines the phase between $\mathbf{E}_\mathrm{s}$ and the dipole oscillation $\boldsymbol{\mu}$. Therefore, the lifetime of the dipole can be reduced as well as enhanced, dependent on the term $\mathrm{Im}\{\boldsymbol{\mu}_0^* \cdot \mathbf{E}_\mathrm{s}(\mathbf{r}_0)\}$. The overall observable field is the superposition of both the emitted and the scattered fields, and by a suitable design of the environment of the dipole, its lifetime and the spatial distribution of its emission can be controlled.

Equivalence of the Classical and Quantum Descriptions

It is not obvious that this purely classical picture is sufficient to describe the spontaneous emission rate of a quantum system. However, a very elegant formulation of the quantum picture reveals the similarity between the quantum and classical treatment by expressing the photonic mode density by the dyadic Green's function $\overleftrightarrow{\mathbf{G}}$ [14]. This similarity [51] was discussed in detail by Xu et al. [52]: The radiated energy $\mathcal{E}_\mathrm{clas}$ derived in the classical picture is proportional to the corresponding spontaneous emission rates γ_QED derived by quantum electrodynamics. Therefore, the spontaneous emission rates can be calculated via

$$\frac{\gamma_\mathrm{QED}}{\gamma_\mathrm{0,QED}} = \frac{\mathcal{E}_\mathrm{clas}}{\mathcal{E}_\mathrm{0,clas}}. \tag{2.10}$$

This result is of major importance as it allows to calculate lifetime changes in the framework of classical electrodynamics. Then, also well-known numerical techniques, such as the finite-difference time-domain technique [45, 53, 54] can be applied.

2.1.2. Spontaneous Emission Into a Cavity Mode

Mode Volume and Quality Factor

An optical resonator alters the photonic mode density drastically as it supports only a discrete set of specific modes, i.e., the possible solutions of Maxwell's equations with the boundary conditions implied by the cavity geometry. These cavity modes have two important characteristics: the quality (Q-) factor and the mode volume V_eff. The mode volume V_eff is a measure for the spatial extension of a mode and given by

$$V_\mathrm{eff} = \frac{\int \varepsilon(\mathbf{r})\mathbf{E}^2(\mathbf{r})d^3(\mathbf{r})}{(\varepsilon(\mathbf{r})\mathbf{E}^2(\mathbf{r}))_\mathrm{max}}, \tag{2.11}$$

where $\mathbf{E}(\mathbf{r})$ is the mode's electric field distribution.

The Q-factor of a cavity is generally defined as the ratio of energy stored in the cavity to the power dissipated in one cycle multiplied by 2π. At a resonance frequency

$f_0 = \omega_0/2\pi$ this evaluates to [55]

$$Q = 2\pi \times \frac{\text{energy stored}}{\text{energy dissipated per cycle}} = 2\pi \times \frac{U}{(dU/dt)/f_0} = \omega_0 \times \frac{U}{\mathrm{d}U/\mathrm{d}t}. \tag{2.12}$$

The differential equation for the stored energy

$$\frac{\mathrm{d}U}{\mathrm{d}t} = -\frac{\omega_0}{Q}\, U \tag{2.13}$$

implies an exponential decay of the electric field of the form

$$E(t) = E_0\; e^{-\omega_0 t/2Q}\; e^{-i\omega_0 t} \tag{2.14}$$

inside the cavity. The Fourier transform of the electric field $E(t)$ is the spectral distribution of the field $E(\omega)$ and has a Lorentzian shape with a width $\delta\omega$ of ω_0/Q which results in the alternative formulation for Q

$$Q = \frac{\omega_0}{\delta\omega} = \omega_0\tau, \tag{2.15}$$

where τ is the lifetime of the field inside the cavity.

Emission Rates and the Purcell Factor

The free-space decay rate of a two-level atom (with levels denoted by the indices $1, 2$) deduced using the Weisskopf-Wigner theory evaluates to [36]

$$\Gamma_0 = \frac{\omega_0^3 \mu_{12}^2}{3\pi\hbar\varepsilon_0 c^3}, \tag{2.16}$$

where ω_0 is the transition frequency and μ_{12} the transition dipole moment.

The dynamics of the same atom inside a cavity is changed due to the different photonic mode density. Dependent on the exact properties of cavity and emitter and their interaction strength, two different cases can be distinguished: the weak and the strong coupling regime. Which case is present is determined by three parameters (Fig. 2.1): the photon decay rate of the cavity κ, the free-space decay rate of the atom Γ_0, and the atom–cavity field coupling constant g, given by $g = \wp_{12}\epsilon_\omega/\hbar \times f$. $\wp_{12}$ is the dipole matrix element, $\epsilon_\omega = \sqrt{\hbar\omega/\varepsilon_0 V_{\text{eff}}}$ the field per photon in the cavity volume, and f a factor between 0 and 1 for accounting for the field strength at the emitter's position.

In the strong coupling regime, i.e., $g \gg \Gamma_0, \kappa$, and the atom in resonance with the cavity mode, the emitted photons from the atom are likely to be reabsorbed before

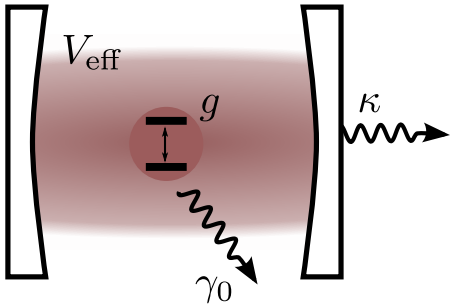

Figure 2.1.: Whether the atom–cavity system is in the strong or weak coupling regime is dependent on the free-space decay rate of the atom Γ_0, the photon decay rate of the cavity κ, and the atom–cavity field coupling constant g.

leaving the cavity and the population of the excited state undergoes a damped oscillation with the vacuum Rabi frequency g. The coupling splits the system's initially twofold degenerate levels, and the emitted light features a spectral doublet.

In the weak coupling regime, the photon emission is an irreversible effect, the photon leaves the cavity before being reabsorbed. In this case, the main effect is that the radiative lifetime of the atom is altered. Both cases, an enhancement but also an inhibition of spontaneous emission can occur, dependent on the detuning and position of the atom with respect to the cavity mode.

In resonance and with perfect alignment and position of the atom with respect to the cavity field mode, the emission rate is given by [14]

$$\Gamma_{\max} = \frac{3\ \lambda^3}{4\pi^2}\left(\frac{Q}{V}\right)\ \Gamma_0 \tag{2.17}$$

with Q and V the quality factor and the mode volume of the cavity. The factor

$$F = \frac{3\ \lambda^3}{4\pi^2}\left(\frac{Q}{V}\right) \tag{2.18}$$

is known as the Purcell factor [56]. The proportionality of the enhancement to Q/V explains why cavities with spatial dimensions on the order of the wavelength and high Q-factors are the key to observe strong modification of the emission rate.

The reduction of the lifetime by emission enhancement in a cavity was first observed for highly excited Rydberg atoms [47]. The opposite, the suppression of the emission of atoms could also be demonstrated shortly after [48].

2.2. Microsphere Resonators

2.2.1. Whispering Gallery Modes

An impressive acoustic phenomenon is present in the dome of St. Paul's cathedral: In the gallery on the base of the dome, a whisperer can be heard all along the gallery if he speaks in the direction along the outer gallery wall. This effect, that was first explained by Lord Rayleigh [57], can be observed in many buildings with a circular gallery, such as the Befreiungshalle near Kelheim with a dome of a diameter of 29 m, shown in Fig. 2.2. Especially when the observer is on the opposite site of the dome, the speaker can only be heard if he speaks out into the gallery, perpendicular to the direct connection to the listener. Merely nothing can be heard when he speaks directly towards him [58].

The first explanation of this phenomenon by Lord Rayleigh that standing resonant waves are responsible was later corrected: If the speaker speaks into the gallery, the sound waves are guided along the rigid walls by reflection and do not spread freely as in the case when the speaker addresses the listener directly [59].

A similar guiding effect can occur when a light beam strikes on a curved interface between a medium with higher (n_1) to lower (n_2) index of refraction. A simple explanation can be given by geometrical optics (see Fig. 2.3): If the incident angle α of the light ray on the interface is larger than the critical angle $\theta_c = \arcsin(n_2/n_1)$, light is

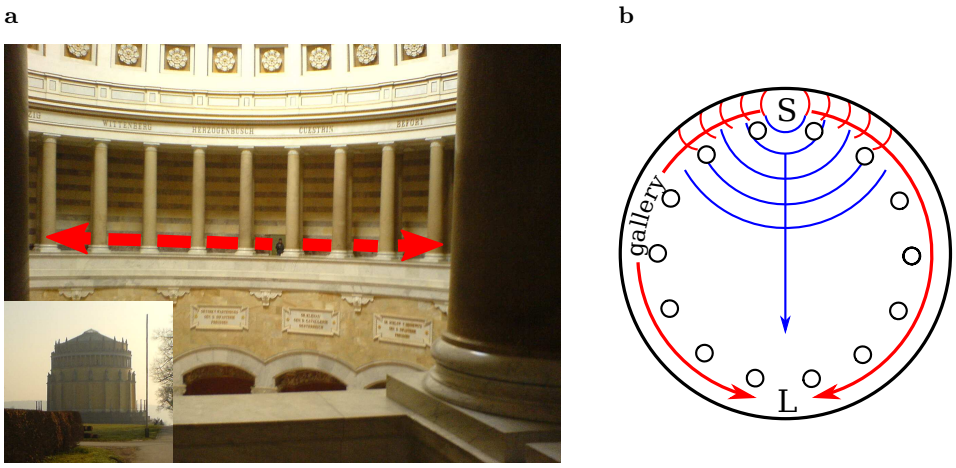

Figure 2.2.: a: Image of the gallery in the dome of the Befreiungshalle at Kelheim (lower inset). b: The sound waves are guided and refocused by the walls, if the speaker (S) speaks into the gallery (red). When the speaker addresses directly to the listener (L), almost nothing can be heard, as the wave spreads freely (blue).

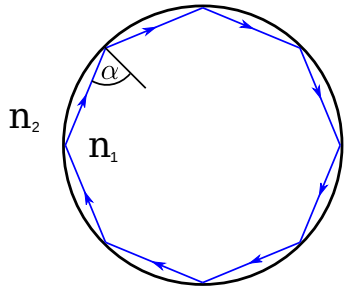

Figure 2.3.: Simple ray optics picture of whispering gallery modes: If the incident angle α is larger than the critical angle $\theta_c = \arcsin(n_2/n_1)$, the beam is totally reflected at the boundary.

totally internally reflected. On a spherical boundary, the light can be guided along the inner surface. If the beam accumulates a multiple of 2π in phase on one round trip, the primary and secondary beam interfere constructively and a resonance can be observed. These resonances are called *whispering gallery modes* due to the similarity to the sound effects described above. These are the eigenmodes of the light in a spherical resonator.

2.2.2. Analytical Solution of the Wave Equation for a Dielectric Microsphere

The starting point to find and analyze the electromagnetic eigenmodes of a dielectric sphere are Maxwell's equations:

$$\begin{aligned} \nabla \cdot \mathbf{D} &= \rho & \nabla \times \mathbf{E} + \frac{\partial \mathbf{B}}{\partial t} &= 0 \\ \nabla \cdot \mathbf{B} &= 0 & \nabla \times \mathbf{H} - \frac{\partial \mathbf{D}}{\partial t} &= \mathbf{J} \end{aligned} \tag{2.19}$$

where $\mathbf{E}$ is the electric field and $\mathbf{B}$ is the magnetic induction. $\mathbf{D}$ and $\mathbf{H}$ are the electric displacement and the magnetic field given by

$$\begin{aligned} \mathbf{D} &= \varepsilon_0 \mathbf{E} + \mathbf{P}, \\ \mathbf{H} &= \frac{\mathbf{B}}{\mu_0} - \mathbf{M}, \end{aligned} \tag{2.20}$$

with $\mathbf{P}$ the electric polarization and $\mathbf{M}$ the magnetization. ε_0 and μ_0 are the vacuum permittivity and permeability, respectively. Under the assumption that the medium under consideration is linear, isotropic, and homogeneous, supplementary *constitutive*

relations can be formulated:

$$\begin{aligned}\mathbf{J} &= \sigma\mathbf{E},\\ \mathbf{B} &= \mu\mathbf{H}\\ \mathbf{P} &= \varepsilon_0\chi\mathbf{E},\end{aligned} \tag{2.21}$$

where σ, μ, and χ are the conductivity, permeability and electric susceptibility of the medium and are introduced as phenomenological coefficients. It is further assumed that the fields are time-harmonic, i.e., the fields can be represented in the form:

$$\mathbf{E}_c(t) = \mathbf{E}_0 e^{-i\omega t} \tag{2.22}$$

with a complex amplitude $\mathbf{E}_0$. The field $\mathbf{E}(t)$ can be chosen to be real via considering the real and imaginary part of $\mathbf{E}_c(t)$. It is important to mention that σ, μ, and χ are frequency dependent functions $\sigma(\omega)$, $\mu(\omega)$, and $\chi(\omega)$. Plugging Eqs. (2.20) to (2.22) into Maxwell's equations Eq. 2.19 and applying $(\nabla\times)$ from the left yields

$$\begin{aligned}\nabla\times(\nabla\times\mathbf{E}) &= \omega^2\varepsilon\mu\mathbf{E}\\ \nabla\times(\nabla\times\mathbf{H}) &= \omega^2\varepsilon\mu\mathbf{H}.\end{aligned}$$

With some vector algebra the harmonic vector wave equations can be obtained:

$$\nabla^2\mathbf{E} + \mathrm{k}^2\mathbf{E} = 0 \tag{2.23}$$

$$\nabla^2\mathbf{H} + \mathrm{k}^2\mathbf{H} = 0, \tag{2.24}$$

where the complex permittivity $\varepsilon = \varepsilon_0(1+\chi) + i\frac{\sigma}{\omega}$ and $\mathrm{k}^2 = \omega^2\varepsilon\mu$ are introduced.
The strategy to find the solution for vector equations in 2.23 and 2.24 is to solve the scalar Helmholtz equation for ψ

$$\nabla^2\psi + \mathrm{k}^2\psi = 0. \tag{2.25}$$

Then,

$$\begin{aligned}\mathbf{M} &= \nabla\times(\mathbf{r}\psi)\\ \mathbf{N} &= \frac{\nabla\times\mathbf{M}}{k}\end{aligned} \tag{2.26}$$

are solutions for the vector wave equations Eq. 2.23.

As the symmetry of the system is spherical, it is best to solve Eq. 2.25 in spherical polar coordinates:

$$\frac{1}{r^2}\frac{\partial}{\partial r}\left(r^2\frac{\partial\psi}{\partial r}\right)+\frac{1}{r^2\sin\theta}\frac{\partial}{\partial\theta}\left(\sin\theta\frac{\partial\psi}{\partial\theta}\right)+\frac{1}{r^2\sin\theta}\frac{\partial^2\psi}{\partial\phi^2}+\mathrm{k}^2\psi=0 \tag{2.27}$$

With the ansatz

$$\psi(r,\theta,\phi)=R(r)\Theta(\theta)\Phi(\phi)z_n(\rho)$$

the odd and even solutions are

$$\begin{aligned}\psi_{eml}&=\cos m\phi P_l^m(\cos(\theta)).\\ \psi_{oml}&=\sin m\phi P_l^m(\cos(\theta)).\end{aligned} \tag{2.28}$$

$P_l^m(\cos(\theta))$ are the *associated Legendre functions*. The order m and the degree l are positive integers with $l\geq m$. $z_l(\rho)$ is either of the *spherical Bessel functions* of the first, second or third kind[1] j_l, y_l, $h_l^{(1)}=j_l+i\,y_l$, and $h_l^{(2)}=j_l-i\,y_l$. ρ is the dimensionless size parameter $\mathrm{k}r$. As the functions $\cos m\phi$, $\sin m\phi$, $P_l^m(\cos\theta)$, and $z_l(\rho)$ form a complete set, all functions that satisfy Eq. 2.25 can be expanded as an infinite series in the functions Eq. 2.28. Inserting Eq. 2.28 in Eq. 2.26 leads to

$$\begin{aligned}\mathbf{M}_{eml}=&\frac{-m}{\sin\theta}\sin m\phi P_l^m(\cos\theta)z_l(\rho)\hat{\mathbf{e}}_\theta\\ &-\cos m\phi\,\frac{\mathrm{d}P_l^m(\cos\theta)}{\mathrm{d}\theta}z_l(\rho)\hat{\mathbf{e}}_\phi,\\ \mathbf{M}_{oml}=&\frac{m}{\sin\theta}\cos m\phi P_l^m(\cos\theta)z_l(\rho)\hat{\mathbf{e}}_\theta\\ &-\sin m\phi\,\frac{\mathrm{d}P_l^m(\cos\theta)}{\mathrm{d}\theta}z_l(\rho)\hat{\mathbf{e}}_\phi,\\ \mathbf{N}_{eml}=&\frac{z_l(\rho)}{\rho}\cos m\phi\;l(l+1)P_l^m(\cos\theta)\hat{\mathbf{e}}_\mathbf{r}\\ &+\cos m\phi\,\frac{\mathrm{d}P_l^m(\cos\theta)}{\mathrm{d}\theta}\frac{1}{\rho}\frac{\mathrm{d}}{\mathrm{d}\rho}\left[\rho z_l(\rho)\right]\hat{\mathbf{e}}_\theta\\ &-m\sin m\phi\,\frac{\mathrm{d}P_l^m(\cos\theta)}{\mathrm{d}\theta}\frac{1}{\rho}\frac{\mathrm{d}}{\mathrm{d}\rho}\left[\rho z_l(\rho)\right]\hat{\mathbf{e}}_\phi,\end{aligned}$$

[1] The spherical Bessel functions of third kind are also known as the *spherical Hankel functions*.

$$\begin{aligned}\mathbf{N}_{oml} = \frac{z_n(\rho)}{\rho} \sin m\phi \; l(l+1) P_l^m(\cos\theta)\hat{\mathbf{e}}_\mathbf{r} \\ + \sin m\phi \; \frac{\mathrm{d}P_l^m(\cos\theta)}{\mathrm{d}\theta} \frac{1}{\rho} \frac{\mathrm{d}}{\mathrm{d}\rho} \left[\rho z_l(\rho)\right] \hat{\mathbf{e}}_\theta \\ + m \cos m\phi \; \frac{\mathrm{d}P_l^m(\cos\theta)}{\mathrm{d}\theta} \frac{1}{\rho} \frac{\mathrm{d}}{\mathrm{d}\rho} \left[\rho z_l(\rho)\right] \hat{\mathbf{e}}_\phi. \end{aligned} \tag{2.29}$$

The electric and the magnetic field are connected by $\nabla \times \mathbf{E} = i\omega\mu\mathbf{H}$, and the most general solution for the **E**- and **H**-field is

$$\begin{aligned}\mathbf{E} &= \sum_{s=o,e} \sum_{m=0}^{\infty} \sum_{l=m}^{\infty} B_{sml}\mathbf{M}_{sml} + A_{sml}\mathbf{N}_{sml}, \\ \mathbf{H} &= \frac{k}{i\omega\mu} \sum_{s=o,e} \sum_{m=0}^{\infty} \sum_{l=m}^{\infty} B_{sml}\mathbf{N}_{sml} + A_{sml}\mathbf{M}_{sml} \end{aligned} \tag{2.30}$$

The time evolution of the modes is easily added via multiplication by $e^{-i\omega t}$.

If the coefficients B_{sml} are all zero, the **E**-field does not have a component in the radial direction, the field mode is called *transverse electric* (TE). In the case that all A_{sml} are zero, the **H** field has no radial component, the field is said to be *transverse magnetic* (TM).

Natural modes

Until now, no further assumptions for the geometry were introduced. In order to find the modes of the dielectric sphere with a radius a from the general Eq. 2.30, the first step is to set the origin of the coordinate system in the center of the sphere. The fields have to be finite at the origin, which determines $z_l(\rho)$ to be $j_l(\rho)$. Outside the sphere, both j_l and y_l are well behaved and the expansion of the field in this region has to consider both these functions. Therefore, j_n is replaced by $h_l^{(1)}$, as well as the parameters k_1 and μ_1 of the sphere by k_2 and μ_2 of the surrounding medium.

For a TE mode, the boundary conditions

$$\begin{aligned} E_\theta^i = E_\theta^e \quad E_\phi^i = E_\phi^e, \\ H_\theta^i = H_\theta^e \quad H_\phi^i = H_\phi^e, \end{aligned} \qquad \text{at } r = a,$$

have to be fulfilled at the sphere surface. The superscripts i and e stand for the internal and external fields. This leads to the transcendent equations defining the coefficients of

the field,

$$B^i_{eml} j_l(\mathrm{k}_1 a) = B^e_{eml} h^{(1)}_l(\mathrm{k}_2 a),$$
$$\frac{1}{\mu_1} B^i_{eml} [\mathrm{k}_1 a \; j_l(\mathrm{k}_1 a)]' = \frac{1}{\mu_2} B^e_{eml} [\mathrm{k}_2 a \; h^{(1)}_l(\mathrm{k}_2 a)]'. \tag{2.31}$$

The prime denotes differentiation with respect to the argument $\mathrm{k_i} r$. Exactly the same equations hold true for the odd coefficients B_{oml}. For a given l, these conditions are fulfilled only by a discrete set of $x = \mathrm{k}_2 a$, given by the roots of the transcendental equation

$$\frac{[Nx \; j_l(Nx)]'}{\mu_1 j_l(x)} = \frac{[x \; h^{(1)}_l(x)]'}{\mu_2 h^{(1)}_l(x)}, \tag{2.32}$$

where the relative refractive index $N = n_1/n_2 = \mathrm{k}_1/\mathrm{k}_2$ was introduced.

A similar equation can be found for the TM modes:

$$\frac{[Nx j_l(Nx)]'}{N^2 j_l(Nx)} = \frac{\mu_2 [x h^{(1)}_l(x)]'}{\mu_1 h^{(1)}_l(x)}. \tag{2.33}$$

Eqs. (2.32) and (2.33) can be transformed to

$$\Delta_{\mathrm{TE}} = [Nx j_l(Nx)]' \mu_1 h^{(1)}_l(x) - \mu_2 [x h^{(1)}_l(x)]' N^2 j_l(Nx) = 0. \tag{2.34}$$
$$\Delta_{\mathrm{TM}} = [Nx \; j_l(Nx)]' \mu_2 h^{(1)}_l(x) - \mu_1 j_l(x) [x \; h^{(1)}_l(x)]' = 0. \tag{2.35}$$

For a given radius of the sphere a and a given number l, the roots ρ_n of Eqs. (2.34) and (2.35), labeled by the radial mode number $n = 1, 2, 3 \ldots$, define the frequencies of the *natural modes* (see Fig. 2.4). These are the modes of the electromagnetic field that can be supported by the sphere. As neither of the equations is dependent on m, the natural modes are degenerate in m and the labeling follows the conventions $\mathrm{TE}_{n,l}$ and $\mathrm{TM}_{n,l}$, respectively.

A short comment on the m degeneracy: It is lifted for not completely spherical resonators. In this case, the spherical symmetry is broken. To observe this splitting, the width of the resonances have to be smaller than the splitting. For small spheres of a few microns as they are used in the experiments presented in this thesis, this will not be the case, and therefore will not be discussed.

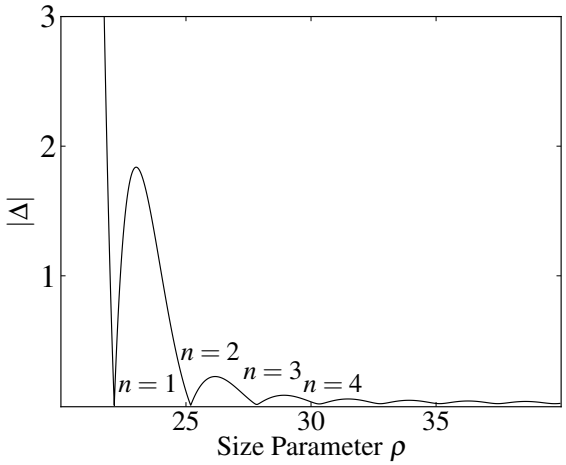

Figure 2.4.: The natural modes of a sphere are defined by the roots of the function $\Delta_{\mathrm{TE}} = [Nxj_l(Nx)]'\mu_2 h_l^{(1)}(x) - \mu_1 j_l(x)[xh_l^{(1)}(x)]'$ of which the absolute value is plotted. l is chosen to be 30, the refractive index of the sphere is 1.59, of the surrounding medium 1. The roots that define the radial mode numbers $n = 1, 2, 3, 4$ are indicated.

Field Distribution of the Whispering Gallery Modes

The vector fields of the natural modes are given by inserting the three parameters ρ_n, l, and m in Eqs. (2.29) and (2.30). n is denoted as the *radial* mode number, as the radial distribution of the field intensity has n maxima inside the sphere. For different values of n, the normalized radial intensity distributions of the field for $l = 30$ are plotted in Fig. 2.5a. For $n = 1$, the field is strongly confined at the surface of the sphere, with increasing n the field spreads more towards the center of the sphere. However, the relative amount of evanescent field outside the sphere is also increasing with increasing n. In the geometrical picture of the whispering gallery modes in Fig. 2.3, modes with $n = 1$ correspond to rays having incident angles close to the critical angle. After one turn, such a mode has to interfere constructively. For modes with smaller angle of incidence, the field is not confined that close to the surface and the field can interfere constructively after two or more turns. This corresponds to modes with higher n.

The angular distribution is given by the *angular* mode numbers l and m. The ϕ dependences can be seen directly: The functions $\cos m\phi$ and $\sin m\phi$ provide $2m$ maxima of the field on the equator plane. The θ dependence is given by the associated Legendre functions $P_l^m(\cos\theta)$. The θ dependence of the normalized field intensity distribution along the surface of the sphere is shown for different values of m with $n = 1$ and $l = 30$. The field is symmetric around $\pi/2$, revealing $l - m + 1$ maxima.

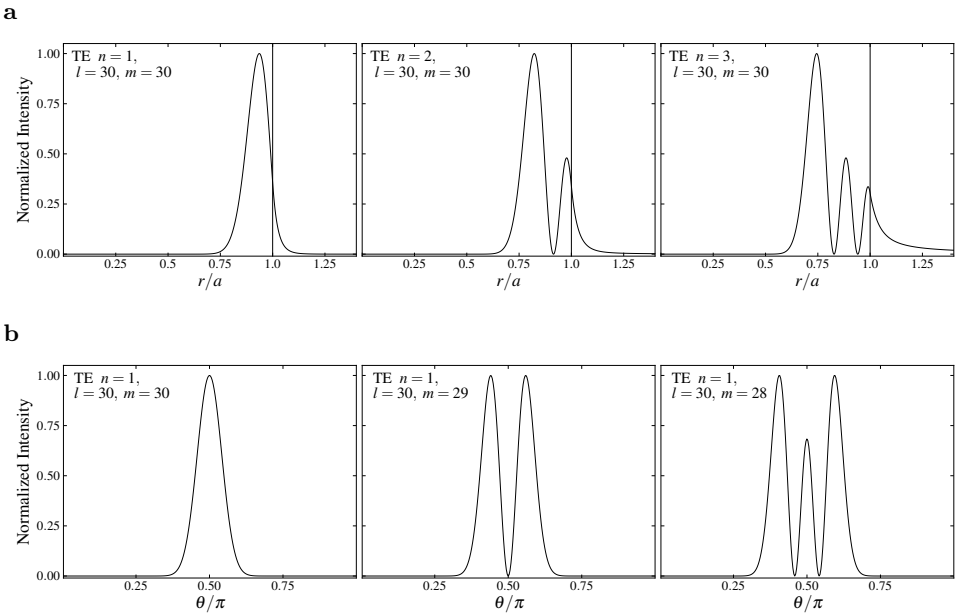

Figure 2.5.: a: Radial field intensity for a TE mode with different n, normalized to the intensity maximum. For higher n, the share of the evanescent field increases. b: Angular field intensity on the surface of the sphere for different values of m with $l - m + 1$ field maxima.

Bringing together the radial and the angular distribution, one can plot the fields on the xy- and xz-plane, shown in Fig. 2.6. Especially the leakage of the field outside the sphere for higher n modes can be seen very clearly.

For larger spheres, appropriate approximation for the spectral positions of the resonances and the field distributions of the whispering gallery modes can be derived (see, for example, Schiller [60] and Gorodetsky and Ilchenko [61] and references therein). However, the angular mode number l has to be higher than 30 to have an acceptable error [60]. The spheres used in this work do not fulfill this condition, they are too small to use these approximations and the full theory has to be used to calculate the resonances.

2.2.3. Mie Theory and Whispering Gallery Modes

When light strikes on an object, the light can change its direction, the effect known as *scattering*. The scattering direction and intensity are strongly dependent on the exact size, shape, and material of the object, as well as on the wavelength of the light. For the scattering from dielectric spheres, pronounced, narrow peaks are visible in the scattered

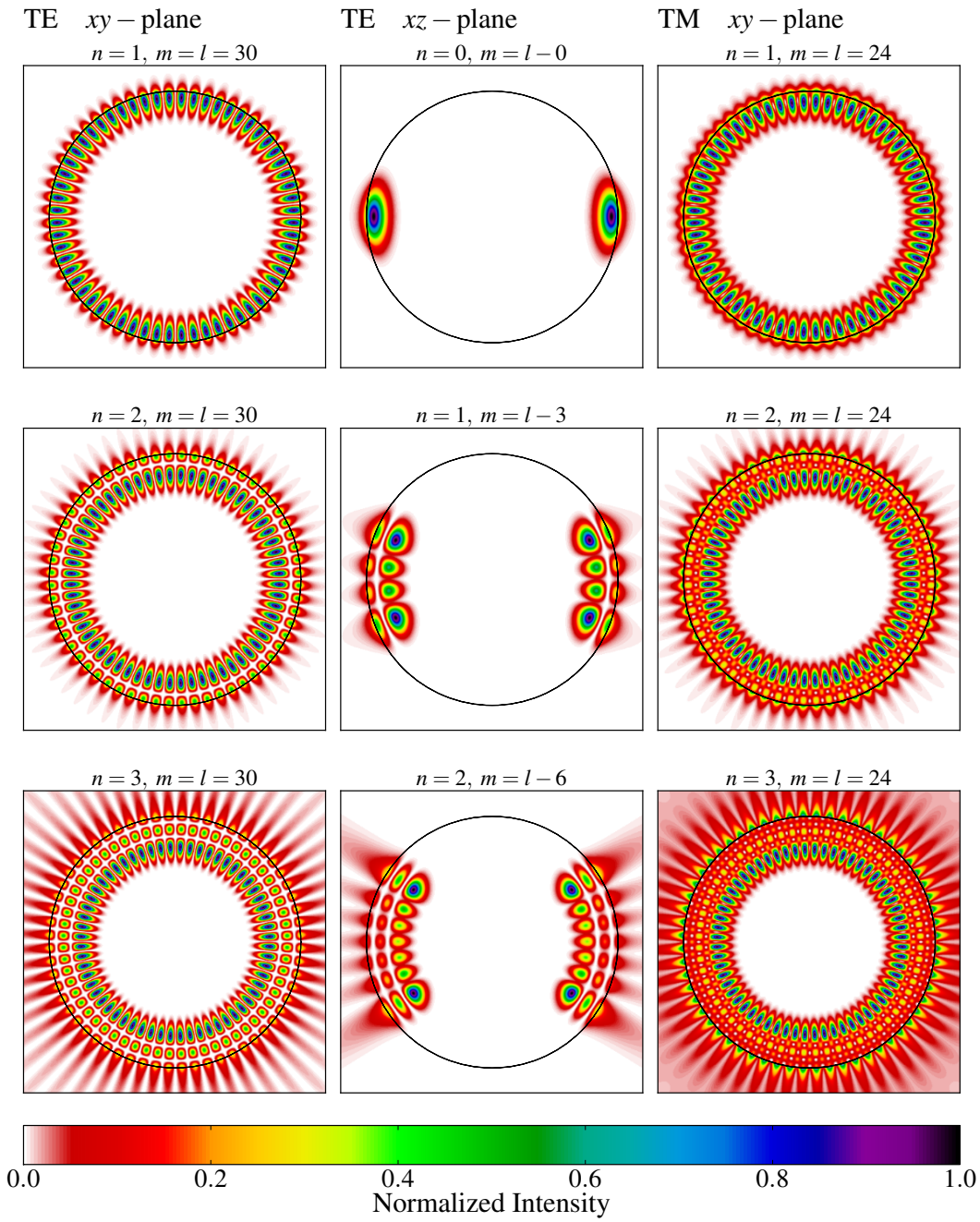

Figure 2.6.: Field intensity of the electric field on the xy- and xz-plane distribution for TE and TM modes with different n, l, and m. The surface of the sphere is indicated by the black line. The TM field is discontinuous at the surface.

light. The theoretical explanation of scattering by small particles goes back to 1908 and was developed by Gustav Mie [62]. The treatment of the scattering by a spherical particle is very similar to the considerations to find the eigenmodes of the sphere: The incoming and scattered fields are expanded in terms of the basis functions in spherical coordinates in Eq. 2.29. If the incoming wave is a plane wave, only the coefficients A_{o1l} and B_{e1l} are non-zero, denoted as a_l and b_l and are given by [63]

$$a_l = \frac{N^2 j_l(Nx)\left[x j_l(x)\right]' - j_l(x)\left[N x j_l(Nx)\right]'}{N^2 j_l(Nx)\left[x h_l^{(1)}(x)\right]' - h_l^{(1)}(x)\left[N x j_l(Nx)\right]'}, \tag{2.36}$$

$$b_l = \frac{j_l(Nx)\left[x j_l(x)\right]' - j_l(x)\left[N x j_l(Nx)\right]'}{j_l(Nx)\left[x h_l^{(1)}(x)\right]' - h_l^{(1)}(x)\left[N x j_l(Nx)\right]'}, \tag{2.37}$$

where the permeability is assumed to be one and the same nomenclature is used as in Eqs. (2.32) and (2.33). The scattering cross section C_{sca} is given by:

$$C_{\mathrm{sca}} = \frac{2\pi}{k^2} \sum_{n=1}^{\infty} (2n+1)(\mid a_n \mid^2 + \mid b_n \mid^2), \tag{2.38}$$

The values of a_l and b_l for a certain l are dominant under the condition that the denominator vanishes which turns out to be similar to the Eqs. (2.32) and (2.33). Therefore, the scattering or Mie resonances are identical to the natural frequencies where the whispering gallery modes occur.

The scattering cross sections for a polystyrene sphere with a diameters of around 4.8 µm and 7.6 µm are shown in Fig. 2.7 for the spectral range between 650 and 700 nm. In such calculations, the material dispersion has to be taken into account. This is done by fitting the dispersion of the refractive index by $n = 1.5663 + 0.00785\mu\mathrm{m}^2/\lambda^2 + 0.000334\mu\mathrm{m}^4/\lambda^4$ [64].

The different modes are clearly visible and are labeled with their radial and angular mode numbers. With increasing size, the distance between TE and TM modes with the same n and $\Delta l = 1$ (the free spectral range), is decreasing.

2.2.4. Microspheres as Resonators

Q-Factor of a Microsphere

The Q-factor introduced in Section 2.1.2 is a measure for the ability to store light within the cavity. In a resonator, usually more than one loss channel contribute to the overall loss rate, each of them associated with a specific Q-factor.

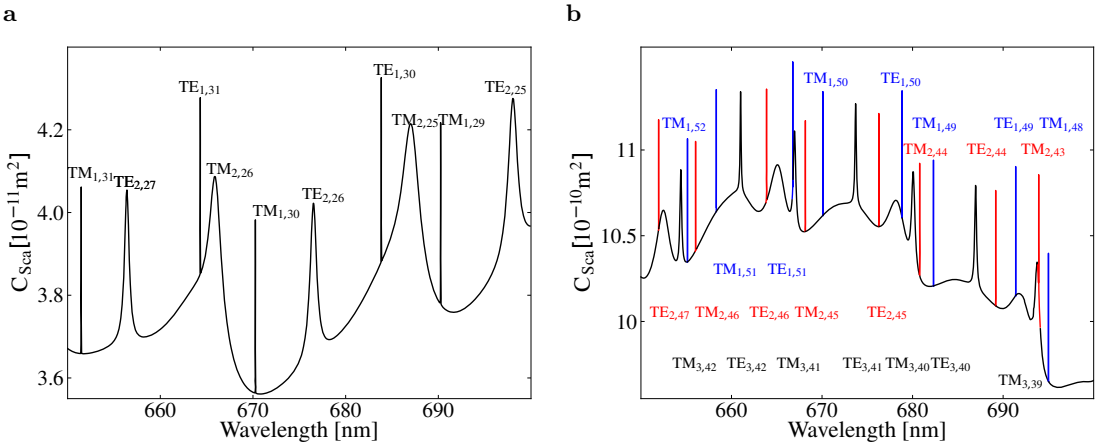

Figure 2.7.: Calculated scattering cross section for two spheres with diameters of a: 4.843 µm and b: 7.668 µm. For the larger sphere in b the modes with $n = 1, 2, 3$ are colored in blue, red, and black, respectively, for easier assignment of the labeling.

In a spherical microresonator, four main loss mechanisms contribute to the overall Q-factor:

- the intrinsic radiative (or curvature) losses of the cavity Q_{rad},
- the absorption losses in the material Q_{abs},
- the scattering losses on the surface Q_{scat} due to imperfection of the surface, and
- losses due to adsorbed water and contamination on the surface Q_{cont}.

The overall Q-factor is then given by

$$\frac{1}{Q} = \frac{1}{Q_{\mathrm{rad}}} + \frac{1}{Q_{\mathrm{abs}}} + \frac{1}{Q_{\mathrm{scat}}} + \frac{1}{Q_{\mathrm{cont}}}. \tag{2.39}$$

For small spheres, the intrinsic losses dominate because the curvature of the surface is too strong to provide total internal reflection. However, to obtain high Purcell factors (Eq. 2.15) reflecting better coupling between an emitter and the cavity, the mode volume should also be small. For that reason, there exist optimal radii of spheres for which best results are expected [38].

Among the multitude of cavity configurations, microsphere resonators are of special interest because they provide highest Q-factors as well as small mode volumes [37]. Q-factors up to 1×10^{10} are possible in the visible range with fused silica microspheres [65]. Furthermore, microsphere resonators with these superior properties can be realized from very different materials and a wide range of optical active doping materials. For example, lasing could be demonstrated in microdroplet [66, 67], polymer [68], and silica micro-

spheres [69, 70], doped or coated with dye molecules and semiconductor nanocrystals. They are also ideal constituents for more complex structures as photonic molecules or coupled resonator optical waveguides [71, 72]. Strong-coupling of emitters to microspheres could also be observed [40, 73], and they were employed as model systems to study fundamental analogies between quantum optical systems and photonic structures as well [39, 74, 75].

2.3. Gold Nanospheres as Optical Antennas

Antennas are a cornerstone of modern communication. Their ability to convert the energy of a localized electric current into propagating electromagnetic waves and vice versa is the today's basis for data transmission and reception. Specific antenna designs allow to control the directional emission pattern. Common to all these designs is that the dimension of the antenna has to be in the order of $\lambda/2$ to obtain an antenna resonance at the desired wavelength. In this case, the antennas fully support the emission of the wave and are most efficient.

This is one reason why the study of antennas for optical frequencies is still a young and emerging research field, while antennas for radio frequencies are established for more than 80 years: The dimensions of the antenna structures have to be on the submicrometer range for visible light [76, 77]. However, with the advances in fabrication and the better control on this size scale, the road is prepared for the investigation of optical antenna systems, or more generally, the interaction of light and emitters in the vicinity of metal (nano-)structures.

One of the most prominent effects occurring when metal structures interact with emitters is SERS, surface-enhanced Raman scattering [78, 79]. Raman scattering, the inelastic scattering of light by a molecule under the creation or annihilation of a vibration quantum of the molecule, is usually very inefficient, as it is a process of second-order. By employing metal nanostructures, however, the signal can be enhanced by 14 orders of magnitude, so that even the Raman signal of single molecules could be observed by Kneipp et al. [80] and Nie and Emory [81].

Not only the effects on non-linear processes like Raman scattering or second-harmonic generation [82] are of interest: The seminal studies of Drexhage and coworkers [46, 83, 84] explored the influence of the proximity of a metal layer on the fluorescence properties of dye molecules. They could show how the lifetime and the direction of the molecules' fluorescence is changed due to the presence of the metal and since then, numerous studies (see for example [85–93]) investigated the influence of different metal structures

on the properties of emitters nearby. Depending on the exact experimental configuration, quenching (suppression) and enhancement of emission could be observed. To understand this, the interaction of emitters, metal structures, and emitters will be discussed in the following, the concepts of a new research field that has opened up: plasmonics.

2.3.1. Localized Surface Plasmons

The Dielectric Function in the Drude Model and Volume Plasmons

The optical properties of metals in the visible range are governed by the electrons in the conduction band. These electrons can be excited to collective oscillations, which are described as quasi-particles, the *plasmons* [94]. They are the quantized, harmonic solutions of the classical Maxwell's Eqs. (2.19) inside the metal.

The Drude model describes the conduction band electrons as free electrons in a plasma sea and one can start with a simple equation of motion for an electron, accelerated by an electric field $\mathbf{E}$:

$$m^\star \ddot{\mathbf{x}} + m^\star \gamma \dot{\mathbf{x}} = -e\mathbf{E}. \tag{2.40}$$

$m^\star$ and e are the electron's effective mass and its charge. The second term accounts for damping, mainly due to collisions of the electrons. The solution of Eq. 2.40 for a harmonic driving field $\mathbf{E}(t) = \mathbf{E}_0 e^{-iwt}$ is given by

$$\mathbf{x}(t) = \frac{e}{m^\star(\omega^2 + i\gamma\omega)}\mathbf{E}(t). \tag{2.41}$$

These oscillations can be connected to the macroscopic polarization $\mathbf{P}$ via $\mathbf{P} = -ne\mathbf{x}$, where n is the electron density. Using Eq. 2.20 one finds

$$\mathbf{D} = \varepsilon_0 \left(1 - \frac{\omega_\mathrm{p}^2}{\omega^2 + i\gamma\omega}\right)\mathbf{E}, \tag{2.42}$$

where $\omega_\mathrm{p} = \sqrt{\frac{ne^2}{\varepsilon_0 m^\star}}$ is the plasma frequency of the free electron gas. Furthermore, the dielectric function $\epsilon(\omega)$ defined by $\mathbf{D} = \varepsilon_0\epsilon(\omega)\mathbf{E}$ can be expressed by

$$\epsilon(\omega) = 1 - \frac{\omega_\mathrm{p}}{\omega^2 + i\gamma\omega} \tag{2.43}$$

or

$$\epsilon(\omega) = \epsilon_1(\omega) + i\epsilon_2(\omega) \tag{2.44}$$

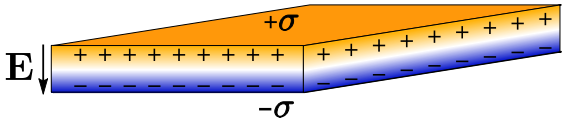

Figure 2.8.: A volume plasmon: the longitudinal oscillation of the electron cloud, in a thin slab. The displacement of the charge distribution establishes an electric field, acting as restoring force.

with the real and imaginary components

$$\epsilon_1(\omega) = 1 - \frac{\omega_\mathrm{p}^2\tau^2}{1+\omega^2\tau^2} \quad \text{and} \quad \epsilon_2(\omega) = \frac{\omega_\mathrm{p}^2\tau}{\omega(1+\omega^2\tau^2)}, \tag{2.45}$$

respectively, where $1/\gamma = \tau$ was used.

For low frequencies, it can be shown that the metal is absorptive and the complex refractive index $\tilde{n}(\omega) = \sqrt{\epsilon(\omega)}$ can be introduced [95] .
For high frequencies, the dielectric function reduces to

$$\epsilon(\omega) = 1 - \frac{\omega_\mathrm{p}^2}{\omega^2} \tag{2.46}$$

and with the definition of k following Eq. 2.24, one obtains the dispersion relation for transverse electromagnetic waves

$$\omega^2 = \omega_\mathrm{p}^2 + k^2c^2, \tag{2.47}$$

with $c = 1/\sqrt{\varepsilon_0\mu_0}$, which can only be fulfilled for $\omega > \omega_\mathrm{p}$. Transverse electromagnetic waves are forbidden for $\omega < \omega_\mathrm{p}$, the metal is reflective.

In the special case that $\omega = \omega_\mathrm{p} = 0$, ϵ vanishes and $\mathbf{D} = 0 = \varepsilon_0\mathbf{E} + \mathbf{P}$. Therefore, the electric field is a pure depolarization field. This can be interpreted as a collective displacement in a thin slab of the electron gas within the metal (Fig. 2.8) leading to surface charges $\sigma = \pm neu$ on the slab boundaries, which establishes an electric field $\mathbf{E} = \frac{neu}{\varepsilon_0}$. It acts as a restoring force on the displaced electron cloud and the equation of motion for the displacement is

$$\begin{aligned} nm\ddot{u} &= -\frac{n^2e^2u}{\varepsilon_0} \\ \ddot{u} + \omega_\mathrm{p}^2 u &= 0. \end{aligned} \tag{2.48}$$

Therefore, ω_p is the natural frequency of a free oscillation of the electron density. The

quanta of this oscillation are the so-called *plasmons*, or, more precisely, volume plasmons, to distinguish them from oscillations on the surface or localized oscillations in nanometer-sized particles.

It has to be mentioned that the Drude model of a free electron gas can describe the dielectric function $\epsilon(\omega)$ very accurately, but for high frequencies the model breaks down due to interband transitions. This drawback can be overcome by introducing a resonance in Eq. 2.40:

$$m\ddot{\mathbf{x}} + m\gamma\dot{\mathbf{x}} + m\omega_0^2\mathbf{x} = -e\mathbf{E}. \tag{2.49}$$

This modification, known as the Drude-Lorentz model, is of significant importance, as for the finite-difference time-domain (FDTD) method an analytic expression for $\epsilon(\omega)$ is needed [96].

Plasmons at an Insulator–Metal Interface: Surface Plasmon Polaritons

For an interface between a conductor and a dielectric, Maxwell's equations allow another kind of solutions, *surface plasmon polaritons*, propagating along the interface [97]. Their possibility to confine and manipulate an electromagnetic wave below the diffraction limit is the characteristic feature of plasmonics [98].

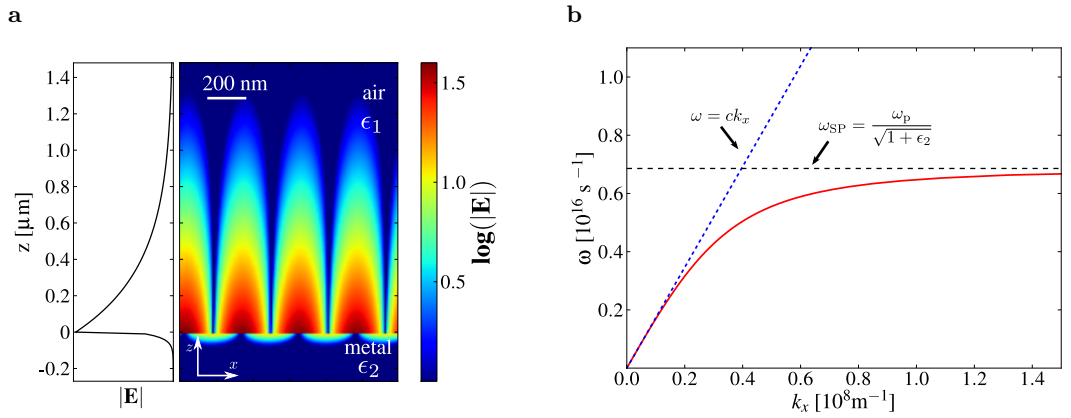

Figure 2.9.: a: Field distribution of a surface plasmon polariton at an interface of gold and air. The vacuum wavelength of the field is 650 nm, ϵ_2 is taken from ref. [99]. The curve on the left presents the field strength along a cut along the z-direction, showing the decay on both sides of the interface. b: Dispersion relation for surface plasmon polartions using the Drude model and a plasma frequency $\omega_p = 13.71 \times 10^{15}\,s^{-1}$ for gold [100]. For small k_x, the dispersion approaches the light line $\omega = ck_x$, for large k_x the value $\omega_{SP} = \omega_p/\sqrt{1+\epsilon_2}$.

The solutions of Maxwell's equations have to fulfill the boundary condition at the interface [95], where the normal component of the **D**-field and the tangential component of the **H**-field have to be continuous. This leads to the conditions for the wavevectors in the z-direction (Fig. 2.9a) k_1 and k_2 within the dielectric and the metal, respectively:

$$\frac{k_2}{k_1} = -\frac{\epsilon_2}{\epsilon_1}. \tag{2.50}$$

The field distribution at an air–gold interface is shown in Fig. 2.9a for a field with $\lambda = 650\,\text{nm}$ in free space using experimental data from Johnson and Christy [99] for the dielectric function of gold. The surface plasmon polaritons decay exponentially in both materials, typically on the order of half the wavelength (300 nm) in air and the skin depth (20 nm) inside metal.

With the wavevector k_0 in free space for the field, the dispersion relation for the wavevector in x-direction k_x becomes

$$k_x = k_0\sqrt{\frac{\epsilon_1\epsilon_2}{\epsilon_1 + \epsilon_2}}. \tag{2.51}$$

Using the Drude model (Eq. 2.46) for ϵ, the dispersion relation is depicted in Fig. 2.9b. For small k_x, the dispersion curve adapts the light line $k = \omega/c$. At large k_x, the $\omega \to \omega_{\text{SP}} = \omega_{\text{p}}/\sqrt{1+\epsilon_2}$, and therefore, the group velocity goes against 0, i.e., the surface plasmon polariton is of electrostatic characteristic.

The Drude model fails at higher frequencies, however, it reveals that the dispersion curve stays on the left side of the light line. Therefore, it is not possible to directly excite surface plasmon polaritons with light, since not both energy and momentum conservation can be fulfilled at the same time. More complex configurations using prisms or gratings have to be applied to excite surface plasmon polaritons [14, 97].

Plasmons in Metal Nanoparticles

Closely related to the surface plasmons polaritons are the *localized surface plasmons*, occuring in metallic nanoparticles. In contrast to the volume plasmon and surface plasmon polariton, a light field can excite the conduction band electrons directly to collective oscillations in a nanoparticle (see Fig. 2.10a).

The theoretical framework that reveals the optical response of a spherical metal particles in a light field is again Mie theory introduced in Section 2.2.3 [101]. Normalized scattering spectra of gold nanospheres with three different diameters in air are shown in Fig. 2.10, where the experimentally determined values for the complex refractive index

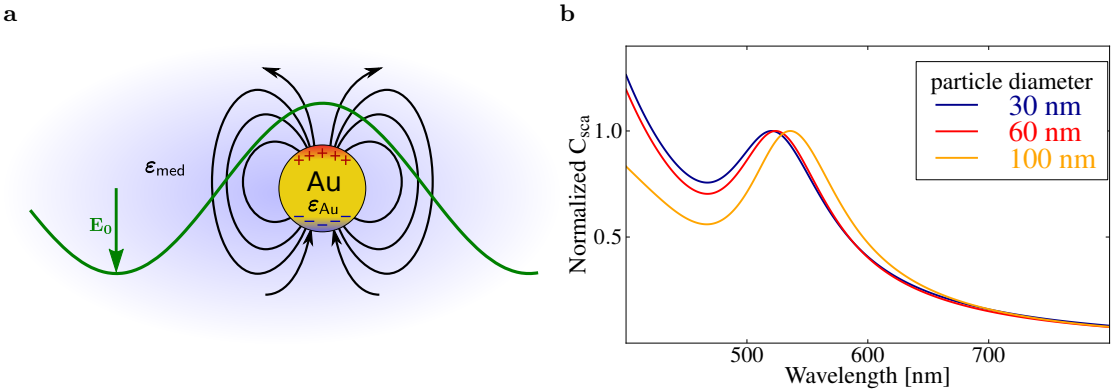

Figure 2.10.: a: Excitation of a localized surface plasmon. The light wave excites the conduction band electrons to a collective oscillation. b: Normalized calculated scattering cross section of gold nanoparticles in air with different sizes using Mie theory.

from Johnson and Christy [99] are used. The size-dependent resonance around 550 nm is associated with the excitation of the localized surface plasmon.

The effects of scattering and absorption of light by small metallic particles was already exploited by the Romans, as can be seen in the British Museum: The glass in the Lycurgus Cup (400 AD) has a greenish color (see Fig. 2.11), but when lightened up from inside, the color is a bright red. When the light falls *on* the cup, the light that is seen by the eye is the light that is scattered back by the metallic particles incorporated in the glass. These particles have a scattering resonances in the green, the greenish glow. When the light shines through the glass, the red color originates from the remaining light that is neither absorbed nor scattered out of the beam.

It is very instructive to consider the case of a particle with a diameter d well below the incident wavelength λ, the so-called Rayleigh regime. In this case, the field does not vary significantly over the particle and the quasi-static approximation can be applied. The response of the particle to the light field can be determined by solving Maxwell's equations for the nanosphere in a static electric field. It turns out that a static electric field induces a dipole moment in the sphere with a dipole moment of [63]

$$\mathbf{p} = 4\pi\varepsilon_0\epsilon_m a^3 \frac{\epsilon_s - \epsilon_m}{\epsilon_s + 2\epsilon_m}\mathbf{E}_0, \tag{2.52}$$

where a is the sphere radius, ϵ_m and ϵ_s are the respective dielectric functions of the surrounding medium and the sphere, and $\mathbf{E}_0$ is the homogeneous incident field. The field outside the sphere is just the superposition of the incident field and the field of the

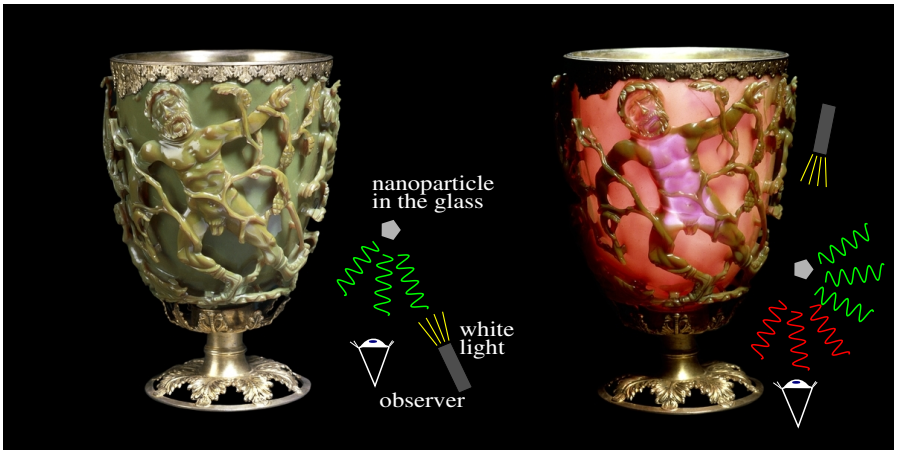

Figure 2.11.: The Lycurgus Cup from 400 AD: In the glass, gold and silver nanoparticles are incorporated. When the light shines on the glass, the color that is seen stems from the light that is scattered back. If the cup is illuminated from inside, the color is the residual light that is not scattered or absorbed by the nanoparticles. Images courtesy of *www.britishmuseum.org*

induced dipole:

$$\mathbf{E}_{\text{out}}(\mathbf{r}) = \mathbf{E}_0 + \frac{3\mathbf{n}(\mathbf{n}\cdot\mathbf{p}) - \mathbf{p}}{4\pi\varepsilon_0\epsilon_m}\frac{1}{r^3}, \tag{2.53}$$

where r is the length of $\mathbf{r}$ and $\mathbf{n}$ is the unit vector $\mathbf{r}/r$.

If the static field $\mathbf{E}_0$ is replaced by a time-harmonic field $\mathbf{E}_0 e^{-i\omega t}$, the induced dipole starts to radiate, leading to the scattering as described above by Mie theory. Also a resonance condition can be found: In Eq. 2.52 the dipole moment is maximal for a minimal $|\epsilon_s + 2\epsilon_m|$, the so-called Fröhlich condition. This is associated to the excitation of a *dipole surface plasmon*. If the resonance condition is fulfilled, a maximal field enhancement can be observed at the *poles* of the metal nanosphere. It is obvious that the simplified model does not include the size-dependence of the resonance shown in Fig. 2.10b. However, Mie calculations show that the localized surface plasmon resonance for small particles converges towards the dipole surface plasmon limit.

In all the previous considerations, the implicit assumption was made that the dielectric function $\epsilon(\omega)$ is not a function of the size. This is correct for particles with diameters larger than 20 nm [102, 103] and in this work, only particles above this limit are employed, but one has to keep in mind that below that limit quantization and surface effects occur [102].

Spherical nanoparticles are a model system to study localized surface plasmons as the solution of the fields associated with them can be obtained analytically. Nevertheless,

recent advances in the chemical, lithographic, and electron-/ion-beam preparation allow all kinds of particles, structures, and coupled systems with different shapes and sizes and a variety of materials, allowing to find plasmon resonances almost over the complete visible range [104–108]. Especially the formation of so-called *hot spots* in narrow gaps between plasmonic structures has recently drawn a lot of attention [107, 109–112].

2.3.2. Metal Nanoparticle as Antennas for Optical Frequencies

In a fluorescence measurement, where emitters are excited by a laser and the fluorescence is analyzed, a metal (nano-)structure can alter the field distribution of the incoming excitation light, and this can already change the fluorescence behavior of the emitter nearby the structure. Furthermore, a metal structure does also "respond" to the charge oscillations in the excited emitter. Therefore, three effects have to be considered in the analysis of the fluorescence of emitters near a metal structure

- a change of the excitation field,
- modified transition rates and a modified angular distribution of the emission, and
- introduction of new nonradiative channels.

Depending on the shape and material of the structure, its position and orientation, and the excitation and emission wavelength of the emitter, the effects sum up to an overall enhancement or quenching of the emission in optical fluorescence experiments.

In the following, these aspects will be discussed in more detail for metal nanospheres.

Localization of the Excitation Field

When a laser beam is focused onto a metallic nanospheres, strong field enhancement occurs on the poles of the nanosphere, where the axis is defined by the polarization of the incoming light. There are two effects that add up to this field localization: first, the *lightning-rod effect* [113] and second, the excitation of a localized surface plasmon as described above. The first effect is due to screening of the interior of the sphere by the electron gas and the concentration of the field lines due to the boundary conditions.

The calculation of the fields around a metallic nanosphere is straight forward for an isolated sphere and the illumination with a plane wave by applying the Mie theory, as already seen above. However, a closed form solution for the slightly more complex geometry of a metallic sphere on a glass interface is not available, and numerical methods have to be applied. One powerful tool is the finite-difference time-domain method (FDTD). In this method, the simulation area is discretized by a grid and the field evolution is directly calculated by the Maxwell equations in the (discretized) time-domain [114]. In

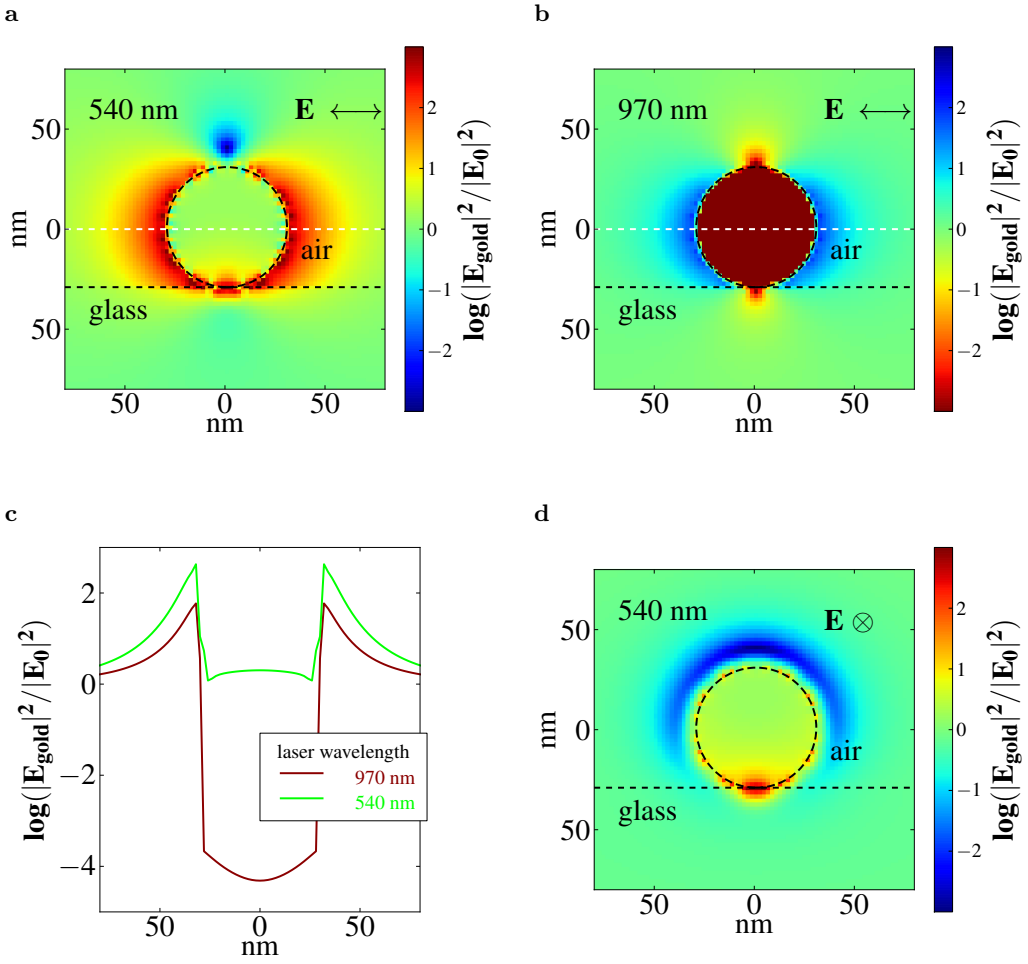

Figure 2.12.: Plots of FDTD calculation of the field-intensity enhancement around a gold nanosphere with a diameter of 60 nm on a glass substrate with index of refraction of $n = 1.4$.. a and b: Intensity ratio between the field $\mathbf{E}_{\text{gold}}$ with and the undisturbed field $\mathbf{E}_0$ without the gold sphere on the plane parallel to the incident light field with a wavelength of 540 and 970 nm, respectively. c: Intensity ratio along the dashed white lines in a and b. d: Intensity ratio on the plane orthogonal to the incident light field. The borders of the gold sphere and the glass substrate are indicated by the dashed, black lines.

this work, FDTD simulations were performed using a commercial FDTD package [115].

The field distribution $\mathbf{E}_{\text{gold}}$ around a gold nanosphere with a diameter of 60 nm placed on a glass interface in a tightly focused Gaussian laser beam (NA=1.4) is numerically calculated for two different laser wavelengths, 540 nm and 970 nm. The first wavelength is centered directly in the plasmon resonance, the second far off resonance. In the

experiments of this work, these are the excitation wavelengths. For normalization, the field $\mathbf{E}_0$ is also simulated without the gold nanosphere. The nanosphere is centered in the origin, the electric field is aligned along the x-coordinate. The normalized intensity ratio $\mathbf{E}_{\text{gold}}/\mathbf{E}_0$ without the sphere on the xz-plane is plotted for both wavelengths Fig. 2.12a and b, i.e., the plane parallel to the polarization of the electric field $\mathbf{E}$.

The difference for the two wavelengths is clearly visible: For both, the field is enhanced around the sphere on the xy-plane. However, in the case where the wavelength matches the plasmon resonance, the field intensity enhancement around the sphere is ten times higher than in the case of the off-resonant laser beam (Fig. 2.12c). Furthermore, the interior of the sphere is almost field free for the off-resonant laser beam, while in the resonant case the field inside the nanosphere is comparable to the field without the nanosphere. This highlights the difference between the resonant case, where a plasmon is excited, and the pure screening effect in the off-resonant case.

In the plane orthogonal to the polarization of the incident beam, the field is attenuated for both cases. As an example, the data for 540 nm is shown in Fig. 2.12d.

Therefore, depending on the position with respect to the nanostructure and/or the polarization of the incoming beam, an emitter can observe an excitation field that might vary from strongly enhanced to attenuated.

Change of Dipole Emission in the Vicinity of a Metal Nanoparticle

In the vicinity of a metallic nanoparticle, both the radiative and the nonradiative decay rates of the emitter are changed. The radiative decay rate is altered by the self-field $\mathbf{E}_{\text{s}}$ as described in Eq. 2.9. The second effect only shows up in close proximity: a new nonradiative decay channel opens via direct energy transfer to the gold sphere.

Ruppin [116] calculated both radiative and nonradiative rates using a classical approach: The radiative rate can be found by calculating the field scattered by the dipole–nanosphere system [117], evaluating the Poynting vector, and integrating the energy flux through the surface of a large sphere, enclosing the system [63]. The nonradiative rate is given by the rate at which energy is absorbed in the sphere. Classically, the nonradiative decay can be interpreted as induced currents in the sphere that dissipate into heat by the resistivity of the metal. The nonradiative rate is given by [116]

$$\gamma_{\text{nr}} = \frac{1}{2} \int\limits_{V_{\text{sph}}} \sigma(\omega) |\mathbf{E}(\mathbf{r}, (\omega))|^2 d\mathbf{r}, \tag{2.54}$$

where $\sigma(\omega) = \text{Im}\{\epsilon(\omega)\}\omega\varepsilon_0$ is the conductivity of the metal.

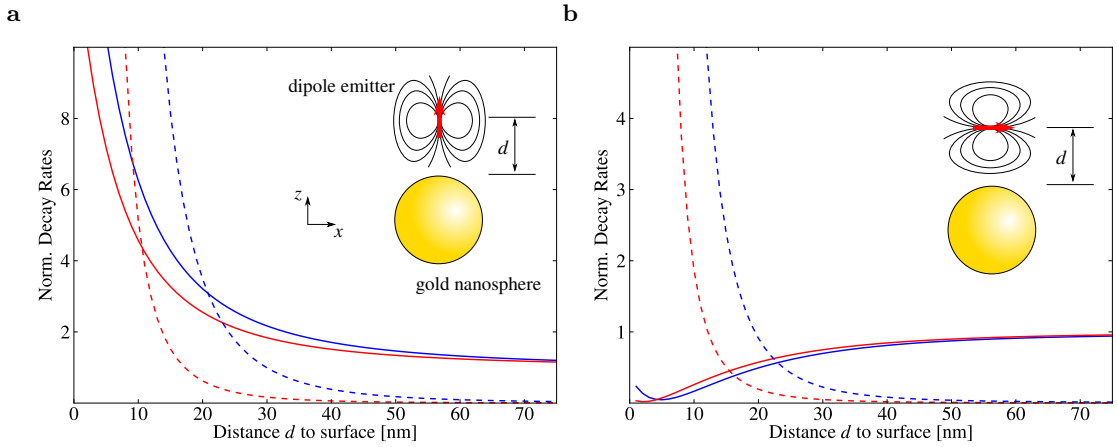

Figure 2.13.: Radiative (full lines) and nonradiative (dashed lines) decay rates for a dipole emitter with emission wavelengths 580 nm (blue) and 700 nm (red) close to a gold sphere with a diameter of 60 nm as a fucton of the distace d from the sphere's surface. The rates are normalized to the free space radiative decay. The dipole orientation is indicated in the picture.

Using the model of Ruppin [116], the radiative γ_r and the nonradiative γ_{nr} decay rates for dipoles as a function of the distance to a gold nanosphere are shown in Fig. 2.13, normalized to the radiative rate of the respective free dipole. The emitter is assumed to have an intrinsic quantum yield of one. The diameter of the gold sphere is 60 nm, the dielectric function is again obtained from Johnson and Christy [99]. With the sphere located in the origin and the dipole on the z-axis, two polarizations of the dipole are considered: the dipole moment $\boldsymbol{\mu}$ parallel to the z-axis and parallel to the x-axis (see insets). Furthermore, the calculations are performed for two different emission wavelengths, one (580 nm) in resonance with the surface plasmon, the second (700 nm) well above the resonance.

For both polarizations, γ_{nr} is more strongly enhanced for 580 nm than for 700 nm, as the dipole couples more efficiently to the plasmon resonance. The same is true for γ_r and dipole oriented parallel to the sphere surface (Fig. 2.13a). However, when the dipole moment is oriented perpendicular to the surface, the emission is suppressed by the gold nanosphere.

2.3.3. Overall Effect on the Emission

To obtain the overall effect, one has to examine the following three influences:

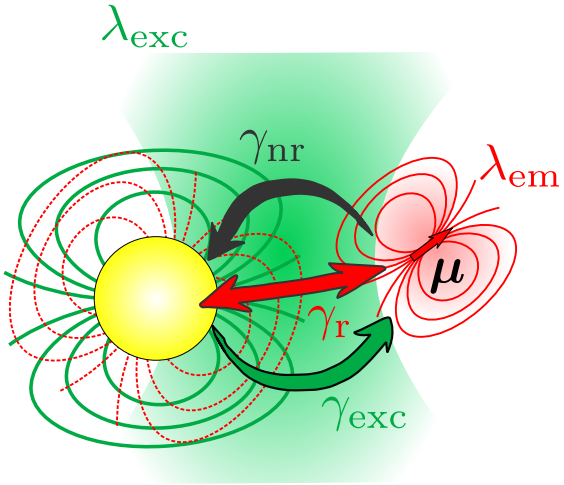

Figure 2.14.: Influences of a metal nanoparticle on the fluorescence: 1. The particle changes the excitation field and therefore the excitation rate γ_{exc}. 2. The dipole observes its own field scattered back by the nanoparticle, the self-field $\mathbf{E}_{\mathrm{s}}$, changing the radiative emission rate γ_{rr}. 3. A new decay channel is introduced by dissipation of energy at a rate γ_{nr} in the particle. Due to the resonance of the plasmon, all three effects are dependent on the wavelength.

1. the modification of the excitation by redistribution of the exciting field,
2. the influence on the radiative decay, and
3. the contribution of the new nonradiative decay channel.

These effects are sketched in Fig. 2.14. As already indicated above, depending on the exact experimental configuration, enhancement or reduction of the fluorescence intensity is observed [90, 118], as it is very nicely shown in one experiment by Anger et al. [44] by varying the distance between a single molecule and a gold nanosphere attached to a scanning probe.

2.4. Conclusion

In this chapter, it was shown how the properties of emitters are altered by their environment. The two possibilities that are studied in this work, microsphere resonators and metallic nanoantennas, have been discussed. The photonic mode density which is determined by the emitter's surrounding defines the emission properties. Thus, a future challenge is to design structures with photonic mode densities that provide spontaneous emission as desired.

CHAPTER 3

A Multifunctional Setup for Hybrid Investigation and Assembly

Today's optical experiments on the nanoscale face two major limitations:

First, optical investigation of ever smaller physical systems hits the point where important properties of the subject of interest become smaller than what can be "seen" and identified by optical microscopy. The shape, the size, or the environment, which can determine the emission, are "hidden" within the resolution limit. Therefore, additional experimental techniques are required to collect further information.

Second, to get a step further than the sole investigation, e.g., to study the influence of the environment, it is necessary to have the tools to intervene actively and manipulate on the sample, e.g., to change the position or surrounding of an emitter.

To overcome these limitations, the experimental setup used in this work combines an optical microscope with scanning probe techniques. At the heart of the setup there is an inverted confocal microscope, a standard device in research laboratories nowadays. Two different scanning probe techniques can be employed to supplement the optical setup: an atomic force microscope (AFM) and a scanning near-field optical microscope (SNOM). This allows investigation and manipulation with nanometer resolution and precision via the AFM and – besides the optical near-field investigation – manipulation on the micrometer scale with the SNOM.

The assembly and coupling of fundamental photonic entities under direct optical observation of such high precision can not be obtained by direct nanofabrication like lithographic or self-assembly techniques. Furthermore, there is the possibility of a characterization of the individual constituents *before* and further modification of the systems *after* assembly in such a *hybrid* approach.

3.1. Optical Setup

3.1.1. Confocal Microscopy

Conventional Microscopy

The resolution of an optical imaging system is its capability to reproduce the details of an object in the generated image. Due to the wave nature of light, the resolution is limited, as diffraction does not allow transfer of a point-like object into a point-like image. The function that describes the image of a point-like object is the *point-spread function* (psf) or *point-transfer function*. The transfer of the electromagnetic wave by a source is best described using the theory of Fourier transformation, and the psf of a microscope with round apertures in the light path turns out to be a two-dimensional Airy pattern perpendicular to the optical axis. Mathematically, this is the result of the convolution of a delta function for the point source and a two-dimensional aperture function[1]. Along the optical axis, the analysis is slightly more complicated, but the psf has the form of a squared sinc-function Webb [119].

Following Webb [119], the reduced optical units ζ and ρ can be defined for the z-dimension along the optical axis and the r-dimension (perpendicular to the optical axis), respectively:

$$\zeta(z) = \frac{2\pi}{n\lambda}\mathrm{NA}^2 z, \tag{3.1}$$

$$\rho(r) = \frac{2\pi}{\lambda}\mathrm{NA} r, \tag{3.2}$$

where $\mathrm{NA} = n\sin\theta$ is the numerical aperture of the objective with n being the index of refraction of the medium between the objective lens and the object and θ the half-angle of the maximum light cone that can enter (or exit) the first (or last) lens. λ is the wavelength of the light. In the image plane ($\zeta = 0$), the psf in radial and axial direction

[1] This is a function of the form $\mathrm{circ}(\sqrt{x^2+y^2}) = 1$ for $\sqrt{x^2+y^2} \leq 1$, and 0 elsewhere. To be exact, the Airy pattern is the result applying the paraxial approximation, but differs only slightly from the exact solution [119].

are then given by

$$p_{\text{radial}}(\zeta = 0, \rho) = 2J_1^2(\rho)/\rho^2 \tag{3.3}$$

$$p_{\text{axial}}(\zeta, 0) = \left(\frac{\sin \zeta/4}{\zeta/4}\right)^2, \tag{3.4}$$

and the three-dimensional psf $p_{3\text{D}}$ is the product of these two functions.

To compare different imaging systems, resolution has to be quantified. A common way is to define a criterion when two point-like objects of same intensity are considered to be distinguishable in the image. For the widely-used Rayleigh criterion this is the case when the maximum of the Airy pattern of the first is above the first minimum of the Airy pattern of the second point in the image. This corresponds to a dip with an intensity of 74% compared to the maximal intensity. For a microscope with the psfs given above, the resolution Δr in radial direction evaluates to

$$\Delta r = 0.61\,\lambda/\text{NA}. \tag{3.5}$$

Along the optical axis, it is possible to define a criterion similar to Rayleigh's , i.e., stating that the maximum of the first psf overlays with the minimum of the second psf. However, this would result in a dip with a depth slightly less pronounced (81% of the maximal intensity) than that of the Rayleigh criterion. Demanding the same decrease of 26% of the signal for separating two points, the resolution Δz along the optical axis is given by

$$\Delta z = 2.1\,n\lambda/\text{NA}^2. \tag{3.6}$$

Although it is possible to define a resolution criterion along the optical axis, it is not feasible to resolve two points in a single image. The focus has to be changed to take images of different planes and another problem of conventional microscopy turns up: The image of a certain focal plane is always spoiled by the light that originates from out-of-focus regions. Therefore, conventional microscopy is often limited to two-dimensional samples.

Confocal Microscopy

The resolution in fluorescence microscopy can be increased by the use of the technique of confocal microscopy. In contrast to conventional wide-field microscopy, not the whole field of view is illuminated. Fig. 3.1 shows a schematic of a realization of a confocal microscope with one objective for excitation and detection. A point-like source in the

conjugated plane of the combined collimator–objective imaging system is ”imaged” into the sample, and, therefore the excitation and the detection path share one focal area in the object domain (”confocal microscopy”). The overlay and separation of excitation and detection path are realized by a beam splitter.

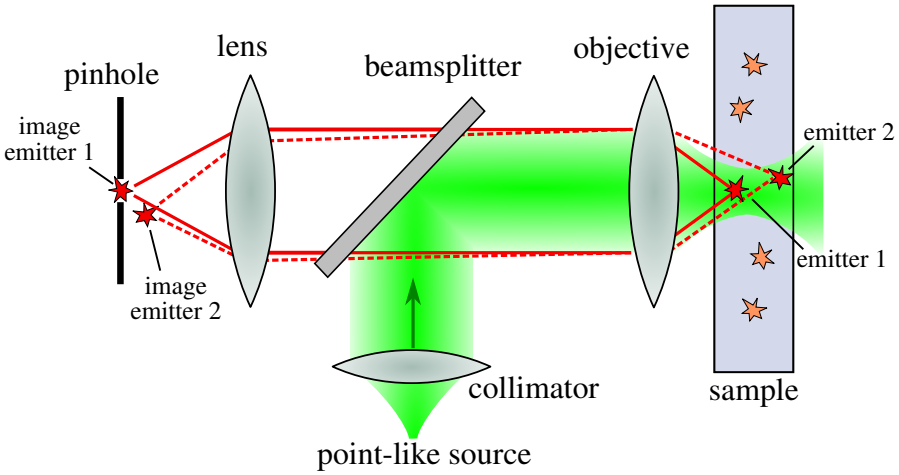

Figure 3.1.: Principle of confocal microscopy.

The change of the illumination scheme does also influence the resolution of the optical system: Psfs similar to the three-dimensional psfs that describe the imaging process now define the illumination, and the overall psf of the system is the product of these psfs:

$$p_{\mathrm{conf}}(\zeta, \rho) = p(\zeta, \rho) \times p(\zeta, \rho) \tag{3.7}$$

The resolution is therefore enhanced. A radial resolution

$$\Delta r = 0.44\,\lambda/\mathrm{NA}, \tag{3.8}$$

and an axial resolution

$$\Delta z = 1.5\,n\lambda/\mathrm{NA}^2 \tag{3.9}$$

can be obtained using the 26% criterion for the dip depth from the Rayleigh criterion. The changes of the resolution in the radial direction and along the optical axis are depicted in Fig. 3.2. The higher resolution that can be achieved by a confocal microscope is not the major improvement of the imaging system. Two other features introduced by the confocal configuration are even more important: First, all light not stemming directly from the focal area is almost completely suppressed and therefore the calculated resolution can be reached in all three dimensions. Second, the intensity outside the main

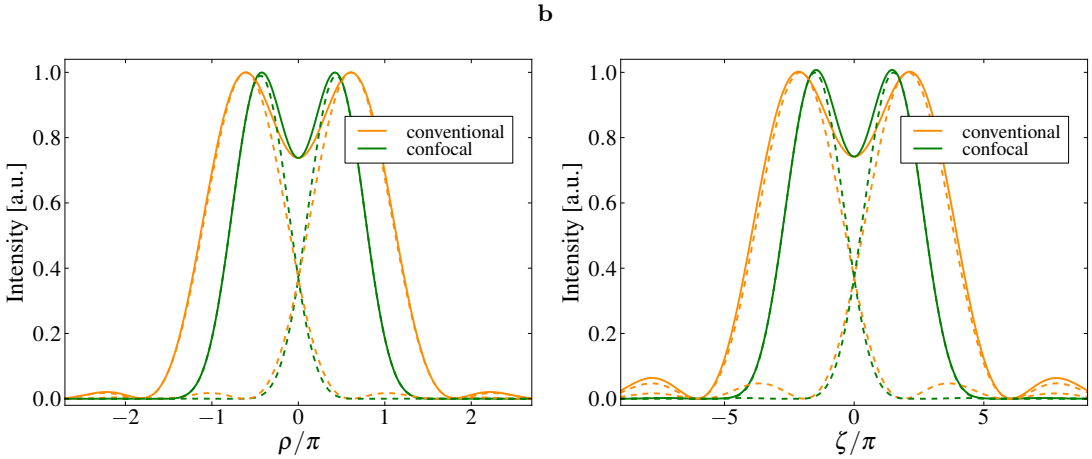

Figure 3.2.: Resolution perpendicular (a) and along (b) the optical axis for a conventional (orange) and a confocal (green) setup. The dashed lines show the point-spread functions of the individual sources separated to result in a dip of 74% of the maximal intensity. Besides the better resolution, the advantage of confocal microscopy is the reduced intensity in the side lobes of the individual point-spread function.

peak of the psf in the side lobes is drastically reduced and therefore, dim objects next to much brighter ones can be resolved. This is illustrated in Fig. 3.1: With the objective and a further lens behind the beam splitter, a virtual image is produced, and the area of the excitation focus is spatially selected with a pinhole. Therefore, emitter 2 which is slightly out off the focus does not only experience a weaker excitation field than emitter 1 which is in the focus, but also its emission is mostly blocked by the pinhole. The background from outside the focus is suppressed. Moving the focus through the sample (either by scanning the beam or the sample) and recording the intensity transmitted through the pinhole, can produce a three-dimensional image, a technique of special importance in biology and life science [120].

A feature that comes for free in a confocal setup is the possibility to produce high excitation densities when the excitation light is focused down to a diffraction-limited spot. These high densities are required to collect a reasonable amount of upconversion fluorescence from nanocrystals doped with rare-earth ions (Chapter 4) and to excite single nitrogen vacancy centers in diamond (Chapter 5).

Experimental Realization

The realization of the confocal setup for fluorescence microscopy is shown in Fig. 3.3. Dependent on the investigated particles, different laser sources can be used:
For the excitation of single nitrogen vacancy centers in diamond (see Chapter 5), two continuous wave lasers in the green wavelength region are used: an Argon ion laser with a wavelength of 514 nm (*Spectra Physics, BeamLok 2800*) and a frequency-doubled, diode-pumped Nd:VO_4 laser at 532 nm (*Coherent Verdi V10*). For time-resolved measurements, a diode-pumped, frequency-doubled Ytterbium-doped fiber amplifier with an adjustable repetition rate from 1 MHz to 80 MHz and a pulse width below 80 ps also at 532 nm (prototype laser from *PicoQuant*) is employed.
The *Coherent Verdi V10* can also pump a wavelength-tunable Ti:Sapphire laser (*Coherent Mira 900*), that is operated at 973 nm to excite upconversion fluorescence in $NaYF_4$ nanocrystals, codoped with Ytterbium and Erbium (see Chapter 4). A chopper wheel (*Stanford Research Systems, SR450*) can modulate this excitation laser. This modulation is fast enough to perform time-resolved measurements on the upconversion crystals.

The different lasers are coupled in appropriate single-mode optical fibers and the emerging Gaussian beam from the second end facet is collimated with an objective. To get the smallest focal volume of the excitation light, the beam is widened with a telescope as it has to overfill the entrance aperture of the objective with regard to smallest excitation foci. Furthermore, the telescope allows to decollimate the excitation beam slightly to compensate for chromatic aberration and match the excitation and detection foci: Since the excitation wavelength differs significantly from the detection wavelength in some of the experiments, the objective is not capable to correct the chromatic aberration alone. A filter (laser-line filters for green laser and a color glass for the infrared, respectively) blocks all unwanted additional light from the excitation beam. A beam sampler (*Thorlabs BSF10-A*) with a reflectivity of about 5% brings the excitation light onto the objective. The beam sampler is wedge-shaped to avoid interference from beams reflected from its front and backside. An oil-immersion objective with an NA of 1.4 (*Olympus PlanApo, 60×*) focuses the excitation light onto the sample, as well as it collects the light emitted from the sample. The objective is mounted on a z-piezo stage (*Piezosysteme Jena, PXY 102*), the sample is placed on a combination of a mechanical and a piezo xy-stage (*Piezosysteme Jena, MIPOS 3*). 95% of the collected fluorescence light is transmitted through the beam sampler, before the excitation light is filtered out by suitable filters in the different experiments: Long pass filters (color glasses *Schott*

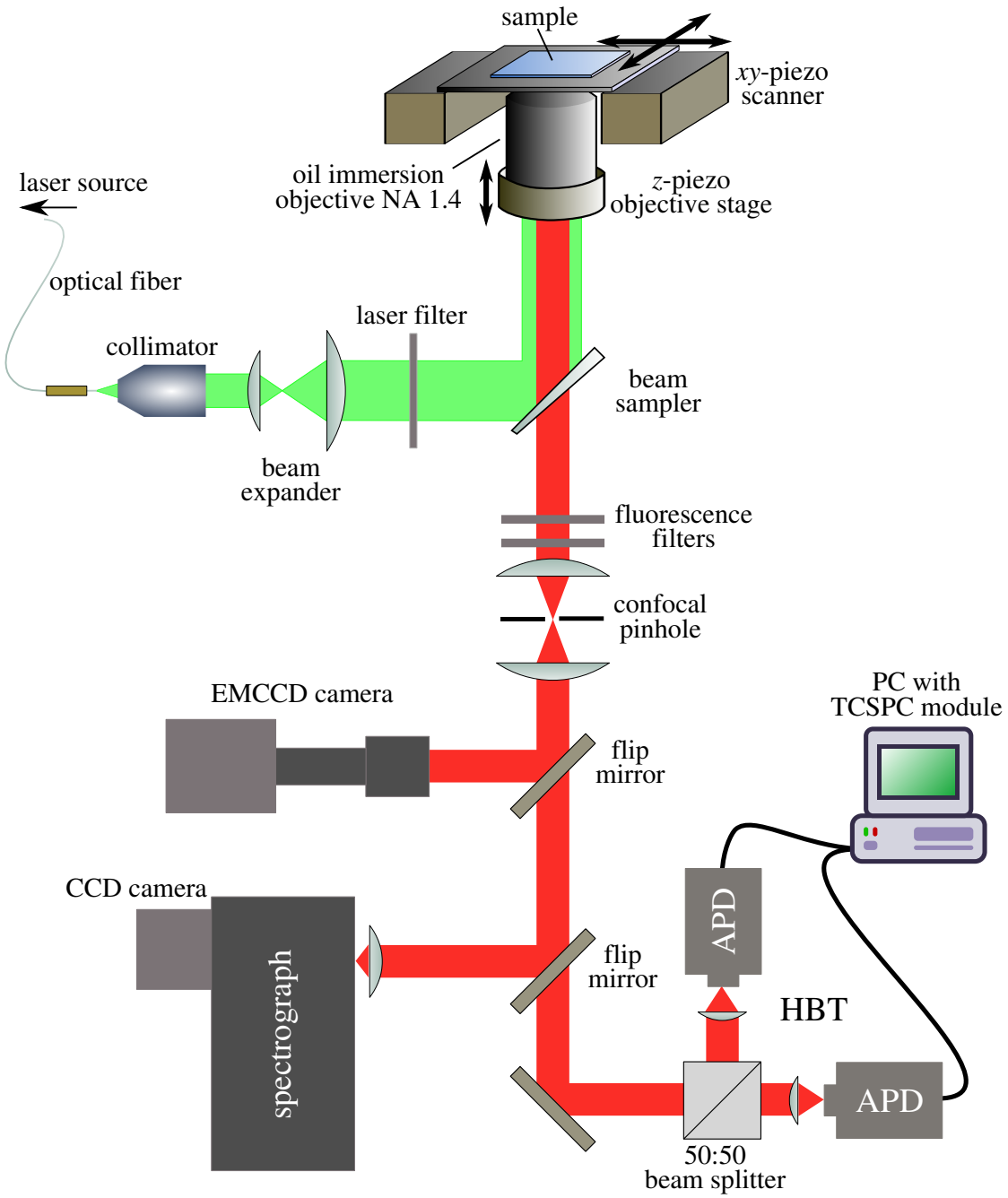

Figure 3.3.: Scheme of the confocal optical setup.

OG550, OG590, RG630) block out the different green lasers, multiple short passes (*Linos CALFLEX X*) block the near-infrared laser in the upconversion experiments. A second telescope and a pinhole (diameter of 75 µm) perform the confocal spatial filtering.

For the analysis of the fluorescent light, an electron multiplying CCD (EMCCD) camera (*Andor, iXon*, thermo-electrically cooled), a spectrometer (*Princeton Instruments, Acton 2500i* spectrograph with an *Andor, iDus* camera, thermo-electrically cooled), and avalanche photodiodes (APD) modules (*PerkinElmer, SPCM-AQR-14)*) can be used. The camera allows the rough orientation on the sample and the adjusting of the confocal setup. Spectral information on the emitted light is gathered with the spectrometer. It is equipped with three different gratings with 600, 1200, and 1800 grooves per mm and provides a minimal resolution of 0.05 nm. Depending on the grating, the spectral range that can be covered by a single measurement differs and is limited by the CCD chip of the camera. A so-called Step'n'Glue mode allows to measure a broader range step-by-step. The grating is moved automatically after each measurement step to cover the adjacent spectral region before these measurements are "glued" together for the overall spectrum. The integration times on the chip per step are typically 10 sdash120 s. The APDs have dark count rates smaller than 100 counts/s, usually much lower than signal count rates in the experiments, and provide a maximum quantum efficiency of 70% around 700 nm. Time-correlated single photon counting devices (*TimeHarp200* and *PicoHarp300*, both by *PicoQuant GmbH*) are used to perform time-resolved and autocorrelation measurements, which will be described below.

The inverted confocal microscope was designed and realized by Felix Müller as his diploma thesis and a detailed characterization of the setup can be found therein [121].

3.1.2. Time-Resolved Measurements and Autocorrelation Measurement

Time-resolved measurements are an important source for gathering information when it comes to the characterization of fluorescence processes, especially when the lifetime of a physical system is altered in an experiment.

Measuring on a ns-Timescale

The decay of the fluorescence signal of nitrogen vacancy centers is typically on a timescale of 10-50 ns [34], depending whether it is located in bulk or in a nanocrystal diamond. Since single nitrogen vacancy centers are used in the experiment, each excitation pulse generates one photon only, obviously not enough to record a decay curve. Therefore, the excitation–detection circle has to be repeated: The pulsed green laser source sends an electric pulse with each light pulse to the trigger (synchronization) port of the time-correlated single photon counting (TCSPC) device (Fig. 3.4a). This starts a timer of the

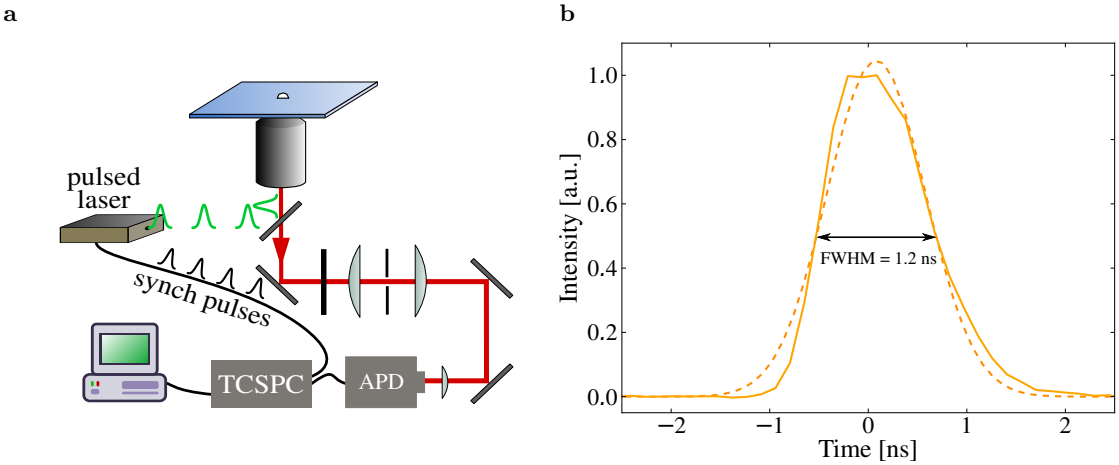

Figure 3.4.: Time-resolved measurements on the ns-range. a: The pulsed laser feeds the time-correlated single photon counting (TCSPC) module with synchronization pulses that start the measurements. The APD stops the measurements. The TCSPC module bins the obtained time differences to obtain the decay behavior after an excitation pulse. b: The fluorescence decay of a gold nanosphere is shown as solid line. The dashed line presents a Gaussian fit which reveals a time resolution of 1.2 ns.

TCSPC module which is stopped by a second (TTL) pulse on the stop port, produced by the APD. Time differences between start and stop events are binned and collected in a histogram, which sums up to the decay curve. The time resolution of the system can be determined by measuring the decay of a fast fluorescence process, as e.g. the decay of the fluorescence of a gold nanosphere with a diameter of 60 nm, typically only several tens of fs [90].

The measured decay is presented as solid line in Fig. 3.4b, and an overall time-resolution of about 1.2 ns is found. Different factors contribute to the finite time resolution: the jitter introduced by the APD when building up the electronic pulse after the impact of the photon, the laser trigger pulse, the pulse width of the laser, and the time resolution as well as binning of the TCSPC. The measurement of the second-order autocorrelation or $g^{(2)}$-function (Eq. 5.1) works quite similar: The emitted light of the fluorescing particle under investigation is "split" by a 50:50 beam splitter, and the photons in each path of the beam splitter are detected with two APDs. One APD starts the measurement, the second APD stops the measurement. The result is a coincidence measurement, i.e., the probability to detect a second photon at a time τ, after a photon was detected at time $\tau_0 = 0$, is determined. By this method, the second-order correlation of the light field is measured. Hanbury Brown and Twiss (HBT) introduced this method

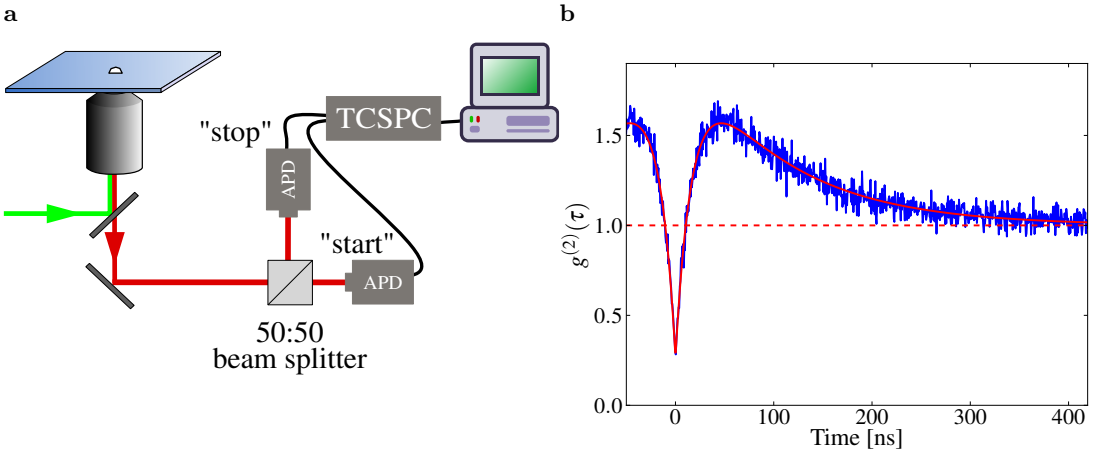

Figure 3.5.: Hanbury Brown and Twiss setup (HBT) to measure the autocorrelation function: The emitted light is divided by a 50:50 beam splitter and the photons in each path are detected with two APDs. The time differences between a "start" and a "stop" event are recorded with the TCSPC module and depicted in a histogram by a computer. b: As a typical example, the autocorrelation function of a single nitrogen-vacancy center in a diamond.

to measure the angular size of Sirius [122] and this is why it is named after them. For the detailed analysis of the measurement of the $g^{(2)}$-functions see Appendix B.2. Due to technical reasons, the stop signal is delayed by additional wiring and this has to be taken into account when analyzing the data.

Measuring on a µs-Timescale

The population and the depopulation of the emitting levels in Er^{3+}ions by an upconversion process assisted by Yb^{3+}ions happens within tens of µs [123], orders of magnitude longer than the decay processes in nitrogen vacancy centers. Therefore, a slightly different measurement scheme has to be applied. The excitation laser is modulated with the chopper wheel with a frequency of 400 Hz, which results in on- and off-times of 1.25 ms. For these longer time-scales, the TCSPC has to be operated in time-tagged time-resolved mode where each detection event from the APD is recorded with an absolute time. The individual detection events have to be correlated to the modulation of the excitation laser: The modulation is detected by a photodiode in the chopper, its control unit produces a corresponding TTL pulse train that is fed into the TCSPC module on an additional input channel (Fig. 3.6a). A Python script carries out the correlation between the laser modulation and the detection events from the recorded

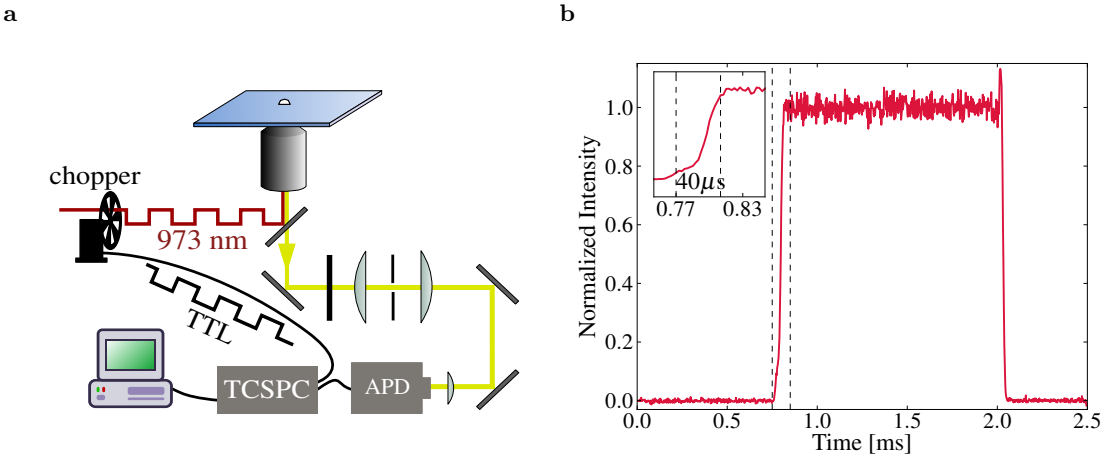

Figure 3.6.: Time-resolved measurements on the µs-range. a: The chopper wheel modulates the excitation laser with a frequency of 400 Hz, and the modulation is fed into the TCSPC via a TTL signal. The detection events are recorded with absolute times, not relative to a start event. b: Measured laser modulation: The rise (decay) from 0 to maximal (maximal to 0) laser intensity takes 40 µs as can be seen in the zoom of the rising edge of the signal (inset).

data. A characterization of the modulated excitation laser is obtained when shining the attenuated laser directly on the APD, as shown in Fig. 3.6b. The rise and decay of the excitation laser takes place in less than 40 µs. This is fast enough to study changes in the rise and decay behavior of upconversion fluorescence introduced by plasmonic structures in Section 4.4.

3.2. Scanning Probes for Investigation and Manipulation

Scanning probe microscopy (SPM), such as scanning-tunneling microscopy (STM) [124], atomic force microscopy (AFM) [125], and the wide variety of their derivatives [126], has become a very powerful tool in surface science, soft-matter physics, or biology [127–129]. Beyond the investigative opportunities provided by SPM, the possibility of controlled manipulation and assembly using the scanning probes has further increased its popularity. First, the positioning and manipulation of single atoms and molecules was demonstrated [130, 131], but the controlled assembly of more complex entities like nanoparticles and complex molecules was also reported [132–134].

Of special importance is the possibility to combine simultaneously nano-probe assembly techniques with an optical microscope setup. In this way the full strength of SPM

can be exploited, and the optical investigation of single nanoparticles and the effects due to manipulation can be studied *in situ*. The optical setup described above can be equipped with two different scanning probe systems: an AFM and a scanning near-field optical microscope (SNOM) to investigate and manipulate on different size scales.

3.2.1. Atomic Force Microscope

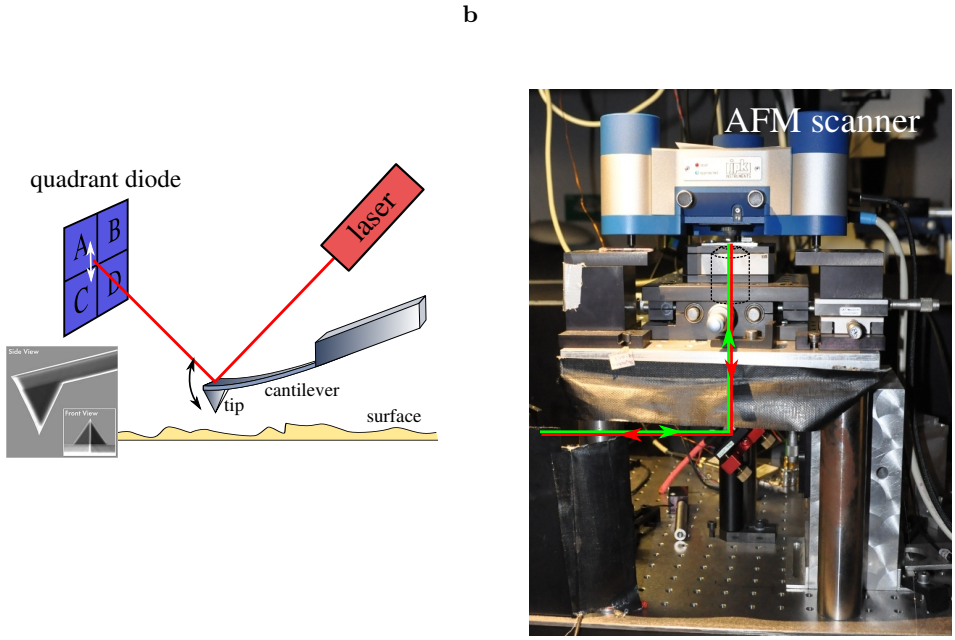

Figure 3.7.: a: AFM principle: Due to the tip–surface interaction, the laser beam reflected by the top side of the cantilever is deflected, and the deflection is read out by a quadrant photodiode. By scanning over the surface and regulating the deflection to a constant value, an image of the topography is obtained. The inset shows an SEM image of the tips used in the experiments. b: Image of the setup: The AFM is mounted on top of the inverted microscope. The beam path and the position of the objective are indicated.

The principle of the AFM technique is shown in Fig. 3.7a: A thin tip at the end of a cantilever (SEM image in the figure) interacts with the surface of the investigated specimen. Van der Waals forces, capillary, or electrostatic forces establish a potential varying with the distance to the surface. Changing the tip's distance to the surface alters interaction strength and changes the deflection of a laser beam reflected by the upper

side of the cantilever which is detected by a quadrant diode. A control loop is used to keep the deflection constant (and therefore the distance to the surface) while scanning the tip over the sample. In this manner the topography of the sample is imaged.

Different operation modes are possible which can be divided in static (or contact) and dynamic (or non-contact) types [127]. In the static mode, the only deflection of the cantilever is monitored. Usually, the tip is in full contact with the sample. In the dynamic mode, the cantilever is excited to an oscillation near its mechanical resonance by a piezo. The surface induced changes of oscillation amplitude, phase, and/or resonance frequency with respect to the driving oscillation, provide the information about the tip–sample interaction. The advantage of the non-contact or "tapping" modes is that it is merely non-invasive: The tip–sample interaction is much weaker compared to that of the contact modes, where the tip is "dragged" over the surface. This dragging, literally a "scratching", can damage soft tissue or reposition the material on the sample. However, this effect is desired when manipulating, i.e., in this mode the tip is pushing or pulling particles on a glass cover slip. So, by alternatingly using contact and non-contact modes, it is possible to manipulate the sample in a controlled way and image the result after each step.

Fig. 3.7b shows a photograph of the AFM on-top of the inverted confocal microscope. The head (*JPK instruments, NanoWizardI BioAFM*) houses the complete tip-scanning unit. The resolution of the AFM image and the precision of the manipulation is in general only limited by the tip shape. However, it turned out that the home-made confocal setup is prone to external vibrations that limit the resolution for the sample height to 1 nmdash2 nm. In future experiments, the sources of these vibrations must be located or a better vibrational isolation has to be implemented. In the experiments, standard silicon tips were used (*NanoWorld AG, Arrow NC*). They have typical tip radii of 10 nm (inset of Fig. 3.7a) and are ideal to investigate and manipulate particles with sizes from a few up to several hundreds of nm.

3.2.2. Scanning Near-Field Optical Microscope

For larger particles, the AFM tips are too fragile for manipulation and another kind of probes is used: tapered optical fibers. A SNOM setup is used to hold these fibers. The fibers are tapered with the help of a micro pipette puller (*Sutter Instrument, P-2000 Laser Based*). Such a tip as seen in a microscope is shown in Fig. 3.8a. The fibers are fused into a micropipette using a CO_2 laser. The micropipette is mounted in a segmented piezo tube (custom made, *EBL Products Inc.*) as shown in Fig. 3.8a. One of the segments

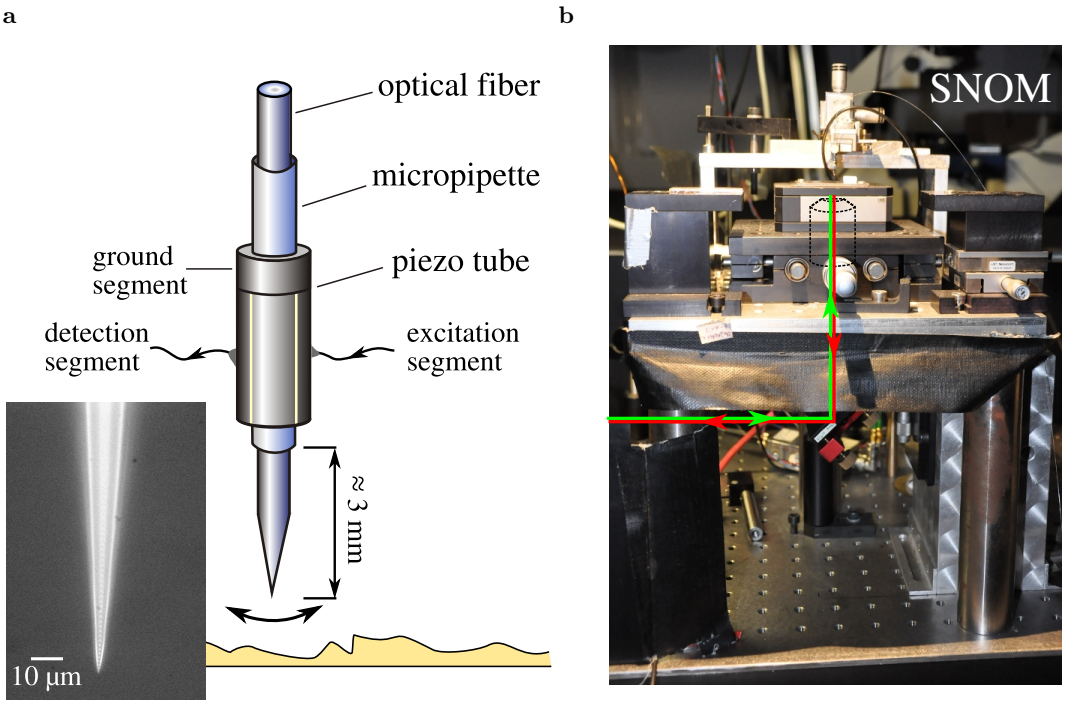

Figure 3.8.: a: Schematic illustration of the SNOM principle: The tapered fiber tip is excited to an oscillation by one of the segments of the piezo tube. The opposite segment detects the response. The damping by the surface provides the feed-back for the control loop. b: Picture of the inverted microscope with the SNOM mounted on top. The microscope objective is indicated as well as the path of excitation (red) and detection light (green) to the beam splitter.

drives an oscillation of the tip, while the opposite segment detects the response of the tip. By scanning the excitation frequency, one finds the tip's eigenfrequency between 20 000 Hzdash70 000 Hz. Similar to the AFM in tapping mode, it is possible to use the oscillation near the eigenfrequency to implement a control loop to the surface [135], since it is damped close to a surface due to weak shear forces caused by adsorbed water and/or van der Waals forces.

The tapered fiber in the piezo tube is attached to the combination of a manual (*Elliot Scientific Ltd., MDE 260 Series*) and a piezo (*Piezosysteme Jena MINITRITOR*) three-axial translation stage. This ensures that not only the sample but also the probe can be moved independently with respect to each other.

For the manipulation of µm-sized polystyrene spheres (see Fig. 5.6) though, it is not necessary to use the automatic control loop to adjust the distance to the sample.

The approach is regulated by hand. However, it is important to know when the tip is in contact with the particles that are manipulated, and the shear force detection is essential.

Like the confocal setup, the SNOM was build by Felix Müller and the details can be found in his diploma thesis [121].

3.2.3. Positioning the Scanning Probe in the Confocal Region

In order to combine the optical microscope with the scanning probe techniques, the probe has to be positioned accurately in the focal area. For the SNOM tip, this is done directly by coupling light into the fiber from the untapered end and center the Airy pattern that is produced by the very end of the tip (see in Fig. 5.6, Fig. 5.7a).

The silicon AFM tips do not allow a similar procedure, as they are not transparent. In a first step, the cantilever is positioned roughly by maximizing the AFM laser intensity far above the sample. Then, with a first approach, the tip is placed about 50 µmdash100 µm above the sample. By shining light through the AFM from above, the arrow-shaped end of the cantilever can be found using the camera. Then it is aligned within the field of view of the microscope (see Fig. 3.9a). After bringing the tip in contact with the surface, the light source is replaced to shine light from the side onto the

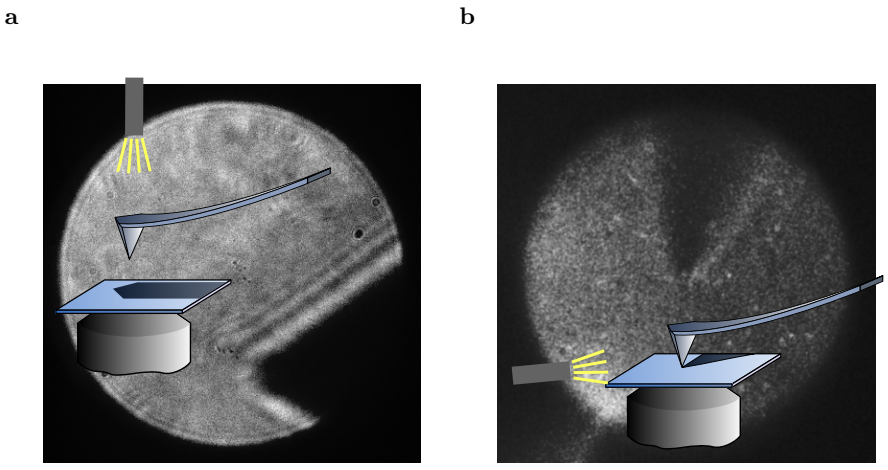

Figure 3.9.: Positioning an AFM tip within the confocal area. a: The shadow of the cantilever is used for a rough positioning. The distance of the cantilever from the sample surface is more than 50 µm. b: The shadow of the tip when approached to the surface is used for fine adjustment of the tip.

sample. The shadow of the tip becomes visible and indicates the contact point of the tip and the sample as shown in Fig. 3.9b. By this method, the tip can be placed easily close to the focus of the optical system with an accuracy of less than 300 nm. To finally assure a particle in the focus is indeed the particle seen in the AFM topography image, it turned out to be most convenient to slightly move the particle out of the focus with the AFM tip and observe the change of emission intensity simultaneously on one of the APDs.

3.3. A Multifunctional Setup for the Nanoworld

The experimental setup presented in this chapter combines two state-of-the-art research techniques: confocal microscopy and scanning probe techniques. In this work, it will be shown that this combination does not only give new insight in the nanoworld, as it allows to directly correlate optical properties to size parameters well below the resolution limit of the optical microscope (Section 4.3.2). In fact, it allows to actively influence and change the experimental conditions (Section 4.4 and Sections 5.3 and 5.4).

Furthermore, emphasis is on the modularity of the current setup should be emphasized again: Different excitation laser sources, different scanning probes, and different optical analysis tools offer a toolbox to perform a wide range of possible experiments. To illustrate this once more at the end of this chapter, the different modules of the setup are depicted below.

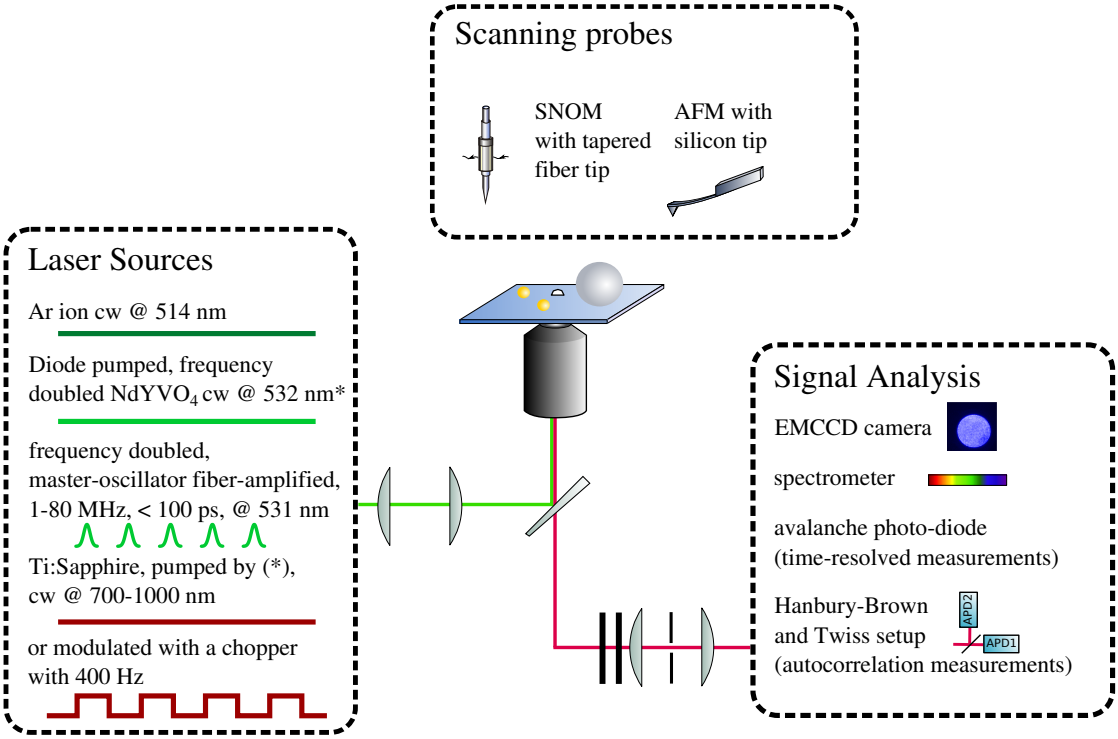

Figure 3.10.: The experimental setup and its modularity offer a versatile tool for the investigation and manipulation on the nano- and micrometer range.

CHAPTER 4

Upconversion in Single $NaYF_4$:Yb^{3+}, Er^{3+} codoped Nanocrystals

During the last decade, research on rare-earth doped materials has attracted a lot of attention, as they provide the most efficient upconversion mechanism based on energy transfers between the hosted rare earth ions. Due to advances in their synthesis methods, the control of size, composition, and even crystal structure on the nanometer scale is nowadays possible. Among all materials, $NaYF_4$ is one of the most interesting hosts, providing highest upconversion yields when doped with rare earth ions.

After an introduction to upconversion mechanisms and the luminescence processes in rare earth ions, the results of the investigation on single $NaYF_4$ nanocrystals codoped with Yb^{3+} and Er^{3+} ions will be presented in this chapter. For the first time, a size dependence of upconversion fluorescence is found for individual particles and a qualitative explanation is given. Furthermore, the possibility to enhance the upconversion emission of single nanocrystals by the controlled coupling to plasmons of gold nanospheres is demonstrated in the last part of the chapter. The publications *Nano Letters*, **9**, 2477, 2009 [Schietinger et al. 2009b], and *Nano Letters*, **10**, 134, 2010 [Schietinger et al. 2010] are based on this research.

4.1. Luminescence of Lanthanoids

4.1.1. Introduction to Rare Earths and Lanthanoids

There is some confusion concerning the elements which are counted as rare earths and lanthanoids: According to the IUPAC (*International Union of Pure and Applied Chemistry*), the 15 lanthanoids together with scandium (Sc) and yttrium (Y) build the group of rare earths [136]. Other classifications omit either Sc and Y or consider rare earths as a synonym for the lanthanoids [137, 138]. Spectroscopists applied the name to the lanthanoids together with the actinoids, as they have similar spectroscopic properties [139]. The term *lanthanoid* is not unambiguously in itself: The IUPAC definition comprises the fifteen elements with atomic numbers 57 (lanthanum) through 71 (lutetium) [136], which can be found in the "footnotes" of the periodic table of the elements. In this group the $4f$-shell is consecutively filled with electrons. Spectroscopists often ignore lanthanum and/or lutetium [139] as they have either an empty or a completely filled $4f$-shell, and therefore no visible or near visible optical absorption and emission. In this work the term lanthanoid will be used in compliance with the IUPAC nomenclature.

Nowadays the term "rare earths" is a misnomer in two ways: In the 18^{th} century the rare earth elements were first discovered in "rare" oxide-type minerals near the Swedish village of Ytterby. Despite their name, these elements are not "rare", all of them are found more abundantly than cadmium, silver, or mercury [140], although they do not have the tendency to occur concentrated in exploitable deposits the way other metals do. The origin for the latter part of the term "rare earths" is the Greek definition of "earths", material that can not be further changed by sources of heat. The name remained even after the demonstration that the rare earth oxides weren't elements themselves.

The similarity of their chemical properties made the separation of the individual elements difficult. It was for the chemist Mosander to show that samples of the elements cerium and yttrium were in fact mixtures of different elements when he extracted lanthanum from a cerium sample and erbium from an yttrium sample in 1839 and 1843, respectively [141]. Until 1907, all other stable rare earth elements (all but promethium) could be isolated only by better separation and analysis methods [142].

The electronic configuration offers the explanation for the strong chemical resemblance of the rare earth elements and the reason for the inclusion of Yttrium and Scandium in this group. All of them are dominantly trivalent, i.e., they tend to give away three of the outer electrons when building chemical bondings. This similarity is responsible for the difficulties in separating these elements. However, with today's sophisticated

chemical separation methods this changes to an advantage: For chemists it is possible to interchange them almost at will in complexes or in crystal matrices allowing, e.g., multiplexed coloring in flat panel displays [143].

4.1.2. Energy Levels and Optical Transitions in Lanthanoids

Lanthanoid luminescence is characterized by relatively sharp peaks with spectral positions mostly independent of the embedding matrix, although the intensities and fine structure may vary [144]. These peaks come from transitions within the $4f$-shell of the electron configuration. The electrons of this shell are shielded from the surrounding by the filled $5s^2$ and $5p^6$ shells which are less energetic but have outer lying orbitals. Therefore the $4f$-shell electrons do not play a role in the chemical bonding between the lanthanoids and the containing matrix, and the influence of the matrix on the transitions within the $4f$-shell is small [143]. As a consequence one observes the sharp-line absorption and emission spectra similar to those of free ions, whether hosted in solutions, complexes, sol-gels, or crystals.

In his posthumously published article "The fascination of the rare earths – then, now and in the future", Brian G. Wybourne described the group of lanthanoids as *"perhaps the most fascinating"*, but the study of their (optical) properties as *"long, torturous, and often controversial"* [138]. As already mentioned, it took more than 100 years to separate and indicate the individual members of this fascinating group, and it took another 60 years to develop a theory to explain their optical properties. The main problem was the observation of $4f-4f$-transitions at all as the electric dipole transitions are forbidden by the Laporte rule[1] and quadrupole transitions were too weak. The basic ideas to solve "The puzzle of rare-earth spectra in solids" were introduced by van Vleck in 1937 [145]. He suggested that the crystal field could distort the electron motion so that the selection rules for the free ion would not longer apply and allow electric dipole transitions. However, it was not until 1962 that Judd and Ofelt independently published their work which was capable to described the observed transition strengths within the $4f$-shells of the lanthanoids [146, 147]. *"It has been in a very real sense the first step in the journey to an understanding of the rare earths and their much heavier cousins, the actinides, but like many journeys into the unknown, the end is not in sight."* [138]

All theoretical considerations start with the levels of the free ion, i.e., the ion does not encounter an external field. The Hamiltonian $\mathscr{H}_{\mathrm{F}}$ describing the free ion with N $4f$ elec-

[1] The Laporte rule states that the parity has to change in an electric dipole transition as the electric dipole operator anticommutes with the parity operator.

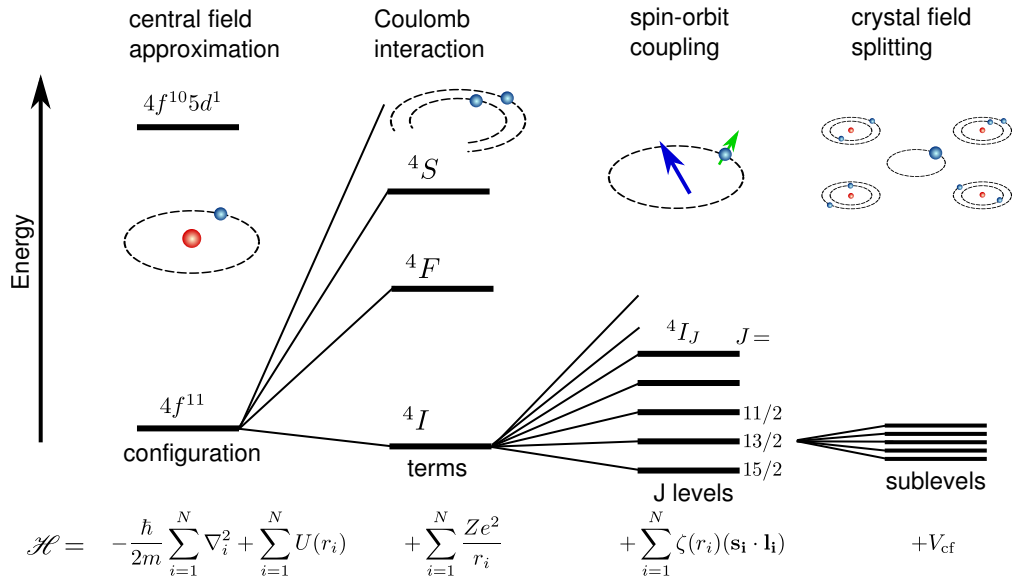

Figure 4.1.: The interactions leading to the level structure in lanthanoid ions based on the example of Er^{3+}.

trons is given by

$$\mathscr{H}_{\mathrm{F}} = -\frac{\hbar}{2m}\sum_{i=1}^{N}\nabla_i^2 + \sum_{i=1}^{N}\frac{Ze^2}{r_i} + \sum_{i<j}^{N}\frac{e^2}{r_{ij}} + \sum_{i=1}^{N}\zeta(r_i)(\mathbf{s_i}\cdot\mathbf{l_i}). \tag{4.1}$$

The first term of the Hamiltonian is the sum of the kinetic energies of the electrons of the $4f$-shell, the second term is the potential energy of the electrons in the field of the nucleus. The third term is the energy due to Coulomb repulsion between pairs of electrons, the last term is the sum of interactions between each electron's spin and its orbital angular momentum, the spin–orbit coupling.

The first two terms of the Hamiltonian are the basis of the so-called *central field approximation*. In this approximation it is assumed that each electron moves independently in the field of the nucleus and a central field $U(r_i)$ originating from the spherically averaged potential fields of each other electron. The Hamiltonian

$$\mathscr{H}_0 = -\frac{\hbar}{2m}\sum_{i=1}^{N}\nabla_i^2 + \sum_{i=1}^{N}U(r_i).$$

of this approximation commutes with all the angular momentum operators and results in degenerate levels (see Figure 4.1) as it is known from the hydrogen atom. The energies of these levels depend on the assumed population of the shells, the so-called *configu-*

ration. All lanthanoid trications have the [Xe]-configuration with the first three shells and the subshells $4s$, $4p$, $4d$, $5s$, and $5p$ filled. The remaining N ($N = 0, 1, 2, \ldots, 14$) electrons of the ions fill partly the $4f$-shell. Close to the $4f^N$ configuration are the energetically higher $4f^{N-1}5d^1$, $4f^{N-1}6s^1$, and $4f^{N-1}6p^1$ configurations. These different configurations are of special importance as they do not have all the same parity and, therefore, transitions between them are allowed and strong enough to be observed, e.g., from the pure metal vaporized by electric discharge. As no distortion of any ligand or crystal fields is present, in these experiments significant information can be obtained of the free ions' levels. The degeneracies of these levels are just given by the number of possible combinations to distribute N equivalent electrons to 14 levels (7 subshells of the $4f$-shell and a factor of two for the spin) which can be expressed by the binomial coefficient $\binom{14}{N}$.

The third term in the Hamiltonian $\mathscr{H}_\mathrm{F}$ in Eq. 4.1 splits each configuration in different *terms* and removes the degeneracy, the total spin S and the total orbital angular momentum L, respectively. The degeneracy of the terms is $(2S+1)(2L+1)$-fold, corresponding to the different M_S and M_L numbers. The labeling of the terms is given by ${}^{2S+1}L_J$, where $2S + 1$ represents the multiplicity of the total spin, L is the total orbital angular momentum, and J the total angular momentum of the $4f$-electrons. Capital letters $S, P, D, F, G, \ldots$ are used to designate the value of $L = 0, 1, 2, 3, 4, \ldots$. It is possible that in a configuration more than one of the terms has the same L and S numbers. Thus, it can be necessary to introduce extra quantum numbers to obtain unique labeling.

It should be further mentioned that this nomenclature derives from the *LS-coupling* scheme, also known as the *Russel-Saunders-coupling*. In this scheme the spin-orbit interaction for an individual electron is either neglected or considered as small compared to the Coulomb interaction between the electrons. The total orbital angular and spin momentum operators sum up to

$$\mathbf{L} = \sum_{i=1}^{N} \mathbf{l_i} \quad \text{and} \quad \mathbf{S} = \sum_{i=1}^{N} \mathbf{s_i},$$

and the total angular momentum $\mathbf{J}$ is just the sum of both: $\mathbf{J} = \mathbf{L} + \mathbf{S}$. The other extreme is the *jj-coupling* regime, where the individual spin-angular momenta of each electron couple to total electron angular momenta $\mathbf{j_i} = \mathbf{l_i} + \mathbf{s_i}$. In this case $\mathbf{J}$ is the sum over all $\mathbf{j_i}$. Spin-orbit coupling in lanthanoid ions is in an *intermediate coupling* regime and the Russel-Saunders nomenclature is not fully appropriate, as the resulting states are mixtures of different terms. However, this notation proves justified as in most cases

a main contribution of one term exists. In either case the spin-orbit coupling removes the degeneracy in J, but the level energy is still independent of m_J.

Since the ion is not isolated in free space but is embedded in a matrix, the ion is affected by the electric field made up by its environment. For the case of a crystal, this is taken into account by introducing the crystal field V_{cf} operator. The complete Hamiltonian $\mathscr{H}$ of the ion in the lattice consists of the free ions part $\mathscr{H}_{\mathrm{F}}$ of Eq. 4.1 amended by V_{cf},

$$\mathscr{H} = \mathscr{H}_{\mathrm{F}} + V_{\mathrm{cf}}. \tag{4.2}$$

V_{cf} lifts the degeneracy in m_J by the Stark effect and splits J-levels into $(2J+1)$ irreducible levels. Furthermore, V_{cf} *admixes in* states of higher energy configurations with opposite parity. This is the reason why electric dipole transitions within a configuration become allowed, as their parity is not pure anymore. Using the crystal field[2] as a perturbation in first order, for two states $\langle\varphi_a|$ and $|\varphi_b\rangle$ of well-defined parity the mixed parity states $\langle\Psi_a|$ and $|\Psi_b\rangle$ are to be found:

$$\langle\Psi_a| = \langle\varphi_a| + \sum_\beta \frac{\langle\varphi_a|V_{\mathrm{cf}}|\varphi_\beta\rangle\langle\varphi_\beta|}{E_a - E_\beta} \tag{4.3a}$$

$$|\Psi_b\rangle = |\varphi_b\rangle + \sum_\beta \frac{\langle\varphi_b|V_{\mathrm{cf}}|\varphi_\beta\rangle\langle\varphi_\beta|}{E_b - E_\beta} \tag{4.3b}$$

where φ_β are states of configurations with higher energy and both kinds of parity. The rate of an electric dipole transition from an initial state Ψ_i to a final state Ψ_f is proportional to the square of transition dipole moment D, which is given by

$$D^2 = |\langle\Psi_i|\mathbf{P}|\Psi_f\rangle|^2 \tag{4.4}$$

with the electric dipole operator

$$\mathbf{P} = -e\sum_{i=1}^{N} \mathbf{r_i}.$$

As $\langle\varphi_a|\mathbf{P}|\varphi_b\rangle = \langle\varphi_\beta|\mathbf{P}|\varphi_\beta\rangle = 0$ because of their equal parity, the expression of the dipole

[2]Usually only a static approximation of the crystal field is used, the motion of the nuclei is neglected.

matrix element D for the states in Eq. 4.3 reduces to

$$D = \langle \Psi_a | P | \Psi_b \rangle = \sum_\beta \left\{ \frac{\langle \varphi_a | V_{\mathrm{cf}} | \varphi_\beta \rangle \langle \varphi_\beta | \mathbf{P} | \varphi_b \rangle}{E_a - E_\beta} + \frac{\langle \varphi_b | V_{\mathrm{cf}} | \varphi_\beta \rangle \langle \varphi_\beta | \mathbf{P} | \varphi_a \rangle}{E_b - E_\beta} \right\} \neq 0. \tag{4.5}$$

However, the admixing is rather weak, and the emission intensities of dipole transitions are comparable to that of magnetic dipole transitions with lifetimes typically in the range of 1×10^{-1}dash1×10^{-3} s.

At this point, all the physical interactions dominating the properties of the lanthanoids level schemes and spectra have been introduced and a qualitative understanding is possible. To fully reproduce the spectra quantitatively, the main effort is the calculation of energies and transition dipole moments. Actually, Eq. 4.5 was only the starting point for Judd [146] and Ofelt [147], who, simultaneously and independently, formulated a theory describing the intensities in the spectra, published independently in August 1962. It is build up on different concepts, including group theory and vector tensor algebra to perform the calculation of Eq. 4.5. The importance of this work can not be overemphasized, as it allowed for the first time a quantitative interpretation of the observed lanthanoid spectra. However, as a correct and full treatment of this theory is going beyond the scope of this work, the reader is referred to the reviews of Walsh [148] and Smentek [149] and the references therein which also give an overview of the recent advancement and possible further development of the theory.

4.1.3. Nonradiative Relaxation of Lanthanoids in Solids

The Nonradiative Relaxation Rate

The electronic excitation in lanthanoid in a matrix can not only decay radiatively by emission of a photon. It can also be mediated by the interaction with the lattice and the creation of one or more phonons as well. Especially in the case of long lifetimes of radiative transitions, nonradiative processes can become imminent. First experiments on such multi-phonon relaxation processes in lanthanoid-doped materials between two electronic states were performed in the late 1960s [150–153]. For the nonradiative decay rate k_{nr} an exponential dependence on the energy gap ΔE between the involved states was found for transition including more than 4 phonons, known as the energy gap law:

$$k_{\mathrm{nr}} = \beta \, \mathrm{e}^{-\alpha \Delta E}, \tag{4.6}$$

with constants α and β. It turns out that for different dopant ions, α remains constant for a specific host crystal, while β has to be adopted for each ion–host pair. β is known as the electronic factor, containing the electronic coupling element.

For the theoretical description of nonradiative processes, the Schrödinger equation $\mathscr{H}\Psi = \mathrm{E}\Psi$ has to include all nuclei (n) and electrons (e) of the system and their interactions [154]:

$$\mathscr{H} = T_\mathrm{e} + T_\mathrm{n} + V_\mathrm{nn} + V_\mathrm{ee} + V_\mathrm{en}, \tag{4.7}$$

T standing for the kinetic, V for the potential energies. The subscripts indicate whether the term is dependent on the electron coordinates, the nuclei coordinate, or on both. For the total wavefunction $\Psi_{l,m}(\mathbf{r},\mathbf{R})$ the ansatz is made

$$\Psi_{l,m}(\mathbf{r},\mathbf{R}) = \phi_l(\mathbf{r})\chi_m(\mathbf{R}). \tag{4.8}$$

where l, m and $\mathbf{r}, \mathbf{R}$ are the quantum numbers and coordinates of the electrons and nuclei, respectively. This ansatz is motivated by the Born-Oppenheimer approximation, where the motion of the nuclei is assumed to be much slower than the electronic motion. The electron wavefunction follows adiabatically the nuclei configuration described by $\mathbf{R}$. Hence, $\mathbf{R}$ becomes a parameter in the solution of the Schrödinger equation for the electrons:

$$\left(T_\mathrm{e} + V_\mathrm{ee} + V_\mathrm{en} + V_\mathrm{nn}\right)\phi_l(\mathbf{r},\mathbf{R}) = \mathrm{E}_l^\mathrm{el}(\mathbf{R})\phi_l(\mathbf{r},\mathbf{R}) \tag{4.9}$$

Inserting Eq. 4.8 into the full Schrödinger equation $\mathscr{H}\Psi = \mathrm{E}\,\Psi$ results in

$$\begin{aligned} \phi_l(\mathbf{r},\mathbf{R})(T_\mathrm{n} + \mathrm{E}_l^\mathrm{el}(\mathbf{R}))\,\chi_m(\mathbf{R}) &= \phi_l(\mathbf{r},\mathbf{R})\mathrm{E}\,\chi_m(\mathbf{R}) \\ -\sum_n \frac{-\hbar^2}{2M_n}[\chi_m(\mathbf{R})\nabla^2_\mathbf{R}\phi_l(\mathbf{r},\mathbf{R}) + 2\nabla_\mathbf{R}\chi_m(\mathbf{R})\nabla_\mathbf{R}\phi_l(\mathbf{r},\mathbf{R})] & \end{aligned} \tag{4.10}$$

The Born-Oppenheimer equation is obtained by multiplying by $\phi_l^*(\mathbf{r},\mathbf{R})$ from the left and integrating over $\mathbf{r}$, if the last term in Eq. 4.10 is disregarded to uncouple nuclei and electron motion:

$$(T_\mathrm{n} + \mathrm{E}_l^\mathrm{el}(\mathbf{R}))\chi_{m,l}(\mathbf{r},\mathbf{R}) = \mathrm{E}\chi_{m,l}(\mathbf{r},\mathbf{R}). \tag{4.11}$$

The electronic energy of the system $\mathrm{E}_l^\mathrm{el}(\mathbf{R})$ appears as a potential energy in the Schrödinger equation for the nuclei motion, the so-called potential energy surface. Eq. 4.11 is the adiabatic approximation, the omitted term in Eq. 4.10 is the non-adiabatic part $\mathscr{H}_\mathrm{NA}$. After solving Eq. 4.11, $\mathscr{H}_\mathrm{NA}$ is the perturbation in Fermi's golden rule to initiate nonradiative transitions.

The electron–lattice interaction V_{en} can be treated in different approaches. Here, the approach by Schuurmans and van Dijk [154] is described. Expanding V_{en} in a Taylor series in the normal mode coordinates $\mathbf{Q}$ of crystal vibrations around the equilibrium position $\mathbf{Q}_0$ gives:

$$V_{\mathrm{en}}(\mathbf{Q_0} + \mathbf{\Delta Q_0}) = V_{\mathrm{en}}(\mathbf{Q_0}) + \sum_i V_i \Delta Q_i + \sum_{ii} V_{ij} \Delta Q_i \Delta Q_j + \ldots, \tag{4.12}$$

with

$$V_i = \left.\frac{\partial V_{\mathrm{en}}}{\partial Q_i}\right|_{\mathbf{Q_0}}, \quad V_{ij} = \left.\frac{\partial^2 V_{\mathrm{en}}}{\partial Q_i \partial Q_j}\right|_{\mathbf{Q_0}}, \quad \text{etc.}$$

In the linear approach, only the first two terms of Eq. 4.12 are considered [154, 155], but for a weak coupling of the electrons to the lattice this was claimed not to be appropriate [156]. In the weak coupling regime, the potential energy surfaces are nearly parallel. This is especially the case for the well-shielded $4f$-shell electrons in lanthanoids. The potential energy surfaces separated by the electronic state energy difference $\Delta\varepsilon \gg \hbar\omega_{\mathrm{phonon}}$ and higher order terms have to be taken into account to connect these surfaces. However, especially Schuurmans and van Dijk [154] succeeded with the linear approach and obtained a more complex energy gap law which can even explain the behavior for energy gaps of a few phonon energies.

In their theoretical approach it turns out to be important to distinguish between two kinds of modes, the so-called *promoting* and *accepting modes*. First, the nuclear wavefunction is expressed as a product of the $3N$ vibrational normal modes $X_{m,l}$ of the crystal:

$$\chi_{m,l} = \prod_{k=1}^{3} N X_{m_k,l} \tag{4.13}$$

where m_k, l is the number of the energy quanta $\hbar\omega_k$ in the mode $X_{m,l}$ and m, l is short for the set m_k, l. At $T = 0$ the nonradiative decay occurs between an initial state $\Psi_{i,0} = \psi_i \chi_{0,i}$ in the vibrational ground state and a final state $\Psi_{f,m_k} = \psi_f \chi_{m_k,f}$. The electronic energy difference $\Delta\mathbf{E}(\mathbf{Q}) = E_i(\mathbf{Q}) - E_f(\mathbf{Q})$ is taken up by the lattice vibration in χ_{m_k}. The nonradiative decay rate k_{nr} can be deduced as [154]

$$k_{\mathrm{nr}} = \frac{2\pi}{\hbar}\rho_E \overline{\left|\frac{\hbar^2}{M}\sum_k J_{if}^k \left\langle \chi_{m,f} \left| \frac{\partial}{\partial Q_k} \right| \chi_{0,i} \right\rangle\right|^2} \tag{4.14}$$

where ρ_E is the density of vibrational states, M the nuclear mass, and the bar indicates an averaging over degenerate vibrational states. With the Condon approximation, i.e.,

J_{if}^k is independent of $\mathbf{Q}$, and inserting (4.13) into (4.14), Eq. 4.14 can be written as

$$k_{\mathrm{nr}} = \frac{2\pi\hbar^3}{M^2}\rho_E\eta\overline{\left|\sum_k J_{if}^k \left\langle X_{m_k,f}\left|\frac{\partial}{\partial Q_k}\right|X_{0_k,i}\right\rangle \prod_{\hat{k}\neq k}\left\langle X_{m_{\hat{k}},f}\mid X_{0_{\hat{k}},i}\right\rangle\right|^2} \quad . \tag{4.15}$$

η is a correction factor with a value between 1 and 2 accounting for the Condon approximation. The matrix element

$$J_{if}^k = \left\langle \phi_i \left| \frac{\partial}{\partial Q_k} V_{\mathrm{en}} \right| \phi_f \right\rangle / \Delta E(\mathbf{Q}) \tag{4.16}$$

is driving the transition between the two electronic states and the modes with largest J_{if}^k are called promoting modes. The evaluation of $\left|\left\langle X_{m_k,f}\left|\frac{\partial}{\partial Q_k}\right|X_{0_k,i}\right\rangle\right|^2$ shows that the number of promoting modes is restricted to $p \ll N$ and that promoting modes can only take the energy of a single quantum $\hbar\omega_k$. The rest of the energy, $\mathbf{\Delta E}(\mathbf{Q}) - \hbar\omega_{\mathrm{prom}}$, has to be taken up by the accepting modes occuring in $\prod_{\hat{k}\neq k}$. Furthermore, the maximum frequency modes dominate the transition, and one can assume that only modes of maximum frequency ω_{M} contribute to the transition. As the energy has to be conserved, the number of quanta absorbed by the accepting modes has to be

$$\sum_{\hat{k}\neq k} m_{\hat{k}} = \mathbf{\Delta E}(\mathbf{Q})/\hbar\omega_{\mathrm{M}} - 1 \quad , \tag{4.17}$$

By inserting the explicit form of the vibrational normal modes X, which (in a harmonic approximation of V_{nn}) are the solutions of the harmonic oscillator, the new energy gap law is derived:

$$k_{\mathrm{nr}} = \frac{\pi\eta\hbar^2}{M\varepsilon}\left(\omega_{\mathrm{M}}\sum_k^p \left|J_{if}^k\right|^2\right)\frac{S^m e^{-S}}{m!} \quad . \tag{4.18}$$

m counts the number of high-energy phonons that fit in the energy gap $\mathbf{\Delta E}(\mathbf{Q})$ minus the energy of one promoting phonon. ε is the typical level spacing of the accepting levels, so the factor $1/\varepsilon$ replaces ρ_E with the additional averaging over degenerate states in Eq. 4.15. $S = \sum_{\hat{k}} S_{\hat{k}}$, where $S_{\hat{k}}$ are the so-called Huang-Rhys factors [157]:

$$S_{\hat{k}} = \frac{1/2\, M\omega_{k,f}^2 \delta\mathbf{Q}_k^2}{\hbar\omega_k, f} \tag{4.19}$$

with $\delta\mathbf{Q}_k$ the displacement $Q_{f,0} - Q_{i,0}$ of the configuration. However, for $m \geq 2$ Stirling's approximation for $m!$ can be used and one finds the exponential behavior as in the experimental energy gap law Eq. 4.6. The main improvement of the energy gap law

Eq. 4.18 is that it is capable to describe the non-exponential behavior when the energy gap $\Delta E(\mathbf{Q})$ is in the range of only a few phonon energies.

The approximations made in its derivation have to be kept in mind. For example, experiments by Auzel et al. [158, 159] and Menezes et al. [160, 161] indicate that the restriction to phonons with the maximal frequency ω_{M} is too strict and an effective phonon mode has to be chosen to fit the experimental data, including the contribution from modes of lower frequencies.

However, the effective modes do not differ significantly from ω_{M}, and from Eq. 4.18 it is obvious that the larger m that is needed for the transition, the smaller k_{nr} is. Therefore, a low maximal phonon energy is required to suppress nonradiative decays.

Saturation Effects and Phonon Bottleneck in Nonradiative Decays

In the theory described in the previous section, the nonradiative decay of an individual ion within a phonon bath is described, though Auzel and Pellé [162] have shown that in glasses containing lanthanoids this approach is not suitable under certain conditions: In the case of high lanthanoid-doping concentration and/or high excitation density, k_{nr} is reduced [159, 163, 164] for energy gaps larger than $3.2\,\omega_M$. As this effect is not observed in crystals, the behavior is assumed to be related to the amorphous structure of the glasses. The short-range order distance prevents phonons from propagation away in the material, the diffusion length is much shorter than in crystals. The characteristic energy of $3.2\,\omega_M$ is the energy carried by the promoting term as shown above. Therefore, the localization of the phonons is responsible for a filling of the accepting modes in the phonon diffusion volume v_{diff} around an ion which has undergone a nonradiative transition. Other ions located in v_{diff} encounter these partially filled accepting modes. So if the concentration of excited ions in v_{diff} is too high, nonradiative decays are suppressed.

With the temperature dependent energy gap law [155, 165] based on the theory of Huang and Rhys [157], Auzel and Pellé [159] developed a formula for k_{nr} as a function of the temperature T and the average number of ions $\bar{x}$ contributing to the filling of a common accepting mode:

$$k_{\mathrm{nr}}(T,\bar{x}) = k(0,\bar{x}=1)\,e^{-S_0(2\bar{n}+1)}(\bar{n}+1)^{(1+\bar{x})N}\frac{S_0^{(1+\bar{x})N}}{[(1+\bar{x})N]!}\left(\frac{N_p}{S_0}\right)^2 \tag{4.20}$$

N is the number of phonons which have to be absorbed by the accepting mode due to the nonradiative process occurring in a single ion, $\bar{n} = (e^{(\hbar\omega_M)/kT}-1)^{-1}$ is the occupation number of the mode at temperature T. N_p stands for the number of promoting modes.

Instead of one ion, an average of $\bar{x}$ ions contribute simultaneously to the filling. Without the additional factor $1 + \bar{x}$ before N, Eq. 4.20 reduces to the isolated ion case. By this approach, phonon diffusion length could be found of a few tens of Å, in excellent agreement with other measurement techniques like heat capacity and sound velocity measurements [159] or Raman scattering [164].

Although crystals are used in this work, their size of a few nanometers could have a similar effect: Diffusion of the phonons is not possible in nanocrystals besides bridging the gap to the cover slip substrate, resulting in a comparable phonon bottleneck.

4.2. Upconversion Luminescence of Lanthanoids

The process of converting photons into photons with higher energies is called upconversion (UC). Typically, light in the visible wavelength range is generated from infrared or near-infrared (NIR) light, but also ultraviolet light can be provided by UC processes. A well-known example is the conversion of NIR into green visible light in a crystal with nonlinear polarizability by second harmonic generation. This process is widely used in simple laser pointers as well as in high-power pump lasers [166].

4.2.1. Different Upconversion Mechanisms

A multitude of processes exists that can transform photons into energetically higher photons. A selection of the most important UC processes is shown in Fig. 4.2.

a) The process of anti-Stokes Raman scattering is sketched in Fig. 4.2a. Here, the initial state is a vibronically excited ground state that absorbs a photon. The excited virtual level emits to the ground state. As the excited level is virtual, the terminology of absorption and emission is not correct: it is better to refer to it as an (inelastic) scattering process. The photon gains the energy of the vibration which is in the order of 100dash1000 cm^{-1}.

b) In Fig. 4.2b two-photon excitation is shown. If the energy gap between ground and excited state is too large for single photon absorption, the gap can be bridged with the help of a virtual state and the simultaneous absorption of two photons.

c) Second harmonic generation (SHG) (Fig. 4.2c) is but one example of nonlinear mechanisms not involving any metastable excited state. The main difference to the other processes described here is the coherence of the resulting emission in consequence of the zero lifetime of the excited, virtual levels. SHG can also be explained by a classical model. The polarization $\mathbf{P}$ is a function of the electric field

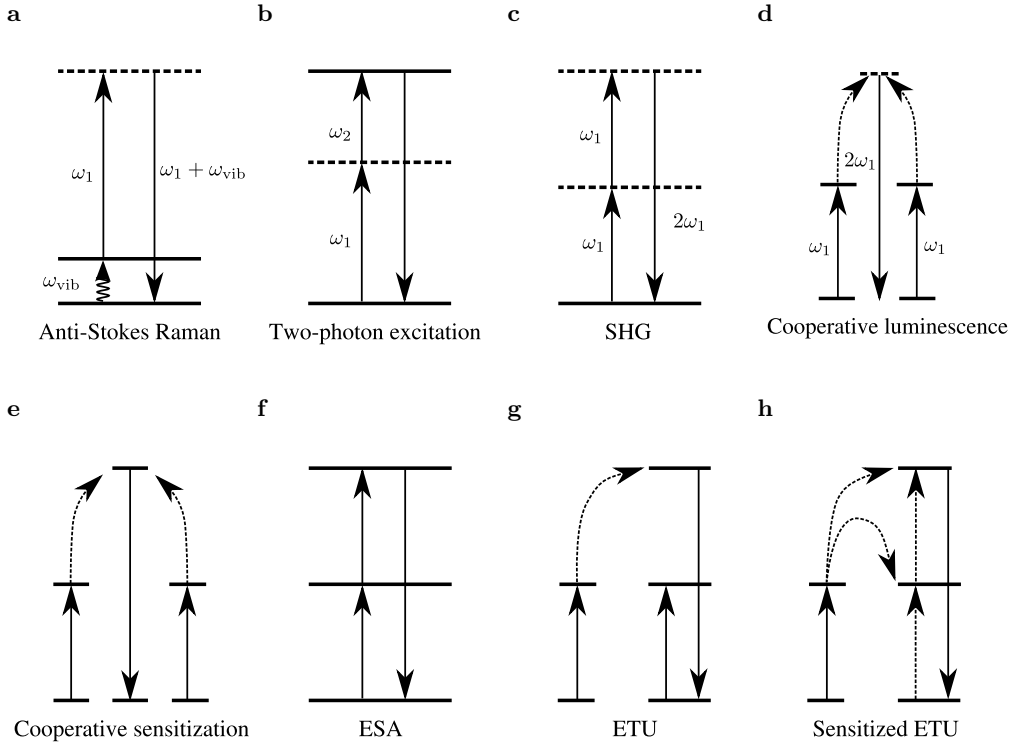

Figure 4.2.: Different upconversion mechanisms. Real, metastable levels are depicted as full lines, virtual levels by dashed lines (see text for details).

E with nonlinear terms: $\mathbf{P} = \epsilon_0(\chi^{(1)}\mathbf{E} + \chi^{(2)}\mathbf{E}^2 + \dots)$. Obviously, a monochromatic field with frequency ω_0 produces higher harmonics in the polarization **P**.

d) Cooperative processes are illustrated in Figs. 4.2d and 4.2e, respectively. In the case of cooperative luminescence two excited states radiate cooperatively with the help of a virtual state, resulting in a photon with double energy.

e) In the case of cooperative sensitization (Fig. 4.2e) two excited systems transfer their excitation energies jointly by exciting a third system to a real level.

f) Excited state absorption (ESA) is the consecutive absorption of two photons (see Fig. 4.2f): First, a photon excites the system to a metastable level. If the lifetime of this level is long enough, a second photon can further excite the system in an even higher state. However, as two real, metastable levels are excited, this mechanism can be more efficient as the previous ones.

g) In Fig. 4.2g energy transfer UC (ETU) is displayed: An excited system transfers its energy to a second, already excited system, leading to a higher excitation from

Table 4.1.: Typical UC efficiencies [167, 168] of the processes in Fig. 4.2

Fig. 4.2	**Mechanism**	**Typical Example**	**Efficiency η_{norm}**
a	Anti-Stokes Raman	Silicon Crystals	$\sim 1 \times 10^{-13}\,\mathrm{cm^2\,W^{-1}}$
b	2-photon excitaion	CaF_4:Eu^{2+}	$\sim 1 \times 10^{-13}\,\mathrm{cm^2\,W^{-1}}$
c	SHG	KDP	$\sim 1 \times 10^{-11}\,\mathrm{cm^2\,W^{-1}}$
d	cooperative luminescence	$YbPO_4$:Yb^{3+}	$\sim 1 \times 10^{-8}\,\mathrm{cm^2\,W^{-1}}$
e	cooperative sensitization	YF_3:Yb^{3+},Tb^{3+}	$\sim 1 \times 10^{-6}\,\mathrm{cm^2\,W^{-1}}$
f	ESA	SrF_2:Er^{3+}	$\sim 1 \times 10^{-5}\,\mathrm{cm^2\,W^{-1}}$
g	ETU	YF_3:Er^{3+}	$\sim 1 \times 10^{-3}\,\mathrm{cm^2\,W^{-1}}$
h	Sensitized ETU	$NaYF_4$:Yb^{3+};Tm^{3+}	$\sim 1 \times 10^{-1}\,\mathrm{cm^2\,W^{-1}}$

which emission occurs.

h) Closely related to this is the sensitized ETU shown in Fig. 4.2h. Both excitation steps of the emitting system are performed by energy transfers from a sensitizer. The sensitizer has a high absorption rate at the pumping wavelength, thus it collects efficiently the pump energy before transferring the excitation to the acceptor.

As diverse as the origins of the UC mechanisms are, as widely spread is the range of efficiencies being observed. A first measure for the UC yield is the quantum efficiency $\eta_{\mathrm{QE}} = \mathrm{VIS_{emit}}/\mathrm{NIR_{abs}}$, the ratio of visible photons emitted to the number of NIR photons absorbed. Since the emission intensity of nonlinear optical processes of order n usually scales with the order n of the excitation power density $P_{\mathrm{exc}}/\mathrm{cm}^2$, and $P_{\mathrm{exc}}/\mathrm{cm}^2$ varies over orders of magnitude in different experiments [3], a better figure to compare efficiencies is a normalized efficiency $\eta_{\mathrm{norm}} = \eta_{\mathrm{QE}}/(P_{\mathrm{exc}}/\mathrm{cm}^2)^{(n-1)}$. Table 4.1 summarizes typical efficiencies of the described UC mechanisms in Fig. 4.2. The efficiency figures explain why lanthanoid codoped materials (last row in the table) arouse a great deal of interest: They outperform all other UC materials with different mechanisms by several orders of magnitude. With this outstanding capability, a wide range of possible applications spans from laser materials [166], nanoscale biolabels [169, 170] over lighting and display technology [171, 172], temperature sensors [173], NIR quantum counters [174], to the increase of solar-cell efficiency [32].

[3] E.g., the difference between a cw and a fs-pulsed excitation scheme is of the order of 10^{13}.

4.2.2. Nonradiative Energy Transfer

Energy transfer is the process where a donor system is excited by radiation and transfers (parts of) the energy to an acceptor. As energy transfers play the key role in the energy transfer UC processes, a basic explanation of energy transfers between ions in solids is provided here.

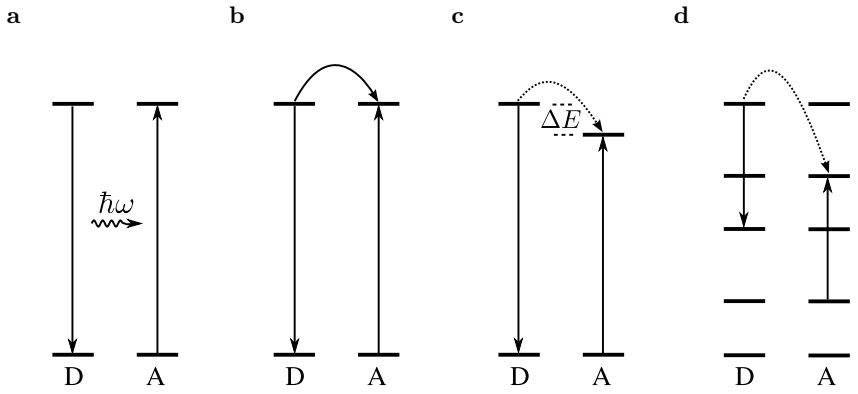

Figure 4.3.: Different energy transfer (ET) mechanisms between a donor (D) and an acceptor (A). a and b: In the radiative, resonant case a photon is emitted and gets reabsorbed, while in the nonradiative, resonant case the interaction is by direct coupling of the multipole components of donor and acceptor. c: An energy gap ΔE between the energy levels can be bridged by creation (Stokes) or annihilation (anti-Stokes) of phonons. d: Any two level pairs can be involved in the ET process (cross-relaxation).

One mechanism of energy transfer is the emission of the energy by the donor followed by absorption by the acceptor, Fig. 4.3a. In general, the donor's emission is not directed at the acceptor and therefore this process is not efficient. However, an optical element such as an optical resonator can enhance the transfer by directing the emission and extending the interaction time via photon storage [175].

The interaction between donor and acceptor can be much more efficient if the acceptor is close enough to the donor to couple directly by dipole–dipole interaction (Fig. 4.3b). This is the well-known Förster resonant energy transfer which was first observed in solutions of dye molecules [176]. Also semiconductor nanocrystals [177], quantum wells [178], or ions in solids [179] can be employed as donors or acceptors. Since the emission intensity of the acceptor is normally enhanced by the presence of the donor, the donor is often also called sensitizer. The acceptor is also known as the activator as it decreases the lifetime of the donor. Following Förster's approach, with increasing donor–acceptor

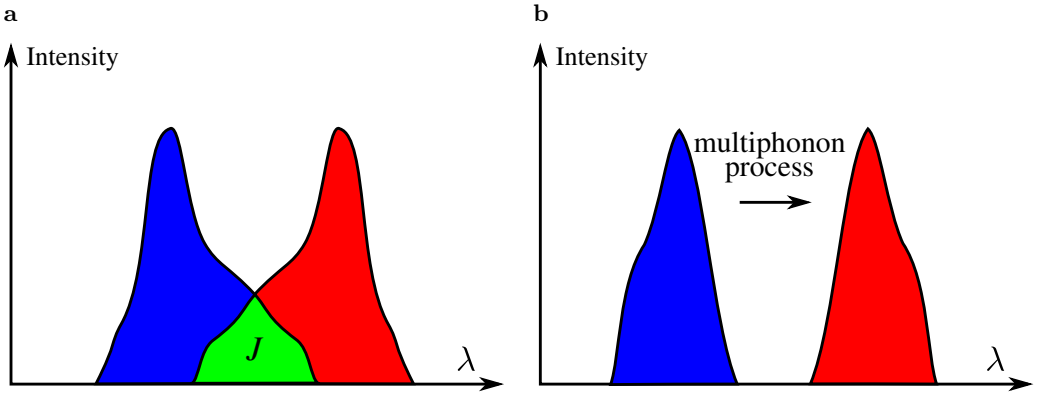

Figure 4.4.: a: The energy transfer rate in a Förster transfer process is directly proportional to spectral overlap J (green) of the donor's emission (blue) and the acceptor's absorption (red) spectrum. b: In solids, no spectral overlap is needed. An energy gap can be bridged by multiphonon creation or annihilation.

distance r the transfer rate k_{ET} reduces dramatically:

$$k_{ET} = \frac{1}{\tau_D}\left(\frac{R_0}{r}\right)^6. \tag{4.21}$$

Here, τ_D is the fluorescence lifetime of the donor and R_0 is the Förster radius. R_0 is determined by the dipole–dipole interaction and is defined as

$$R_0 = \frac{9\,Q_0\,(\ln 10)\kappa^2\,J}{128\,\pi^5\,n^4\,N_A},$$

where Q_0, κ, n, and N_A are the quantum efficiency of the donor, the so-called dipole orientation factor, the refractive index of the surrounding, and Avogadro's number, respectively. J is the spectral overlap integral (see Fig. 4.4a), given by

$$J = \int f_D(\lambda)\epsilon_A(\lambda)\lambda^4\,\mathrm{d}\lambda. \tag{4.22}$$

f_D is the normalized donor emission spectrum and ϵ_A the acceptor molar extinction coefficient. Typical Förster radii are in the order of 2dash10 nm [180]. The strong distance dependency of the transfer rate makes the Förster resonant energy transfer ideal to record the change of distances in molecular processes [181], and to obtain very local light sources in optical near-field microscopy techniques [182, 183].

The main differences between a radiative and a nonradiative dipole–dipole interaction should be mentioned: First, the transfer efficiency for the radiative case scales with r^{-2}

and with r^{-6} for the nonradiative case. Second, the fluorescence lifetime depends on the distance only in the nonradiative case.

Förster's theory of dipole–dipole interaction is only an approximation as pointed out by Dexter [184]: For close vicinity of donor and acceptor, higher multipole and exchange interactions should be considered in the theory. This is especially the case for ions in crystalline or glassy matrices. A generalization Eq. 4.21 for electric multipole interactions can be written as

$$k_{ET} = \frac{1}{\tau_D}\left(\frac{R_0}{r}\right)^s. \tag{4.23}$$

The exponent s is
– 6 for dipole–dipole interaction,
– 8 for dipole–quadrupole interaction,
– 10 for quadrupole–quadrupole interaction.
In fact, higher multipole interaction can play a significant role in lanthanoid-doped materials, as dipole transitions are only weak (see Section 4.1.2) and the distance between interacting ions is on the range of the lattice constant (which is on the order of a few Å).

The energy transfer rate between two ions with excited states of different energies (Fig. 4.3c) should drop to zero as the spectral overlap integral J (Eq. 4.22) vanishes. However, energy transfers between lanthanoids can appear even with energy mismatches ΔE as high as several $1000\,\mathrm{cm}^{-1}$. They occur due to the creation or annihilation of multiple phonons (see Fig. 4.4b) during the transfer process [155], a Stokes or anti-Stokes process, respectively. These multiphonon sidebands can not be seen in usual absorption or fluorescence spectroscopy because the $4f$-electrons coupling to the phonons is very weak. Nevertheless, the sidebands can be revealed by laser excitation spectroscopy [185].

The energy transfer rate k_{ET} is strongly dependent on the energy gap ΔE and can be expressed in an energy gap law [155] similar to that of nonradiative transitions:

$$k_{ET}(\Delta E) = k_{ET}(0)\,\mathrm{e}^{-\beta\Delta E}, \tag{4.24}$$

where β is a constant unique for the matrix material, and the same restrictions to its applicability as Eq. 4.6.

Energy transfers do not necessarily have to include ground states of the donor and/or the acceptor (Fig. 4.3d). Any two level pairs can be involved in the process. This is obvious as only energy differences, not absolute energy, can be exchanged. If the final energy level of both transfer partners is below the excited state of the donor, such a

process is called cross-relaxation. Cross-relaxation processes between similar ions play the dominating role in photon avalanche upconversion, a phenomenon in lanthanoid-doped material where the emission increases by orders of magnitude when excitation is slightly in excess of a critical intensity [174, 186].

4.2.3. Energy Transfer Upconversion

In 1966, Auzel [187] investigated upconversion in Tm^{3+} in tungstate and germanate glass, which contained additionally Yb^{3+} ions. He proposed as explanation to consider cases where the acceptor for an energy transfer is already in an excited state. He concluded from his experiment, that the Yb^{3+} ions act as *sensitizer* by absorbing the pump photons. Then, the excitation energies are transfered consecutively to the *activator*, the Tm^{3+} ions. By this, the energy of several pump photons are accumulated in the activator and light with a shorter wavelength can be emitted as UC fluorescence.

This effect, called sensitized energy transfer upconversion (ETU), is depicted for an Yb^{3+}, Er^{3+} ion pair in Fig. 4.5. Typically, in materials codoped with those ions, strong UC fluorescence emission can be observed in the blue, green, and red wavelength range. The transition $^2F_{7/2} \rightarrow {}^2F_{5/2}$ excites the Yb^{3+} by absorption of a photon with a wavelength around 980 nm. This transition is much stronger than the corresponding Er^{3+} transition $^4I_{15/2} \rightarrow {}^4I_{11/2}$. In the second step, the excitation energy in the Yb^{3+} is transfered to the Er^{3+} $^4I_{11/2}$ level. Then, the following steps play the major roles in filling the emitting levels:

i) The green emitting levels $^2H_{11/2}$ and $^4S_{3/2}$ can be filled by a second ET to the level $^4F_{7/2}$ and a successive nonradiative decay.

ii) To populate the red emitting level $^4F_{9/2}$, one possible path is the nonradiative decay to the $^4I_{13/2}$ level followed by the an energy transfer step.

iii) The $^4I_{13/2}$ can also be reached by a cross-relaxation process: One Er^{3+} ion relaxes $^2H_{11/2}/\,^4S_{3/2} \rightsquigarrow {}^4I_{9/2}$ by exciting a second ion from the ground state to the $^4I_{13/2}$ level.

iv) The blue emitting levels $^2H_{9/2}$ and $^4F_{5/2}$ can only be reached by a three-photon process with involving three ET steps. One possible way to populate these levels is by further excitation of the red emitting level $^4F_{9/2}$ by an additional ET step.

Step iii) effectively quenches the green emission and the result of the cross-relaxation is two ions in lower states, a further ET is needed to obtain visible emission. Therefore, the concentration of Er^{3+} ions is usually kept low to avoid these effects.

The excitation power dependence of ETU was investigated and modeled in detail [188]

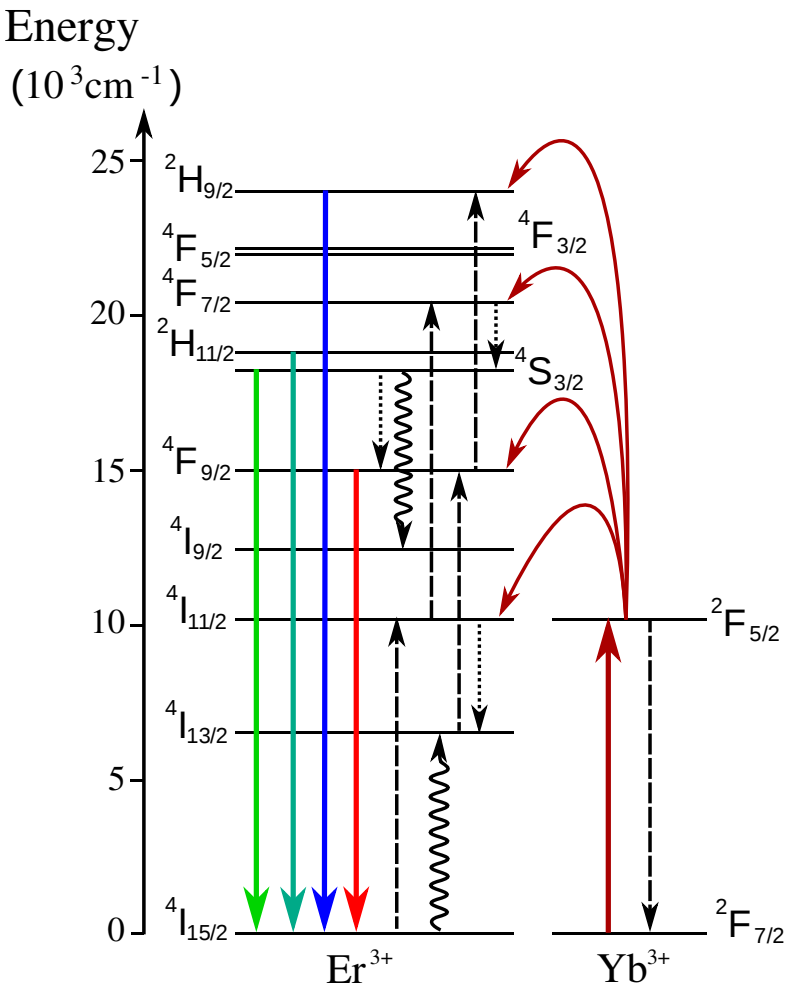

Figure 4.5.: Sensitized ETU scheme for an Yb^{3+}, Er^{3+} ion pair system. The dashed, and curly arrows denote ET and cross-relaxation steps, dotted and full arrows nonradiative and radiative transitions, respectively. Two or more excitations are successively transfered from the sensitizer (Yb^{3+}) to the activator (Er^{3+}). The energy of multiple pump photons can be accumulated, resulting in UC fluorescence.

for a single ion species. In general, it is assumed that a n-photon process has a pump power dependence of n, when saturation is not considered. But for ETU, the situation is more complex as real metastable levels are involved. A complex rate equation model including all possible transitions has to be solved to understand the power dependence. The considerations in Pollnau et al. [188] can be generalized to a system with two different ions (see Appendix A). The result is surprising: The power dependence for the upconversion emission intensity $I_i(P_{\text{pump}})$ of a level that needs i photons is not fixed and

might vary between

$$I_i(P_{\text{pump}}) \propto P_{\text{pump}}^{-1} \tag{4.25}$$

$$\vdots \tag{4.26}$$

$$I_i(P_{\text{pump}}) \propto \ldots P_{\text{pump}}^{i} \tag{4.27}$$

depending on the energy transfers and decay rates, and the pump power P_{pump}. This is especially astonishing, since an increased excitation power might lead to reduced emission from a level under certain conditions.

4.3. Combined Upconversion Spectroscopy and Atomic Force Microscopy Studies on Single $NaYF_4$:Yb^{3+}, Er^{3+} Codoped Nanocrystals

The combination of spectroscopic studies on the UC fluorescence with AFM gives new insights on the processes that take place in nanocrystals: First, the power dependence of the emission from a cluster of nanocrystals is investigated under high excitation densities. Here, the AFM assures that the cluster is small enough that it "fits" in the focus of the excitation laser. Second, the UC fluorescence in single nanocrystal is analyzed with respect to its size that is revealed by the AFM.

Properties of the Nanocrystals, Sample Preparation and Experimental Setup

As highlighted in Section 4.2.1, ETU exceeds the performance of other upconversion mechanisms by orders of magnitude and opens new fields of application. But besides the efficiency, a further requirement for many purposes, e.g., biolabeling and coating, is a uniform, nanometer-scale size of the upconversion particles. So, the quest for the most capable host/dopant configurations comes along with the search for synthesis protocols to obtain high-quality particles with narrow size-distributions and it is still ongoing [6, 169, 189–194].

The most efficient UC nanocrystals today are $NaYF_4$:Yb^{3+}, Er^{3+}/Tm^{3+} codoped nanocrystals, converting NIR photons around 975 nm to red, green, and blue light [195]. They occur in two different crystal structures: the cubic (or α-) phase, and the hexagonal (or β-) phase. The hexagonal phase has the highest reported UC efficiency [196], the cubic phase is less efficient by a factor of around 10. The high upconversion

yield is explained by the very low energy of the dominant phonon modes between 300dash400cm^{-1} [195]. Nonradiative transitions over larger energy gaps are unlikely (Eq. 4.18), and so they do not compete with the radiative transitions. In these crystals, up to 50 % of the absorbed photons are converted to photons with higher energies even under moderate excitation intensities [197].

The nanocrystals investigated in this chapter were synthesized in the research group of Prof. Güdel at the University of Bern [6, 198]. The cubic $NaYF_4$ nanocrystals are codoped with 20% of Yb^{3+} and 2% of Er^{3+}, i.e., the Yb^{3+} and Er^{3+} ions replace 20% and 2% of the Y^{3+} ions in the crystal lattice, respectively. The amount of the dopants is critical for the UC performance as indicated above and gives best results for this concentration. Here, the undesired cross-relaxation processes do not occur between the individual Er^{3+} ions, as their distance is too large. Furthermore, the amount of Yb^{3+} has to be adjusted to avoid saturation of the ET steps. When too many sensitizing Yb^{3+} ions are in the excited state within the relevant energy transfer vicinity around an accepting Er^{3+} ion, relaxation by direct depopulation to the ground state can lower the UC efficiency.

The synthesis of the nanocrystals does not result in single-sized particles but in a size distribution with a peak at 15 nm of particle diameter and a standard deviation of 5 nm [6]. As this size distribution is rather broad, it allows to study nanocrystals with the same chemical composition on a wide size range, which will be done in Section 4.3.2.

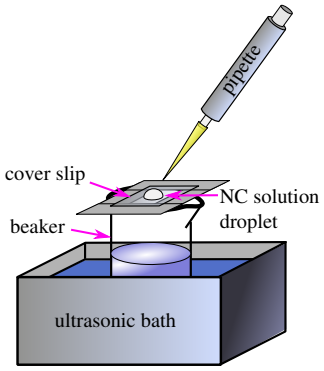

Figure 4.6.: Sample preparation: During the drying process, the sample is stored on a support in an ultrasonic bath to avoid agglomeration.

The nanocrystals are in solution of toluene or chloroform with typical concentration between 0.1dash1% wt. As the solvent is highly volatile even when stored in the fridge, the concentration of the solution has to be adjusted each time of sample preparation. The

solution is drop-casted on a cleaned coverslip. To avoid agglomeration of the particles during evaporation of the solvent, the coverslip itself is stored on a support mount on a beaker in a ultrasonic bath during this process (see Fig. 4.6). By this method, small clusters of nanocrystals as well as single nanocrystals are deposited on the coverslip. After this, the sample is transfered to the microscope. As the focus of the NIR excitation light does not coincide with the detection focus of the upconversion fluorescence (see Section 3.1.1), the clusters are a necessity to find the focal position along the optical axis. As their emission is strong enough to be detected even when out of focus and therefore allow the adjustment.

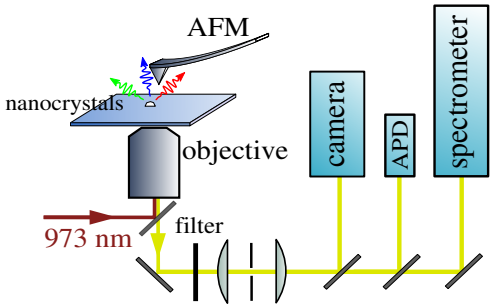

Figure 4.7.: Setup configuration for the studies on single upconversion nanocrystals: The AFM in combination is mounted on top of the confocal microscope.

The sketch in Fig. 4.7 shows the experimental configuration. The excitation is provided by continuous wave laser light at 973 nm of a Ti:sapphire laser. For all the following experiments the spectrometer is loaded with the 600 g/mm grating. The details can be found in Chapter 3.

4.3.1. Observation of Non-Ground State Transitions

As upconversion spectroscopy has been done either on bulk samples or on ensembles of nanocrystals, excitation densities were rather low. Typical densities are up to a few tens of $\mathrm{W\,cm^{-2}}$ (e.g. Suyver et al. [196], Chen et al. [199]). To study a few or single nanocrystals, excitation densities have to be in the range of 1×10^5 to 1×10^6 $\mathrm{W\,cm^{-2}}$ to get enough emission. The high excitation density results in a change of the power dependence of the upconversion processes, as already discussed and saturation can not be neglected. Furthermore, the level scheme in Fig. 4.5 has to be amended by higher levels and radiative transitions not to the ground state, leaving the Er^{3+} in an excited state.

The AFM image and the UC fluorescence spectrum of a cluster of $NaYF_4$ codoped

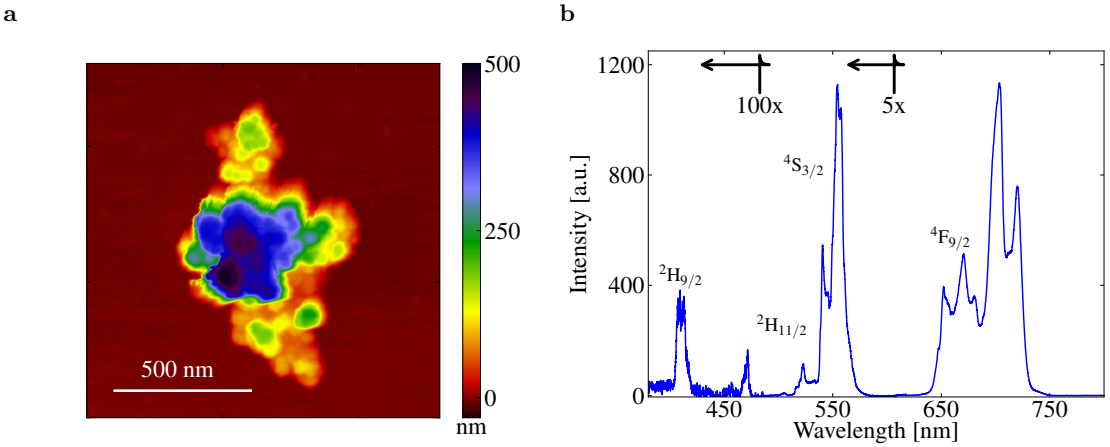

Figure 4.8.: a: AFM image of a cluster of NaY_4:Yb^{3+}, Er^{3+}. b: Corresponding UC fluorescence spectrum excited with a 973 nm cw laser at $0.8 \times 10^6\,W\,cm^{-2}$. For better visibility, parts of the spectrum are enhanced by a factor of 100 and 5, respectively, indicated in the graph by arrows. The emission bands are labeled by the level's names from which the emission originates by transitions to the ground state $^4I_{15/2}$.

nanocrystals are shown in Fig. 4.8a and b. For the spectrum, the integration time per step is 15 s. The emission around 405 nm, 520 nm, 540 nm, and 650 nm are assigned to transitions from the levels $^2H_{9/2}$, $^2H_{11/2}$, $^4S_{3/2}$, and $^4F_{9/2}$, respectively, to the ground state $^4I_{15/2}$. Spectra under different excitation intensities between 380 and 580 nm are shown more in detail in Fig. 4.9a. Further transitions are visible around 450 nm and 472 nm. A change of the shape of the green emission around 560 nm with increasing excitation intensity is clearly observable. To highlight this change, the green parts of the spectra, normalized to the peak at 540 nm, are shown in Fig. 4.9b for four different excitation intensities. From level energies recorded by Dieke [137], possible associated transitions can be found:

– $^4F_{3/2} \rightarrow {}^4I_{15/2}$ for 450 nm,
– $^2P_{3/2} \rightarrow {}^4I_{11/2}$ and $^2K_{15/2} \rightarrow {}^4I_{13/2}$ for 472 nm, and
– $^2H_{9/2} \rightarrow {}^4I_{13/2}$ and $^2G_{7/2} \rightarrow {}^4I_{11/2}$ for 560 nm.

Further information about the transitions can be obtained by investigating the excitation power dependence of the UC fluorescence. For that purpose, the different contributions in the green emission have to be separated. The spectrum recorded under weakest excitation intensity, where the influence of higher photon processes is smallest, is subtracted from all spectra with higher excitation intensities after normalizing to the peak around 540 nm. The result is shown in Figs. 4.9c and 4.9d. The two different

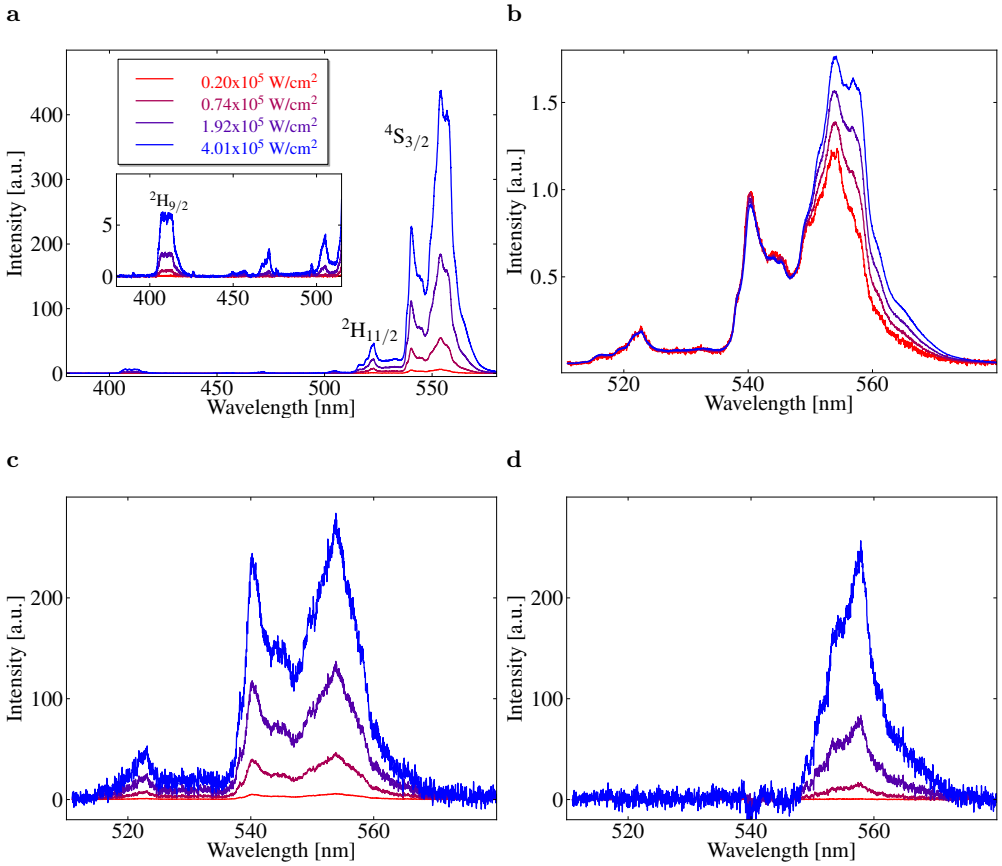

Figure 4.9.: a: Detailed spectra of blue and green UC fluorescence for different excitation intensities. b: The spectra normalized to the peak height at 540 nm. The change in the shape of the spectrum indicates contribution from another transition. c and d: Differential spectra (see text) of the transitions $^2H_{11/2}$, $^4S_{3/2} \rightarrow {}^4I_{15/2}$ and the second transition that contributes to the green UC fluorescence.

transitions do not change their shape with increasing excitation intensity.

The excitation power dependence of the different transitions are shown in Fig. 4.10a. None of the fluorescence intensity curves can be fitted with an ordinary function of the form

$$I = c \cdot P^a, \tag{4.28}$$

where I is the emitted intensity, P the excitation intensity, and a the fitting parameter. For all transitions the slope of the curve decreases with increasing excitation intensity. Nevertheless, the data sets can be fitted for the range of lower and higher excitation intensities with functions as suggested in Eq. 4.28 with exponents a_{low} and a_{high} (Fig. 4.10b).

a

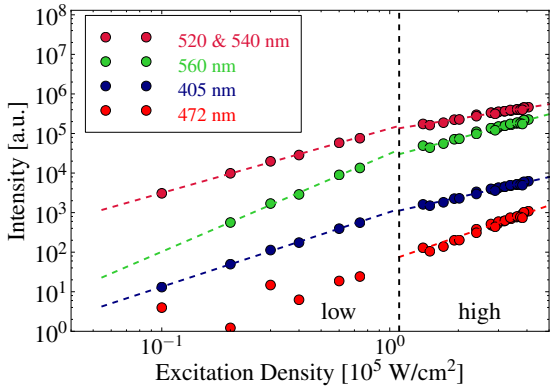

b

wavelength [nm]	a_{low}	a_{high}
405	1.9	1.3
472	–	1.9
520 & 540	1.6	0.9
560	2.5	1.5

Figure 4.10.: a: Excitation intensity dependence of the UC fluorescence for the transitions. The wavelength numbers in the legend denote the center peaks of the emission. b: Fitted exponents of the transitions for the different regimes.

For the weakest emission band around 450 nm, a fit for the low excitation intensity range is omitted, as the fluorescence intensity is too weak. As the dependence for the transition with the main peak at around 405 nm ($^2\text{H}_{9/2} \rightarrow {}^4\text{I}_{15/2}$) has another power dependence as the emission peaked at 560 nm, it can be concluded that these transitions do not originate from the same level and the latter can be attributed to the transition $^2\text{G}_{7/2} \rightarrow {}^4\text{I}_{11/2}$. As the emission around 472 nm has the highest exponent, it is reasonable to assume that an even higher level than $^2\text{G}_{7/2}$ is involved in this transition. The appropriate assignment is therefore the transition $^2\text{P}_{3/2} \rightarrow {}^4\text{I}_{11/2}$.

4.3.2. Size-Dependence of Upconversion Emission in Single Nanocrystals

In semiconductor physics, size-dependent emission is a well-known phenomenon. If the dimensions of the structure become smaller than the excitonic Bohr radius, the confinement restricts the electrons and holes on discrete energy levels which depend on the dimensions of the confining structure. Quantum wells, quantum wires, and quantum dots with their unique properties have been studied extensively (see Ref. [200] and references therein). Since $4f$-electrons are closely localized in the orbitals around the ion's nucleus, confinement of the emitting dipole wavefunction can not play a role for lanthanoids. However, size dependence of lanthanoid-doped materials has been observed. The underlying mechanisms can be divided in three main groups:

1. Reducing the surrounding material results in a change of the dielectric environment of the emitting ions, altering the spontaneous emission due to a change of the photonic density of states [201].
2. For nanometer sized particles, surface effects become important. On crystal sites close to or on the surface, the luminescent lanthanoid ions experience a different crystal field, altering the exact position of the energy levels of the $4f$-electrons [202–204]. Furthermore, organic groups (e.g. OH^--, CO_3^{2-}-, or CH-groups) adsorbed on the surface provide high-energetic vibrational modes as nonradiative channels that can change and quench the emission [205, 206]. This negative side-effect of nano-sized material can be compensated by advanced surface chemistry [206] and core/shell particles [207].
3. Confinement effects in the host crystal can affect the lanthanoid's emission. In bulk ZnS the band gap is lower than the gap between the ground and the first excited state of Eu^{2+}. Therefore, in Eu doped ZnS, no intra-ion transition can be observed, as an bound exciton state is formed at the Eu^{2+} [208]. Decreasing the size of the crystal below 4 nm increases the band gap due to the confinement. The excited state of the Eu^{2+} is moved into the band gap and the intra-ion transition can be observed [203]. The influence of acoustic phonon confinement on thermalization within a J-level's sublevels and the transition of so-called hot bands has been intensively studied by Liu et al. [209–211].

So far, all experiments investigating confinement effects of the host particle that directly affect the lanthanoid emission were done on ensembles of nanocrystals. Especially in size-dependent measurements, ensemble measurements suffer from the intrinsic averaging over a large number of particles with sizes within the ensemble's size-distribution. For obtaining more detailed information on the emission properties of lanthanoid-doped nanocrystals, it is necessary to investigate single nanocrystals.

To localize single nanocrystals, the sample is scanned with the xy-piezo actuator of the sample stage and the emission within the focal spot is observed with an avalanche photo diode (APD). Sample sites that exhibit very weak emission are further examined with the AFM to guarantee that a single nanocrystal is in the focus. If this is the case, UC fluorescence spectra of the crystal are recorded under different excitation intensities. The image of a typical AFM scan is shown in Fig. 4.11. It is possible to clearly distinguish three different nanocrystals between 6 and 48 nm. They are well separated by more than 500 nm, a distance that allows to investigate single particles independently with the confocal microscope.

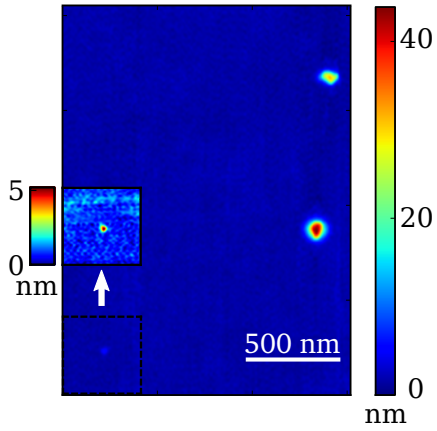

Figure 4.11: Image of a typical AFM scan: Three $NaYF_4$ particles are clearly distinguishable. The inset shows the smallest particle with an height scale. The lateral distance between the particles is large enough to investigate individual particles optically.

The count rates on the APD are in the range from a few hundred up to 10,000 counts per second, depending on the size of the crystal. The spectra of two nanocrystals of different sizes are shown in Fig. 4.12 for excitation intensities of 0.25 mW and 1.00 mW, respectively, which correspond to excitation densities of around $0.8 \times 10^5\,\mathrm{W\,cm^{-2}}$ and $3.2 \times 10^5\,\mathrm{W\,cm^{-2}}$. The spectra are recorded with integration times per step of 120 s for the smaller particle in Fig. 4.12a and 60 s for the bigger one in Fig. 4.12b.

Intensity Dependence of Green and Red Emission

At first glance, for both particles the intensity of the green emission band increases more than the intensity of the red emission band with the enhanced excitation density. The ratio of green to red emission intensity, the GRR, can be defined as the figure of merit. The rise of the GRR with increasing excitation power can be explained using the level scheme in Fig. 4.5. After the first ET process, the Er^{3+} ion is in the $^4I_{11/2}$ state. From this level, it can relax nonradiatively with the rate k_{nr1} to the $^4I_{13/2}$ as already described in Section 4.2.3. The other possibility is a second ET to reach the level $^4F_{7/2}$ with a rate k_{ET2}. While k_{nr1} is independent of the excitation power, k_{ET2} is directly dependent on the occupation probability $N_{S,1}$ of the sensitizing Yb^{3+} $^2F_{5/2}$ level (Appendix A). This, in turn, increases with increasing excitation power. As the probability for the nonradiative decay to the $^4I_{13/2}$ is given by $k_{nr}/(k_{nr1} + k_{ET2})$, for higher excitation intensities the probability for the process

$$^4I_{11/2} \xrightarrow{k_{nr}} {}^4I_{13/2} \xrightarrow{k_{ET3}} {}^4F_{9/2}$$

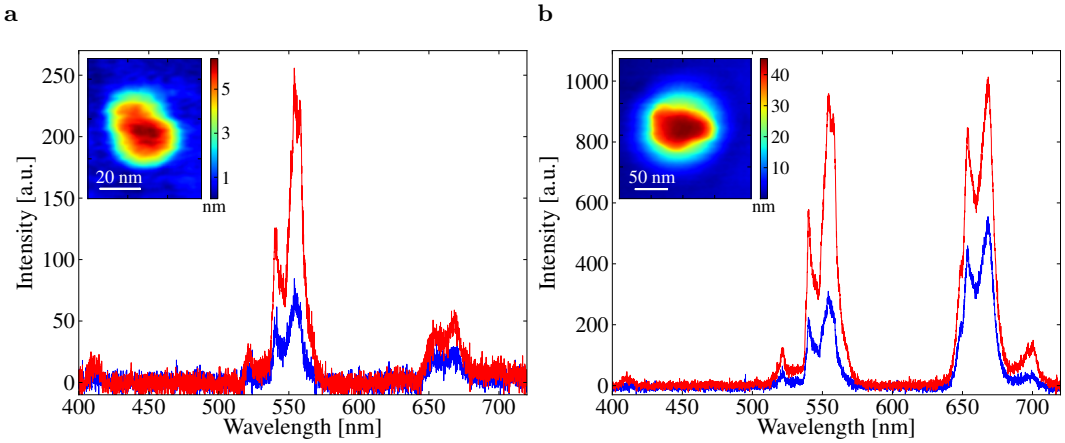

Figure 4.12.: Upconversion fluorescence spectra for two different nanocrystals under excitation intensities of $0.8 \times 10^5\,\mathrm{W\,cm^{-2}}$ (blue curves) and $3.2 \times 10^5\,\mathrm{W\,cm^{-2}}$ (red curves), respectively. The insets show the corresponding AFM scans of the nanocrystals. For both particles the green to red emission ratio (GRR) is increasing with increasing excitation power. Under both excitation intensities, the GRR is much higher for the smaller particle compared to the larger one.

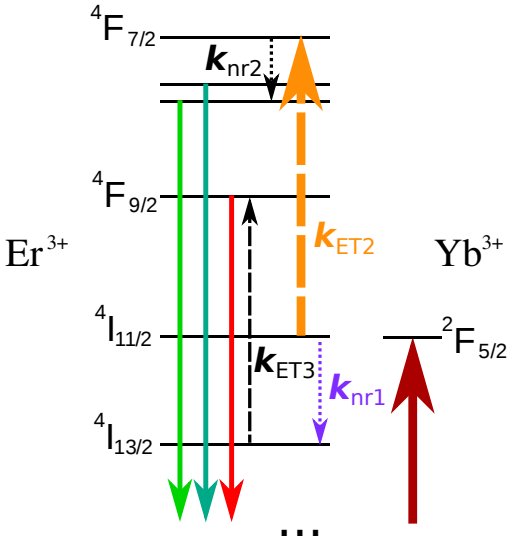

Figure 4.13: Explanation of the increase of the GRR with increasing excitation intensity: While k_{nr1} is a constant, the rate k_{ET2} is proportional to the occupation probability $N_{\mathrm{S},1}$ of the Yb^{3+} $^2F_{5/2}$ level. With increased excitation, ρ_{S} is increased by enhanced absorption, and it results in the overall stronger population of the green emitting levels.

to reach the red emitting level is reduced compared to the process

$$^4I_{11/2} \xrightarrow{k_{\mathrm{ET2}}} {}^4F_{7/2} \xrightarrow{k_{\mathrm{nr2}}} {}^4S_{3/2},\ ^2H_{11/2}\ ,$$

that populates the green emitting levels.

Size-Dependence of Upconversion Emission in Single Nanocrystals

Comparison of the spectra of both particles in Fig. 4.12 under the same excitation conditions reveals that the GRR is dependent on the individual particle as well. Therefore, for nanocrystals with different UC fluorescence intensities the spectra are taken and the particles are scanned with the AFM. The integration times per step for the spectra lie between 30 s for the biggest particle and 120 s for the smallest particle. To obtain the emission intensities of the green and red emission bands the spectra are normalized to the integration time and integrated from 500 nmdash600 nm and 620 nmdash720 nm, respectively. The sum of both is denoted as the total intensity. The measured intensities are critically dependent on the exact position of the particle within the confocal laser focus, and drifting of the particle within the focus due to thermal effects or creep of the piezo introduces an error that is estimated to be on the order of 15%.
For particles with extensions lower than 50 nm, the AFM tip is of comparable size and the AFM scan reflects the convolution of the tip and the particle, not the particle's real shape. For that reason, the height is chosen as a measure for the size of the particle as the height is measured correctly and not distorted by the tip shape. However, due to vibration of the sample stage, the height is subject to an error of about 1 nm. In Fig. 4.14a the total intensity is plotted against the particle height. A strong nonlinear increase of the fluorescence emission is observed with height h, since the volume and therefore the number of upconverting ions scales with the cube of the height as a rough approximation.

The GRR for the four different particles is shown in Fig. 4.14b. Starting at a value around 2.7, with increasing size the GRR reduces and saturates for the larger particles at a value of about 0.6. The "color" of the nanocrystals changes with its size, until it reaches the color of the bulk material.

Previously, the introduction of additional nonradiative channels by organic surface groups were held responsible for the opposite effect as observed here, the decrease of the GRR with decreasing size, observed by Song et al. [212] in Yb^{3+}/Er^{3+} codoped Y_2O_3. These additional nonradiative channels explained also a quenching of the UC fluorescence. Unfortunately, the experimental details are not reported, not allowing a direct comparison of the two experiments. However, additional quenching seems not to be relevant in our experiment: Comparing the total emission intensities for the two smaller nanocrystals with those of the two larger ones can be done using the above cubic dependency h of the intensity. Within the error limits, the emission intensities of the

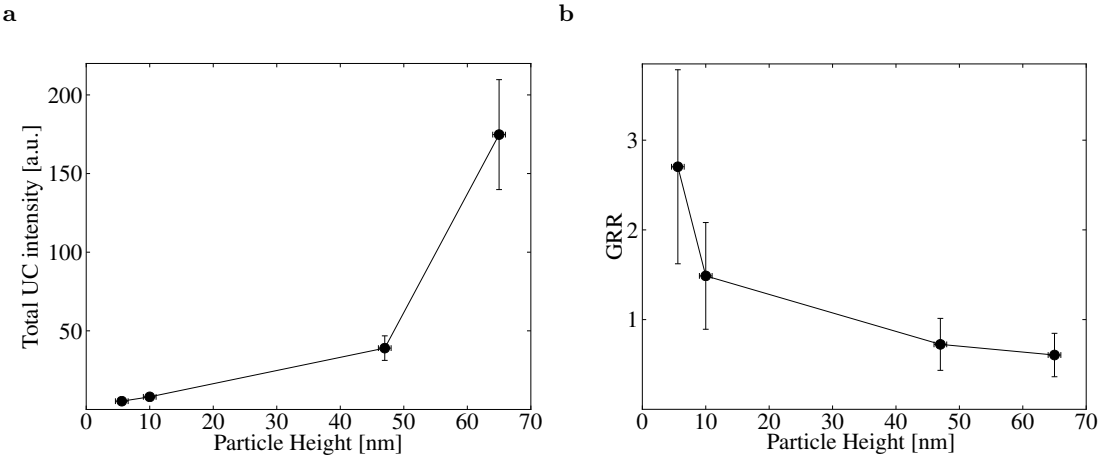

Figure 4.14.: a: Total upconversion fluorescence intensity versus the particle heigth h. The intensity increases as the number of emitting ions in the nanocrystal scales approximately with h^3.

smaller particles seem to be higher or in accordance to an h^3 law defined by a fit using the intensities of the two larger particles. This indicates that quenching seems not to have a significant higher impact than for the larger particles.

To understand the color change observed in the experiment, it is necessary to take into account the properties of optical phonons in nanocrystals. For semiconductor nanocrystals, various theoretical approaches to model the phonon properties were employed to explain quantitatively the Raman scattering spectra and measurements on electron–phonon coupling [213–216].

While the phonons in bulk material are delocalized, as a result of the limited geometry of the nanocrystals, the phonon modes have to be confined and a new class of modes appears: surface phonon modes. As a result of the boundary conditions, the density of phonon states is changed, too: The possible modes have to ”fit” into the crystal, which reduces the number of possible modes. Additionally, the impurities and the high surface to volume ratio can be responsible for stress inside the nanocrystals, a further source for a change in the phonon properties.

The data collected for the nanocrystals does not justify the quantitative usage of the level model, since too many parameters are unknown, e.g., lifetimes of the individual levels, the quantum yield, and the exact particle shape. At least a qualitative understanding is possible: First, the confinement given by the nanocrystal does not allow propagation of the phonons, neither of the promoting nor of the accepting modes. Furthermore, as

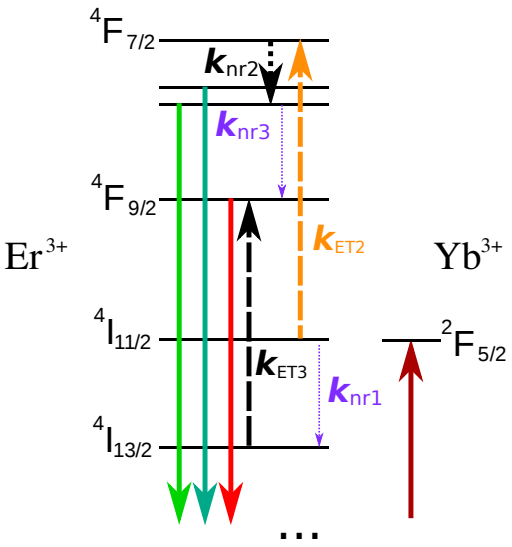

Figure 4.15: Change of the GRR with size: A reduced phonon density of states reduces the multiphonon decay rate k_{nr1}, the intermediate step to populate the red emitting level $^4\mathrm{F}_{9/2}$. Also the nonradiative decay from the green emitting levels are less probable, resulting in the increase of the GRR with decreasing size.

the phonon density of states is reduced, the numbers of these modes are reduced as well. Both these effects suppress the nonradiative processes. The result of such a phonon bottleneck [159, 217] is analogue to the previous case of stronger excitation, increasing the GRR, but in this case k_{nr1} decreases while k_{ET2} stays constant. This reduces the population probability of the intermediate $^4\mathrm{I}_{13/2}$ level which is an intermediate step to populate the red emitting level $^4\mathrm{F}_{9/2}$ (Fig. 4.15). The second possible excitation path of this level by nonradiative decay from the green emitting levels with decay rate k_{nr3} is also less probable. The red emission is reduced.

The here shown size dependence of upconversion fluorescence of individual nanocrystals is of major interest. As semiconductor nanocrystals, these crystals could be used as biolabels, where different sizes, and therefore different colors, could be functionalized specifically to bind and mark different biological components. Furthermore, ”phonon engineering” using heterostructures [218] could be used to further alter the upconversion fluorescence at will, opening the road for a new kind of tailored nanomaterials.

4.4. Plasmon-enhanced Upconversion in Single Nanocrystals

As discussed previously in this chapter, a lot of effort has been made made to improve the UC efficiency of lanthanoid-doped nanomaterials. Another possibility to enhance fluorescence emission is to make use of plasmonic structures as described in Section 2.3. Recently, several experiments used plasmons to enhance the UC emission [219–223], and a theoretical model was introduced [224]. In this section, the influence of gold spheres on the upconversion fluorescence of individual $NaYF_4$:Yb^{3+}, Er^{3+} codoped nanocrystals is investigated.

Sample Preparation and Experimental Setup

The nanocrystals that are employed in this experiment were prepared by the group of Prof. T. Nann [225] applying a microwave assisted synthesis method [226]. The obtained nanocrystals are bi-modal, i.e., two different lateral extensions of approximately 5 nm and 30 nm are present. A transmission electron microscope (TEM) micrograph of the particles is shown in Fig. 4.16. From these nanocrystals, only the larger ones are used in the following experiment. The plasmonic structures are build with gold nanospheres (*BBInternational*) with a size of 60 nm (*BBI GC60*) and 30 nm (*BBI GC30*).

The samples are prepared by spin-coating 40 µL of the nanocrystal solution on a cleaned coverslip followed by a second spin-coating step of the same amount of the gold nanosphere solution, both at a speed of 1500 rpm.

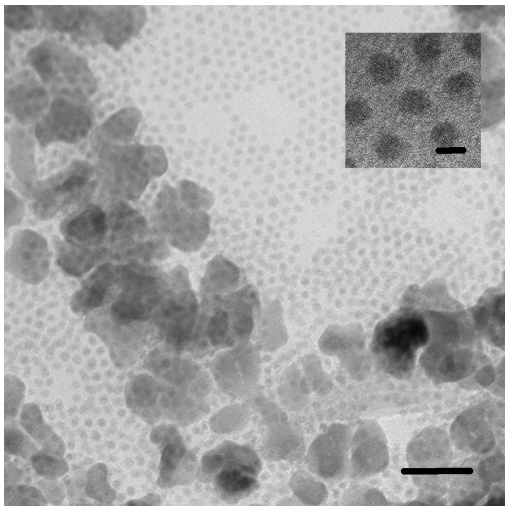

Figure 4.16: TEM of the bi-modal set of $NaYF_4$:Yb^{3+}, Er^{3+} codoped nanocrystals used to investigate plasmon-enhanced UC. The scale bars are 50 nm and 5 nm for the inset. (Image provided by Prof Thomas Nann [225].)

In contrast to the previous experiments in this chapter, the setup is extended by a chopper wheel in the excitation path and a single photon counting module (*PicoQuant PicoHarp 300*) in time-tagged time-resolved mode, to allow for time-resolved measurements on the codoped nanocrystals (see Fig. 4.17). For the details see Chapter 3.

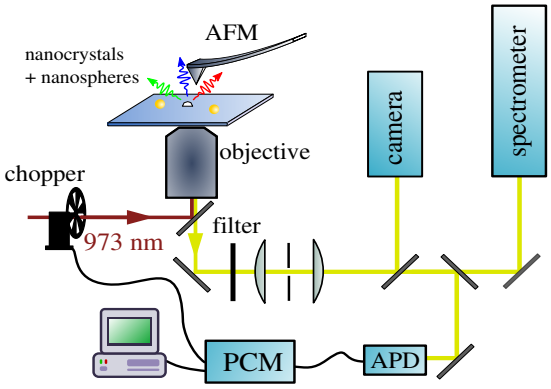

Figure 4.17.: Sketch of the setup configuration. In addition to the previous experiment, a chopper wheel and a photocounting module are used for time-resolved measurements.

In a preliminary step, a bare single nanocrystal has to characterized. By scanning the sample and monitoring the upconversion signal on the APD, a nanocrystal is located, placed in the focus. An AFM scan of the focal region is made. In the case of more than one nanocrystal in the scan region, coincidence between one of the nanocrystals in the AFM scan and the one in the focus has to be ensured. This is done by moving the suspected particle in and out of the focus while observing the UC fluorescence intensity on the APD. All the following measurements were done under an excitation density of approximately $2 \times 10^5\,\mathrm{W\,cm^{-2}}$.

4.4.1. Characterization of the Bare Nanocrystal

The UC fluorescence spectrum of a single nanocrystal is shown in Fig. 4.18. The typical green ($^2\mathrm{H}_{11/2}$, $^4\mathrm{S}_{3/2} \rightarrow {}^4\mathrm{I}_{15/2}$) and red ($^4F_{9/2} \rightarrow {}^4\mathrm{I}_{15/2}$) emission bands are present. The inset illustrates the corresponding AFM scan of the nanocrystal. It turns out that the height of all nanocrystals is well below 30 nm, allowing to distinguish clearly the nanocrystals from both the small and large gold spheres. Contrary to the excitation with laser light of 514 or 532 nm (see Section 5.4.3), no emission from the gold spheres is observable under excitation with light of 973 nm.

To investigate the dynamics of the UC fluorescence the excitation light is modulated by the chopper wheel with a frequency of approximately 400 Hz, providing on- and off-

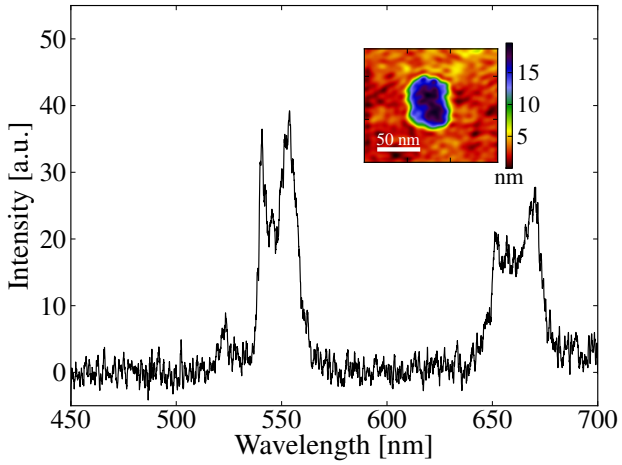

Figure 4.18.: Spectrum of a single $NaYF_4$ nanocrystal codoped with Yb^{3+}, Er^{3+} displaying the typical upconversion fluorescence bands in the green and the red. An AFM scan image of the same nanocrystal is shown in the inset.

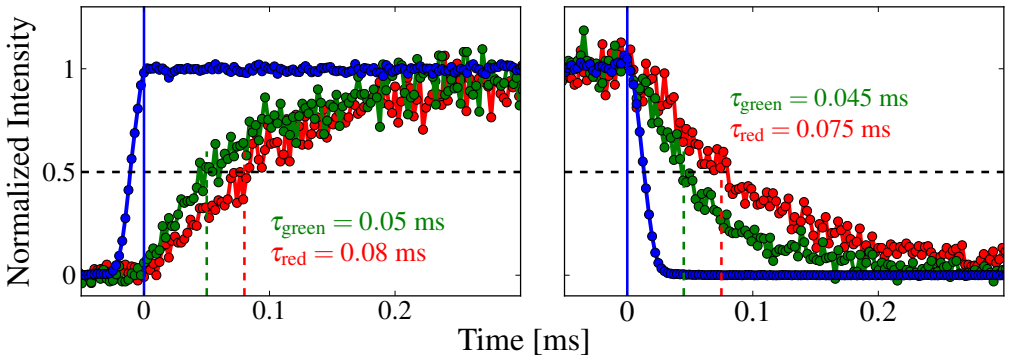

Figure 4.19.: Rise (left) and decay time (right) for the green (green curve) and red (red curve) UC fluorescence bands. The laser intensity is plotted for comparison (blue curve). Neither rise nor decay can be fitted with by exponential curves because of the complexity of the level scheme (see text).

times of 1.25 ms. The APD signal is recorded by the photon counting module. Additional filters can be used to separate the green and red emission bands, and the UC fluorescence dynamics for both bands are shown in Fig. 4.19. Both the rise and the decay times of the UC fluorescence signal are shorter for the green emission band.

Neither the rise nor the decay times of the signals can be considered to be mono-exponential (see Appendix A.2), as none of the nonradiative transitions and energy transfer steps are fast enough to be neglected in the rate equations [195]. Secondly, the

individual emitting Er^{3+} ions fill different (bulk-like) lattice sites [227] and surface sites with differing crystal fields. These inhomogeneous effects add to the non-exponential behavior.

The time constants for the rise and the decay for both UC fluorescence bands are of the same magnitude. As discussed in Appendix A.2, without the knowledge of at least some of the time constants within the lanthanoid system, it is not possible to extract any further information about the lifetimes of the individual levels from this data. However, as a measure for the rise and decay times, it is reasonable to determine the time τ it takes the signal to rise (decay) to half of its maximal value as the figure of merit. For $t = 0$ the time is chosen when the laser reaches (leaves) the maximum (minimum) intensity. The decay time constants observed here are in very good agreement with previously reported values by Wang et al. [207].

4.4.2. Plasmon-Enhanced Emission

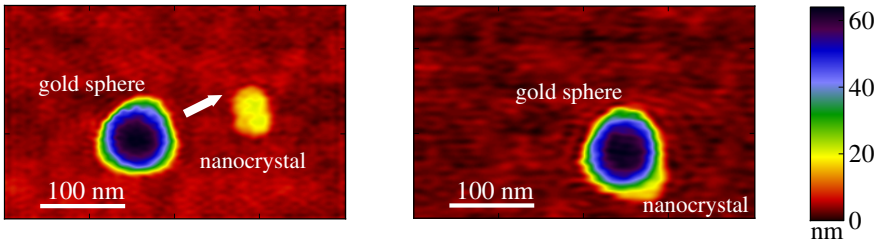

Figure 4.20.: a: A gold sphere with a diameter of 60 nm is positioned in the vicinity of the pre-characterized nanocrystal using the AFM. b: The gold sphere is brought in direct contact with the nanocrystal.

Influence of a Single 60 nm Gold Sphere

In a first investigation, a single gold sphere with a diameter of 60 nm is used to study its influence on the UC fluorescence of the codoped nanocrystal. A single gold sphere can be distinguished by its size and its more regular shape from the nanocrystals using the AFM and it is brought in the vicinity of the nanocrystal (Fig. 4.20).

After the gold sphere is in contact with the nanocrystal, the spectrum is taken and the time-evolution under chopped excitation is recorded. The spectrum of the coupled nanocrystal–gold sphere system is shown in Fig. 4.21a (blue curve), together with the spectrum of the bare nanocrystal (violet). The excitation density and spectrometer

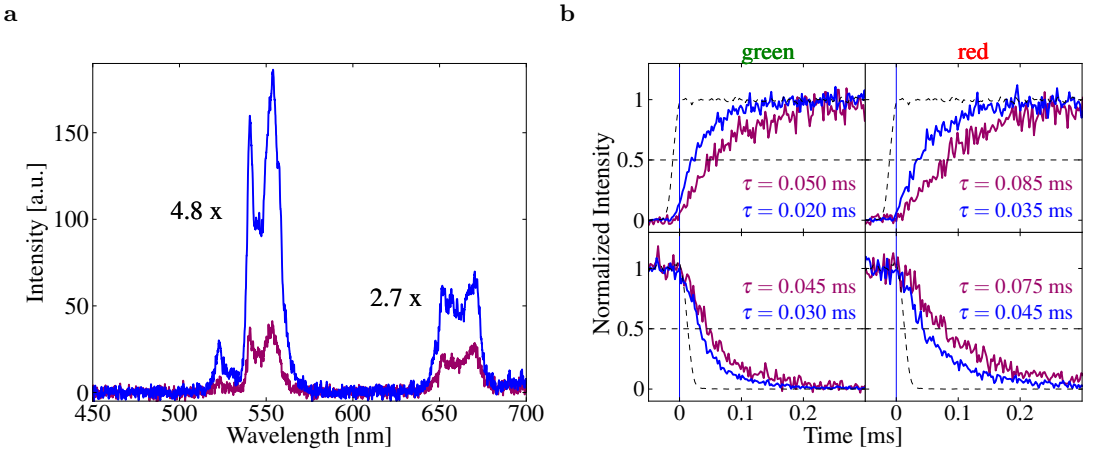

Figure 4.21.: a: Plasmon-enhanced UC fluorescence spectrum of the single nanocrystal (blue curve). Compared to the bare nanocrystal (violet curve), the green emission band is stronger enhanced than the red emission band. The numbers in the graph indicate the enhancement factors for the particular band. b: Rise (upper) and decay (lower) curves for the green (left) and the red (right) UC emission band, without (violet) and with (blue) plasmonic enhancement. For both bands the rise and decay times are reduced by the coupling to the gold sphere plasmon. The modulated excitation laser signal is indicated by the dashed curve.

settings are the same for both spectra so that the intensities of the spectra can be compared directly. By employing the gold sphere, the emission from the nanocrystal is drastically enhanced, the overall emission is enhanced by a factor of 3.8. However, the enhancement is not equal for the emission bands: While for the green emission band the enhancement factor is 4.8, the red emission increases by a factor of 2.7 under the influence of the gold sphere. The error for the enhancement factors is estimated to be less than 2%. The plasmonic enhancement effect is also reflected by the reduction of the rise and decay times of the fluorescence signal as can be seen in Fig. 4.21b.

There are different effects contributing to the emission enhancement and the reduction of the rise and decay times, affecting the excitation or having an impact on the emission. First, on the excitation side, the localized field around the gold sphere (Section 2.3.2) enhances the field density for the Yb^{3+} ions, resulting in a stronger absorption, denoted as 1 in Fig. 4.22. On the emission side, the coupling of the emitting transitions to the plasmon of the nanosphere enhances the emission rates (marked as 2 in Fig. 4.22). Furthermore, the same effect has to be taken into account for the transitions involved in the energy transfers and increasing the energy transfer rates (3 in Fig. 4.22). As a last

effect, a new nonradiative decay channel is introduced by nonradiative energy transfers to the gold sphere, reducing the quantum yield by quenching and reducing the time constant of the decay (4 in Fig. 4.22).

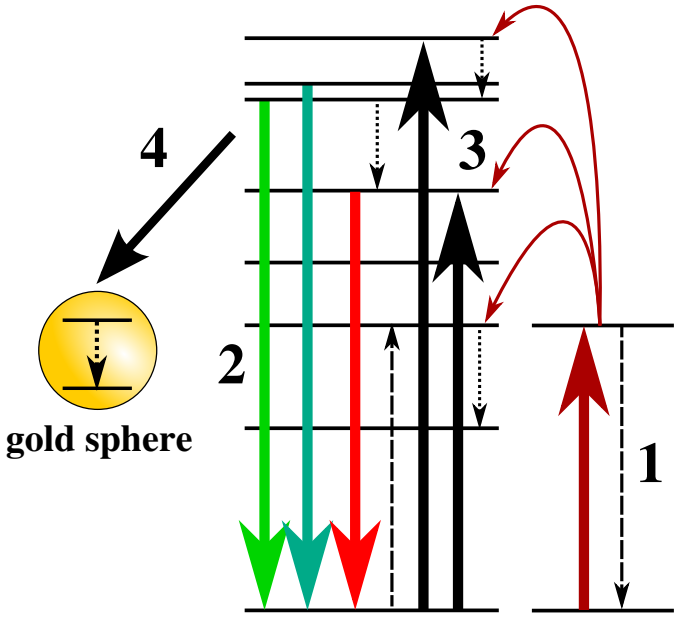

Figure 4.22.: Plasmonic effects that occur in the energy transfer UC. 1: The incoming excitation light is increased by the local fields build up by the gold sphere. 2: The emission rate is enhanced due to the coupling to the plasmon. 3: The same effect enhances the transitions involved in the energy transfers and may increase the energy transfer rate. 4: Quenching due to nonradiative energy transfer to the gold sphere.

As the plasmon resonance around 540 nm of the gold sphere and the green emission band overlap better, one would indeed expect a stronger influence on the green emission process. However, the higher enhancement factor can more likely be explained by the process already described in Fig. 4.11: The excitation intensity is increased by the introduction of the sphere. Thus, it becomes more probable that a second energy transfer step further excites the Er^{3+} ion by the transition $^4I_{11/2} \rightarrow^4 F_{7/2}$ before the nonradiative decay $^4I_{11/2} \rightarrow^4 I_{13/2}$ can take place, which is the intermediate step to fill the red emitting $^4F_{9/2}$ level.

The enhancement factors observed are much higher than the predicted enhancement by Esteban et al. [224] for energy transfer upconversion, but the model of their calculation does neither cover the influence on the energy transfer rates nor nonradiative processes. This influence varies significantly with the exact position of the gold nanosphere in respect to the nanocrystal and the polarization axis of the excitation light. For different

configurations and different nanocrystals, values between 2 and 4.8, and 1.6 and 2.7 were observed for green and red UC fluorescence, respectively. The highest values observed here are not a fundamental limit, improvement is still possible, e.g., by changing the size or shape of the nanocrystals and the gold particles.

The influence of the polarization of the excitation laser beam can be studied by inserting a $\lambda/2$-waveplate in the excitation. Due to the geometry of the setup, the $\lambda/2$-waveplate is also present in the detection path and alters the detected emission light by etaloning-effects and the spectra can not be compared to the previous ones. While rotating the plate the UC fluorescence intensity is examined on the APD. The spectrum with the polarization aligned for maximum and minimum intensity is shown in Fig. 4.23a. This is the case when the polarization is aligned parallel ($\parallel$) and perpendicular ($\perp$) to the axis defined by the centers of nanocrystal and gold sphere, respectively. The factors between the minimum and maximum for the green and red emission bands are higher than those between the emission from the bare nanocrystal and the coupled nanocrystal–gold sphere system. Perpendicular to the axis defined by nanocrystal and gold sphere, the excitation intensity on the nanocrystal is even lower than in the case without the gold sphere, but the quenching effects are fully present.

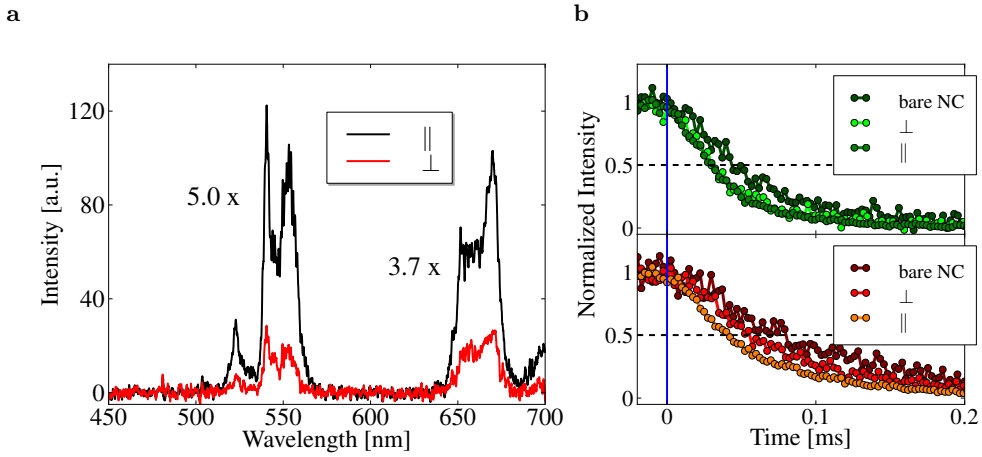

Figure 4.23.: Polarization-dependence of the UC fluorescence. a: Spectrum for excitation polarization aligned along ($\parallel$) and perpendicular ($\perp$) to the axis defined by the centers of nanocrystal and gold sphere. The factors between minimum and maximum polarization are denoted in the graph. b: Decay curves under the two polarization orientations for green (left) and red (right) emission band. For comparison, the decay of the bare emission in the nanocrystal is shown, too.

The decay curve of the UC fluorescence signal for maximum and minimum polarization

is shown in Fig. 4.23b, together with the decay curve of the emission from the bare nanocrystal. The decay for the green emission band is similar for both polarizations and shorter than the decay in the bare nanocrystal, as one would expect. For the red emission band, under both excitation polarizations the decay is shorter than that in the bare nanocrystal, but is different for each polarization orientation. There are two possible explanations: First, the excitation path can be altered and the numerical solution of the rate model in Appendix A.2.2 verifies that the enhanced excitation intensity can indeed shorten the decay time of emitting levels. Second, under enhanced excitation intensity, further upconversion steps to higher levels starting from the red emitting level $^4F_{9/2}$ could also reduce the decay rate of the level, as this depopulation path is also strongly dependent on the excitation intensity.

Sandwich Configuration and Formation of Hot Spots

A refined experimental configuration can be assembled with gold nanospheres with a smaller diameter of 30 nm. In the case of 60 nm nanocrystals, the geometry of the particles allows the nanocrystal to "disappear beneath" the gold spheres. Furthermore, the nanocrystal is below the region where maximal field enhancement of the excitation is expected (see Fig. 2.12b). Using gold spheres with a diameter of 30 nm, the nanocrystal is sandwiched between two gold nanospheres step by step. Such a configuration is of high interest, as it is possible to form "hot spots" between the two gold spheres.

In Fig. 4.24a, the assembly steps towards the sandwich configuration are shown. After each assembly step A to D, the UC emission is studied. In configuration A, the gold nanospheres and the NC are well separated by a gap of more than 20 nm so that the NC's emission is only marginally influenced by the spheres. Then, one of the gold spheres is moved towards the NC (B). As expected, the emission is enhanced and the rise and decay times are reduced. This is shown for the green emission in Fig. 4.24b and c. The enhancement by a factor of 1.8 is not as strong as for a single 60 nm particle. By bringing the gold nanosphere in full contact with the NC (C), the rise and decay times are further decreased, while the overall emission intensity is unchanged. This can be explained by the following consideration: In configuration B, excitation and emission are enhanced, and the gold sphere is still too far to introduce significant quenching of the emission. However, in full contact, additional quenching eats up any further amplification of the fluorescence. The second particle more than doubles the effect of the first particle: The intensity of the sandwich configuration D is by a factor of 1.9 higher than in the configurations B and C and 3.5 times as high as in A. The error is again below 2%. For

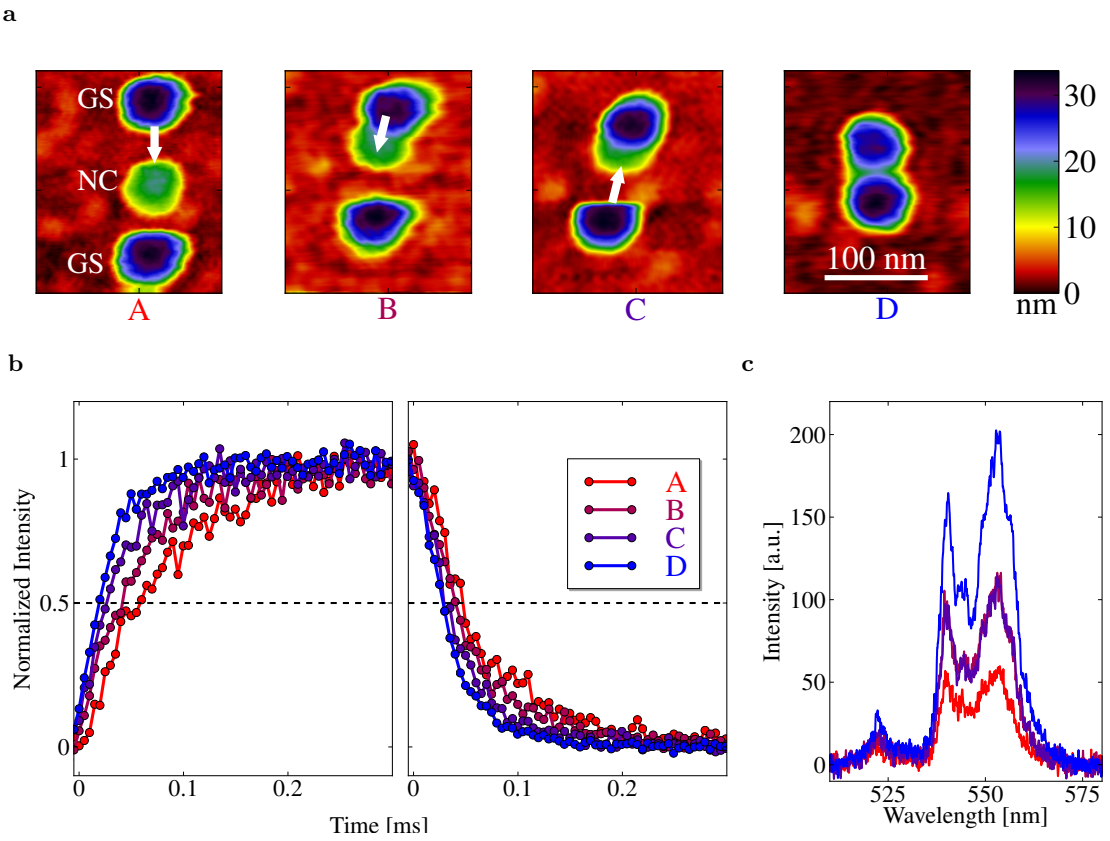

Figure 4.24.: Assembly steps of a plasmonic sandwich. a: A nanocrystal (NC) of 25 nm in diameter is stepwise sandwiched between two gold spheres of 30 nm in diameter. The arrows indicate how the gold nanospheres moved towards the NC. b and c: Corresponding rise and decay curves and spectra of each configuration A to D.

the red emission, in configuration B the enhancement factor is 1.3, but drops to 1.1 for the gold sphere in contact (C). In configuration D, the emission is 2.1 times stronger than from the bare nanocrystal.

The enhancement of the sandwich configuration is higher than the pure addition of the effects of two single gold nanospheres. The first nanosphere enhances the green and red emission by 80% and 30%, respectively. The second nanosphere increases the nanocrystal's emission by an additional 170% and 70% of the bare nanocrystal intensity. This is strong evidence that a hot spot is formed within the gap of the two gold nanospheres.

4.5. Final Remarks

In this chapter, the results of extensive studies on $NaYF_4$:Yb^{3+}, Er^{3+} codoped nanocrystals have been presented:

The power dependence of the UC fluorescence of different emission lines in the regime of high excitation density was investigated, and they were attributed to possible transitions in the Er^{3+} ions. On the single nanocrystal level, a size dependence could be found in the emission. Responsible for that is an altered phonon density of states and distribution in the nanocrystals. Finally, the influence of gold nanosphere with different sizes was studied.

However, the excitation and relaxation scheme within the Yb^{3+}, Er^{3+} system is very complex (see Fig. 4.5). For this reason it does not make sense to fit the data to an equally complex rate equation model without *a priori* knowledge of at least some of the individual transition rates. Nevertheless, all the observed phenomena can be explained very well qualitatively using the rate equations in Appendix A. In future experiments, including time-resolved measurements and pumping the emitting levels directly, time constants involved in the upconversion processes could possibly be extracted directly (see Section 6.2). This would allow for a quantitative modeling.

CHAPTER 5

Controlled Coupling of Single-Quantum Emitters to Resonant Structures

Single-photon sources are a key ingredient for the realization of quantum information systems by optical techniques. Among the sources for single photons that are available, individual nitrogen–vacancy (N–V) centers in diamond are of special interest, as they provide single-photon emission under ambient conditions. In diamond nanocrystals, these nitrogen–vacancy centers are ideal candidates to be employed in more complex photonic structures: by controlled assembly with other fundamental entities like microcavities it is possible to manipulate the properties of the single-photon emission.

In this chapter, after discussing the basic properties of nitrogen–vacancy centers, two different examples of such a *hybrid* approach to assemble different fundamental photonic entities are being presented:

- The on demand coupling of single N–V centers to spherical microresonators.
- The possibility to enhance the emission of single N–V centers by plasmonic structures, namely gold nanospheres.

This is for the first time, that the dielectric environment of a single-photon source could be actively influenced on demand to change the emission properties. Parts of the research presented here are also published in *Nano Letters*, **8**, 3911, 2008 [Schietinger et

al. 2008], *Nano Letters*, **9**, 1694, 2009 [Schietinger et al. 2009a], and *Journal of Physics B: Atomic, Molecular and Optical Physics* , **42**, 114001, 2009 [Schietinger et al. 2009c].

5.1. Single-Photon Sources

In 1865, James Clerk Maxwell published *A dynamical theory of the electromagnetic field*, which formulated for the first time the theoretical concept that postulated electromagnetic radiation, the famous four equations which became later known as the *Maxwell equations* [228]. It was thought that these equations were the finalization of the electromagnetic theory, but only 35 years later, Planck had to quantize the energy in order to attain the law of black body radiation [229]. Shortly after in 1905, this lead Einstein to his explanation of the photoelectric effect [230]. By thermodynamic considerations he derived that the entropy of the light field is similar to a "discontinuous medium" with particles he denoted as *light quanta*. He concluded that quanta of frequency ν have an energy of $h\nu$, where h is the Planck constant. The development of a theoretical foundation for the quantization of the electromagnetic field started in the late 1920s and was completed in the 1940s with the full theory of *quantum electrodynamics* [231].

The ever-growing interest in the smallest entity of the electromagnetic field, the single photon, is mainly driven by the possibility to use them as quantum carriers of one bit in quantum information schemes, the so-called quantum bit or qubit. For example, quantum key distribution such as the BB84 protocol [232] can be implemented using single photons [233]. Furthermore, it has been show theoretically and experimentally that quantum computation is achievable on the basis of linear optics with single photons [234, 235].

Different procedures can be used to produce single photons [33]: It is possible to attenuate light pulses in order to approximate single photons or to apply non-linear processes with a post-selection scheme, but the most straightforward way is the use of a single quantum system like an atom, an ion, or a semiconductor quantum dot. The fluorescence of such a system is naturally restricted to one photon per excitation-cycle.

When applying the simple method of attenuating light pulses to have approximately one photon per pulse, the underlying statistics of the photon number distribution per pulse remains the same as it was before the attenuation. For pulses from a thermal light source this is a Bose-Einstein distribution, for laser pulses (which is coherent light) the Poisson distribution. Therefore, one has to keep the average number of photons in a pulse low to avoid two photon pulses that would, for example, allow an eavesdropper to extract information without being discovered in quantum cryptography. But this means

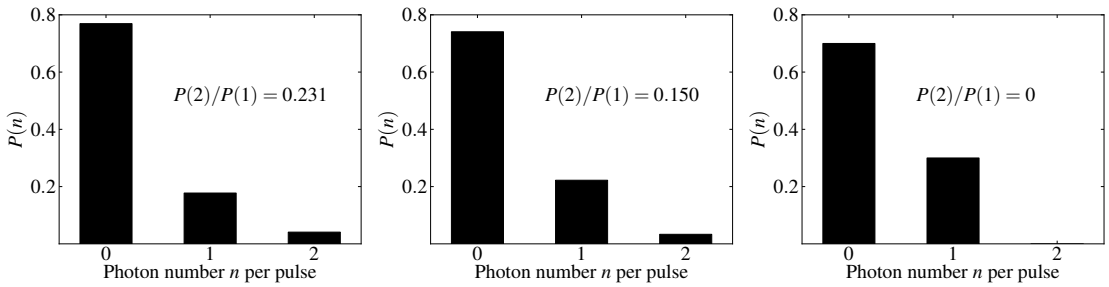

Figure 5.1.: Probability $P(n)$ for the number of photons per pulse for attenuated thermal (left) and laser (middle) light, and a single-quantum emitter all with an average of 0.4 photons per pulse. Also shown is the rate between two- and one-photon pulses for thermal and coherent light.

that a large number of pulses does not carry any photon at all (see Fig. 5.1) which restricts the maximal rate. The situation is slightly better for single photons generated in non-linear processes followed by post-selection, but the absolute production rate is also restricted by statistics [236].

For "real" single-photon sources – single quantum systems intrinsically capable to produce only a single photon after a single excitation – this is different (see Fig. 5.1): Within a pulse, only one photon is possible. However, the experimental challenge is to efficiently collect the fluorescence from the emitter to achieve a reasonable rate of single photons.

Closely connected to the photon number distribution is the autocorrelation or second-order correlation function of the quantized electromagnetic field given by

$$G^{(2)}(t,\tau) = \left\langle E^{(-)}(t)E^{(-)}(t+\tau)E^{(+)}(t+\tau)E^{(+)}(t)\right\rangle = \langle : I(t)I(t+\tau) : \rangle$$

where :: indicates normal ordering. This is a measure for the joint probability to detect a photon at a time $t+\tau$ after having detected a photon at a time t. For a statistically stationary field, it is convenient to introduce the normalized second-order correlation function

$$g^{(2)}(\tau) \equiv g^{(2)}(0,\tau) = \frac{G^{(2)}(0,\tau)}{|G^{(1)}(0)|^2} \tag{5.1}$$

with

$$G^{(1)}(0) = \left\langle E^{(-)}(0)E^{(+)}(0)\right\rangle,$$

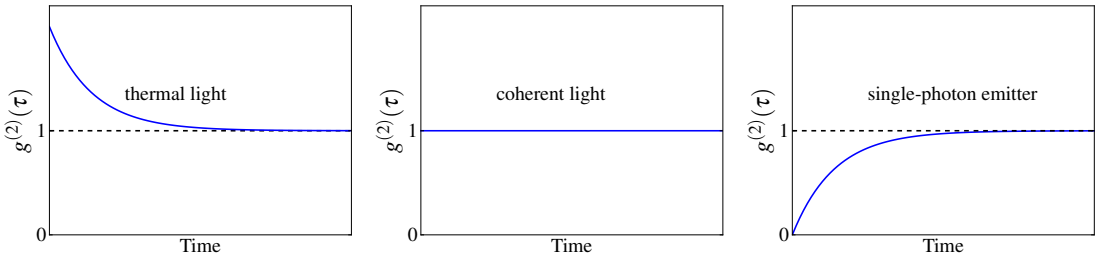

Figure 5.2.: $g^{(2)}$-function for a thermal (left), coherent (middle), and a single-photon light source.

the first-order correlation function at $t = 0$ which is in this case a measure for the average intensity.

For all sources, whether thermal, coherent, or single-photon emitters, the emission of photons is uncorrelated for large values of τ, and $g^{(2)}(\infty) = 1$. The differences occur around $\tau = 0$, shown in Fig. 5.2: For a thermal light source, the probability to detect a second photon is higher directly after a first photon has been detected, the emission is *bunched* and $g^{(2)}(0) > 1$. Coherent light, like the emission of a laser, is completely uncorrelated, i.e., the probability for the detection of a second photon is the same for all times τ after the detection of a first photon: $g^{(2)}(\tau)$ is constant and equals one. A single-photon emitter can only emit a single photon at $t = 0$. Therefore, the probability to detect a second photon at $\tau = 0$ is zero, and $g^{(2)}(0) = 0$. It takes time to re-excite the emitter and emit the second photon and the $g^{(2)}$-function rises to 1, where the slope of the rise behavior is determined by the excitation and decay rates of the emitter (see Appendix B.1.1). In contrast to thermal and coherent light fields, single-photon emission has no classical equivalent and is also referred to as a special kind of *non-classical* light.

When a single-photon emitter is excited continuously, any temporal correlation between two photons is lost after a few excitation–emission cycles and the photons come completely randomly in time. This is indicated by the $g^{(2)}$-function having a value of one. In many cases where single-photon sources are employed, it is not sufficient to have such a random stream of single photons. A continuous train of deterministic single-photon pulses is desired. This single photons "on demand" can be obtained by pulsed excitation. First, the excitation pulse has to be strong enough to have an excitation probability close to one. Second, the pulse has to be short enough that within the pulse duration not a second excitation is taking place. Third, it is obvious that the lifetime also sets the width of the time interval in which a photon detection can be expected. Therefore, two consecutive excitation pulses have to be separated by a time span signif-

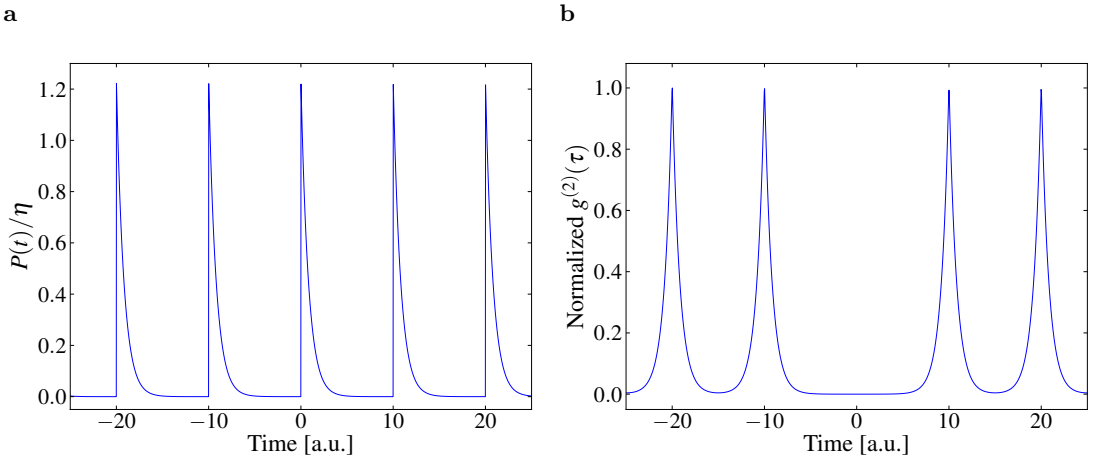

Figure 5.3.: Pulsed excitation of a single-photon emitter every 10 time units. a: Single-photon pulse train. Probability to detect a photon, normalized to the overall detection efficiency η of the setup. After each excitation pulse, the probability of detection decays proportional to the excited state probability. b: Normalized $g^{(2)}$-function of the single-photon source in a.

icantly larger than the lifetime of the emitting state to avoid an overlap of succeeding photon pulses. After each excitation pulse, the probability to detect the photon decays with the occupation probability of the emitting state, multiplied by the overall detection efficiency η of the setup (see Fig. 5.3a).

The corresponding second-order correlation of the single-photon source under pulsed excitation is shown in Fig. 5.3b. The probability to detect a second photon after the measurement has been started by a first photon is only given after the re-excitation by a further pulse. Around $\tau = 0$, no second photon is present and therefore $g^{(2)}$ is zero as in the case of continuous excitation.

Single-photon emission and antibunching was demonstrated with a variety of physical systems: atoms [237], ions [238], semiconductor quantum dots [22, 239], molecules [24], and defect centers in diamonds [240], and research and development is still ongoing.

From these implementations, defect centers in diamonds are outstanding in the convenience of their usage: Stable single-photon operation is possible at ambient conditions without any additional experimental equipment than a fluorescence setup, making them ideal constituents in hybrid assemblies.

5.2. Nitrogen–Vacancy Centers in Nanocrystal Diamonds

More than 500 optical defect centers are known in diamond, with emission spanning a wide spectral range from the ultraviolet to mid-infrared [241]. Among these defects, the nitrogen–vacancy defect is the best studied. It consists of a nitrogen atom replacing a carbon atom in the lattice and an adjacent free lattice site, a vacancy, as shown in Fig. 5.4a. N–V centers are present in most natural and synthetic diamonds. To increase their concentration, the diamond which has to host substitutional nitrogen atoms in the lattice is irradiated with high-energy particle beams, such as electrons, protons, neutrons, ions, or γ-rays, followed by annealing with temperatures around 700 °C. This method was first reported in 1965 by du Preez [242]. The irradiation breaks out individual, covalently bound carbon atoms, leaving unoccupied sites in the lattice. At around 700 °C, these vacancies can migrate in the lattice and get trapped at the nitrogen atoms to form the N–V center [243]. In the last few years, the method of direct implantation of single nitrogen atoms was developed and allows the placement of single N–V centers closely under the surface into very pure bulk diamond samples [244].

While a controversial discussion about the correct theoretical treatment and the exact electronic configuration of the nitrogen–vacancy (N–V) center is still taking place at the moment[1], many of the optical properties have been determined experimentally:

Two different electronic configurations of the N–V centers exist: the uncharged N–V^0 and the charged N–V^- centers [248]. The N–V^0 has a zero-phonon line (ZPL) at 576 nm, the N–V^- at 637 nm. While the N–V^0 center is built from the three dangling bond electrons from the C atoms around the vacancy together with the two unbound electrons from the nitrogen, the N–V^- captures an extra electron from the surrounding, and 6 electrons contribute to the electronic configuration. Both have a C_{3v} symmetry, revealed by polarization measurements on the emitted light [249] and the fact that uniaxial stress also effects the zero phonon absorption line [243].

The N–V^- centers, predominant in the experiments presented in this work, have an orbital singlet ground state and a degenerate orbital doublet excited state, see Fig. 5.4b. Furthermore, electron parametric resonance [250] and optical detected magnetic resonance measurements [251, 252] as well as spectral hole burning [253] suggest that both the ground and excited state of the N–V^- center are spin triplet states, $^3A_2$ and ^3E, respectively. The two orbitals of the excited states E_x and E_y are orthogonal to each other and oriented in a plane orthogonal to the z-axis defined by the nitrogen atom and the vacancy, giving rise to orthogonally polarized emission [254]. The ground state spin

[1] see Hossain et al. [245], the comment by Gali and Kaxiras [246], and the reply by Hossain et al. [247]

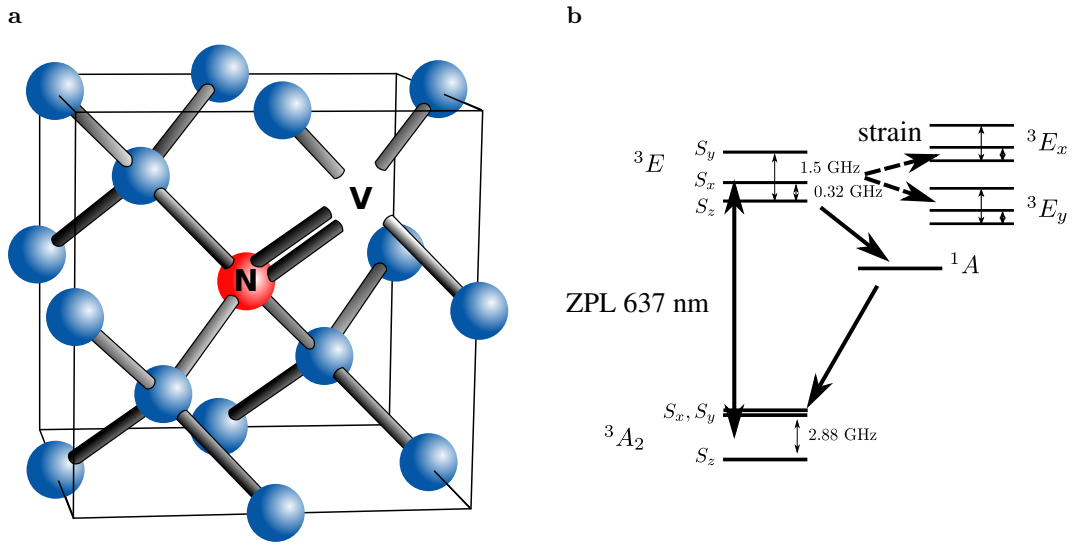

Figure 5.4.: a: Structure of the nitrogen–vacancy (N–V) center: Under irradiation of the diamond with high-energetic particles, vacancies are created in the lattice. Annealing mobilizes the vacancies, and they can get captured in sites neighboring a nitrogen atom. b: Energy level scheme of the N–V$^-$ center. The ground and excited states are a spin-triplets ^3A and ^3E, respectively. The ground state is split into $m = 0$ (S_z) and $m = \pm 1$ (S_x, S_y) levels, the excited state is split into $m = -1$ (S_x), $m = 0$ (S_z), and $m = 1$ (S_y). If additional strain is present, the excited triplet is further split into an E_x and an E_y branch.

levels are split by 2.88 GHz into a spin singlet with $m_z = 0$ and a spin doublet with $m_z = \pm 1$. Just recently, also the level splitting of the excited state could be unraveled [255]. The different spin states of ^3E are split by energy differences of about 0.32 and 1.5 GHz, respectively.

From dephasing measurements done with four-wave mixing and second-order correlation $g^{(2)}(\tau)$ measurements on single N–V$^-$, one can infer the existence of at least one additional level, a spin singlet A_1, with relatively long lifetime, that relaxes non-radiatively [34]. After the excitation into the ^3E state, intersystem crossing is possible due to spin-orbit coupling [34]. This results in a pronounced bunching feature in the $g^{(2)}$-function (see Appendix B.1.1). However, it is not clear how many of these metastable levels are present, neither is their energy. Recently, a four-level scheme gained more and more support, especially after the detection of a further weak ZPL feature at 1042 nm [256, 257].

The absorption and emission of the N–V$^-$ center couples to the phonons of the dia-

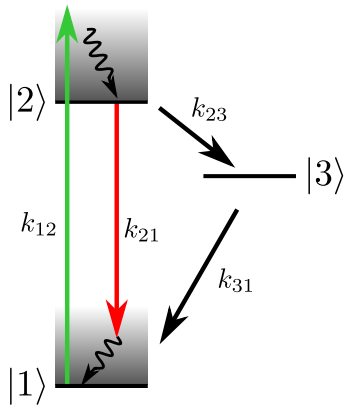

Figure 5.5.: Simplified level scheme of the fluorescence emission from a N–V$^-$ center as realized in the experiment. The 514 nm or 532 nm laser line of the Argon ion or frequency-doubled Nd:VO_4 laser, respectively, pumps the N–V center from the ground state $|1\rangle$ in the phonon sidebands of state $|2\rangle$, followed by fast nonradiative relaxation to the vibrational ground state of $|2\rangle$, from which either fluorescence occurs into the phonon sidebands of the ground state takes place or the metastable level $|3\rangle$ is populated.

mond crystal and pronounced phonon sidebands are visible in the fluorescence spectrum. Even at low temperatures only around 4% are emitted into the ZPL. When excited with photons of energies higher than that of the ZPL, phonon relaxation towards lower lying states is considered to be fast compared to the radiative lifetime, allowing to model the system without considering these processes. Furthermore, if spins are not playing a role as in the experiments for this thesis, the level scheme can be further simplified. A widely utilized three-level scheme is presented in Fig. 5.5, where the additional spin and strain splitting is neglected. This level scheme is sufficient to describe most of the dynamics occurring in the fluorescence of N–V$^-$ centers [258]. The implication of this level scheme, especially for the form of the $g^{(2)}$-function, is discussed in detail in Appendix B.

In 2000, Kurtsiefer et al. [240] described that single N–V$^-$ centers can emit non-classical light and in 2001, single-photon emission from N–V$^-$ centers in diamond nanocrystals could be demonstrated [259]. Since then, N–V$^-$ centers were used as single-quantum emitters in experiments for quantum key distribution [260, 261] and a commercial version of such a system is available [262].

5.3. Coupling Single-Quantum Emitters to High-Q Modes of a Microsphere Resonator

There are two major reasons for the interest in coupling single quantum emitters to microcavities: The first is the fundamental interest in cavity quantum electrodynamics processes. The second reason is the –application driven– wish to have a deterministic output of single photons with high rates, supported by the Purcell effect.

In this section, the coupling of single N–V^- centers in diamond nanocrystals to the high-Q modes of a polystyrene (PS) spherical microresonators is demonstrated. In the hybrid approach used here, both the emitter and the cavity can be characterized separately, and a controlled coupling is possible.

5.3.1. Preparation Steps

Sample Preparation and Experimental Setup

The diamond nanocrystals employed in these experiments are commercially available (*Microdiamant AG MSY 0-0.05*), their intended use is grinding powder. The diamonds are formed in a high-pressure/high-temperature synthesis. They are mono-crystalline with an average diameter of 25 nm and provided in an aqueous suspension [263]. The suspension has to be cleaned of organic contamination. Therefore, after the suspension is centrifuged with a relative centrifugal force of 14000, the supernatant is decanted and the precipitate is re-dispersed in purified water. This procedure is repeated 4 times. After these steps, the amount of nanodiamonds in the suspension varies significantly and the further dilution has to be determined experimentally. Typically, 5dash10 parts of water are added to one part of suspension. A solution of a polymer (polyvinyl alcohol (PVA)) is added, to have an overall concentration of the polymer around 0.05% in the solution. The addition of the polymer avoids the agglomeration of the nanodiamonds. The solution is spin-coated on a cleaned coverslip with a rotational speed of 1500dash2000 RPM.

The PS microsphere resonators are provided by *microParticles GmbH*. Spheres with nominal diameters around 5 µm are used, with typical standard variation of $< 3\%$ [264]. The spheres are transfered from aqueous suspension to isopropanol by centrifugation, decanting the water, and adding the isopropanol. It turned out during the experiments that using isopropanol as the solvent lead to a better homogeneity of the spatial distribution of the spheres on the sample. The suspension is diluted by a factor of 500 and drop-casted onto the coverslip. The experimental configuration in which the sample is investigated includes the SNOM for manipulation of the micrometer sized microres-

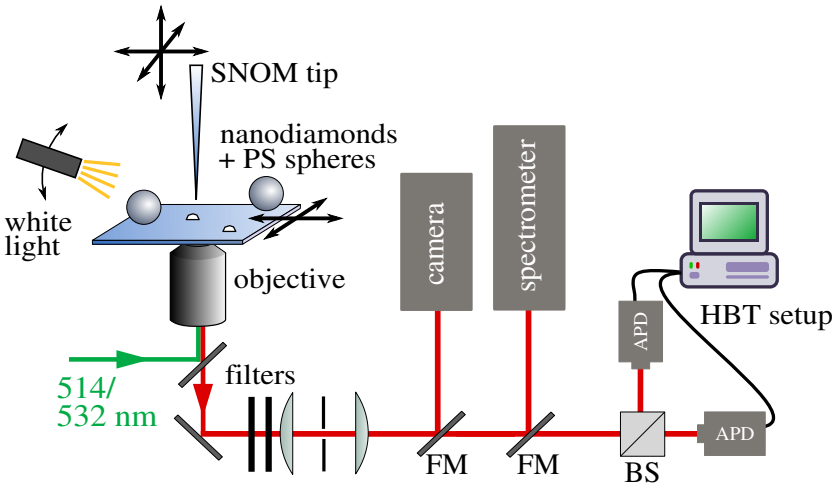

Figure 5.6.: Experimental configuration: The SNOM is mounted to manipulate the microsphere, the HBT setup allows for the measurement of the $g^{(2)}$-function.

onators and the HBT setup (see Fig. 5.6). As the excitation laser, the 514 nm line of the Argon ion laser is used. The excitation laser light is filtered out by color glass filters, either an OG550 or the combination of this filter with an RG630.

Attaching a Polystyrene Microsphere to the SNOM Tip

In a preliminary step, a PS sphere has to be attached to the SNOM tip. Therefore, a small part of the laser light is coupled into the fiber tail of the SNOM. This allows to localize the SNOM precisely while approaching the sample. This is shown in Fig. 5.7a: The sample is illuminated with white light from above, and both a sphere and the SNOM probe can be seen in the camera image. The SNOM probe is then brought in contact with the coverslip without the automatic shear-force control loop, but by adjusting the z-piezo by hand. Then, the probe is retracted for around 4.5 µm, and the sphere is brought into full-contact with the SNOM probe by using the manual xy-translation stage. Retracting the probe reveals whether the sphere is attached to the tip. The procedure is repeated until the sphere eventually sticks to the probe. The microscope image of a sphere, 4.83 µm in diameter, attached to a SNOM probe is presented in Fig. 5.7b.

The exact mechanism why the PS spheres stick to the probe is not completely clear, but it is probably a combination of Van der Waals and electro-static forces, as well as adhesion due to a deposited water film from the surrounding humidity.

Before an individual N–V center is coupled to a microsphere, a nanodiamond con-

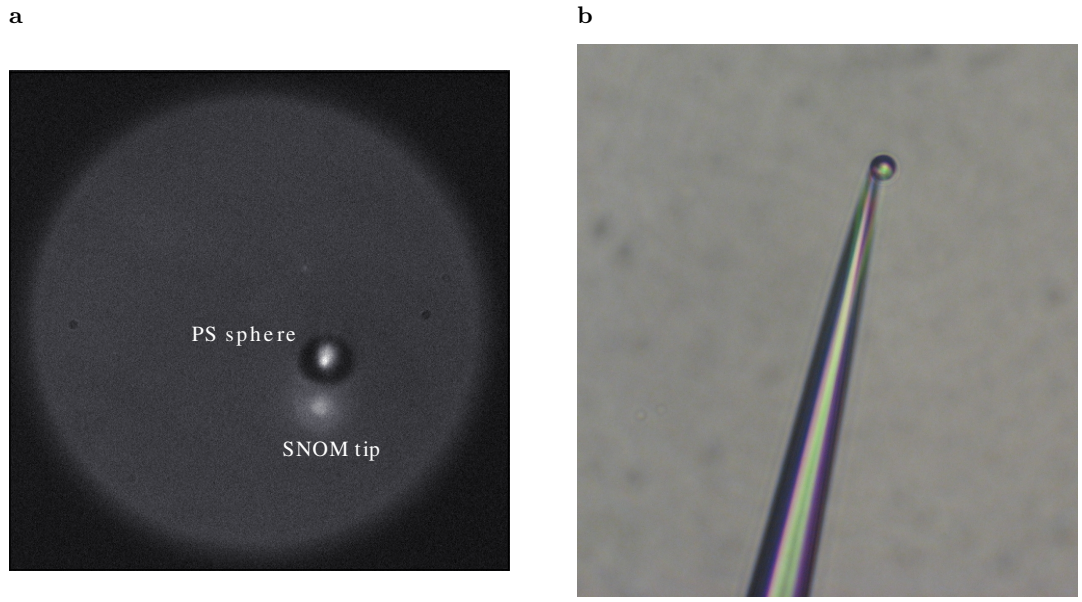

Figure 5.7.: a: With illumination by white light from above and laser light coupled in the fiber tail of the SNOM, both a sphere and the tip of the SNOM probe can be observed simultaneously. b: Microscope image of a sphere with a diameter of 4.83 µm attached to a SNOM probe.

taining a single N–V center has to be found on the sample and characterized. For this reason, the SNOM probe is retracted and the sphere is "stored" in a safe distance above the coverslip.

Locating a Single N–V Center

The excitation power for the N–V centers is relatively high compared to organic dye molecules. In this experiment, the excitation power is 0.3 mW which corresponds to an excitation density of around $3 \times 10^5\,\mathrm{W\,cm^{-2}}$. Therefore, organic molecules photo-bleach within less than a second when they pass through the focus. The most successful procedure to locate a single N–V center is to scan the sample by hand back and forth along one axis to delete emission from residual organic contamination, while the emission from the sample is observed on the APDs. Non-bleaching emission is immediately analyzed with the HBT setup (see Section 3.1.2) and within a few seconds, it is possible to decide whether the emitter has single-photon characteristics indicated by an antibunching dip in the measured autocorrelation function. Typical count rates from the diamond emission on the APDs are 9×10^4 to $4 \times 10^5\,\mathrm{s^{-1}}$. The background count rates are determined on

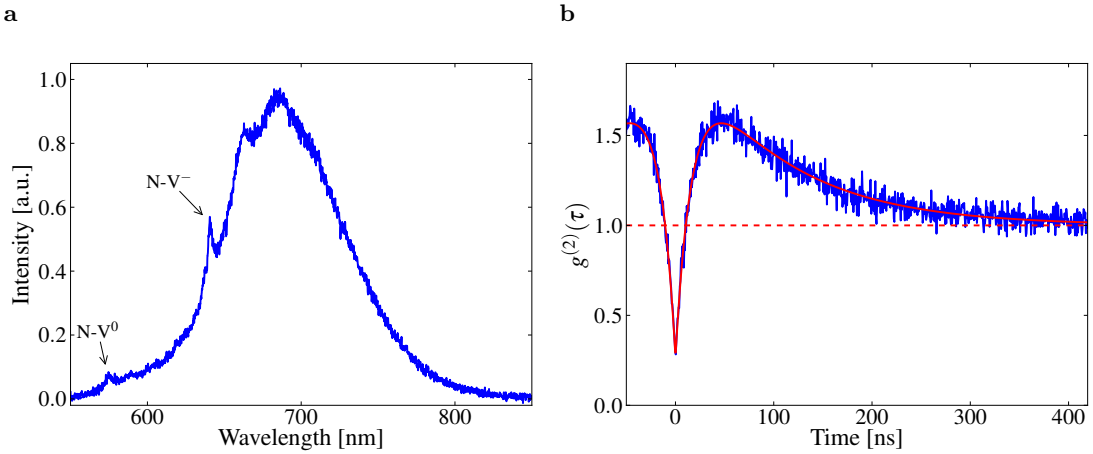

Figure 5.8.: a: Spectrum of a single N–V center. Both ZPLs of the N–V^0 and the N–V^- configuration are observed in nearly all investigated N–V centers. b: $g^{(2)}$-function of the emission of the N–V center. The antibunching dip goes down to 0.27, indicating single-photon emission, limited by background emission from the coverslip. The bunching feature is indirect evidence of a metastable state.

a sample spot next to the nanodiamond and are between $8 \times 10^3\,\mathrm{s}^{-1}$dash$3.5 \times 10^4\,\mathrm{s}^{-1}$.

5.3.2. Characterization of the Bare Diamonds

Spectrum and Second-Order Correlation Function

After locating a nanodiamond with a single N–V center, the spectrum and the $g^{(2)}$-function of the emission are recorded. The spectrum obtained with an integration time of 20 s per step and using the grating with 1200 g/mm is presented in Fig. 5.8a. In the detection path the color glass OG550 blocks the excitation laser. The spectrum shows both the ZPLs at 576 nm of the N–V^0 and at 637 nm of the N–V^- electronic configuration. For nearly all N–V centers investigated in the scope of this work, both ZPLs were observable, indicating that all the N–V centers in nanodiamonds undergo a continuous process of charging and discharging. For the experiments, only N–V centers with dominant emission of the N–V^- configuration were chosen. The pronounced emission on the longer wavelengths side of the ZPL is due to phonon-assisted emission. The simplified scheme that illustrates for the fluorescence mechanism is shown in Fig. 5.5: After excitation into the phonon-sidebands and a fast phonon relaxation to the exciting level, from where either the system decays radiatively, or, the intersystem crossing to the singlet state takes place. This singlet is either deshelved by further excitation into the

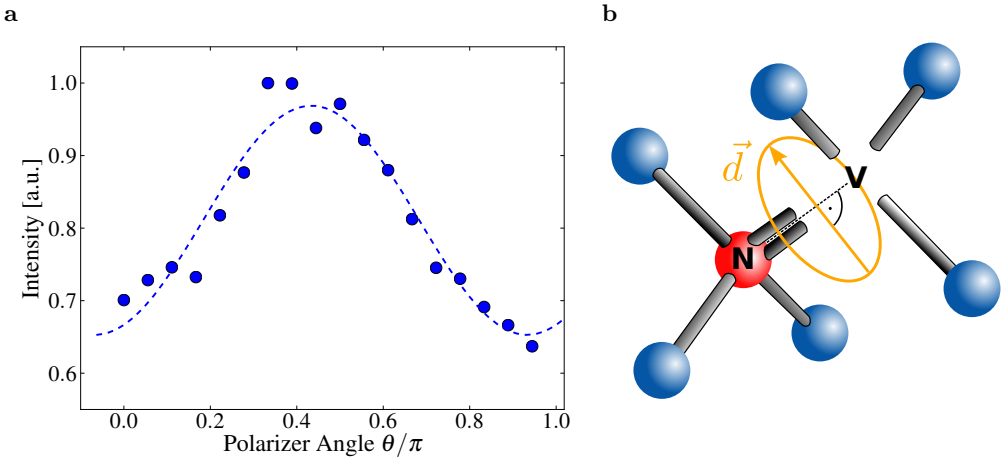

Figure 5.9.: Partially polarized emission from a single N–V center. a: Detected emission intensity as a function of the angle θ of a polarizer placed in the detection path. The intensity in the minimum is 65% of the maximal intensity. b: Explanation of the polarization: The emission stems from two orthogonal dipoles that span a plane orthogonal to the N–V axis.

phonon sidebands or a combination of radiative and nonradiative decay into the ground state [265].

The $g^{(2)}$-function is plotted in Fig. 5.8b (blue curve). The experimental autocorrelation function is corrected for the decreasing probability to measure the stop photons at larger times and normalized to one for large times to obtain the $g^{(2)}$-function (see Appendix B.2). The value at $\tau = 0$ drops down to a value of 0.27, proving that the emission from the nanodiamond has really single-photon characteristics. The background due to fluorescence of the glass under these high excitation densities limits the depth of the dip. The bunching ($g^{(2)} > 1$) around 70 ns is due to metastable singlet state that traps the emitter in a non-emitting condition. The red curve is a fit using the scheme depicted in Fig. 5.5 (see Appendix B.1.1). The time-constants $\tau_{ij} = 1/k_{ij}$ obtained by the fitting are $\tau_{12} = 84$ ns, $\tau_{21} = 47$ ns, $\tau_{23} = 36$ ns, and $\tau_{31} = 187$ ns, where indices refer to the level-scheme in Fig. 5.5. However, there is some ambiguity in assigning these values to all the decay rates, as discussed in more detail in Appendix B.2.

Polarization of the Emission from a Single N–V

The polarization of the emission is studied by mounting a polarization filter in the detection part. For different polarization angles θ the spectrum is taken and the emission

intensity is determined by integrating the spectrum. As the experimental setup is not free of polarizations effects[2], the data is corrected with a calibration curve obtained by mapping an unpolarized white light source. The normalized emission intensity of an individual N–V center as a function of the polarizer angle θ is shown in Fig. 5.9a, the dashed curve is a fit of the form $1 - \cos^2\theta + \phi$. The light emitted by the N–V center is partially polarized for this N–V, the reduction from maximal to minimal intensity is 35%, corresponding to a visibility of $(I_{\max} - I_{\min})/(I_{\max} + I_{\min}) = 0.2$.

The reason for the polarization anisotropy of the emitted light is the symmetry of the excited state, which only allows dipole moments of the optical transition in a plane orthogonal to the N–V axis [249, 266], shown in Fig. 5.9b. Thus, the detected emission intensity is anisotropic, and the anisotropy is a function of the angle between the N–V axis and the optical axis.

5.3.3. Coupling the N–V Center to the Microsphere

After the characterization of the bare N–V center, the SNOM probe with the attached microsphere is lowered and the microsphere is positioned right above the nanodiamond containing the N–V center (see schematic in Fig. 5.10). This can be achieved by illuminating the whole setup from above with white light while exciting the nanodiamond at the same time. By using an appropriate intensity of white light the diamond's fluorescence is comparable to the transmission microscopy picture intensity of the SNOM tip/microsphere composite and both can be seen with the EMCCD (see Fig. 5.11a and b). It is obvious that the full freedom of motion in the xy-plane for both the sample stage and the SNOM probe is mandatory: for the sample to place the N–V center in the focus and for the SNOM to place it directly above the nanodiamond.

After positioning, the microsphere is lowered with the z-piezo and the damping of the oscillation of the tip is observed on an oscilloscope. To attach the nanodiamond to the sphere, the microsphere is brought in full contact with the sample (indicated by the full damping of the oscillation) and retracted again. During the whole procedure, the emission of the N–V center is controlled on the camera. If the emission of the N–V center vanishes while retraction, the nanodiamond is successfully tacked to the microsphere. If this is not the case, the procedure of lowering and rising the sphere is repeated. Additionally, the sphere can be dragged in full contact across the nanodiamond to enhance the probability of attaching it.

The individual steps to attach the nanodiamond to the microsphere are summarized

[2] e.g., the beam sampler shows a polarization dependent transmission

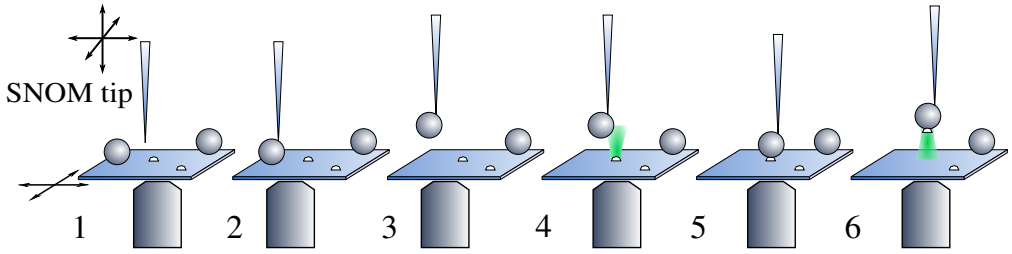

Figure 5.10.: On demand coupling of the of single N–V centers in a nanodiamond to the microsphere resonator. After attaching a sphere (1–3), an N–V center is located and characterized (4). Then, the nanodiamond is attached by bringing the sphere into full contact with the sample (5). After elevating the nanodiamond-microsphere system, the coupling of the N–V emission to the WGM-resonances can be studied.

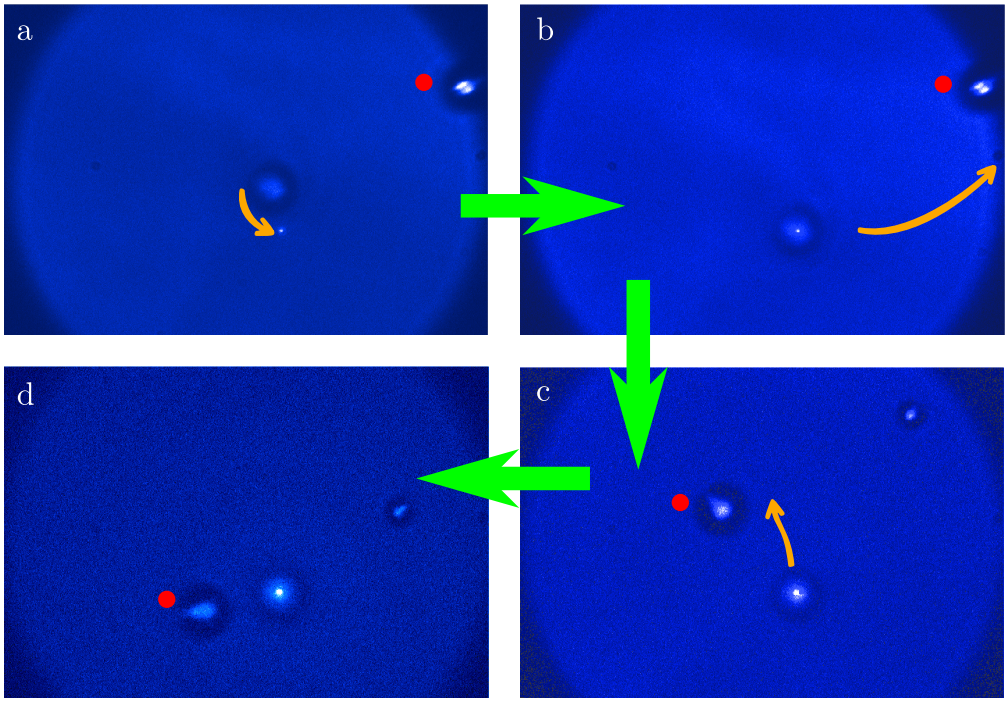

Figure 5.11.: Pictures taken by EMCCD camera: The sample is illuminated with white light from above while a diamond with a single defect is excited by the laser. a: The sphere at the tip is approached to the diamond. b: After positioning the sphere, the diamond is picked up. c and d: After elevating the sphere with the diamond, the sample can be moved underneath. The red dot indicates the same position in each picture as can be seen also from an additional microsphere resting on the substrate.

in the sketch in Fig. 5.10:

1. locating a microsphere,

2. attaching the microsphere to the SNOM probe,
3. retracting the probe, storing the microsphere,
4. locating a N–V center and characterization,
5. attaching the N–V center by bringing the sphere in full contact, and
6. characterization of the emission of the nanodiamond at the microresonator.

After the nanodiamond with the single emitter is attached, the coupled system can be elevated and the sample can be moved underneath, illustrated in Fig. 5.11c and d.

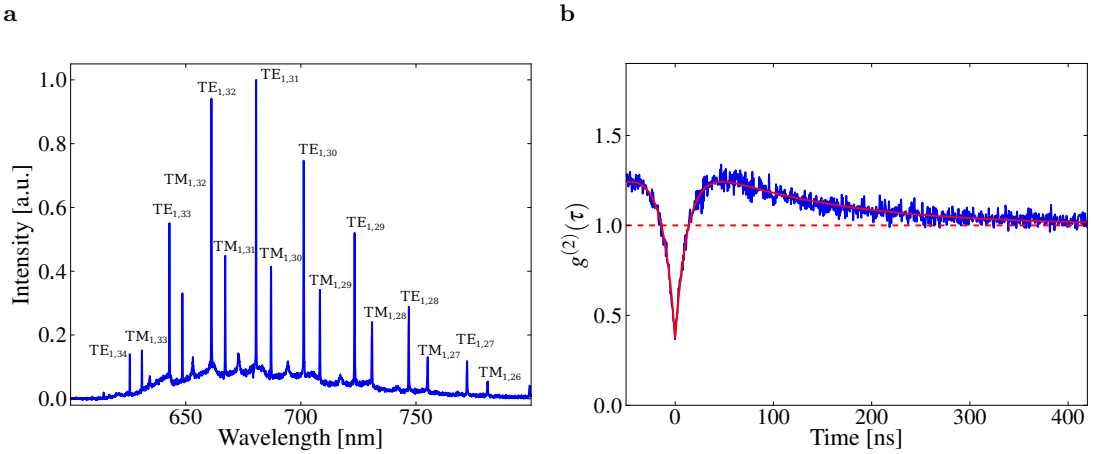

Figure 5.12.: a: Spectrum of the emission of a single N–V center coupled to a microsphere resonator. The most dominant resonances with radial mode numbers $l = 1$ are labeled by comparison with calculated Mie scattering spectra. b: $g^{(2)}$-funcition of the fluorescence. Additional background by PS fluorescence limits the depth of the antibunching dip to a value of $g^{(2)}(0) = 0.37$.

5.3.4. Emission of the Coupled N–V Center

The emission properties of the N–V center coupled to the microsphere resonator are investigated when the microsphere is retracted from the surface for about 2 µmdash5 µm to avoid a perturbation by the substrate. The fluorescence spectrum is shown in Fig. 5.12a, the integration time per step is 15 s, the grating used has 1800 g/mm. An additional RG630 color glass filter is used to suppress Raman-scattered and fluorescence light from the PS sphere. The spectrum features pronounced peaks, arising from the emission into the whispering gallery modes with radial mode numbers $n = 1$. Smaller peaks of modes with higher radial orders are also visible. The resonances can be labeled by fitting their spectral position with the calculated Mie scattering spectra of a sphere, with the sphere radius as the only free fitting parameter. A sphere radius of 2.450 µm is found. As an example, the resonances of the $TE_{1,33}$ and $TM_{1,32}$ are fitted with Lorentzian functions. They have full-widths at half maximum (FWHM) of 0.19 and 0.22 nm, corresponding to Q-factors of 3.4×10^3 and 2.95×10^3, respectively. However, the fit with an Lorentzian line-shape is not completely justified: The spectral width of the resonances is too narrow to neglect the spectrometer resolution, which has a theoretical limit of 0.05 nm. The real Q-factors might be even higher: Deconvolution of the resonance lines with a Gaussian[3]

[3]The Gaussian is used as an approximation of the real line shape function of the spectrometer.

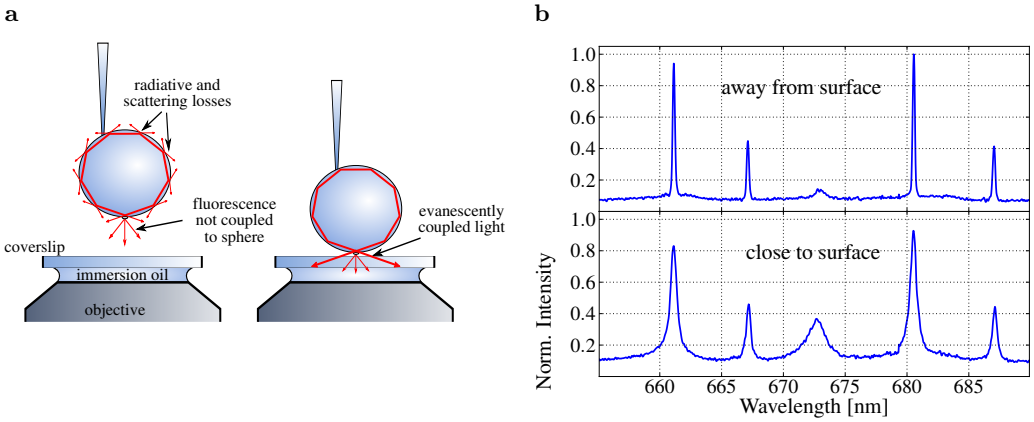

Figure 5.13.: a: Left: The detected emission from the coupled N–V center/microsphere system stems from fluorescence not coupled into the sphere modes and radiative and scattering losses of the whispering gallery modes. Right: When the sphere is close to the surface, additional evanescent coupling between the whispering gallery modes and the coverslip is a further loss mechanism, reducing the Q-factor as can be seen in b: Close-up of the spectrum away (upper) and close to the surface (lower plot).

of the width of the resolution of the spectrometer results in Q-factors of 3.65×10^3 and 3.1×10^3. For other spheres, Q-factors up to 5.5×10^3 were observed.

Theoretically, Q-values derived by Mie theory are higher than 2.5×10^5 at 650 nm for a sphere with a comparable radius. A very recent measurement where a tunable laser was coupled into the fiber of the SNOM tip–microsphere system revealed that indeed much better resonances exist. It appears that the m-degeneration of modes with a common pair of n and l is lifted, either due to the influence of the tip and/or an intrinsic asymmetry of the sphere. Therefore, the resonances observed with the spectrometer might be the composition of these lines, additionally broadened by the spectrometer resolution.

The $g^{(2)}$-function of the emission from the coupled system is presented in Fig. 5.12b. The single-photon characteristics are still present, however the dip with a value of 0.37 is not as deep as for the uncoupled system, due to higher background fluorescence from the PS of the sphere. The fitting parameters for the red curve are $\tau_{12} = 40\,\text{ns}$, $\tau_{21} = 22\,\text{ns}$, $\tau_{23} = 120\,\text{ns}$, and $\tau_{31} = 184\,\text{ns}$. The lifetime of the emitting level $|2\rangle$ is reduced, but as stated before and explained in Eq. B.6 the fit procedure results in different values for different starting parameters.

When the sphere is getting close to the surface, light can directly couple into the coverslip over the evanescent part of the whispering gallery mode. This introduces a new

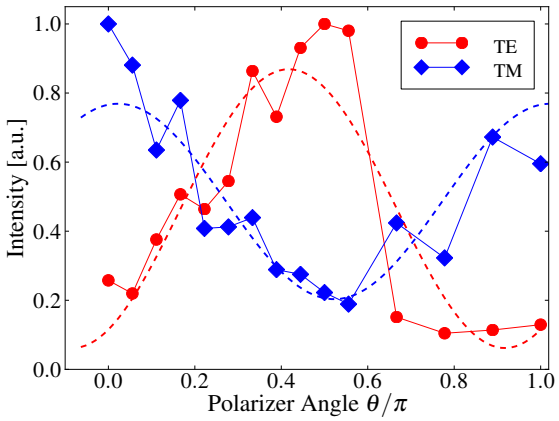

Figure 5.14.: Polarization of the whispering gallery mode emission analyzed by a polarizer in the detection path. For both the TE and TM mode a strong polarization is observable.

loss mechanism and the Q-factor is reduced (Fig. 5.13a). This can be observed directly in the spectrum of the coupled system, shown in Fig. 5.13b. Not all the resonances are influenced equally because the loss for the different modes is not equal due to their different radial field distribution (Fig. 2.4). Furthermore, the highest-Q modes are influenced the most by loss mechanisms (see section below). However, an advantage of the closeness and the coupling into the coverslip is an enhanced mode-to-background ratio, as more light gets coupled in direction of the collecting objective.

Polarization of the Modes

The polarization of the TE and TM modes is analyzed by a polarizer in the detection path. The intensity of an individual whispering gallery mode is evaluated by integrating over its resonance peak and subtraction of the background from the diamond emission that is not coupled to the WGM for the different positions of the polarizer. Fig. 5.13b represents the results for a $TE_{1,30}$ and a $TM_{1,29}$ mode, with the data sets fitted with $a+b\sin^2\theta+\phi$ functions (dashed lines). The strong polarization dependence that is found can be explained in two ways: First, the SNOM probe introduces a strong distortion on the surface of the sphere. As the probe is attached to the sphere on the side, the symmetry of the sphere is broken and there is a preferential equator plane for both the TE and TM modes. Second, as the emission of the diamond itself is partially polarized it can therefore only couple to certain preferential equator planes.

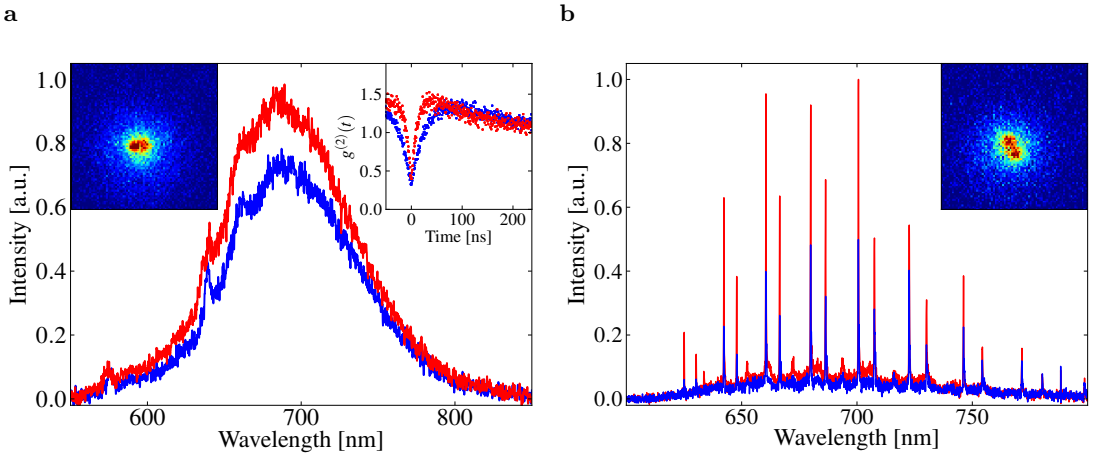

Figure 5.15.: Coupling two single quantum emitters to the same microsphere resonator. a: Fluorescence spectra of two nanodiamonds on the coverslip. Right inset: measured $g^{(2)}$-functions of the fluorescence light from the two nanodiamonds. b: Fluorescence spectra of the same nanodiamonds attached to the sphere and individually excited by the focused laser. The picture insets show the nanodiamonds both excited simultaneously with the laser focus in between the diamonds: In the picture inset of a one nanodiamond is already attached to the sphere and approached to the second still resting on the substrate. In the inset of b both nanodiamonds are attached to the sphere.

5.3.5. One-by-one Coupling of Single N–V Centers On Demand

The previous method to couple single N–V centers to a microsphere is not restricted to the single emitter case. After attaching a first quantum emitter, it is possible to proceed with a second one. In Fig. 5.15a, the spectra of two different nanodiamonds each containing a single N–V center are shown, with the corresponding $g^{(2)}$-functions in the right inset.

A first nanodiamond (diamond 1) with a single defect center is selected and attached to a microsphere as described above. Then, the coupled system can be retracted and a second nanodiamond (diamond 2) with a single defect center is identified on the substrate. After the approach of the microsphere with diamond 1 towards diamond 2 (shown in the left inset of Fig. 5.15a), diamond 2 is also attached to the sphere (see inset of Fig. 5.15b). Both diamonds can now be excited individually. As can be seen from the spectra of each N–V center on the sphere Fig. 5.15b, the fluorescence from both single defect centers in diamond 1 and diamond 2 couples to the same whispering gallery modes of the microsphere resonator. This demonstrates the on demand coupling of two quantum emitters one-by-one to shared high-Q modes of a microsphere resonator.

5.3.6. Coupling to Preselected Microsphere Resonators

In order to establish coupling of narrow emission lines, such as the zero-phonon line of the single N–V center at low temperature, to a single resonator mode, a PS microsphere with a resonance matching the ZPL has to be identified before starting the assembly. Additionally, in a system of increasing complexity, e.g., consisting of single emitters and two or more coupled resonators, a precise matching of resonator resonances with respect to each other is mandatory.

This can be achieved by applying a preselection scheme to the microsphere resonator. Therefore, before a sphere is chosen for the coupling procedure, it is characterized with the help of its scattering spectrum. After locating a single sphere with the EMCCD camera, the sphere is illuminated from the side and the scattered light is collected with the microscope objective. Light from a particular region is spatially filtered out with the confocal pinhole and dispersed via the spectrograph. By scanning the sample an optimum position to observe the resonances of the spheres via the scattered light is chosen. A typical spectrum obtained from a sphere with a diameter of around 4.83 µm is shown in Fig. 5.16a. Besides symmetric peaks, also resonances with slightly asymmetric shape from so-called van de Hulst dielectric surface waves [267] are present. Dependent on the exact spatial position and the incident angle of the light on the sample, the shapes of the resonances change from a regular to a Fano-kind type.

Individual peaks with a FWHM corresponding to Q-factors of around 1000 are present around 650 nm. These resonances correspond to modes with radial numbers $n > 1$. Whispering gallery modes with a higher Q-factor, i.e., with $n = 1$, can not be observed in the scattering spectra as already reported previously by Ashkin and Dziedzic [267]. The reason for that will be explained below. Therefore, these modes have to be deduced using Mie theory by precisely determining the position of $n = 2$ modes from the scattering spectra.

The explanation for the absence of the modes with highest Q-factors in the scattering spectra can be found by calculating the scattering spectrum of a sphere with and without absorption. This is done for a mode with $l = 30$, and the result is shown in Fig. 5.16b. Radiation loss of polystyrene spheres with an index of refraction of $N = 1.59$ and a size of 4.83 µm limits the Q-factor of the $n = 1$ mode to values well-above 10×10^5. Additional loss arises from absorption of the material polystyrene, scattering due to surface roughness, as well as scattering of light into the sample substrate. These losses can be taken into account phenomenologically by introducing an imaginary part N_i to the refractive index of the sphere N_{sphere} to obtain comparable Q-factors to the ones

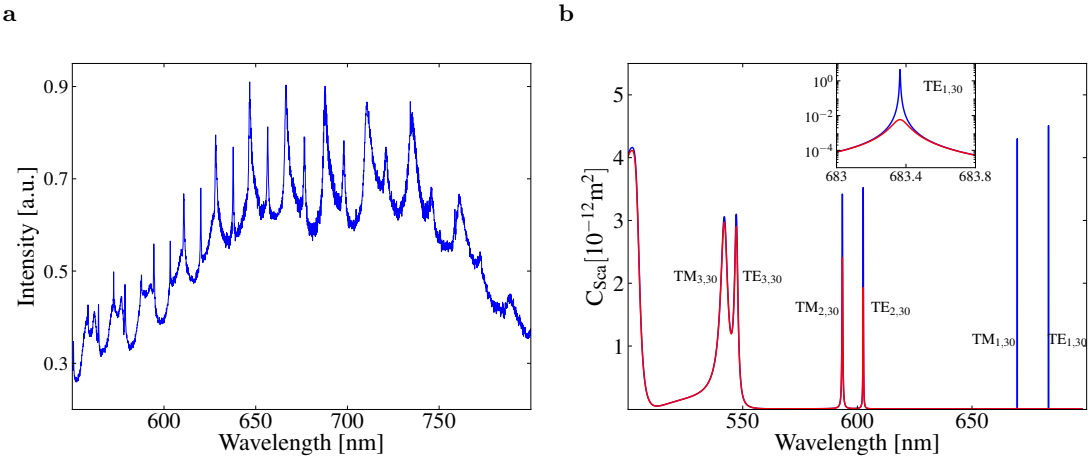

Figure 5.16.: a: Spectrum of white light scattered from a sphere with a diameter around 4.83 µm. Only modes with $n > 1$ can be observed. b: Calculated Mie-scattering of the whispering gallery modes with angular mode number $l = 30$ with (red curve) and without (blue curve) additional loss. The sphere radius is 4.83 µm, and the imaginary part N_i of the refractive index is 0.0001 for the red curve. Inset: Close-up of the $TE_{1,30}$ mode. The scattering intensity from this mode is reduced by a factor of 30.

experimentally observed of around 5000. With this additional loss the calculation shows a dramatic drop of the scattered intensity from $n = 1$ modes as shown in Fig. 5.16b (red curve). It is thus apparent that high-Q whispering gallery modes with $n = 1$ can not be observed in the scattered light. However, the effect is much less pronounced for modes with $n = 2$. The Q-factor is also reduced, but the scattered energy is comparable to that of the non-absorbing sphere.

In order to obtain the exact spectral positions of all resonances of the spheres the calculated spectrum is fitted to the experimental one using the sphere diameter as the fit parameter. An expanded plot of a part of the scattering spectrum is presented in Fig. 5.17 (red curve). Below, the calculated scattering spectrum is shown (blue curve). The fitted size of the sphere is 4.834 µm in diameter.

After this precharacterization, the sphere is attached to the SNOM probe and a nanodiamond with a single N–V center is attached to the sphere. The emission spectrum of the coupled N–V center/microresonator system is also shown in Fig. 5.17 (green curve). Modes with radial mode numbers of $n = 1$ are clearly visible. These resonances are in very good agreement with the calculated Mie resonances. The spectral positions match with an accuracy of less than 0.2 nm. This shows that within this limit a preselection of spheres with a well-defined spectral position of high-Q modes is possible. The limit of

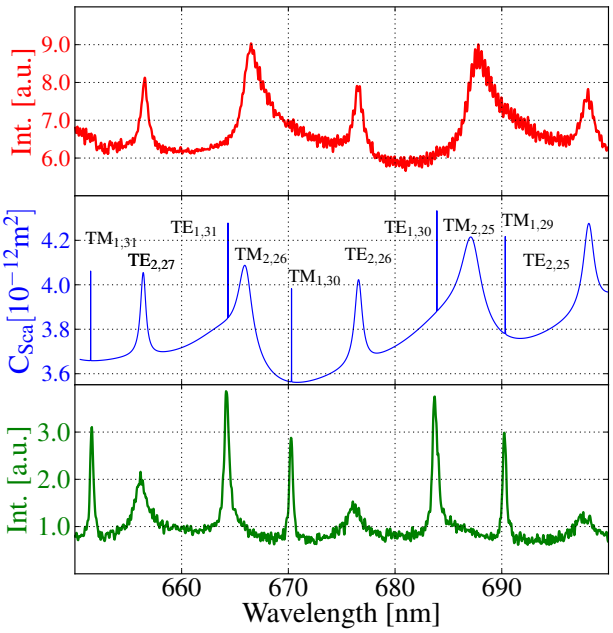

Figure 5.17.: Preselection of a microsphere resonator: Upper curve: spectrum of white light scattering from the sphere. Only modes with radial mode numbers $n > 2$ are observed. Middle curve: derived, full Mie scattering spectrum with the diameter as the only fitting parameter. Lower curve: Fluorescence of a N–V center coupled to the sphere. Modes with $n = 1$ are present. Within an accuracy of less than 0.2 nm, the high-Q modes can be predicted.

accuracy mainly arises from the resolution limit of the spectrometer, and, when calculating the spectrum of a wide spectral range, from the uncertainty of the dispersion relation of polystyrene. Therefore, an improved resolution will allow selection of microspheres with high-Q resonances matching the emission of the ZPL of the N–V-centers a priori. At least spheres can be chosen such that resonances can be fine-tuned when necessary (e.g., at low temperatures) via electrical fields [268] or digital tuning [269].

The controlled coupling of single N–V centers to high-Q modes of microspheres as it is described in this section offers the possibility to eventually enhance the ZPL emission in future experiments for the generation of narrow-band single photons, a basic requirement for fundamental quantum optical experiments where, e.g., indistinguishable photons are required. However, very recent theoretical works also suggests that entanglement of separate N–V centers can be established over shared modes of a microsphere resonator [270, 271].

5.4. Plasmon Enhanced Single-Photon Emission

The lifetime of the excited state in N–V$^-$ centers is typically 11.6 ns in bulk diamond [272]. In nanocrystals, the lifetime is longer. In this case, the effective index of refraction of the surrounding is usually lower than 2.4 (the value of diamond), and the radiative transition rate scales with this value [273]. These relatively long lifetimes (compared to, e.g. quantum dots [274]) limit the possible total single-photon count rate (see Section 5.1) and the temporal determination of the emitted photon pulse. As pointed out in Chapter 2 it is possible to change the dielectric surrounding to enhance the radiative lifetime of an emitter. In this section, it will be shown how the drawback of long lifetimes of the N–V centers in nanodiamonds can be overcome by employing nanoantennas consisting of gold nanospheres in a hybrid assembly. With the help of the AFM, a nanodiamond containing a single N–V centers is incorporated between two gold nanospheres step-by-step and the changes of the emission characteristics of different configurations are analyzed with the optical setup.

5.4.1. Finite-Difference Time-Domain Simulations of the Enhancement Effects

Before the assembly, the effect of gold nanospheres on a dipole emitter is estimated by simulations with the commercial package FDTD Solutions [115]. The simulations have to be divided into two parts: First, the enhancement of the excitation field at the position of an emitting dipole is calculated to obtain the increase of the excitation rate γ_{exc} since it is directly proportional to the excitation field intensity. Second, from the emitted power of a dipole one can directly derive the enhancement of the emission rate as described in Eq. 2.9.

The basic configuration for the simulation is a truncated pyramid with an index of refraction of 2.4 on a silica block, resembling the nanodiamond crystal on the coverslip in the experiment. The height (15 nm) and the side-length (60 nm) of the pyramid's base are typical values obtained from AFM measurements (see below). The results for this bare nanodiamond configuration are then compared to setups where one and two gold nanospheres with a diameter of 60 nm are close to the crystal, respectively.

Excitation

The excitation field is simulated with an incoming pulse with a central wavelength of the excitation laser (532 nm). The Gaussian beam is chosen to have its focus at the

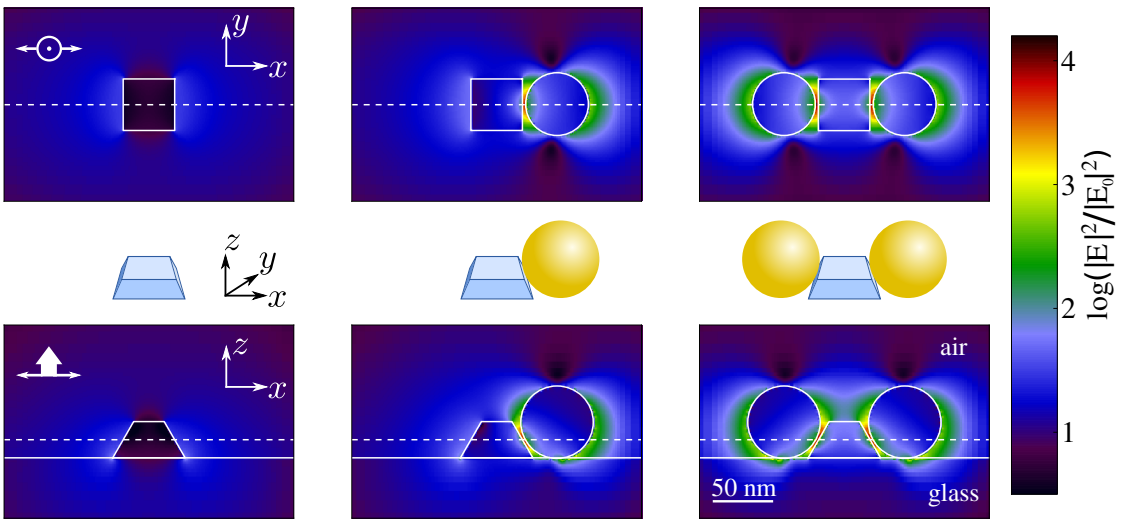

Figure 5.18.: FDTD simulation of the excitation field: Shown is the intensity change due to the nanodiamond and the gold spheres for the three configurations realized in the experiments. The excitation beam is entering from $-z$ with a wavelength of 532 nm and an NA of 1.4, polarized parallel to the x-axis. The formation of spots of field enhancement as high as 1×10^4 can be observed at the contact points of diamon and gold spheres.

silica block – vacuum interface and a NA of 1.4 as given in the experimental setup. The polarization of the beam is parallel to the axis defined by the nanocrystal and the nanosphere.

The factor of the intensity enhancement of the electric field on a plane 15 nm above the substrate and on an orthogonal plane through the particles midpoints is depicted in Fig. 5.18 for three different configurations (dashed lines in the images indicate the intersection of the planes). It is worth mentioning that the field is already disturbed by the nanodiamond itself and not homogeneous within the nanodiamond. This implies that differences in the excitation efficiency can arise due to different positions of the N–V center inside the nanocrystal. When a gold sphere is attached to the nanodiamond a region with strongly enhanced electric field intensity builds up at the interface between the nanocrystal and the gold sphere. Due to the high index of refraction of the nanodiamond, the symmetry of the field distribution around a bare gold sphere is lost, as it has been shown in Fig. 2.12a in Section 2.3.2. A second gold sphere on the opposite side introduces a similar field enhancement there.

The excitation field intensity I with one and two gold nanospheres inside the nanodiamond along the dashed lines normalized to the intensity inside the bare nanocrystal

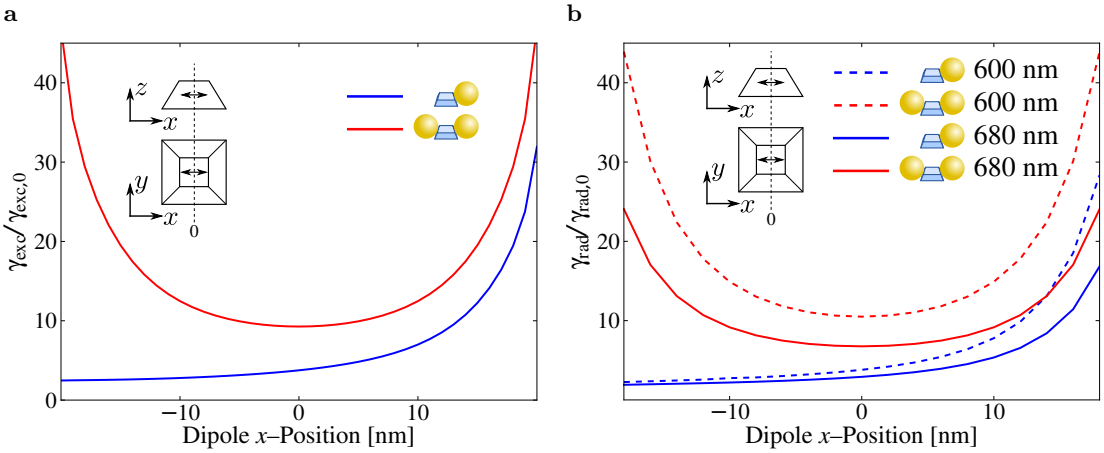

Figure 5.19.: Results of the FDTD simulation along the dashed line in Fig. 5.18. a: Enhancement of the excitation rate for one (blue curve) and two gold spheres (red curve). b: Enhancement of the radiative decay rate for a dipole emitting at 600 nm (dashed line) and at 680 nm (full line) in the single (blue curve) and the double gold sphere (red curve) configuration. In neither the excitation nor the emission case, any collective effect can be observed as the distance between the two spheres is too large.

are depicted in Fig. 5.19a. As the excitation rate γ_{exc} of a dipole emitter is directly proportional to this intensity $\gamma_{\mathrm{exc}} = \sigma I$ with the absorption cross-section σ as the proportionality constant, this reflects also the enhancement of the excitation rate $\gamma_{\mathrm{exc}}/\gamma_{\mathrm{exc,0}}$, where $\gamma_{\mathrm{exc,0}}$ is the excitation rate in the bare nanocrystal. Depending on the exact position of the dipole, the enhancement factor varies drastically, for the single as well as for the double gold sphere configuration.

Emission

The radiative rate γ_{rad} can also be obtained by FDTD simulation (see 2.1.1). Therefore, the emitted power of a dipole on different positions along the dashed line in Fig. 5.19a is calculated for the different configurations. The results for two different emission wavelengths of a dipole aligned along the dashed line is shown in Fig. 5.19b. The emission wavelengths chosen for the simulations are 600 nm and 680 nm, the spectral position of the emission maxima of the neutral and the charged N–V center, respectively. The enhancement of the radiative rate is stronger for the dipole with shorter wavelength, because it is closer to the plasmon resonance of the gold sphere. Like in the case for the excitation, the enhancement is strongly dependent on the exact position of the dipole.

An important point revealed by the simulations is that the field distribution is strongly

influenced by the particle shape. The high refractive index of 2.4 of diamond disturbs the field much stronger than lower index materials. This is the first reason why it is not possible to compare the experimental data directly to the simulations: The AFM does not allow to fully resolve the shapes of the nanodiamond particles used in the experiment. Second, the exact position of the N–V center inside the nanodiamond can not be determined with the accuracy that would allow a quantitative comparison with the experimental results. However, the simulations show clearly that under the right conditions, i.e. polarization of the excitation light and dipole orientation with respect to the gold nanospheres, strong enhancement can be expected for the excitation and the emission rate of a N–V center in a nanodiamond.

When the distance between the two gold nanospheres gets even smaller a collective effect, the formation of a so-called *hot spot* occurs. Such hot spots can not be found in the simulations. The distance between the spheres is not small enough, especially as the high refractive index of diamond further lengthens the optical distance between them.

5.4.2. Experimental Setup and Sample Preparation

The AFM is used in the experimental setup to assemble the nanodiamonds and the gold nanospheres to the emitter–antenna configuration, depicted in Fig. 5.20. On the optical side, the cw-laser and the pulsed laser at 532 nm can be chosen for excitation of the N–V centers. The pulsed excitation allows the direct measurement of the lifetime of the radiative state. The camera, the spectrometer, and the HBT setup supplement the experimental setup. For the details the reader is referred to Chapter 3.

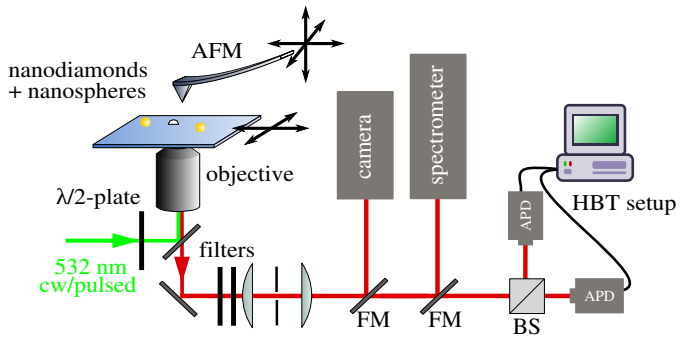

Figure 5.20.: Setup for the hybrid assembly of a coupled system of a single-photon emitter and a plasmonic nano-antenna: The AFM allows the manipulation on the nanoscale. Two lasers allow cw and pulsed excitation.

In two consecutive steps, the nanodiamonds and the gold nanospheres are spin coated

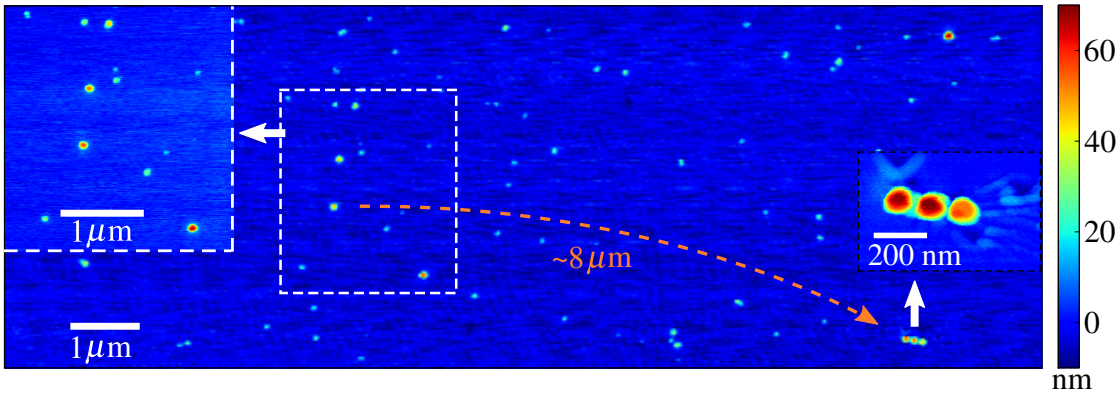

Figure 5.21.: AFM topography scan of the sample. The insets show close-ups of four gold nanospheres and several nanodiamonds (left) and three gold nanospheres already collected (right). Since the nanodiamonds have irregular shapes and heights below 30 nm, the gold spheres can be easily identified by the round shape and sizes well-above 50 nm. In the right inset, also dragging grooves in the PVA film are visible from the manipulation process. The orange arrow indicates the distance over which the diamond is transported with the AFM. Distances larger than 10 µm can be covered.

onto the sample. The first step of spin-coating the nanodiamonds is similar to the procedure described in Section 5.3.1, where an aqueous suspension of nanodiamonds with an average size of 25 nm containing a small amount of PVA is spin-coated with a rotational speed of 2000 RPM. The gold nanospheres are deposited in the second spin-coating step, using the undiluted solution of spheres with sizes of 60 nm (*BBInternational, BBI GC60*) and a rotational speed of 2000 RPM.

Before starting the detailed investigation, an appropriate region on the sample has to be chosen: Both a nanodiamond with a single N–V center and several gold nanospheres have to be in close vicinity. The gold nanospheres can be seen with white light illumination in transmission mode as dark spots on the EMCCD. An additional confocal scan of the sample is used to locate a suitable nanodiamond. From an AFM scan of the same region an estimate of less than 3% of the nanodiamonds contain a single N–V center. The size difference and the irregularity of the diamond shape allows to clearly distinguish between the gold nanospheres and the nanodiamonds. In a next step, the nanospheres are collected by pushing with the AFM cantilever in contact mode nearby the nanodiamond (see Fig. 5.21). Individual nanospheres were moved over distances larger than 10 µm.

A rather high concentration of the PVA in the spin coated nanodiamond solution results in a 7dash10 nm thick polymer film, out of which the nanoparticles have to be

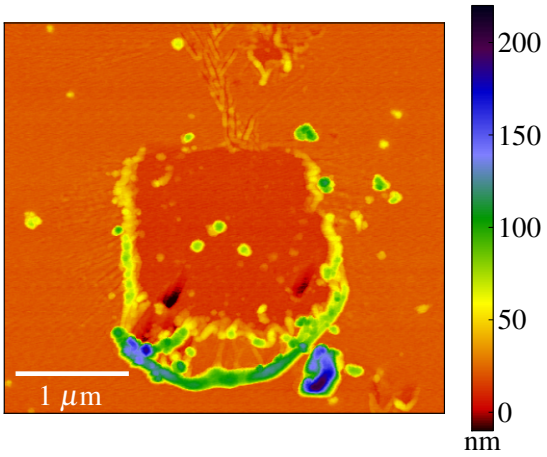

Figure 5.22.: A thin layer is built by the PVA from the nanodiamond solution. With the AFM, this layer can be removed to assure a flat surface and avoid influence caused by the polymer.

"dug out" (see Fig. 5.22). To avoid any influence by asperity of the surface by bulging the polymer, a polymer free area is prepared by scratching with the AFM tip, uncovering the silica surface of the coverslip. On this flat surface, the nanoassembly can be performed.

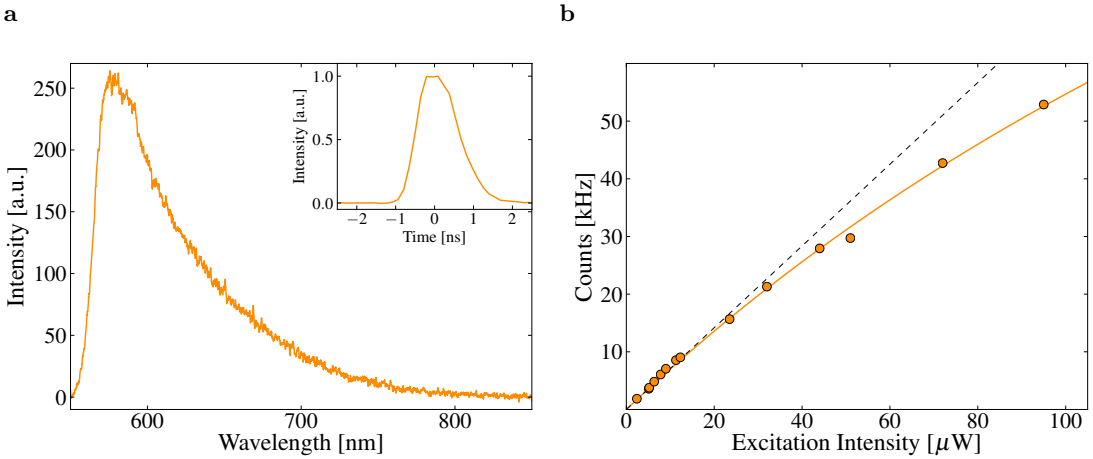

Figure 5.23.: Gold fluorescence. a: Spectrum of the emission, excited with 58 µW at 532 nm. Only the long wavelength emission tail can be observed, due to filtering. The inset shows the measured time evolution of the gold fluorescence. The emission decays in less than a 1 ns, and the measurement reflects rather the time resolution of the experimental setup than the decay of the emission. b: Saturation curve of the emission. Besides the fit with a function that includes saturation behavior (red curve), a linear fit of the low energy data points is also shown (dashed curve) to emphasize the saturation effect.

5.4.3. Optical Characterization of the Uncoupled Constituents

After these preliminary steps, the fluorescence of the gold nanospheres and the N–V center are investigated separately before bringing them together in a coupled system.

Fluorescence of the Gold Nanospheres

The spectra of a single gold nanosphere is presented in Fig. 5.23a under excitation with 58 µW of 532 nm laser light. The fluorescence of gold nanoparticles is attributed to an excitation of an $d \rightarrow sp$ interband transition, followed by relaxation via surface plasmon emission [275]. As a color glass (*Schott KV570*) is used to filter out the excitation light, only the long-wavelength tail of this emission can be observed. Although the quantum yield of the fluorescence is rather low (1×10^{-4} to 1×10^{-3} [276]), it turns out that under the high excitation intensities that are needed to observe the N–V center fluorescence, the gold emission is of comparable intensity. In the coupled system, this emission adds as background to the emission of the N–V center and corrupts its single-photon characteristics. The relaxation of the gold fluorescence is on a time scale of

several tens of fs [275], much faster than that of the N–V centers and beyond the time resolution of the experimental system (see Section 3.1.2). Therefore, the measured decay curve of the gold fluorescence displays the impuls e response function of the setup and has a width of 1 ns.

Fig. 5.23b shows the saturation behavior of the gold emission. The experimental data (red dots) are fitted with a saturation curve of the form

$$I = \eta\, R_{\max} \frac{I_{\mathrm{exc}}/I_{\mathrm{S}}}{1 + I_{\mathrm{exc}}/I_{\mathrm{S}}}, \tag{5.2}$$

with η the overall detection efficiency, $R_{\max}$ the maximal rate, I_{S} the saturation intensity, and I_{exc} the excitation intensity, as introduced in Appendix B.1.2. As can be seen from comparison with a linear fit of the data points of lower intensity, a significant saturation is present.

Emission Properties of the N–V Center

The spectrum and the measured $g^{(2)}$-function of the N–V center are depicted in Fig. 5.24a and its inset, respectively. The spectrum shows again both ZPLs of the uncharged and the charged center, this time, with a slightly stronger emission from the N–V^0 than in the spectra shown in the previous section (Figs. 5.8a and 5.15a). The value $g^{(2)}(\tau = 0)$ is with a value of 0.14 well-below 0.5, indicating that it is indeed a single-quantum emitter with two different charge states (see inset). This is supported by the lifetime measurements of the emitting level, shown in Fig. 5.24b: It is not possible to model the decay with a monoexponential function, whereas a biexponential function $A\,\exp(t/\tau_1) + B\,\exp(t/\tau_2)$ models the data very well. For two different diamonds, time constants τ_1 and τ_2 around 75 ns and 30 ns were found independently with an error of 3 and 4 ns, respectively, and different weights of A and B. These can be indeed the time constants of the excited state decays of the two different charge states. This should be confirmed by further investigations, especially by filtering out the respective spectral region of each charge state. The inset in the figure displays the image of an AFM scan of the nanodiamond. The irregular shape of the particle with a bulge allows to monitor its orientation after each manipulation step.

This is of major importance: Due to the orientation of the optical active dipole (see Fig. 5.9b) not only the emission is polarized (Fig. 5.9a), but also the excitation efficiency is dependent on the polarization of the exciting laser. This dependency as well as the superb degree of control over the nanodiamonds orientation is shown in Fig. 5.25a:

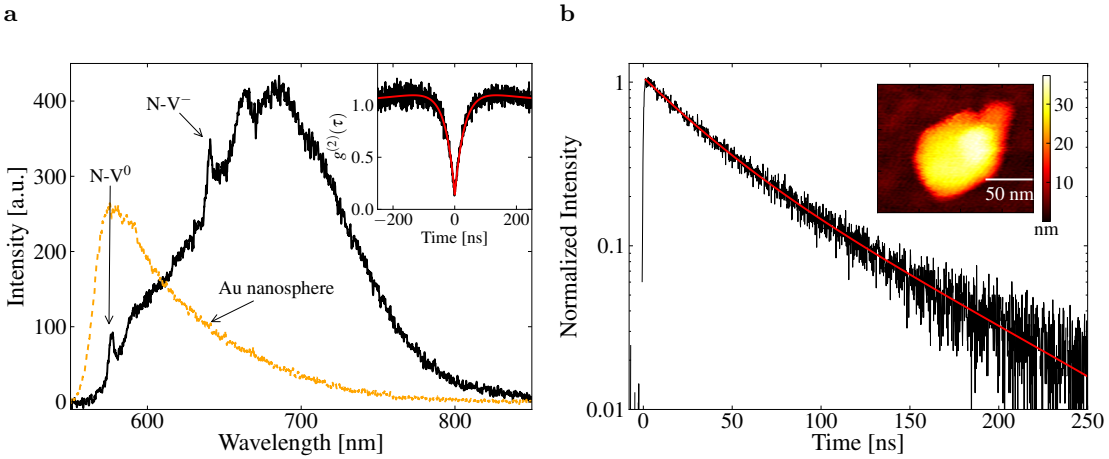

Figure 5.24.: a: Spectrum of the bare N–V center (black curve) and the gold nanosphere (orange curve), respectively (cut-off at 550 nm is due to filtering). The ZPL of both the charged and the uncharged state are visible. The inset displays the measured $g^{(2)}$-function of the N–V center, dropping to 0.14 at $\tau = 0$. b: Lifetime measurement of the decay of the N–V center (black curve). A biexponential function fits the data well, reflecting both charge configuration. The inset shows the AFM scan image of the investigated nanodiamond.

The AFM is used to turn the nanodiamond (see the insets) and its orientation can be determined, here defined by one of the edges with respect to the image. The angle of rotation is around 75°. In both positions the fluorescence intensity is measured as a function of the polarization angle of the excitation light by turning a $\lambda/2$-plate in the excitation path. The data is fit with a $c_0 \cos^2\theta + c_1$ dependency, where saturation effects are considered. Both curves show the same modulation with a factor of 2.5 between minimal and maximal intensity, but with a phase difference of around 80°, in very good agreement with the rotation angle derived from the AFM images.

In Fig. 5.25b, the fluorescence intensity from the single N–V center as a function of the excitation power is presented. The data is corrected by subtracting the background emission from the glass, collected next to the nanodiamond. The observed saturation behavior is fitted with the model in Eq. 5.2. A maximal count rate $\eta\, R_{\mathrm{max}}$ (where η is the detection efficiency and R_{max} the maximal emission rate of the N–V center) of around 1×10^5 kHz can be reached driving the emitter in saturation. Rates of $k_{12} = 1/209$ ns, $k_{\mathrm{r}} = 1/41$ ns, $k_{23} = 1/255$ ns, and $k_{31} = 1/293$ ns fit the $g^{(2)}$-function in the inset of Fig. 5.24a using the simplified rate model in Fig. 5.25b, but these numbers have to be considered carefully, as discussed in Appendix B.1.1. However, as an estimate, the total

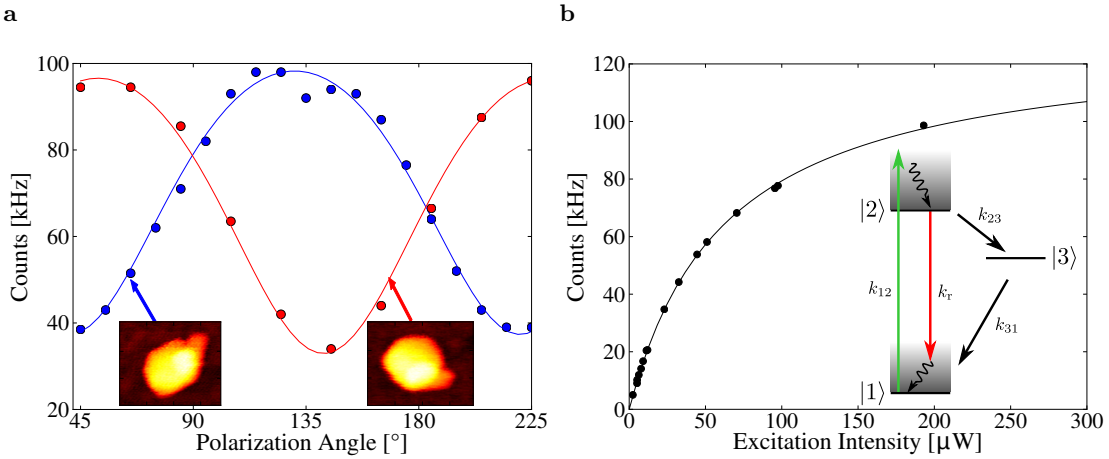

Figure 5.25.: a: Dependence of the fluorescence intensity on the polarization orientation of the excitation laser and demonstration of the control: For two orientations of the nanodiamond (indicated by the position of a characteristic bulge, see insets of AFM scans), the dependence on the polarization of the laser shows a modulation with a factor of 2.5 between minimal and maximal intensity. The rotation is clearly reflected in the phase difference between the curves. The solid curves are fits with a $\cos^2\theta$ dependency. b: Saturation of the diamond emission. The solid curve is a fit with $R_{\mathrm{max}} = 130\,\mathrm{kHz}$ and $I_{\mathrm{sat}} = 62\,\mu\mathrm{W}$.

number of emitted photons can be derived to be (see Eq. 5.5)

$$R_{\mathrm{max}} = \frac{k_{31}\,k_{\mathrm{r}}}{k_{23} + k_{31}} \approx 1 \times 10^7\,\mathrm{Hz}, \tag{5.3}$$

which would lead to a detection efficiency of the setup of $\eta \approx 1\%$, when a quantum efficiency of 0.7 is assumed [34]. This value seems to be too low by a factor of roughly ten, a fact that has been reported previously [277], but the origin is not totally clear: In studies on the linewidth of individual N–V centers significant trapping in dark states was observed by Shen et al. [278], which might also be connected to the change of uncharged and charged states of the N–V center.

5.4.4. Hybrid Assembling of the Plasmonic Nanoantenna

After the precharacterization of the constituents, the assembly to a coupled single-photon emitter/plasmonic nanoantenna system can be commenced. As already shown by the theoretical considerations depicted in Fig. 2.13, it is not sufficient to solely bring the different parts into vicinity of each other. The exact position of the gold sphere relative

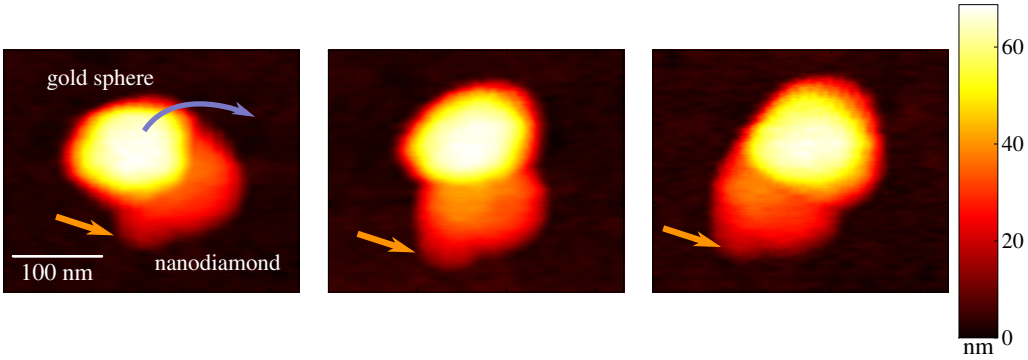

Figure 5.26.: As the enhancement is crucially dependent on the gold sphere's position with respect to the dipole position and orientation of the N–V center within the nanodiamond, the gold sphere is "moved" around the nanodiamond to find the position maximal enhancement. The orange arrows mark a characteristic bulge in the nanodiamond shape, proving that really the gold sphere is solely moved.

to the N–V center and its dipole orientation decide on the overall effect of the gold nanosphere as an antenna on the emission of the N–V center. Fig. 5.26 shows how an optimal position of the gold nanosphere is explored by successively moving the gold sphere around the nanodiamond while the count rate on the APD is observed.

When this optimization is completed, the emission of the N–V center is investigated, before a second gold nanosphere is added on the opposite site of the nanocrystal with the help of the AFM, and again, the properties of the emission are studied.

AFM scan images of these three configurations are presented in Fig. 5.27: the bare nanodiamond, the nanodiamond with a single gold nanosphere, and sandwiched between two gold nanospheres as optical antennas.

The emission properties of the N–V center in these different configurations change under the influence of the plasmonic antenna effect and these changes will be analyzed in the following.

5.4.5. Plasmon-enhanced Emission of a Single-Photon Source

Spectral Changes

The spectra of the emission of the bare N–V center in comparison to the same N–V center coupled to a single and to two gold nanospheres are shown in Figs. 5.28a and 5.28b, respectively. For both configurations, the spectra with the excitation laser aligned parallel

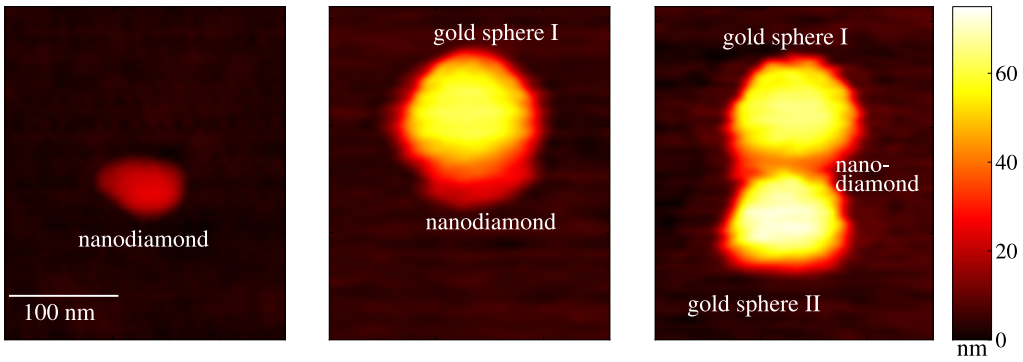

Figure 5.27.: AFM scan images of the three configurations of the hybrid nanoassembly which are investigated: The bare N–V center in the nanodiamond (left), coupled to one (middle), and coupled to two gold spheres as nanoantennas (right).

and perpendicular to the axis defined by the particle centers are shown, in the following referred to as "parallel" and "perpendicular". The intensities of the spectra in each of the graphs are corrected for the excitation intensities (5.9 µW for the parallel, 6.3 µW for the

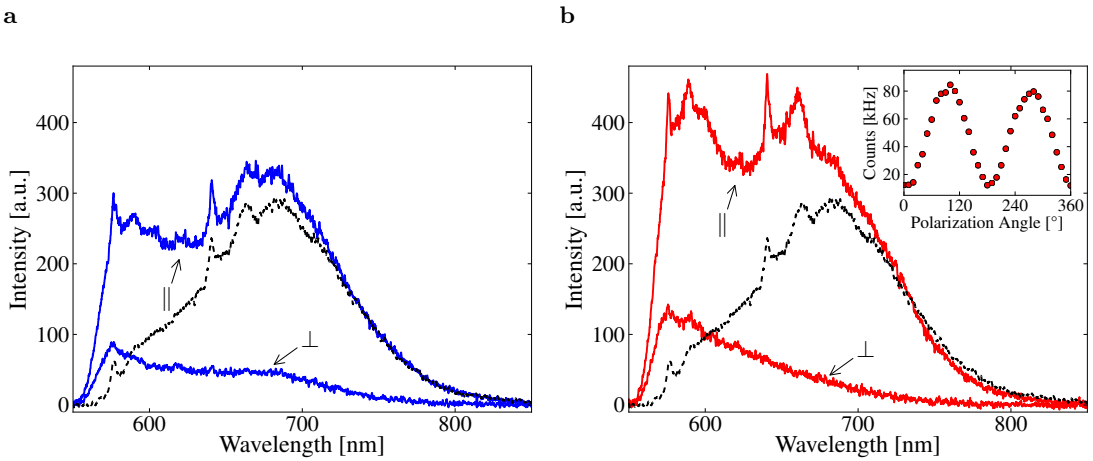

Figure 5.28.: Enhanced emission spectra of the N–V center after coupling to a single (a) and a double (b) sphere plasmonic antenna. For both configurations, the spectra with the indicated polarization orientations are plotted. For comparison, the emission of the bare N–V center (black, dashed curve) is plotted as well, but enhanced by a factor of 6. The inset in b shows the dependence of the N–V center's fluorescence intensity on the polarization of the excitation laser when coupled to the gold spheres, which is much stronger than for the uncoupled center (see Fig. 5.25a).

perpendicular configuration) and saturation effects (see below), so that the intensities can be compared directly. In order to allow better comparison, the spectrum of the bare nanodiamond is plotted enhanced by a factor of 6.

There is a significant change of the shape of the fluorescence spectrum induced by the gold nanoantennas, since the spectrum resembles the overlay of (background) fluorescence from the gold nanosphere and the altered emission of the N–V center. When the polarization of the excitation light is properly adjusted, the overall emission of the coupled system is much stronger than the emission of the bare N–V center.

When the excitation light is polarized perpendicular, both ZPLs and the shoulder of the phonon sidebands around 700 nm can be seen weakly in the single gold sphere configuration. In the system containing two gold spheres as antenna, the background from the gold spheres is the main contribution to the spectrum, only the N–V^0 ZPL is slightly visible. The emission of the NV-center is mostly suppressed, as the excitation light does not penetrate the gap between the two gold spheres.
With the excitation light polarized parallel, the emission of the N–V center is drastically enhanced. The higher energetic part of the emission of the spectra (which is mainly the emission of the neutral N–V^0) seems to be amplified more strongly than the lower energetic side both in configurations with one and two gold spheres, respectively. This might be due to the better overlap of this spectral range with the plasmon resonance of the gold nanosphere with its center around 540 nm (Fig. 2.10b). Therefore, the influence of the antenna is stronger while the N–V center is in the uncharged state, increasing the N–V^0 emission more strongly than that of the N–V^-. However, the fluorescence of the gold nanospheres is also in this spectral range, and it is not possible to separate the enhancement effect from the mere effect of additional background from the gold.

The emission intensity for both configurations is much stronger dependent on the polarization of the excitation light than for the bare N–V center depicted in Fig. 5.24a. For the two gold sphere configuration, the polarization dependence is depicted in detail in the inset of the right graph. In the case of the coupled system investigated, a factor of around 7 is found between maximal and minimal intensity at different polarization alignments. For other nanodiamond – gold nanospheres systems, factors as high as 12 could be found.

A further remarkable feature of the spectra is the obviously increased emission into the ZPLs and the first phonon sidebands in the case of the sandwiched N–V center. Again, this could be the effect of the better overlap of the plasmon resonance with the higher energy parts of both the N–V^0 and the N–V^-.

From here on, the focus is on the capabilities of the coupled N–V center/nanoantenna

systems to generate single-photons with an increased rate and all the following measurements are conducted with the polarization of the excitation light aligned to have maximal emission.

Improved Single-Photon Source Performance

A measurement of the $g^{(2)}$-function reveals, how strong the single-photon character of the emission is influenced by the antenna and the strength of the background can be estimated. It turns out that emission below 590 nm drastically increases the measured value at $\tau = 0$, which is attributed to the fluorescence of the gold nanospheres. Furthermore, emission at wavelengths higher than 750 nm brings in another contribution to the background, which origin is most likely the excitation light. Additional filters (*Schott RG 630* colorglass as a long-pass and *Linos Calflex* as a short-pass) in the detection path are used to filter out this background. While this reduces the overall photon flux, the plasmonic antennas induce such a high enhancement that even with this extra filtering, the total photon count rates are much higher than that of the unfiltered, uncoupled N–V center. Due to the different charge states of the N–V center, the recorded fluorescence emission does not originate from a single emissive state, but is a mixture of the fluorescence of the two emitting states of the N–V^0 and N–V^- configuration. This could be neglected for the bare N–V center, as the emission of the uncharged center was comparable weak, but when coupled to the plasmonic antennas, this is not justified, as the spectra in Fig. 5.28 indicate.

The measured $g^{(2)}$-functions of the emission under cw excitation in the different configurations are presented in the insets of the graphs Figs. 5.29a and 5.29b. The narrower dip is due to the higher transition rates introduced by the gold. The value at $\tau = 0$ is not as small for the coupled systems, neither with one nor with two gold spheres, as it is for the bare N–V center. This is partially due to the gold background fluorescence, but also the limited time resolution does not allow to fully resolve the exact characteristic at $\tau = 0$ (see Appendix B.7). Under pulsed excitation with a repetition rate of 2.5 MHz and an averaged intensity of 550 nW, the autocorrelation measurements show residual peaks at $\tau = 0$. The integrated areas have magnitudes of 20% (A) and 30% (B) of the peaks at $\tau = 1/2.5\,\mathrm{MHz} \times n$ (with $n = 1, 2, 3, ...$). The peaks result from background emission from the gold spheres and the coverslip. The drawback of enhanced background due to the gold emission which is spoiling the single-photon character can in principle be easily surpassed: As the gold fluorescence is much faster, it can be filtered out by time-gating the detection in the pulsed excitation scheme.

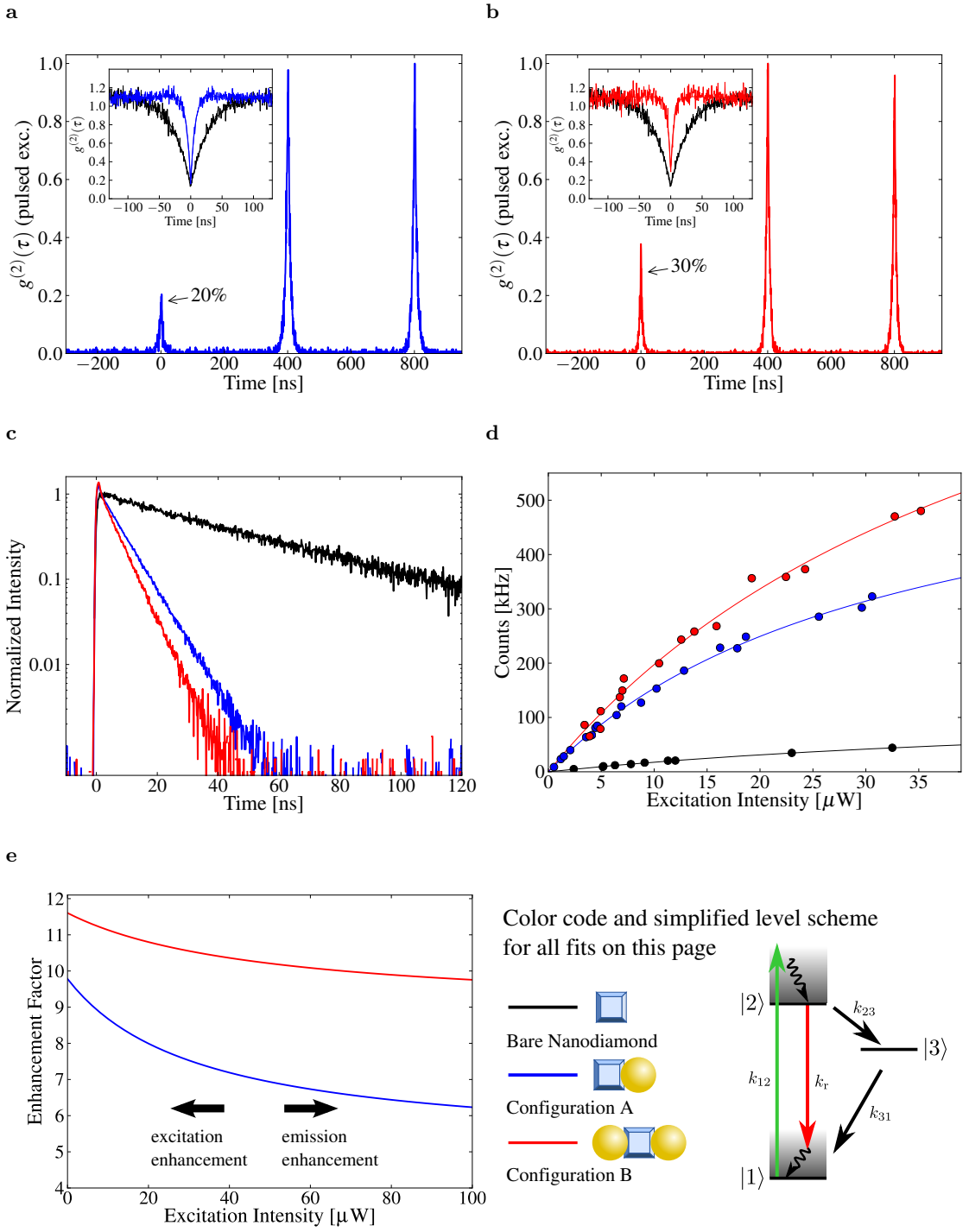

Figure 5.29.: Influence of the gold nanospheres on the emission properties of a single N–V center. a and b: Measured $g^{(2)}$-functions under pulsed excitation and the corresponding $g^{(2)}$-functions under cw excitation in the insets. c: Lifetime measurements. d: Saturation behavior. d: Enhancement factors deduced from the saturation curve. For the detailed discussion see the text.

To get a better understanding of the processes that lead to the enhanced emission, the decay of the fluorescence signal in a time-resolved measurements and the saturation behavior of the N–V center emission in the different configurations are investigated. The decay behavior is presented in Fig. 5.29c, where the decay curves are normalized to one at time $t = 1\,\mathrm{ns}$ after the exciting laser pulse. At this time, the emission of the gold nanospheres is negligible. The decay rate is drastically enhanced by the gold nanoantennas. The $1/e$ time is reduced by a factor of 6.3 and 8.6, when coupled to one and two gold spheres, respectively, compared to the $1/e$-time of the bare nanodiamond. The overall decay rate k_{dec} is the sum of all depopulation rates $k_{\mathrm{dec}} = k_{\mathrm{r}} + k_{23} + k_{\mathrm{nr}}$ of the emissive state, the radiative rate k_{r}, the intersystem-crossing rate k_{23}, and the rate for nonradiative decay k_{nr}. Because of that, the reduced lifetime of the emissive state can be due to a faster radiative decay of the state, but also due to unwanted additional nonradiative decay channels introduced by the gold nanospheres (see Section 2.3.3).

By comparison of the saturation behavior of the uncoupled and coupled system it is possible to learn more about the influence of the nanoantennas on the N–V emission. The measured saturation curves are depicted in Fig. 5.29d. They are corrected for the background emission of the gold nanosphere and the substrate which is estimated from the $g^{(2)}$ measurements in Figs. 5.29a and 5.29b, respectively. The experimental count rates C_{det} are fitted by saturation functions of the form

$$C_{\mathrm{det}} = \eta \frac{\phi\ k_{12}}{1 + \phi\ k_{12}/R_{\mathrm{max}}}, \tag{5.4}$$

where η is the detection efficiency, ϕ is the quantum efficiency and

$$R_{\mathrm{max}} = k_{31} k_{\mathrm{r}} / (k_{23} + k_{31}) \tag{5.5}$$

the maximal count rate, when $k_{12} \to \infty$ (see Appendix B.1.2) Dividing the saturation curves of the antenna configurations by the saturation curve of the N–V center in the bare nanodiamond brings forward the enhancement factors as a function of the excitation intensity I_{exc}, shown in Fig. 5.29e.

For small excitation intensities, the count rate is C_{det} directly proportional to the excitation rate k_{12} and the enhancement factor reflects the enhanced excitation due to the increased excitation field intensity. Enhancement factors of 9.8 and 11.6 can be found for the two configurations with one and two gold nanospheres, respectively.
At high excitation powers, the maximal emission rate is limited by the radiative decay rate k_r. Therefore, the saturation measurement confirms that indeed this rate is en-

hanced: For the maximal emission rate $R_{\max}$ enhancement factors of 5.3 and 9.0 can be deduced for the two configuration, respectively, from fits with the model in Eq. B.9.

The deduced enhancement factor for the excitation is higher than that of the emission. This is expected, since the local-field effects are stronger for the 532 nm excitation light than for the emitted red and NIR light due to the better overlap with the plasmon resonance.

It can not be ruled out that the only influence of the nanoantennas that contribute to the observation of enhanced emission from the N–V center increase of the radiative rate k_r. A reduction of the lifetime of the singlet state ^{1}A is also possible and would also result in an enhanced overall rate. However, a significant change of this rate can not be validated by the fits of the measured $g^{(2)}$-function. Therefore, it is legitimate to assume that neither this nor the intersystem crossing rate k_{23} is affected by the nanoantenna. Furthermore, FDTD simulations show no significant change in the far-field emission pattern of the N–V center. Therefore, the enhanced maximal emission rate $R_{\max}$ translates directly into the enhanced emission rate k_{r} (Eq. 5.5).

Under these assumptions it is possible to estimate the quantum efficiency ϕ of the N–V center when an initial value of 0.7 for the bare N–V center is assumed. When the antenna is build from one gold sphere, ϕ is reduced to a value of 0.6, in the case of two gold spheres, ϕ recovers to the original value of 0.7. So, it appears that by optimizing the position of the first gold nanosphere the distance to N–V center is close enough to open a nonradiative decay channel, which reduces the quantum efficiency. The second antenna particle only enhances the emission, enhancing the overall quantum yield back to its initial value.

To summarize, the nanoscale assembly and deterministic coupling of diamond nanocrystals and gold nanoparticles was demonstrated as a excellent method to control the emission properties of a single nitrogen-vacancy color center. The coupling to plasmon resonances realizes an efficient, long-term stable single-photon source at room temperature. With further improvement of the assembly, it is a promising approach to boost the signal-to-noise ratio, of special interest in single-spin read-out experiments in N–V centers [279, 280].

5.5. Towards Tailored Emission of a Single-Photon Source

In this chapter, two methods were presented to couple single N–V centers to resonant structures. In the first section, the single-photon emitters were attached to micrometer-sized Polystyrene spheres one-by-one on demand, acting as dielectric microresonators

with high-Q whispering gallery modes. These resonances were in the fluorescence spectrum of the single-photon emitter, and a high degree of polarization of the emission within individual TE and TM modes could be observed.

In the second approach, plasmonic nanoantennas were used to increase the emission of the N–V center. It was shown that not only the excitation field is enhanced by the nanoantenna by approximately one order of magnitude, but also the radiative rate is dramatically enhanced by nearly the same amount due to the coupling to the surface plasmons of the gold nanospheres.

The broad emission of the N–V does not restrict the resonant structures with respect to the exact spectral position of their resonances. However, in future experiments it will be of importance to have resonances matching spectrally with the ZPL of the N–V center, with different and/or more sophisticated designs. This could lead to a further increase of the emissive rate and a spectrally narrow single-photon source [281] with well-defined spatial emission patterns [282, 283]. Therefore, the approach could be extended to different metal nanostructures, either synthetically (spheres, rods, or wires) or lithographically produced.

Furthermore, neither of the approaches is limited to the utilization of N–V centers, but other color centers in diamonds, semiconductor nanocrystals, or even single organic molecules can be incorporated as active materials, paving the way for the realization of robust and efficient photonic and plasmonic nanoelements.

CHAPTER 6

Summary and Outlook

The experiments that were performed in the frame of this thesis cover a broad variety of physical aspects of current research topics: nanophotonics with nanocrystals, single-photon sources, plasmonics with nanoantennas, cavity quantum electrodynamics. This broadness naturally evolved from rather restricted questions at the beginning, e.g., whether it would be possible to study upconversion on a single nanocrystal level. These questions lead to the need for an experimental setup which would extend the purely optical investigation which was achieved by the amendment of the confocal microscope setup by an atomic force microscope (AFM) and an scanning near-field optical microscope (SNOM), respectively. From these experiments new questions arose, and some issues need additional investigation to be fully clarified. Furthermore, the potential of the multifunctional setup promises many further compelling experiments improving the control on the nanoscale in photonics and its neighboring fields like the emerging area of plasmonics.

However, before providing an outlook on possible future advances, it seems to be expedient to recall the results that could be obtained in this work.

6.1. Summary

Two different kinds of emitter systems were studied and further employed in hybrid photonic structures: $NaYF_4$ nanocrystals that are doped rare-earth ions and nanodiamonds that contain single nitrogen-vacancy centers which determined the basic structure of the

work.

In **Chapter 4** the research done on **$NaYF_4$ nanocrystals codoped with Yb^{3+} and Er^{3+}** is covered. These nanocrystals show superior upconversion efficiencies due to the underlying mechanism, the energy transfer upconversion, when the excitation is in resonance with a ground state excitation in the Yb^{3+}, namely at a wavelength around 973 nm. In a first step, the power dependence of the upconversion fluorescence from a cluster of nanocrystals was investigated. A power induced change of the spectral shape of the green fluorescence band was found. For all spectral bands that are present between 400 nm and 580 nm the power dependence was studied in more detail and a change of the exponent for the exponential fits was observed for all bands. With the collected information, the bands could be assigned to probable transitions within the Er^{3+} ion's level scheme.

For the first time, combined optical upconversion and AFM measurements were performed on a single nanocrystal level. While studying the upconversion fluorescence with the confocal setup, it has been assured that indeed a single nanocrystal was investigated at a time and its size could be determined by the AFM. This lead to the discovery of a strong size dependence of the spectral composition of the upconversion signal [Schietinger et al. 2009b]. With decreasing size of the nanocrystals, the intensity of the green emission band (mainly from the transitions $^2H_{11/2}$, $^4S_{3/2} \rightarrow {}^4I_{15/2}$) increases dramatically compared to the intensity of the red band ($^4F_{9/2} \rightarrow {}^4I_{15/2}$). The ratio between green and red emission increases from a value of 0.6 well below 1 for nanocrystals with heights well above 15 nm to a value of 2.7 for a crystal with a height of 7 nm. This means that the intensity of green emission is weaker than the red emission for larger nanocrystals, changing to the situation that the main contribution originates from the green emission for smaller ones. A possible explanation of additional decay channels on the surface is dismissed, since the overall emission is not further quenched for the smallest nanocrystals. It is suggested that for nanocrystals with sizes smaller than 10 nm the interaction with the optical phonons is reduced: First, the phononic density of states is altered and second, the spatial mode of the phonon mode has to fulfill the boundary conditions given by the nanocrystal's shape which lowers the field strength of the phonon mode for emitting Er^{3+} ions at the surface and the phonon–ion interaction. Furthermore, in the nanocrystals, a diffusion of phonons is circumvented. All this leads to an effective phonon bottleneck, suppressing nonradiative decays, changing the population distribution of the emitting levels.

For the first time, plasmonically enhanced upconversion was achieved by the controlled assembly of single nanocrystals with sizes of around 30 nm with gold nanospheres. With

the help of the AFM the gold spheres were installed as nanoantennas in a controlled way [Schietinger et al. 2010]. During the assembly, the upconversion fluorescence of the nanocrystals was analyzed after each assembly step by means of the intensity, its spectrum, and the temporal evolution of the emission. In a first configuration a nanocrystal is coupled to a single gold sphere of a diameter of 60 nm. The overall emission was enhanced by a factor of 3.8, however, the enhancement differs significantly for the green and red emission band with factors of 4.8 and 2.7, respectively. Time-resolved measurements revealed that both the excitation and decay rates are enhanced by the nanoantenna. The enhanced excitation rate is also held responsible for the differing enhancement factors. In a second configuration, a nanocrystal was placed between two 30 nm gold spheres. While the enhancement is not as strong as before, the different effects like enhancement, quenching, and, especially, strong evidence for the formation of a hot spot could be observed.

Both effects investigated in this work, tunable color with size and enhanced emission by metallic antennas, could further fuel the already vivid research on upconversion materials, especially in the context of photovoltaics [284].

In **Chapter 5** the focus is on individual **Nitrogen–Vacancy Centers** as outstanding single-photon sources to be employed in future complex nanophotonic systems. Their extraordinary photo-stability and the possibility to operate them at ambient conditions is an advantage that allows a new class of photonic experiments and applications without the restrictions given by a cooling apparatus or the experiment's duration.

For the first time, the emission of single N–V centers incorporated in nanodiamonds were deterministically coupled to the high-Q whispering gallery modes (WGM) of polystyrene microspheres with diameters of a few µm [Schietinger et al. 2008]. This was achieved by picking up a microsphere with the probe of a SNOM and attaching a preselected nanodiamond to it. The sharp resonances of the WGM could be observed within the emission spectrum of the nanodiamond, while the single-photon characteristic of its emission was preserved. Q-values as high as 5.5×10^3 could be found for the spheres. The technique was extended to couple more N–V centers to an resonator one-by-one, with the N–V centers' emission sharing the same modes of the microsphere. Finally, an approach was introduced to precharacterized microspheresby means of the spectral position of their resonances before the coupling, which allows to preselect frequency-matched microresonator [Schietinger et al. 2009c].

For the first time, the enhancement of the emission of single N–V centers in nanodiamonds by the coupling to a nanoantenna has been demonstrated [Schietinger et al.

2009a], in a similar way as described above for the upconversion nanocrystals. An enhancement of both the excitation and emission rate by approximately an order of magnitude could obtained. Most remarkably, this boost of the performance was achieved preserving the single-photon property of the emission.

A major challenge in the future will be to gain full control over the spontaneous emission process of photons, controlling the emission wavelength, emission point of time, and spatial distribution of the emitted field, tailoring the emission at will. The combination of resonant photonic and plasmonic structures will play a key role. With the realization of coupling of a single-photon source on demand to the different resonant fundamental structures shown in this work, a first step could be made towards this ultimate goal, fully-controlled emission, specially tailored for any particular purpose.

6.2. Outlook

Evidently, this work has to be considered as a starting point for a lot more interesting research to come in the near future. Not only do some issues need clarification, it is the marvelous combination of optical methods with scanning probe techniques in the experimental setup which opens an incredibly large playground for all kind of fascinating experiments. Some thoughts about possible future research approaches shall be presented here:

Clarifying the Size-Dependence Mechanism in Upconversion Fluorescence in Codoped $NaYF_4$ Nanocrystals

An unanswered question in the investigation on the upconverting $NaYF_4$ nanocrystals is the true nature of the size-dependence in the spectral distribution of the upconversion fluorescence as reported in Section 4.3.2. The transition rates have to be determined in detail with time-resolved measurements as it is shown in Fig. 6.1. Pumping directly the levels $^2H_{11/2}/^4S_{3/2}$ and $^4F_{9/2}$ at their high-energetic and time-resolved detecting at their low-energetic flanks, respectively, can provide information of the actual lifetimes of these levels. It has to be pointed out that this has to be done for different nanocrystal sizes to uncover whether the relaxation within each emission band is a subject of change itself due to acoustic phonon confinement as it was discovered for low-temperatures by Liu et al. [209, 210]. This would be an interesting study itself.

For a determination of the nonradiative transition rates and their possible size-dependence, it is possible to excite the levels $^4F_{7/2}$ and $^2H_{11/2}/^4S_{3/2}$, and detecting the emission dy-

namics of the respective levels $^2H_{11/2}/^4S_{3/2}$ and $^4F_{9/2}$ that are reached via multi-phonon decays. With the help of the lifetimes measured directly as explained before, the nonradiative decay rates can then be derived.

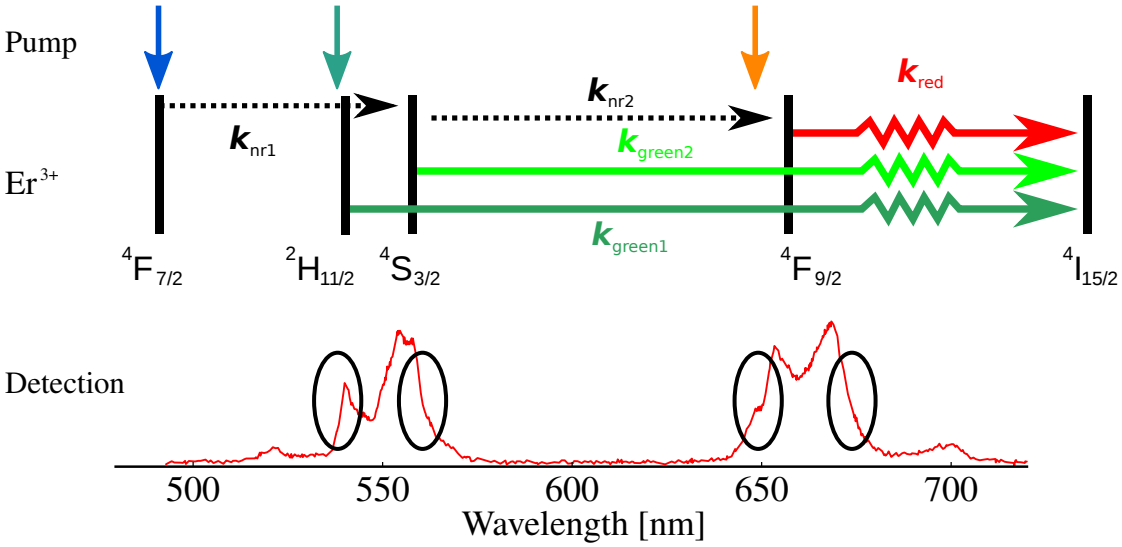

Figure 6.1.: Scheme to determine the lifetimes and the nonradiative transition times: First, the level bands can be pumped directly at their high energetic edge and the emission of low-energetic flank is analyzed. Second, the levels $^4F_{7/2}$ and $^2H_{11/2}/^4S_{3/2}$ and the emission of respective levels $^2H_{11/2}/^4S_{3/2}$ and $^4F_{9/2}$ is detected to identify k_{nr1} and k_{nr2}.

Profound knowledge of the influence of phonons is not only essential to get a full understanding of the optical properties in nanostructures, it might also be a necessity for the future, as nanotechnology further hits the limit where quantization of phonons plays a role. Superstructures might be an approach to design phonon distribution and to have a further lever for designing the photonic response of materials. When the nature of the here reported size-dependence is clarified, other question wait to be answered: What happens when two nanocrystals are brought in contact with the AFM, or what happens when the surrounding is changed for example by introducing a liquid or polymer.

Quantum Nature of Light Measured With a Single Detector

While writing this thesis, fascinating research has already taken place in the lab [Steudle et al. 2011]: Up to now, the method of choice to investigate the autocorrelation of a photon field is the Hanbury Brown-Twiss setup (HBT) described in Section 3.1.2. However, there is no physical reason to do so, in fact, it opens the door for misinterpretation:

Using a beamsplitter and two detectors implies that photons from a single-photon source (Section 5.1) behave like classical, indivisible particles and have to "decide" which path to take when striking the beamsplitter. Though, the photons' wavefunction includes both paths and the features of non-classical light, i.e., the anti-bunching dip measured in an autocorrelation experiment, results from the quantum statistical distribution, and the measurement in one of both arms collapses the wavefunction. The usage of a HBT setup is for technical reasons: The dead times of single-photon detectors like avalanche photodiodes (typically 50 ns) are too long to resolve the antibunching dip which is at least as narrow as the lifetime of the single-photon source's emissive state.

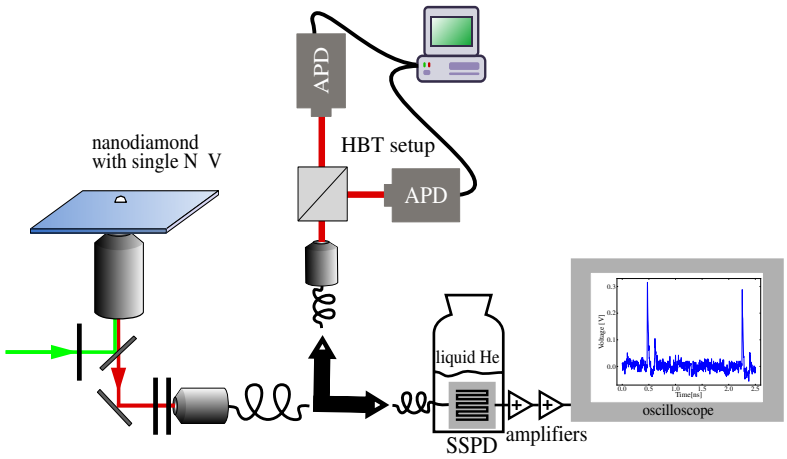

Figure 6.2.: Measurement of non-classical light characteristics with a single detector: The light from a single N–V center in a nanodiamond is analyzed with a standard Hanbury Brown-Twiss setup (HBT) or with a single superconducting single-photon detector.

Superconducting single-photon detectors (SSPD) provide much shorter dead times below 5 ns [285], shorter than the lifetime of a N–V center. Therefore, it is possible to resolve the non-classical characteristic of the emission from a single N–V center. The experimental setup is shown in Fig. 6.2: The light emitted by the N–V center is coupled into an optical fiber and can either be coupled out into the entrance of a HBT setup or directed to a fiber coupled SSPD. The SSPD electronics are fed into an oscilloscope which stores the signal trace whenever two detection events occur within a 200 ns window. These traces are automatically evaluated using a computer script to obtain the time difference between the two detection events. Fig. 6.3 shows that for the first time single-photon characteristics of a light field could be observed with a single detector: The blue curve shows the $g^{(2)}$-function measured with the HBT setup, the green curve the result obtained with the single SSPD, the red curve is a fit of the APD

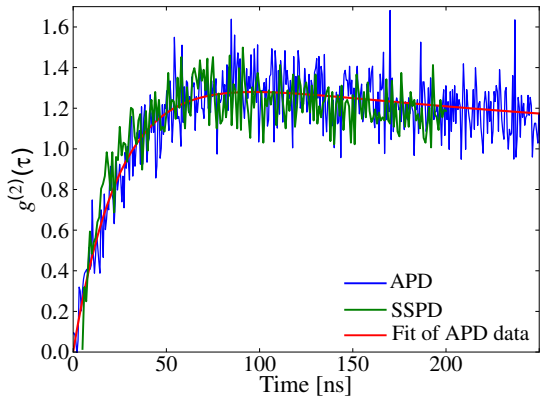

Figure 6.3.: Measured $g^{(2)}$-functions from the two APDs of the standard HBT setup (blue curve) and from the single SSPD (green curve), respectively. The red curve is a fit to the data obtained with the APDs. Both experimental data sets feature the same strong antibunching in the emission of the N–V.

data using Eq. B.4. Both curves correspond, featuring the antibunching dip at $\tau = 0$. This is just one (but very fascinating) demonstration, where an easy to operate single-photon source like the N–V center in a nanodiamond can support research in other fields. Due to a lower detection efficiency, the measurement is time-consuming. Therefore, it is a big advantage to have single-photon source operating at ambient condition without the need of cooling equipment.

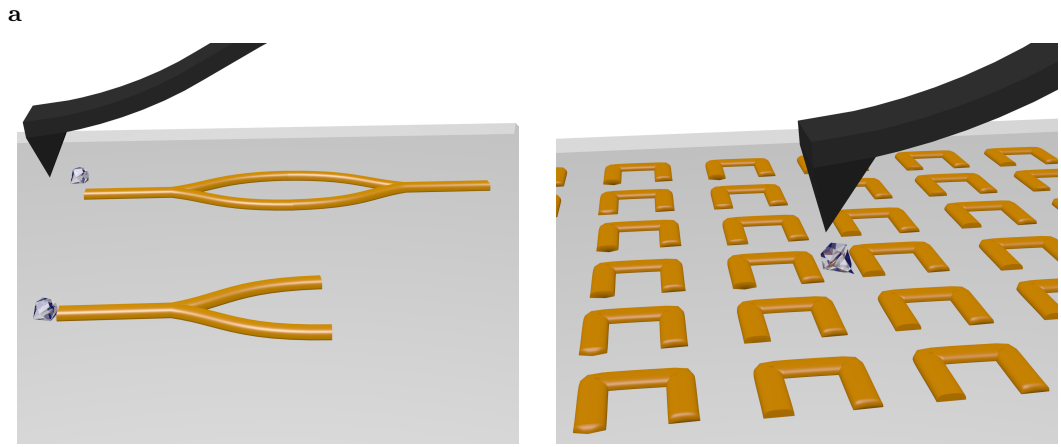

Figure 6.4.: a: Example of a possible realization of a plasmonic beamsplitter and a Mach-Zehnder interferometer using a N–V center as the single-photon feed, assembled with the AFM. b: Single-quantum probe: A single N–V center in a nanodiamond can be used to probe the local field density, as it is depicted for a plasmonic metamaterial.

Utilization of N–V Centers in Single-Emitter Applications

The manipulation techniques for the nanoscale developed in this work can be used for a large number of experiments to build up complex hybrid photonic systems. Especially the combination of single N–V centers in nanodiamonds with metallic structures featuring surface-plasmon polaritons might be a further step towards all-optical, on-chip solutions. In Fig. 6.4a, two such systems are sketched: a plasmonic beamsplitter and a plasmonic Mach-Zehnder interferometer[286].

A stable, solid-state single-quantum system can also function as a local electromagnetic field probe. N–V centers were utilized as local magnetic probes recently [287, 288], and the same is true for the mode density of the electric field component [289]. The increased interest in plasmonic metamaterials with their ability to enhance the fluorescence [290] could be investigated in detail with such a quantum probe.

For many applications, a high single-photon rate is required and many possible schemes to improve the emission behavior and the collection efficiency for single-photon sources have been realized or proposed. Here, the employment of a new antenna concept is suggested. By evaporating gold on polystyrene microspheres (which leads to a gold capping on the upper part of the sphere) followed by plasma etching of the uncovered lower part of the sphere, it is possible to build gold caps that can be attached to SNOM probes (Fig. 6.5a). Placing such a cap above an emitter can alter drastically its emission strength and pattern by the reflected field, dependent whether it interferes construc-

tively or destructively. With more sophisticated fabrication techniques, it might soon be possible to choose the extent of parameters a and b that are depicted in Fig. 6.5b in order to enhance and suppress emission in these directions, respectively. For such an antenna, the emission can be chosen to be well-directed towards the collection optics. For a two-dimensional configuration, the result of a FDTD simulation is presented in Fig. 6.5b: It is clearly visible that the emission is directed with a very small divergence angle, easily to be collected with an objective, even without a high NA.

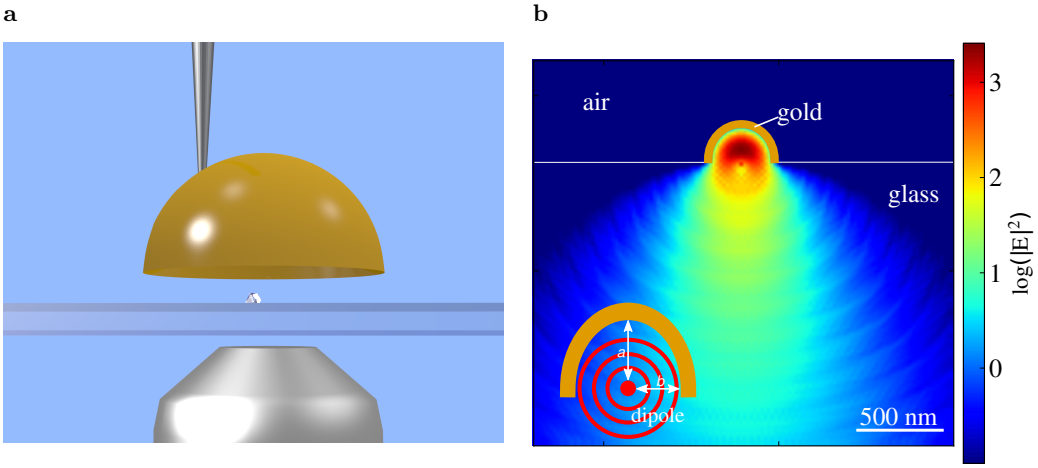

Figure 6.5.: a: Positioning a parabolic antenna above a nanodiamond. b: 2-d FDTD simulation of the emission of a dipole coupled to such an antenna. Not only is the emission into the upper half-space redirected towards the collection optics, but by choosing appropriate parameters a and b, emission towards the collection optics can be enhanced while it is suppressed in the direction perpendicular, to further direct the emission.

Improving N–V Center Performance by Upconversion Nanocrystals

A major disadvantage of N–V centers is the necessity of the very high excitation intensities which causes relatively high background emission, especially when metallic material is present. It is a major advantage of fluorescence from upconversion materials that it is merely free of background emission. This could lead the way to a possible solution, pumping upconversion nanocrystals followed by a transfer of the energy to the N–V center. Assembling upconversion nanocrystals with nanodiamonds containing a single N–V (see Fig. 6.6a) could lead to a direct energy transfer. If this is not sufficient, a metallic particle could mediate the transfer, as it increases the dipole strength.

Another solution to the problem could be a photon/plasmon supply line fed by an

upconversion nanocrystal. The N–V center could pick up the energy from the plasmonic wire or act as an single-photon transistor[291].

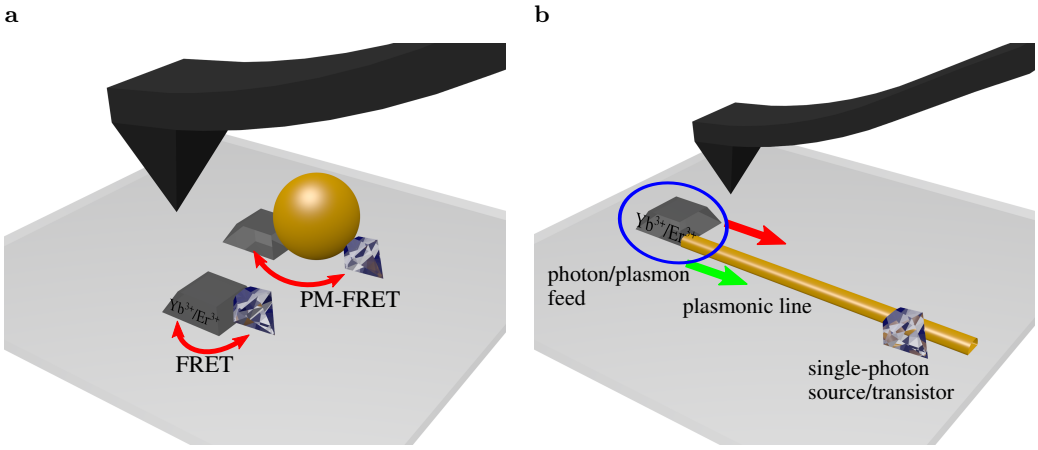

Figure 6.6.: Assembling of $NaYF_4$:Yb^{3+}/Er^{3+} codoped nanocrystals with nanodiamonds containing single N–V centers. a: Either fluorescence resonance energy transfer (FRET) or plasmon-mediated (PM-)FRET might be used for excitation of the N–V center. b: More complex solution to transfer the energy: An upconversion nanocrystal feeds a plasmonic supply line before the N–V center picks up the energy.

Multiple Nitrogen–Vacancy Centers on High-Q Microspheres

As shown in Section 5.3.5, it is possible to couple several N–V centers to the very same microspherical resonator, with the emission sharing the same high-Q modes. This gives the opportunity for a number of following experiments.

The emission into the same mode of more than a single N–V center might be a road to the creation of indistinguishable photons. Therefore, a single resonance line has to be filtered out. However, this line has to be narrow enough and it would be advantageous to find a way to collect the emitted photons more efficiently: a possible solution could be direct collection of the photons through the tapered fiber tip of the SNOM.

Just recently, several schemes have been proposed using the whispering gallery modes to realize building blocks for quantum information processing: The entanglement of separate N–V centers [270], a conditional multi-qubit phase gate [271], and the transfer of quantum information between individual N–V centers [292] have been proposed.

In all these schemes, two prerequisites have to be fulfilled: The transitions of the individual N–V centers have to match and they have to couple to a single microsphere mode. As it was already mentioned, the zero phonon line differs for individual N–V

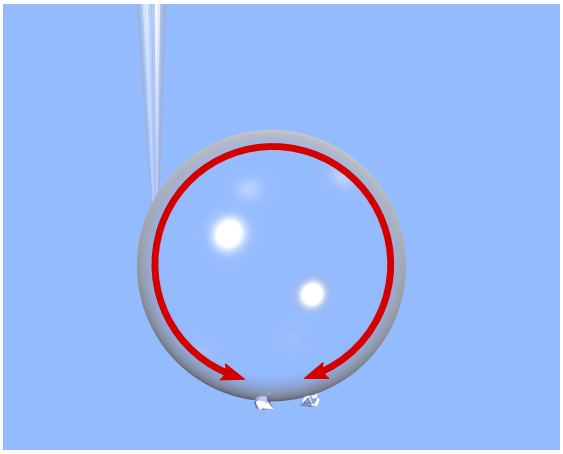

Figure 6.7.: The possibility to couple more than a single N–V center deterministically to a microsphere can be exploited in different application schemes.

centers in nanodiamond. This might be a first restriction, as the N–V centers have to be preselected themselves. Second, directly probing the whispering gallery modes with a tunable laser through the fiber indicated that at least in the plane where the tip introduces a perturbation the m-degeneration might be split.

These examples are just a few of variety of ideas that can be realized based on the physical concepts and the experimental setup developed in this thesis and might define next steps on the long way from single optical entities to complex optical micro- and nanodevices.

Appendices

APPENDIX A

Rate Equation and Power Dependence of Energy Transfer Upconversion

To understand the dynamics of a luminescent systems, their behavior can be modeled using a rate equation. There are two different goals that will be addressed: In the first section, the power dependence of sensitized energy transfer upconversion fluorescence intensity $I_{\mathrm{UC}}(P_{\mathrm{pump}})$. In the second section, the temporal evolution of the UC emission will be modeled with the rate equation.

A.1. Power-Dependence of the Upconversion Signal: the Steady State Case

Rate equations were used to find the dependence of the fluorescence intensity $I(P_{\mathrm{p}})$ of energy transfer (ET) upconversion (UC) on the pumping excitation density P_{p} occurring within a single ion species by Pollnau et al. [188]. In energy transfer upconversion (ETU), two different kinds of ions are involved and the model has to be extended. The goal is to find the function $I_{\mathrm{ETU}}(P_{\mathrm{p}})$ for the case of sensitized energy transfer UC (ETU).

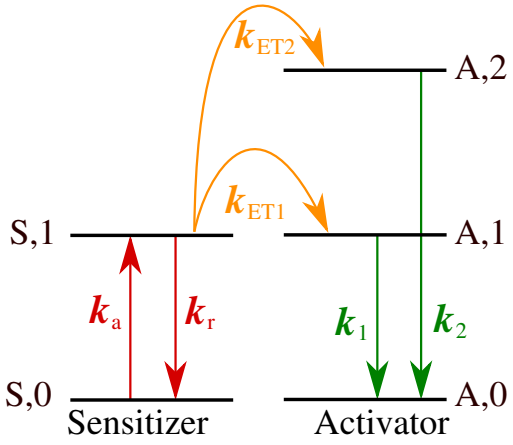

Figure A.1: Simplified level scheme for sensitized ETU.

Starting with the simplified level scheme depicted in Fig. A.1, the time derivatives for the occupation probability N for each level can be written down as:

$$\frac{\mathrm{d}}{\mathrm{d}t} N_{\mathrm{S},0}(t) = -k_{\mathrm{a}} N_{\mathrm{S},0} + k_{\mathrm{r}} N_{\mathrm{S},1} + k_{\mathrm{ET}_1} N_{\mathrm{S},1} N_{\mathrm{A},0} + k_{\mathrm{ET}_2} N_{\mathrm{S},1} N_{\mathrm{A},1} \tag{A.1a}$$

$$\frac{\mathrm{d}}{\mathrm{d}t} N_{\mathrm{S},1}(t) = +k_{\mathrm{a}} N_{\mathrm{S},0} - k_{\mathrm{r}} N_{\mathrm{S},1} - k_{\mathrm{ET}_1} N_{\mathrm{S},1} N_{\mathrm{A},0} - k_{\mathrm{ET}_2} N_{\mathrm{S},1} N_{\mathrm{A},1} \tag{A.1b}$$

$$\frac{\mathrm{d}}{\mathrm{d}t} N_{\mathrm{A},0}(t) = +k_1 N_{\mathrm{A},1} + k_2 N_{\mathrm{A},2} - k_{\mathrm{ET}_1} N_{\mathrm{S},1} N_{\mathrm{A},0} \tag{A.1c}$$

$$\frac{\mathrm{d}}{\mathrm{d}t} N_{\mathrm{A},1}(t) = -k_1 N_{\mathrm{A},1} + k_{\mathrm{ET}_1} N_{\mathrm{S},1} N_{\mathrm{A},0} - k_{\mathrm{ET}_2} N_{\mathrm{S},1} N_{\mathrm{A},1} \tag{A.1d}$$

$$\frac{\mathrm{d}}{\mathrm{d}t} N_{\mathrm{A},2}(t) = -k_2 N_{\mathrm{S},2} + k_{\mathrm{ET}_2} N_{\mathrm{S},1} N_{\mathrm{A},1} \tag{A.1e}$$

where k_{a}, k_{r}, k_{ET_1}, k_{ET_2}, k_1, and k_2 are the absorption and decay rates of the sensitizer, the rates for the two different energy transfers, and the decay rates of the levels of the activator. $N_{\mathrm{X,i}}$ are the occupation probabilities for the levels. The major simplification made in the model is the lack of all nonradiative processes.

In the steady state, all time derivatives vanish and all the equations above are equal to 0. As the above set of equations is still too complex to be solved in closed form, a further simplification has to be made. One may assume that no saturation and depletion effects occur in the sensitizer, i.e. the occupation probability $N_{\mathrm{S},1}$ is a linear function of excitation power:

$$N_{\mathrm{S},1} = \sigma \cdot P_{\mathrm{pump}} \quad . \tag{A.2}$$

With that it is possible to solve for $N_{\mathrm{A},2}$ and one obtains:

$$N_{\mathrm{A},1} = \frac{k_2 k_{\mathrm{ET}_1} N_{\mathrm{S},1}}{k_{\mathrm{ET}_1} k_{\mathrm{ET}_2} N_{\mathrm{S},1}^2 + k_2(k_{\mathrm{ET}_1} + k_{\mathrm{ET}_2}) N_{\mathrm{S},1} + k_1 k_2)} \tag{A.3a}$$

$$N_{\mathrm{A},2} = \frac{k_{\mathrm{ET}_1} k_{\mathrm{ET}_2} N_{\mathrm{S},1}^2}{k_{\mathrm{ET}_1} k_{\mathrm{ET}_2} N_{\mathrm{S},1}^2 + k_2(k_{\mathrm{ET}_1} + k_{\mathrm{ET}_2}) N_{\mathrm{S},1} + k_1 k_2} \tag{A.3b}$$

As the total fluorescence intensity emitted by a level is given by the emission rate k multiplied with the occupation probability, this shows that only in the case that both $N_{\mathrm{S},1} \cdot k_2 \cdot (k_{\mathrm{ET}_1} + k_{\mathrm{ET}_2})$ and $N_{\mathrm{S},1}^2 \cdot k_{\mathrm{ET}_1} \cdot k_{\mathrm{ET}_2}$ are much smaller than $k_1 \cdot k_2$ the power dependence of the upconversion emission is quadratic in $N_{\mathrm{S},1}$ and because of Eq. A.2 quadratic in P_{pump}. If this is not the case, a linear dependence can occur or, in the case of high energy transfer rates k_{ET_1} and k_{ET_2}, even constant emission. This is realistic, as in the latter case all photons are upconverted and the rate is only restricted by $N_{\mathrm{S},1}$. For the intermediate level A,1, the emission intensity dependence varies between P_{pump}^{-1} and P_{pump}. So it is possible that the paradox situation occurs that with increasing P_{pump} the emission intensity is reduced as an energy transfer is more likely.

For systems with $n+1$ levels, similar considerations lead to power dependences $I_i(P_{\mathrm{pump}})$ for the emission of the levels $i = 1, 2, \ldots, n$:

$$I_i(P_{\mathrm{pump}}) \propto P_{\mathrm{pump}}^{-1} \ldots P_{\mathrm{pump}}^{i} \tag{A.4}$$

depending on the rates of the energy transfers and decay rates, and P_{pump}. It is clear that this scheme can become more and more difficult if nonradiative decays are included.

A.2. Rise and Decay of the Upconversion Signal

A.2.1. Simplified Model and Analytical Solution

For the fluorescence signal of an ensemble of equal two level systems, the lifetime τ of the upper level and the excitation rate k are the only relevant values for the time evolution when excited by a laser (when quantum oscillations are not taken into account). After the excitation laser is turned on, the intensity of the fluorescence rises to a steady-state intensity I_0 with a monoexponential behavior of the form $I_0(1 - e^{-(k+1/\tau)/t})$. After turning ogf the pumping, the signal decays with a monoexponential function $e^{-t/\tau}$.

It is often the case in experiments that a system is excited to a higher level and the system relaxes to the emitting level. If the relaxation process is fast compared to the lifetime of the emitting level, this relaxation can be neglected and the observed decay is still monoexponential. However, in lanthanide doped materials the nonradiative relaxation processes have comparable time constants and the emission dynamics of the Er^{3+}ions does not follow an exponential law. To study the time-dependence of the signal of such a system, the level scheme depicted in Fig. A.2 is used. It is a simplified model of the green emission of the Er^{3+}ions where the energy transfer steps are taken into account as transitions with fixed rates k_{01} and k_{13}. This is not true, as these rates are functions of the population probabilities of the states included in the transfers and would have to be treated as in Eq. A.1. However, to qualitatively analyze the rise and decay behavior of the signal under chopped excitation it is sufficient to use the model of Fig. A.2.

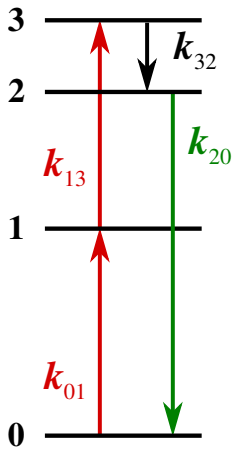

Figure A.2.: Simplified model for the analysis of the time-evolution of Er^{3+}UC fluorescence.

The coupled rate equation can be written in matrix form:

$$\frac{\mathrm{d}}{\mathrm{d}t}\mathbf{N} = A \cdot \mathbf{N} = \frac{\mathrm{d}}{\mathrm{d}t}\begin{pmatrix} N_0 \\ N_1 \\ N_2 \\ N_3 \end{pmatrix} = \begin{pmatrix} -k_{01} & 0 & k_{20} & 0 \\ k_{01} & -k_{13} & 0 & 0 \\ 0 & 0 & -k_{20} & k_{32} \\ 0 & k_{13} & 0 & k_{32} \end{pmatrix} \cdot \begin{pmatrix} N_0 \\ N_1 \\ N_2 \\ N_3 \end{pmatrix} \tag{A.5}$$

where N_i are the population probabilties of the states i and k_{ij} the transition rates from state i to j as indicated in Fig. A.2. The measured UC fluorescence signal intensity on a detector is directly proportional to N_2 multiplied by the transition rate k_{20} and the detection efficiency η.

The solution $\mathbf{N}(t)$ of the system can be obtained with the set of generalized eigenvectors $\mathbf{v}$ to the eigenvalues λ_i which are the non-trivial solutions satisfying

$$(A - \lambda_i \cdot \mathrm{Id})^{k_{\lambda_i}} \mathbf{v_i} = \mathbf{0} \tag{A.6}$$

where k_i is the algebraic multiplicity of the eigenvalue λ_i and Id is the identity matrix. The general solution for $\mathbf{N}(t)$ is given by

$$\mathbf{N}(t) = \sum_{\mathbf{v}_i \epsilon \mathbf{v}} c_{\mathbf{v_i}}\ e^{\lambda_i t} \cdot \sum_{j=0}^{k_{\lambda_i}} \frac{t^j}{j!} \cdot (A - \lambda_i\ \cdot\ \mathrm{Id})^j \mathbf{v}_i\ . \tag{A.7}$$

where the coefficients $c_{\mathbf{v}_i}$ have to be determined by the initial value of $\mathbf{N}(t = t_0)$.

In the time-resolved experiments in Section 4.4, the laser is turned on and off. If the off-time ($k_{01} = 0$) is long enough, the system relaxes completely to the ground state and the initial value when excitation is turned on is again given by $N_0 = 1$ and $N_i = 0$ for $i = 1, 2, 3$. Then, the system evolves to the steady state characterized by $(d\mathbf{N}/dt) = 0$, and the N_i are determined by the solution of the homogeneous system $A \cdot \mathbf{N} = 0$. When the laser is turned off, the decay process starts with this steady state solution for $\mathbf{N}$ as the initial value. Furthermore, the matrix A has to be replaced by A' where the excitation rate k_{01} is 0.

Instead of presenting the general solution of the system which is a lengthy expression, the concrete solutions of $\mathbf{N}(t)$ for some sets of k's are shown in Fig. A.3. For all $k_{ij} = 1$ the time-dependence of N_i, with $i = 1, 2, 3$ after turning on and turning off the pump laser are shown in a and b, respectively. In Fig. A.3a when the excitation is turned on, the emission from level 2 is delayed as the excitation has to undergo the multi-step process to fill this level. In Fig. A.3b when turning the excitation off, the decrease of the UC fluorescence signal is delayed, as the excitation energy which is stored in the non-emitting levels is released and fills the level. The upper graphs in Fig. A.3 c show different decay curves of N_2. For all plots, k_{01} equals 1. One of the quantities k_{13}, k_{32}, or k_{20} is varied in each of the plots, respectively. Starting with the red and ending with the blue curves, k_{ij} takes the values 0.1, 0.5, 2.5 and 12.5. The variation results in a change of the decay curve. However, it is obvious that the rates k_{13} and k_{32} influence the decay behavior of level N_2 equally. Furthermore, the normalized decay curves (lower graphs) reveal that the commutation of any of the three rates does not change the qualitative shape of the decay curve, but only the starting value of the decay. A similar behavior can be found for the rise curves of N_2, but is not shown.

Varying k_{01} and keeping all other rates constant (corresponds to the variation of the excitation power) does not influence the shape of the decay curve, but again only the absolute intensity of the emission, though the variation of the excitation power would also immediately influence k_{13}. Actually, the very simplified model identifies that, besides k_{01}, the different rates contribute equally and exchangeable to the shape of the rise and

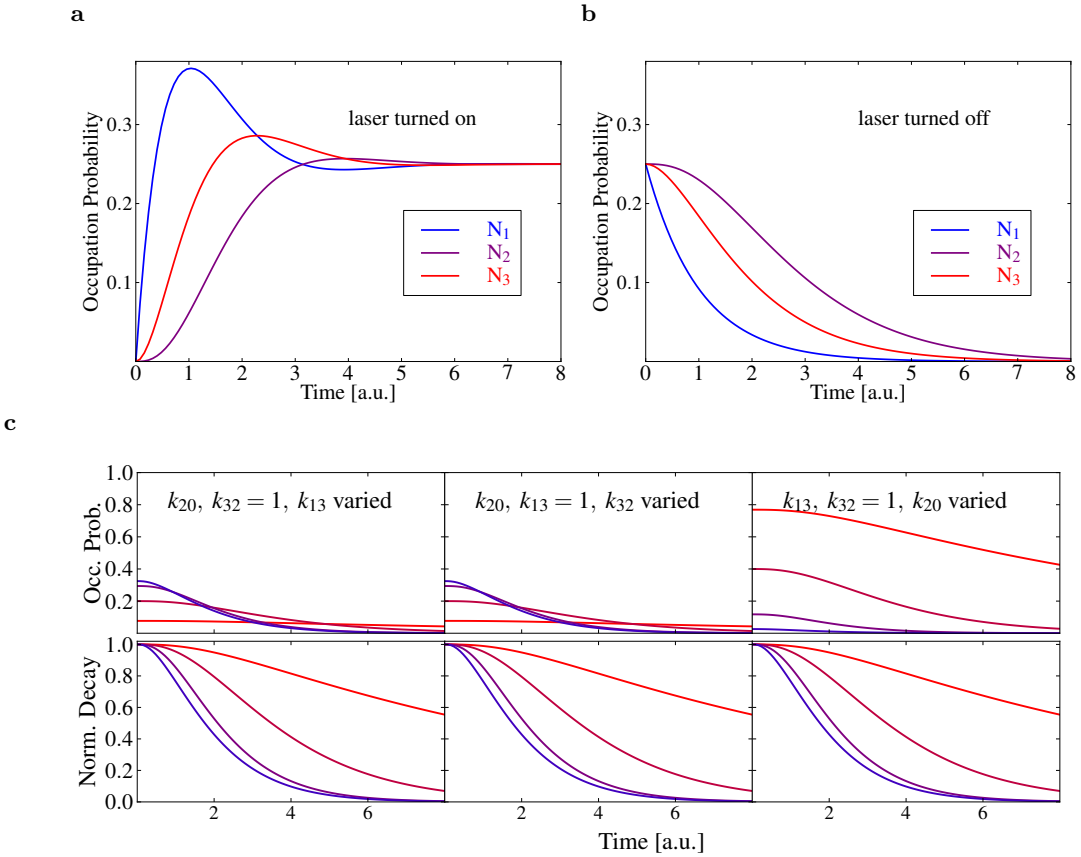

Figure A.3.: Solution for the level scheme in Fig. A.2 under chopped laser excitation. The UC fluorescence signal is directly proportional to N_2. a and b: Filling and emptying of the levels $1, 2$, and 3 for $k_{01} = k_{13} = k_{32} = k_{20} = 1$. c: Upper curves: Decay of the absolute occupation probability of level N_2 with varying values of k_{13}, k_{31}, and k_{20}. Lower curves: The normalized curves show that only the absolute intensity is altered, but not the qualitative shape of the decay curves.

decay curves. Therefore, the interpretation of time-dependent measurements of the UC fluorescence with the goal to derive the individual rates is rather difficult and has to be accompanied by further measurements as quasi-resonant fluorescence measurements.

A.2.2. Numerical Solution

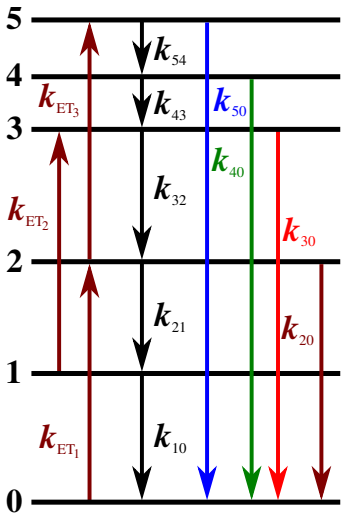

Figure A.4: Model of the ETU solved numerically.

When taking into consideration all process, i.e. radiative and nonradiative decays as well as energy transfers, the system is not linear anymore because of the energy transfer terms, and an analytical solution can not be derived. As an alternative, it is possible to solve the equations numerically.

The straightforward method is integrate numerically the full rate equations for the complete scheme of transitions in Fig. A.4:

$$
\begin{aligned}
\frac{\mathrm{d}}{\mathrm{d}t}S_0 &= -k_{S01}S_0 + k_{S10}S_1 + \sum_{j=0}^{2} k_{\mathrm{ET}_{j+1}}N_jS_1 \\
\frac{\mathrm{d}}{\mathrm{d}t}S_1 &= k_{S01}S_0 - k_{S10}S_1 - \sum_{j=0}^{2} k_{\mathrm{ET}_{j+1}}N_jS_1 \\
\frac{\mathrm{d}}{\mathrm{d}t}N_0 &= \sum_{j=1}^{5} k_{j0}N_j - k_{\mathrm{ET}_1}N_0S_1 \\
\frac{\mathrm{d}}{\mathrm{d}t}N_1 &= -k_{10}N_1 + k_{21}N_2 - k_{\mathrm{ET}_2}N_1S_1 \\
\frac{\mathrm{d}}{\mathrm{d}t}N_2 &= -k_{20}N_2 - k_{21}N_2 + k_{32}N_3 + k_{\mathrm{ET}_1}N_0S_1 - k_{\mathrm{ET}_3}N_2S_1 \\
\frac{\mathrm{d}}{\mathrm{d}t}N_3 &= -k_{30}N_3 - k_{32}N_3 + k_{43}N_4 + k_{\mathrm{ET}_2}N_1S_1 \\
\frac{\mathrm{d}}{\mathrm{d}t}N_4 &= -k_{40}N_4 - k_{43}N_4 + k_{54}N_5 \\
\frac{\mathrm{d}}{\mathrm{d}t}N_5 &= -k_{50}N_5 - k_{54}N_5 + k_{\mathrm{ET}_3}N_2S_1.
\end{aligned}
\tag{A.8}
$$

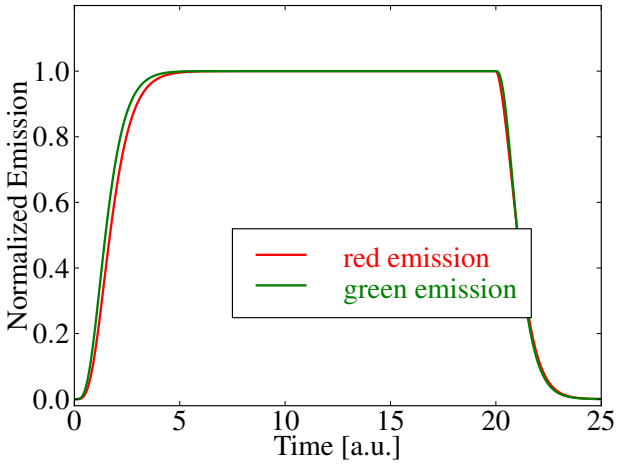

Figure A.5.: Numerical solution for the scheme in Fig. A.4. All rates are set to one besides $k_{21} = 0.3$, $k_{43} = 3$.

The result of such a numerical approach is presented in Fig. A.5. It resembles the analytic solution. It turns out that with non-zero values for all the transition rates in Eq. A.8, rates are not exchangeable anymore, as it was the case for the simplified analytical model.

To conclude, the shapes of the time-evolution and the absolute intensities of the UC fluorescence emission are in general complex functions of *all* rates. Due to the large amount of parameters, fitting of the signal curves in Section 4.4 is not reasonable, but it is possible to explain and obtain quantitatively all observed phenomena with the models.

APPENDIX B

Rate Equation and $g^{(2)}$-Function of the N–V $^-$ center

B.1. Rate Equation for the N–V $^-$ Center in Diamond

As pointed out in Section 5.2, the exact level scheme of the N–V$^-$ center is still under discussion. The simplified level scheme that can explain the time-dynamics of the negatively charged N–V center is depicted in Fig. B.1. In the experiments, the N–V$^-$ center is excited (nonresonantly) from the ground state $|1\rangle$ by laser light with a wavelength of either 514 nm or 532 nm into the phonon sidebands of state $|2\rangle$. The vibrational excitation relaxes on a ps timescale. Then, either a radiative transition into phonon sidebands of the ground state $|1\rangle$ takes place or the metastable state $|3\rangle$ is populated in a so-called intersystem crossing. It is not exactly clear, how the depopulation of the metastable state $|3\rangle$ happens but

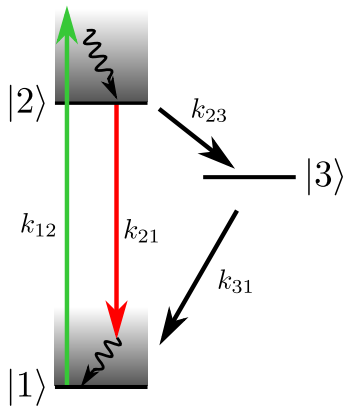

Figure B.1.: Simplified level scheme of the N–V$^-$ center. The nonradiative vibrational relaxation transitions are considered to be fast (curly arrows) compared to the other processes.

recent investigation proved that at least one further singlet state is involved [256, 265]. However, possible radiative emission from these states is very weak [256] and has not to be regarded in the following. Furthermore, for the dynamics of the emissive level it is irrelevant whether one or two singlet states are involved.

For all relaxation processes inside the phonon sidebands (curly arrows) are fast compared to the interstate transitions and their time constants can be neglected.

This leads to the following equations for the time-dependence of the occupation probability n_1, n_2, and n_3, of the states $|1\rangle$, $|2\rangle$, and $|3\rangle$, respectively:

$$\begin{aligned}
\frac{d}{dt}n_1(t) &= -k_{12}\,n_1(t) && +k_{21}\,n_2(t) + k_{31}\,n_3(t) \\
\frac{d}{dt}n_2(t) &= +k_{12}\,n_1(t) && -(k_{21}+k_{31})\,n_2(t) \\
\frac{d}{dt}n_3(t) &= && +k_{23}\,n_2(t) - k_{31}\,n_3(t)
\end{aligned} \tag{B.1}$$

This can be written in matrix form,

$$\frac{d}{dt}\mathbf{n} = A\cdot\mathbf{n} = \frac{d}{dt}\begin{pmatrix} n_1 \\ n_2 \\ n_3 \end{pmatrix} = \begin{pmatrix} -k_{12} & k_{21} & k_{31} \\ k_{12} & -(k_{21}+k_{23}) & 0 \\ 0 & k_{23} & -k_{31} \end{pmatrix}\cdot\begin{pmatrix} n_1 \\ n_2 \\ n_3 \end{pmatrix}, \tag{B.2}$$

and the solution can be again found by diagonalization as described in Appendix A.2.1.

It should be mentioned that the usage of the rate equations implies that coherent quantum effects are not taken into account. This is justified in the scope of this work by two reasons: First, all experiments were done at room temperature, and second, excitation is far from resonance, so that the vibrational relaxation to the emissive state destroys any coherence.

B.1.1. Relation between Rate Equation and Second-Order Correlation

The second-order correlation function $g^{(2)}(\tau)$ is a measure for the probability to detect a second photon at time τ after the detection of a photon at time 0. After the emission of the first photon the system is in the ground state $n_1 = 1$, $n_2 = 0$, and $n_3 = 0$. The probability to detect a photon at time τ is proportional to the occupation probability $n_2(\tau)$ multiplied by the emission rate k_{21} and the detection efficiency η of the system. So the $g^{(2)}$-function is directly proportional to the solution for the occupation probability $n_2(t)$ determined by the system of differential equations in Eq. B.2 with an initial value of

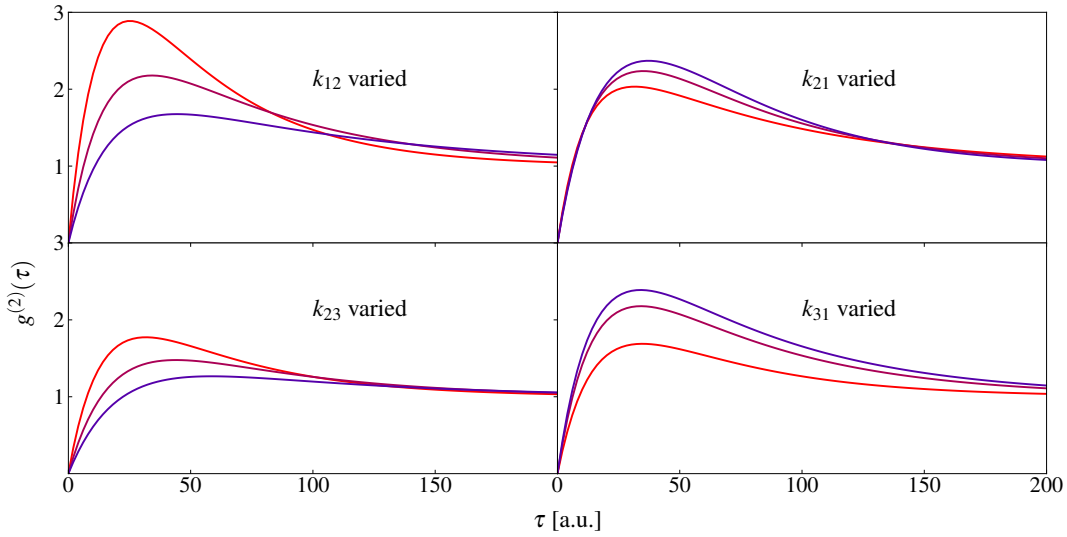

Figure B.2.: Calculated $g^{(2)}$-functions for different sets of k_{12}, k_{23}, k_{23}, and k_{31}.

$\mathbf{n}(0) = (1, 0, 0)$. The normalization is obtained by the limit of the occupation probability for large times $n_2(\infty)$ and one finds

$$g^{(2)}(\tau) = \frac{\eta\, k_{21}\, n_2(\tau)}{\eta\, k_{21}\, n_2(\infty)}, \quad \text{with} \quad \mathbf{n}(\tau = 0) = (1, 0, 0). \tag{B.3}$$

The solution for the $g^{(2)}$-function is

$$g^{(2)}(\tau) = 1 - (1 - A)\, e^{k_1 \tau} + A\, e^{k_2 \tau} \tag{B.4}$$

with

$$k_{1,2} = \frac{-S \pm \sqrt{S^2 - 4\,T}}{2}, \qquad A = \frac{k_2 + k_{31} - k_{12}\frac{k_{23}}{k_{31}}}{k_1 + k_2}, \tag{B.5}$$

$$S = k_{12} + k_{23} + k_{23} + k_{31}, \qquad T = k_{31}(k_{21} + k_{12}) + k_{23}(k_{31} + k_{12}). \tag{B.6}$$

For different values of k_{12}, k_{23}, k_{23}, and k_{31}, the corresponding $g^{(2)}$-function are shown in Fig. B.2. The transition to the metastable singlet state is responsible for the bunching effect: When the emitter has emitted a start photon, the state is not trapped in the metastable state, and the emission of a second photon is more likely than the average emission probability. Neither the height nor the width of the bunching feature are solely

dependent on the rates k_{23} and k_{31} as one might expect, but are determined by all four rates of the system. As can be seen, the dependence of the shape of the curves on the parameters is rather complex, which explains the problems when fitting the experimental curves. Actually, equal curves can be obtained with different sets of parameters.

So far, it was assumed that the relaxation transition $|2\rangle \rightarrow |1\rangle$ is radiative with the rate k_{21}. However, it is also possible that nonradiative processes described by an overall rate k_{nr} induces the transition. This can be taken into account by replacing k_{21} by $k_{\mathrm{r}} + k_{\mathrm{nr}}$ in Eq. B.1. This translates directly into a modified $g^{(2)}$-function with the same replacement in Eq. B.6.

B.1.2. Rate Equation and Saturation

Further information can be derived from the power dependence of the emission intensity under cw excitation. By setting the left hand sides of the modified Eq. B.1 to zero and with the additional condition $n_1(t) + n_2(t) + n_3(t) = 1 \,\forall\, t$ (as the system has to be in either of the states $|1\rangle$, $|2\rangle$, and $|3\rangle$), it is possible to solve for the steady-state occupation probability $\bar{n}_2$. The emission rate R is given by

$$R = k_{\mathrm{r}} \cdot \bar{n}_2 \tag{B.7}$$

and can be expressed by the transition rates

$$R = k_{\mathrm{r}} \frac{k_{12}k_{31}}{((k_{12} + k_{\mathrm{r}} + k_{\mathrm{nr}} + k_{23})k_{31} + k_{12}k_{23})} \tag{B.8}$$

The absorption rate k_{12} can be expressed in terms of the average absorbed power $\langle P \rangle$ and the photon energy $\hbar\omega_{\mathrm{exc}}$ of the excitation laser: $k_{12} = \langle P \rangle / \hbar\,\omega_{\mathrm{exc}}$. $\langle P \rangle$ is connected to the incident excitation intensity I_{exc} by $\langle P \rangle = \sigma I_{\mathrm{exc}}$, where σ is the absorption cross section.

Plugging the expressions for k_{12} and $\langle P \rangle$ into Eq. B.8, the expression for R as a function of the excitation intensity I_{exc} is found:

$$R(I) = R_{\mathrm{max}} \frac{I_{\mathrm{exc}}/I_{\mathrm{S}}}{1 + I_{\mathrm{exc}}/I_{\mathrm{S}}} \tag{B.9}$$

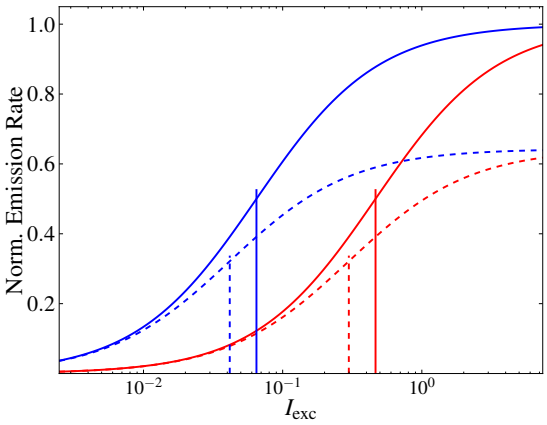

Figure B.3.: Normalized emission rates: The values for $k_r = 1/30$ and $k_{23} = 1/80$ are kept constant. k_{nr} is 1/10 for the blue curves, 1 for the red curves, k_{31} is 1/100 for the solid curves, 1/200 for the dashed curves, respectively. Horizontal lines indicate I_S for each of the curves. The maximal emission rate R_{max} is only dependent on k_r, k_{23}, and k_{31}, but not on the nonradiative decay rate k_{nr}.

with

$$R_{max} = \frac{k_{31}\, k_r}{k_{23} + k_{31}} \tag{B.10}$$

$$I_S = \frac{(k_r + k_{nr} + k_{23})k_{31}}{\sigma\,(k_{23} + k_{31})}\,\hbar\,\omega_{exc} \tag{B.11}$$

R_{max} is the maximal emission rate when $I_{exc} \to \infty$. I_S is the intensity at which the emission rate R equals $R_{max}/2$. It is important to mention that the maximal emission rate is independent of the nonradiative decay rate k_{nr} and therefore is not limited by nonradiative decays. Only the intersystem crossing rate k_{23} and the decay rate k_{31} of the metastable level $|2\rangle$, and the radiative decay rate k_r of $|2\rangle$ define the maximal number of emitted photons. This behavior is depicted in Fig. B.3, where for different transition rates k_{nr}, and k_{31}, the calculated emission rates as functions of I_{exc} are shown in a semi-logarithmic plot.

In an experiment, it is impossible to collect and detect all the emitted photons. The count rate on a detector C_{Det} is related to the R via the overall detection efficiency η by $C_{Det} = \eta R$. However, for the analysis of the changes introduced in an experiment, e.g. by nanomanipulation, it is often not necessary to know the absolute values from the saturation curve. When η does not change during the experiments, the relative changes can be used to analyze the experiment.

B.1.3. Quantum Efficiency

A major figure-of-merit of an emitter is the *quantum efficiency* ϕ, a measure for how likely an excitation relaxes radiatively, given by the ratio between the radiative decay rate k_r and the total depopulation rate $k_\mathrm{r} + k_\mathrm{nr} + k_{23}$ of level $|2\rangle$:

$$\phi = \frac{k_\mathrm{r}}{k_\mathrm{r} + k_\mathrm{nr} + k_{23}}. \tag{B.12}$$

This can be used to express the measured saturation curves C_det as a function of the quantum efficiency:

$$C_\mathrm{det} = \eta \frac{\phi\ k_{12}}{1 + \phi\ k_{12}/R_\mathrm{max}}. \tag{B.13}$$

Thus, under the assumption that intersystem crossing rates and lifetime of the metastable state $|3\rangle$ does not change in the experiment, the enhancement of R_max is given by the enhancement factors of the radiative transition rate k_r. Furthermore, with an initial value for ϕ together with a lifetime measurement of the emissive state, it is possible to evaluate the changes of the quantum efficiency that occur in the experiments.

B.2. Measuring the Second-Order Correlation Function

The normalized second-order correlation of an emitter is not measured directly. What is measured in the HBT start-stop setup as described in Section 3.1.2 is the photon arrival time of a second photon after a first photon has been detected. This is done repeatedly. The time line between the initial photon and the maximal delay time is discretized into time bins $[t, t+\Delta\tau]$ where the detection times are "sorted" in and a total count rate per time bin is the result of the measurements.

In the attempt to recover the $g^{(2)}$-function of single-quantum emitters like N–V centers from such an experiment, different challenges arise:
First, the probability to detect stop photons decreases with time, since the measurement might have been stopped before by a previous photon. This is especially true for high count rates.
Second, it is neither possible to detect all photons from the emitter, nor is it possible to distinguish between the emission from the N–V center and background fluorescence from the sample. Therefore, the measured $g^{(2)}$-function has to be corrected for these contributions.
Third, the limited time-resolution of the system is washing out narrow features in the $g^{(2)}$-function, e.g. the antibunching dip.

In the following, the influence of these points is discussed. The possibility to correct for the effects will also be addressed and/or a quantification of the errors is made.

B.2.1. Correction for Reduced Detection Probability with Time

The measured autocorrelation function for a single N–V center is shown in Fig. B.4. The decline of the signal towards long times is due to the decrease of the probability to detect a photon after longer times since another photon might have stopped the measurement before.

The probability $p(\tau)$ to detect a photon at a time τ after the detection of a photon at time 0 is proportional to the emission probability of a photon $P(\tau)$ times the overall detection efficiency η times the probability that no other photon has stopped the measurement before, given by $1 - \int_0^\tau \eta\, P(\tau')d\tau'$:

$$p(\tau) = \eta\, P(\tau)(1 - \int_0^t \eta\, P(\tau')\, d\tau') \tag{B.14}$$

The number of counts N in the bin counting the detection events of the time interval

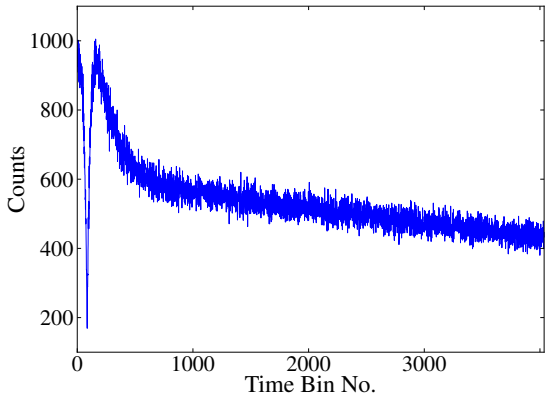

Figure B.4.: Repeatedly measured arrival times of a second photon after a first photon started the measurement at $t = 0$. The probability to detect a photon decreases with time since the measurement might have been stopped by a detection event before.

$[t, t + \Delta\tau]$ is then given by

$$N_{[t,t+\Delta\tau]} = S \cdot \int_t^{t+\Delta\tau} p(\tau')d\tau' \tag{B.15}$$

where S is the number of starting events, directly proportional to the duration of the data acquisition. Eq. B.14 can be rearranged to

$$P(\tau) = \frac{p(\tau)}{\eta\,(1 - \int_0^t \eta\, P(\tau')\, d\tau')} \tag{B.16}$$

In the expression for $P(\tau)$ is still the integral over $P(\tau')$. For $\tau = 0$, it is $P(0) = p(0)/\eta$. For small $\Delta\tau$, it is possible to write

$$P(0 + \Delta\tau) \approx \frac{p(\Delta\tau)}{\eta\,(1 - \eta\, P(0)\, \Delta\tau)} = \frac{p(\Delta\tau)}{\eta\,(1 - \eta\, p(0) \cdot \Delta\tau)}. \tag{B.17}$$

Taking $\Delta\tau$ to be the experimental bin width and using twice Eq. B.15 with the similar approximation for the integral, it is possible to connect $P(0 + \Delta\tau)$ to the experimental data:

$$P(0 + \Delta\tau) \approx \frac{N_{[\Delta\tau,2\Delta\tau]}}{S\,\Delta\tau\,\eta(1 - \eta\, N_{[0,\Delta\tau]}/S)}. \tag{B.18}$$

Now that the expression for $P(\Delta\tau)$ is known, it can be used to derive $P(2\Delta\tau)$ as it is done in Eq. B.17 for $P(0 + \Delta\tau)$. So, $P(\tau)$ can be obtained regressively from the experimental data, if the factor η/S is known. The factor $1/(S\,\Delta\tau\,\eta)$ is only changing

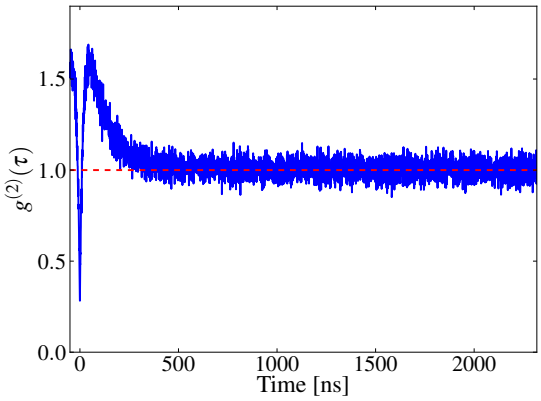

Figure B.5.: $g^{(2)}$-function recovered from the data in Fig. B.4.

the normalization. For large times the emission is uncorrelated and $P(\tau)$ has to be constant. Therefore, η/S can be found with this constraint by fitting the experimental data for long times to a constant function.

The normalized second-order correlation function $g^{(2)}(\tau)$ is directly proportional to the function $P(\tau)$. For large times, the $g^{(2)}$-function. So, normalizing $P(\tau)$ for large times reveals the desired function $g^{(2)}(\tau)$. The measured $g^{(2)}$-function obtained by this procedure from the experimental data in Fig. B.4 is shown in Fig. B.5. The time axis is adjusted to the extra delay between start and stop photon given by the experimental setup.

B.2.2. Limiting Factors for the Depth of the Antibunching Dip

The antibunching dip of a single-quantum emitter theoretically drops down to zero. In real experiments, two factors limit the depth of the dip: background emission and the limited time-resolution.

Influence of Background Emission

The analysis of the single-photon character by measuring the $g^{(2)}$-function of an emitter is always corrupted by detection events that are not triggered by photons from the emitter: Stray light, background fluorescence from the substrate, and the intrinsic dark-counts of the detector add up to an uncorrelated, coherent background. The share of background contribution to the $g^{(2)}$-function has to be determined to decide whether the single-photon character is limited by the background or by the contribution of more than one emitter, but, e.g., with different emission strength.

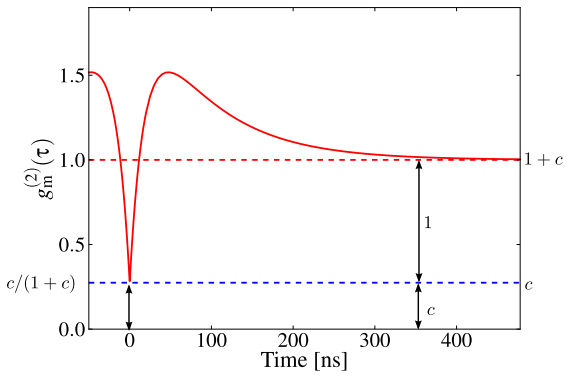

Figure B.6.: Contribution of background counts to the measured $g_{\mathrm{m}}^{(2)}$-functions. The $g^{(2)}$-function of the emitter has a constant offset c. As the normalization to one is done on the long-time tail, c is also normalized to $c/(1+c)$.

Since neither a correlation between individual background detection events nor a correlation between background and signal detection events is present the contribution of the background introduces a constant offset to the emitter's $g^{(2)}$-function, denoted as $g_{\mathrm{e}}^{(2)}$.

Start-stop events contributing to the measured normalized second-order correlation function, denoted as $g_{\mathrm{m}}^{(2)}$ can be either signal–signal, signal–background, background–signal, or -background–background. Denoting the probabilities to detect a signal photon and a background photon as S and B, respectively, the magnitude c of the additional coherent background contribution compared to the emitter's $g_{\mathrm{e}}^{(2)}$-function at long times is given by

$$c = B\,S + S\,B + B^2, \tag{B.19}$$

summing up to the measured

$$g_{\mathrm{m}}^{(2)}(\tau) = d \cdot (g_{\mathrm{e}}^{(2)}(\tau) + c). \tag{B.20}$$

This is shown schematically in Fig. B.6. The normalization to a value of one for the uncorrelated tail of the measured curve $g_{\mathrm{m}}^{(2)}$ for large values of τ includes both the contribution of the background emission and the emission of the single quantum emitter. Therefore, the background contribution to $g_{\mathrm{m}}^{(2)}(\tau = 0)$ is $c/(1+c)$.

For one of the measurements, the background contribution is shown in Fig. B.7. The background emission is around 25% of the signal intensity. It can be seen that the background emission explains the limited depth of the normalized second order correlation

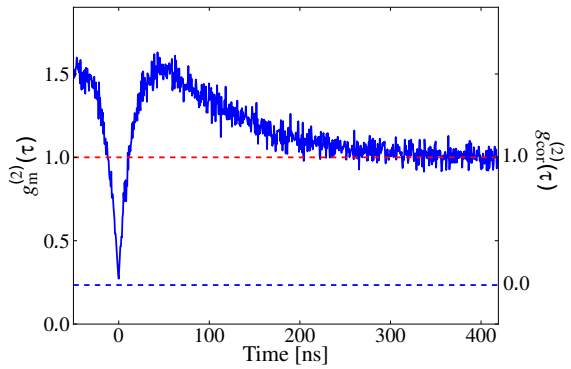

Figure B.7.: Measured $g^{(2)}$-function (blue curve) with the calculated constant offset introduced by the background. The background contribution explains the reduced depth of the antibunching dip for the measured $g^{(2)}_{\mathrm{m}}(0)$.

function in an excellent way.

For all the measured $g^{(2)}$-functions in this work, this background correction reduces the value at $\tau = 0$ to a value close to 0. Throughout this work, the correction was not applied to the data, as for all applications of single-photon sources, a correction is not reasonable.

Limits by the Time-Resolution of the Setup

There are two different factors that limit the time-resolution for the measurement of the $g^{(2)}$-function. First, the identification of the point of time when the photon arrives at the detector is subject to an error. The second is the time-resolution given by the bin width of the time-correlated single-photon counting module in the HBT setup.

The influence of the bin width is illustrated in Fig. B.8a. The red curve is the theoretical $g^{(2)}$-function for typical transition rates observed in the experiments for N–V centers in bare nanodiamonds Section 5.3.2, the blue bars represent the resulting distribution in the time bins with a width of 0.587 ns, also as given in the experiment. Depending on the temporal position relative to $\tau = 0$, different minimal bin values are obtained, as shown in the inset. The binning results in minimal values between 0.02 and 0.03 in the time bin containing $\tau = 0$. The width of the time bins can be reduced which would reduce this error. However, the uncertainty of the exact determination of the photon's arrival time on the detector plays at least a comparable role, and further reducing the bin width has not the desired result which is shown in the following.

The limited time-resolution of the components of the HBT setup results in the un-

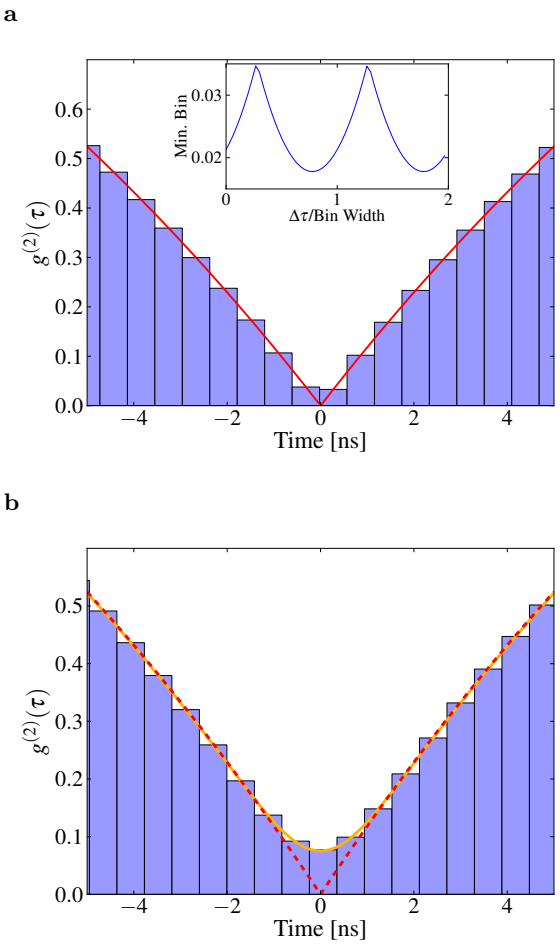

Figure B.8.: a: Influence of the time binning on the depth of the measured $g^{(2)}$-function. The red curve is the theoretical curve, the blue bars represent the resulting measured function with a time bin width of 0.587 ns, as in the experiment. The minimal value is dependent on the relative temporal position of the bins to $\tau = 0$, as shown in the inset. b: Limited time-resolution of the HBT setup components: The dip of the theoretical $g^{(2)}$ (red curve) is washed out (orange curve) and the time-binning does hardly affect the depth of the dip.

certainty of the point of time of the photon detection. The time-resolution has been determined to be around 400 ps for a single APD [293]. It is explained mainly by a temporal jitter introduced by the avalanche process in the APDs, the activating process of the detection. Mathematically, this corresponds to convolving the $g^{(2)}$-function with a Gaussian function with a width of 800 ps (as the time-resolution for both the start and the stop APD add up). The dip of the $g^{(2)}$-function is washed out , shown in Fig. B.8b

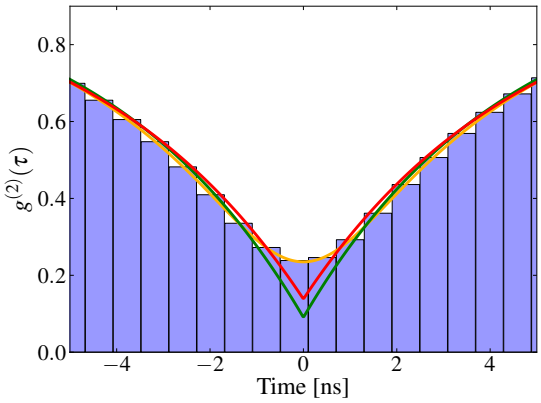

Figure B.9.: Influence of the limited time resolution: The theoretical $g^{(2)}$-function (green curve) is smeared out by the limited time resolution (orange curve), which results in the measured count rates distribution in the time bins in the experiment (blue bars). Fitting the time-bin distribution with a $g^{(2)}$-function model (red curve) reveals an additional error, especially the background contribution is overestimated.

(orange curve). Also presented in the graph is the resulting measured $g^{(2)}$-function, where the time-binning is also accomplished (blue bars).

As can be seen, the time-binning does hardly influence the depth of the dip anymore. Therefore, the bin width of 587 ps is a good trade-off, as the higher bin width enhances the signal-to-noise ratio: The count rate per bin is higher, reducing the typical shot noise in the signal.

A major problem appears when the temporal features are on timescales comparable to the overall time-resolution. This is especially the case for N–V centers coupled to plasmonic antennas in Section 5.4 and results in additional errors in fittings of the antibunching curve. As an example, this is shown in Fig. B.9: The $g^{(2)}$-function (green curve) [1] and background contribution $c = 0.1$) is smeared out by the time-resolution (orange curve), resulting in the distribution in the time-bins (presented by the blue bars). The $g^{(2)}$-function obtained by fitting the time-bin distribution (red curve) shows that the background is overestimated by a factor of around 2. Furthermore, the fitted transition rates do not reflect the correct rates. Therefore, the time constants obtained by fitting the experimental data have to be taken with great care, especially the value of the background contribution.

[1] Transition rates are typical values of the experiment: $k_{12} = 1/75\,\mathrm{s}^{-1}$, $k_{21} = 1/4.8\,\mathrm{s}^{-1}$, $k_{23} = 1/276\,\mathrm{s}^{-1}$, $k_{31} = 1/500\,\mathrm{s}^{-1}$.

List of Own Publications

Peer-reviewed Journals

The following publications appeared in peer-reviewed journals in the context of this work.

Steudle et al. 2011 Quantum Nature of Light Measured With a Single Detector.
G. A. Steudle, S. Schietinger, D. Höckel, S. N. Dorenbos, V. Zwiller, O. Benson. *arXiv*:1107.1353v1.

Barth et al. 2010b Controlled coupling of NV defect centers to plasmonic and photonic nanostructures.
M. Barth, S. Schietinger,T. Schröder, T. Aichele, and O. Benson. *Journal of Luminescence*, 130:1628-1634, 2010.

Barth et al. 2010a Nanoassembled Plasmonic-Photonic Hybrid Cavity for Tailored Light-Matter Coupling.
M. Barth, S. Schietinger, S. Fischer, J. Becker, N. Nüsse, T. Aichele, B. Löchel, C. Sönnichsen, and O. Benson. *Nano Letters*, 10:891–895, 2010.

Schietinger et al. 2010 Plasmon-Enhanced Upconversion in Single $NaYF_4$:Yb^{3+}/Er^{3+} Codoped Nanocrystals.[2]
S. Schietinger, T. Aichele, H. Wang, T. Nann, and O. Benson. *Nano Letters*, 10:134–138, 2010.

[2]Parts highlighted in: Emerging functional nanomaterials for therapeutics. *Journal of Material Chemistry*, 21:13107–13127, 2011.

Schietinger et al. 2009c Coupling single NV-centres to high-Q whispering gallery modes of a pre-selected frequency-matched microresonators.
S. Schietinger and O. Benson. *Journal of Physics B*, 42:114001, 2009.

Schietinger et al. 2009b Observation of size-dependence in multi-color upconversion in single Yb^{3+},Er^{3+} codoped $NaYF_4$ nanocrystals.
S. Schietinger, L. de Souza Menezes, B. Lauritzen, and O. Benson. *Nano Letters*, 9:2477–2481, 2009.

Schietinger et al. 2009a Plasmon-Enhanced Single Photon Emission from a Nanoassembled Metal–Diamond Hybrid Structure at Room Temperature.[3]
S. Schietinger, M. Barth, T. Aichele, and O. Benson. *Nano Letters*, 9:1694–1698, 2009.

Schietinger et al. 2008 One-by-One Coupling of Single Defect Centers in Nanodiamonds to High-Q Modes of an Optical Microresonator.
S. Schietinger, T. Schröder, and O. Benson. *Nano Letters*, 8:3911-3915, 2008.

Prabhakaran *et al.* 2006 Ultrafine luminescent structures through nanoparticle self-assembly.
K. Prabhakaran, S. Götzinger, K. V. Shafi, A. Mazzei, S. Schietinger, and O. Benson. *Nanotechnology*, 17:3802-3805, 2006.

One further publication is mentioned:

Franzl et al. 2004 Exciton Recycling in Graded Gap Nanocrystal Structures.
T. Franzl, T. A. Klar, S. Schietinger, A. L. Rogach, and J. Feldmann. *Nano Letters*. 4:1599, 2004.

Conference Proceedings

Plasmonic-photonic hybrid cavity for tailored light-matter coupling.
M. Barth, S. Schietinger, S. Fischer, J. Becker, N. Nüsse, T. Aichele, B. Löchel, C. Sönnichsen, and O. Benson. *Proceedings of SPIE* 7609, 76090B, 2010.

[3] Parts highlighted in: Diamond Photonics. I. Aharonovich, A. D. Greentree, and S. Prawer. *Nature Photonics*, 5:397–405, 2011.

Room-temperature single-photon sources: design, performance, and applications.
M. Barth, D. Höckel, L. Koch, S. Schietinger, T. Schröder, T. Aichele, and O. Benson. *Proceedings of SPIE* 7681, 76810I, 2010.

Plasmon-enhanced single photon emission from a nano-assembled metal-diamond hybrid structure.
S. Schietinger, M. Barth, T. Schröder, T. Aichele, O. Benson. *Conference on Lasers and Electro-Optics & Quantum electronics and Laser Science Conference.*

One-by-one coupling of single photon emitters to high-Q modes of optical microresonators.
S. Schietinger, T. Schröder, and O. Benson. *Proceedings of SPIE* 7211, 72110K, 2009.

Bibliography

[1] J. L. Hennessy and N. P. Jouppi. Computer technology and architecture: An evolving interaction. *Computer*, 24(9):18–29, 1991.

[2] K. Kendall. Adhesion: molecules and mechanics. *Science*, 263(5154):1720, 1994.

[3] E. Abbé. Beiträge zur Theorie des Mikroskops und der mikroskopischen Wahrnehmung. *Archiv für mikroskopische Anatomie*, 9(1):413–418, 1873.

[4] C. B. Murray, D. J. Norris, and M. G. Bawendi. Synthesis and characterization of nearly monodisperse CdE (E= sulfur, selenium, tellurium) semiconductor nanocrystallites. *Journal of the American Chemical Society*, 115(19):8706–8715, 1993.

[5] Y. Sun and Y. Xia. Shape-controlled synthesis of gold and silver nanoparticles. *Science*, 298(5601):2176, 2002.

[6] S. Heer, K. Kömpe, H. U. Güdel, and M. Haase. Highly Efficient Multicolour Upconversion Emission in Transparent Colloids of Lanthanide-Doped $NaYF_4$ Nanocrystals. *Advanced Materials*, 16(23-24):2102–2105, 2004.

[7] M. A. Herman and H. Sitter. *Molecular beam epitaxy: fundamentals and current status*. Springer-Verlag Berlin, 1989.

[8] Y. Xia and G. M. Whitesides. Soft lithography. *Annual review of materials science*, 28(1):153–184, 1998.

[9] C. L. Haynes and R. P. Van Duyne. Nanosphere lithography: a versatile nanofabrication tool for studies of size-dependent nanoparticle optics. *Journal of Physical Chemistry B*, 105(24):5599–5611, 2001.

[10] R. Ito and S. Okazaki. Pushing the limits of lithography. *Nature*, 406(6799): 1027–1031, 2000.

[11] S. Matsui. Three-dimensional nanostructure fabrication by focused ion beam chemical vapor deposition. *Springer Handbook of Nanotechnology*, pages 211–229, 2010.

[12] C. A. Volkert and A. M. Minor. Focused ion beam microscopy and micromachining. *MRS bulletin*, 32(05):389–399, 2007.

[13] Dieter Bimberg, editor. *Semiconductor Nanostructures*, volume XXII. Springer Verlag, 2008. ISBN 3540778985.

[14] L. Novotny and B. Hecht. *Principles of Nano-Optics*. Cambridge Univ Pr, 2006.

[15] P.N. Prasad. *Nanophotonics*. LibreDigital, 2004.

[16] M. Ohtsu. *Nanophotonics and Nanofabrication*. Wiley-VCH Pub, 2009.

[17] C. J. Hood, T. W. Lynn, A. C. Doherty, A. S. Parkins, and H. J. Kimble. The atom-cavity microscope: single atoms bound in orbit by single photons. *Science*, 287(5457):1447, 2000.

[18] B. Darquié, M. P. A. Jones, J. Dingjan, J. Beugnon, S. Bergamini, Y. Sortais, G. Messin, A. Browaeys, and P. Grangier. Controlled single-photon emission from a single trapped two-level atom. *Science*, 309(5733):454, 2005.

[19] J. McKeever, A. Boca, A. D. Boozer, R. Miller, J. R. Buck, A. Kuzmich, and H. J. Kimble. Deterministic generation of single photons from one atom trapped in a cavity. *Science*, 303(5666):1992, 2004.

[20] S. A. Empedocles, D. J. Norris, and M. G. Bawendi. Photoluminescence spectroscopy of single CdSe nanocrystallite quantum dots. *Physical Review Letters*, 77 (18):3873–3876, 1996.

[21] T. D. Krauss and L. E. Brus. Charge, polarizability, and photoionization of single semiconductor nanocrystals. *Physical Review Letters*, 83(23):4840–4843, 1999.

[22] P. Michler, A. Kiraz, C. Becher, W. V. Schoenfeld, P. M. Petroff, L. Zhang, E. Hu, and A. Imamoğlu. A Quantum Dot Single-Photon Turnstile Device. *Science*, 290 (5500):2282, 2000.

[23] G. Messin, J. P. Hermier, E. Giacobino, P. Desbiolles, and M. Dahan. Bunching and antibunching in the fluorescence of semiconductor nanocrystals. *Optics Letters*, 26(23):1891–1893, 2001.

[24] T. Basché, W. E. Moerner, M. Orrit, and H. Talon. Photon antibunching in the fluorescence of a single dye molecule trapped in a solid. *Physical Review Letters*, 69(10):1516–1519, 1992.

[25] L. Fleury, J. M. Segura, G. Zumofen, B. Hecht, and U. P. Wild. Nonclassical photon statistics in single-molecule fluorescence at room temperature. *Physical Review Letters*, 84(6):1148–1151, 2000.

[26] I. Gerhardt, G. Wrigge, P. Bushev, G. Zumofen, M. Agio, R. Pfab, and V. Sandoghdar. Strong extinction of a laser beam by a single molecule. *Physical Review Letters*, 98(3):33601, 2007.

[27] Y. Akahane, T. Asano, B.S. Song, and S. Noda. High-q photonic nanocavity in a two-dimensional photonic crystal. *Nature*, 425(6961):944–947, 2003.

[28] C. Sönnichsen, S. Geier, N. E. Hecker, G. Von Plessen, J. Feldmann, H. Ditlbacher, B. Lamprecht, J. R. Krenn, F. R. Aussenegg, V. Z. H. Chan, et al. Spectroscopy of single metallic nanoparticles using total internal reflection microscopy. *Applied Physics Letters*, 77:2949, 2000.

[29] T. Klar, M. Perner, S. Grosse, G. Von Plessen, W. Spirkl, and J. Feldmann. Surface-plasmon resonances in single metallic nanoparticles. *Physical Review Letters*, 80(19):4249–4252, 1998.

[30] F. Auzel. Upconversion processes in coupled ion systems. *Journal of Luminescence*, 45(1-6):341–345, 1990.

[31] F. Wang, D. Banerjee, Y. Liu, X. Chen, and X. Liu. Upconversion nanoparticles in biological labeling, imaging, and therapy. *Analyst*, 135(8):1839–1854, 2010.

[32] A. Shalav, B. S. Richards, T. Trupke, K. W. Krämer, and H. U. Güdel. Applications of $NaYF_4:Er^{3+}$ up-converting phosphors for enhanced near-infrared silicon solar cell response. *Applied Physics Letters*, 86:013505, 2005.

[33] Ed. B. Sanders, P. Grangier, and J. Vučković. Focus on Single Photons on Demand. *New Journal of Physics*, 6, 2004.

[34] F. Jelezko and J. Wrachtrup. Single defect centres in diamond: a review. *physica status solidi (a)*, 203(13):3207–3225, 2006.

[35] L. Childress, M. V. Gurudev Dutt, J. M. Taylor, A. S. Zibrov, F. Jelezko, J. Wrachtrup, P. R. Hemmer, and M. D. Lukin. Coherent dynamics of coupled electron and nuclear spin qubits in diamond. *Science*, 314(5797):281, 2006.

[36] P. Meystre and M. Sargent. *Elements of quantum optics*. Springer Verlag, 2007.

[37] V. B. Braginsky, M. L. Gorodetsky, and V. S. Ilchenko. Quality-factor and nonlinear properties of optical whispering-gallery modes. *Physics Letters A*, 137(7-8): 393–397, 1989.

[38] J. R. Buck and H. J. Kimble. Optimal sizes of dielectric microspheres for cavity QED with strong coupling. *Physical Review A*, 67(3):33806, 2003.

[39] A. Mazzei, S. Götzinger, L. S. Menezes, G. Zumofen, O. Benson, and V. Sandoghdar. Controlled Coupling of Counterpropagating Whispering-Gallery Modes by a Single Rayleigh Scatterer: A Classical Problem in a Quantum Optical Light. *Physical Review Letters*, 99:173603, 2007.

[40] Y. S. Park, A. K. Cook, and H. Wang. Cavity QED with diamond nanocrystals and silica microspheres. *Nano Letters*, 6:2075–2079, 2006.

[41] I. Teraoka and S. Arnold. Enhancing the sensitivity of a whispering-gallery mode microsphere sensor by a high-refractive-index surface layer. *Journal of the Optical Society of America B*, 23(7):1434–1441, 2006.

[42] F. Vollmer and S. Arnold. Whispering-gallery-mode biosensing: label-free detection down to single molecules. *Nature Methods*, 5(7):591–596, 2008.

[43] M. Gregor, C. Pyrlik, R. Henze, A. Wicht, A. Peters, and O. Benson. An alignment-free fiber-coupled microsphere resonator for gas sensing applications. *Applied Physics Letters*, 96:231102, 2010.

[44] P. Anger, P. Bharadwaj, and L. Novotny. Enhancement and Quenching of Single-Molecule Fluorescence. *Physical Review Letters*, 96(11):113002, 2006.

[45] F. Kaminski, V. Sandoghdar, and M. Agio. Finite-Difference Time-Domain Modeling of Decay Rates in the Near Field of Metal Nanostructures. *Journal of Computational and Theoretical Nanoscience*, 4(3):635–643, 2007.

[46] K. Drexhage. Influence of a dielectric interface on fluorescence decay time. *Journal of Luminescence*, 1:693–701, 1970.

[47] P. Goy, J. M. Raimond, M. Gross, and S. Haroche. Observation of cavity-enhanced single-atom spontaneous emission. *Physical Review Letters*, 50(24):1903–1906, 1983.

[48] F. De Martini, G. Innocenti, G. R. Jacobovitz, and P. Mataloni. Anomalous spontaneous emission time in a microscopic optical cavity. *Physical Review Letters*, 59(26):2955, 1987.

[49] E. Fermi. Quantum theory of radiation. *Reviews of Modern Physics*, 4(1):87–132, 1932.

[50] W. L. Barnes. Topical review. Fluorescence near interfaces: the role of photonic mode density. *Journal of Modern Optics*, 45(4):661–699, 1998.

[51] H. Morawitz. Self-coupling of a two-level system by a mirror. *Physical Review*, 187(5):1792–1796, 1969.

[52] Y. Xu, R. K. Lee, and A. Yariv. Quantum analysis and the classical analysis of spontaneous emission in a microcavity. *Physical Review A*, 61(3):33807, 2000.

[53] Y. Xu, R. K. Lee, and A. Yariv. Finite-difference time-domain analysis of spontaneous emission in a microdisk cavity. *Physical Review A*, 61(3):33808, 2000.

[54] L. Rogobete, F. Kaminski, M. Agio, and V. Sandoghdar. Design of plasmonic nanoantennae for enhancing spontaneous emission. *Optics Letters*, 32(12):1623–1625, 2007.

[55] J. D. Jackson. *Classical Electrodynamics*. Wiley and Sons, Inc., 3 edition, 1998.

[56] E. M. Purcell. Spontaneous emission probabilities at radio frequencies. *Physical Review*, 69(681):166, 1946.

[57] J. W. S. Rayleigh. *The theory of sound: in two volumes*. Macmillan, 1878.

[58] A. Kuhlicke, M. Barth, and S. Schietinger. Observation of Whispering Gallery Modes in the Befreiungshalle at Kelheim. unpublished, 2007.

[59] A. E. Bate. Note on the whispering gallery of St Paul's Cathedral, London. *Proceedings of the Physical Society*, 50:293–297, 1938.

[60] S. Schiller. Asymptotic expansion of morphological resonance frequencies in Mie scattering. *Applied Optics*, 32(12):2181, 1993.

[61] M. L. Gorodetsky and V. S. Ilchenko. High-Q optical whispering-gallery microresonators: precession approach for spherical mode analysis and emission patterns with prism couplers. *Optics Communications*, 113:133–143, 1994.

[62] G. Mie. Beiträge zur Optik trüber Medien, speziell kolloidaler Metallösungen. *Annalen der Physik*, 25(4):377–445, 1908.

[63] C. F. Bohren and D. R. Huffman. *Absorption and Scattering of Light by Small Particles*. John Wiley & Sons Inc, 1998.

[64] B. M. Möller, U. Woggon, and M. V. Artemyev. Bloch modes and disorder phenomena in coupled resonator chains. *Physical Review B*, 75(24):245327, 2007.

[65] M. L. Gorodetsky, A. A. Savchenkov, V. S. Ilchenko, et al. Ultimate Q of optical microsphere resonators. *Optics Letters*, 21(7):453–455, 1996.

[66] H. M. Tzeng, K. F. Wall, M. B. Long, and R. K. Chang. Laser emission from individual droplets at wavelengths corresponding to morphology-dependent resonances. *Optics Letters*, 9(11):499–501, 1984.

[67] J. Schäfer, J. P. Mondia, R. Sharma, Z. H. Lu, A. S. Susha, A. L. Rogach, and L. J. Wang. Quantum dot microdrop laser. *Nano Letters*, 8(6):1709–1712, 2008.

[68] M. Kuwata-Gonokami and K. Takeda. Polymer whispering gallery mode lasers. *Optical Materials*, 9(1-4):12–17, 1998.

[69] V. Sandoghdar, F. Treussart, J. Hare, V. Lefevre-Seguin, J. M. Raimond, and S. Haroche. Very low threshold whispering-gallery-mode microsphere laser. *Physical Review A*, 54(3):1777–1780, 1996.

[70] S. I. Shopova, G. Farca, A. T. Rosenberger, W. M. S. Wickramanayake, and N. A. Kotov. Microsphere whispering-gallery-mode laser using HgTe quantum dots. *Applied Physics Letters*, 85:6101, 2004.

[71] T. Mukaiyama, K. Takeda, H. Miyazaki, Y. Jimba, and M. Kuwata-Gonokami. Tight-Binding Photonic Molecule Modes of Resonant Bispheres. *Physical Review Letters*, 82(23):4623–4626, Jun 1999.

[72] B. M. Möller, U. Woggon, and M. V. Artemyev. Coupled-resonator optical waveguides doped with nanocrystals. *Optics Letters*, 30(16):2116–2118, 2005.

[73] N. Le Thomas, U. Woggon, O. Schöps, M. V. Artemyev, M. Kazes, and U. Banin. Cavity QED with semiconductor nanocrystals. *Nano Letters*, 6(3):557–561, 2006.

[74] D. S. Weiss, V. Sandoghdar, J. Hare, V. Lefevre-Seguin, J. M. Raimond, and S. Haroche. Splitting of high-Q Mie modes induced by light backscattering in silica microspheres. *Optics Letters*, 20(18):1835–1837, 1995.

[75] D. D. Smith, H. Chang, K. A. Fuller, A. T. Rosenberger, and R. W. Boyd. Coupled-resonator-induced transparency. *Physical Review A*, 69(6):063804, Jun 2004.

[76] P. Mühlschlegel, H. J. Eisler, O. J. F. Martin, B. Hecht, and D. W. Pohl. Resonant optical antennas. *Science*, 308(5728):1607, 2005.

[77] L. Novotny. Effective wavelength scaling for optical antennas. *Physical Review Letters*, 98(26):266802, 2007.

[78] M. Fleischmann, P. J. Hendra, and A. J. McQuillan. Raman spectra of pyridine adsorbed at a silver electrode. *Chemical Physics Letters*, 26:163–166, 1974.

[79] M. Moskovits. Surface-enhanced spectroscopy. *Reviews of Modern Physics*, 57(3): 783–826, 1985.

[80] K. Kneipp, Y. Wang, H. Kneipp, L. T. Perelman, I. Itzkan, R. R. Dasari, and M. S. Feld. Single molecule detection using surface-enhanced Raman scattering (SERS). *Physical Review Letters*, 78(9):1667–1670, 1997.

[81] S. Nie and S. R. Emory. Probing single molecules and single nanoparticles by surface-enhanced Raman scattering. *Science*, 275(5303):1102, 1997.

[82] C. K. Chen, A. R. B. De Castro, and Y. R. Shen. Surface-enhanced second-harmonic generation. *Physical Review Letters*, 46(2):145–148, 1981.

[83] K. H. Drexhage, H. Kuhn, and F. P. Schäfer. Variation of Fluorescence Decay Time of a Molecule in front of a Mirror. *Berichte der Bunsen-Gesellschaft für physikalische Chemie*, 72(2):329, 1968.

[84] C. K. Carniglia, L. Mandel, and K. H. Drexhage. Absorption and emission of evanescent photons. *Journal of the Optical Society of America*, 62(4):479–486, 1972.

[85] A. M. Glass, P. F. Liao, J. G. Bergman, and D. H. Olson. Interaction of metal particles with adsorbed dye molecules: absorption and luminescence. *Optics Letters*, 5(9):368, 1980.

[86] H. Metiu. Surface Enhanced Spectroscopy. *Progress in Surface Science*, 17(3): 153–320, 1984.

[87] K. Sokolov, G. Chumanov, and T. M. Cotton. Enhancement of molecular fluorescence near the surface of colloidal metal films. *analytical chemistry*, 70(18): 3898–3905, 1998.

[88] J. H. Song, T. Atay, S. Shi, H. Urabe, and A. V. Nurmikko. Large enhancement of fluorescence efficiency from CdSe/ZnS quantum dots induced by resonant coupling to spatially controlled surface plasmons. *Nano Letters*, 5(8):1557–1561, 2005.

[89] J. R. Lakowicz. Radiative decay engineering: biophysical and biomedical applications. *Analytical Biochemistry*, 298(1):1–24, 2001.

[90] E. Dulkeith, A. C. Morteani, T. Niedereichholz, T. A. Klar, J. Feldmann, S. A. Levi, F. C. van Veggel, D. N. Reinhoudt, M. Möller, and D. I. Gittins. Fluorescence Quenching of Dye Molecules near Gold Nanoparticles: Radiative and Nonradiative Effects. *Physical Review Letters*, 89:20, 2002.

[91] J. R. Lakowicz. Radiative decay engineering 3. Surface plasmon-coupled directional emission. *Analytical Biochemistry*, 324(2):153–169, 2004.

[92] P. P. Pompa, L. Martiradonna, A. Della Torre, F. Della Sala, L. Manna, M. De Vittorio, F. Calabi, R. Cingolani, and R. Rinaldi. Metal-enhanced fluorescence of colloidal nanocrystals with nanoscale control. *Nature Nanotechnology*, 1:126–130, 2006.

[93] X. Chen, Z. Song, J. Zhang, L. Hu, L. Wen, C. Wang, and S. Li. Analysis on fluorescence intensity reverse photonic phenomenon between red and green fluorescence of oxyfluoride nanophase vitroceramics. *Optics Express*, 15(20):13421–13433, 2007.

[94] K. Kopitzki. *Einführung in die Festkörperphysik*. Teubner, Stuttgart, 15 edition, 1993.

[95] S. A. Maier. *Plasmonics: Fundamentals and Applications*. Springer Verlag, 2007.

[96] A. Vial, A. S. Grimault, D. Macías, D. Barchiesi, and M. L. de La Chapelle. Improved analytical fit of gold dispersion: Application to the modeling of extinction spectra with a finite-difference time-domain method. *Physical Review B*, 71(8): 85416, 2005.

[97] H. Raether. *Surface plasmons on smooth and rough surfaces and on gratings*. Springer-Verlag Berlin, 1988.

[98] J. A. Schuller, E. S. Barnard, W. Cai, Y. C. Jun, J. S. White, and M. L. Brongersma. Plasmonics for extreme light concentration and manipulation. *Nature Materials*, 9(3):193–204, 2010.

[99] P. B. Johnson and R. W. Christy. Optical constants of the noble metals. *Physical Review B*, 6(12):4370–4379, 1972.

[100] S. Tretyakov. On geometrical scaling of split-ring and double-bar resonators at optical frequencies. *Metamaterials*, 1(1):40–43, 2007.

[101] U. Kreibig and M. Vollmer. Optical properties of metal clusters. 1995.

[102] S. Link and M. A. Ei-Sayed. Optical properties and ultrafast dynamics of metallic nanocrystals. *Annual Review of Physical Chemistry*, 54:331–366, 2003.

[103] L. B. Scaffardi and J. O. Tocho. Size dependence of refractive index of gold nanoparticles. *Nanotechnology*, 17:1309, 2006.

[104] J. J. Mock, M. Barbic, D. R. Smith, D. A. Schultz, and S. Schultz. Shape effects in plasmon resonance of individual colloidal silver nanoparticles. *Journal of Chemical Physics*, 116:6755, 2002.

[105] H. Kuwata, H. Tamaru, K. Esumi, and K. Miyano. Resonant light scattering from metal nanoparticles: Practical analysis beyond Rayleigh approximation. *Applied Physics Letters*, 83:4625, 2003.

[106] K. H. Su, Q. H. Wei, X. Zhang, J. J. Mock, D. R. Smith, and S. Schultz. Interparticle coupling effects on plasmon resonances of nanogold particles. *Nano Letters*, 3(8):1087–1090, 2003.

[107] J. Merlein, M. Kahl, A. Zuschlag, A. Sell, A. Halm, J. Boneberg, P. Leiderer, A. Leitenstorfer, and R. Bratschitsch. Nanomechanical control of an optical antenna. *Nature Photonics*, 2(4):230, 2008.

[108] K. L. Kelly, E. Coronado, L. L. Zhao, and G. C. Schatz. The optical properties of metal nanoparticles: the influence of size, shape, and dielectric environment. *Journal of Physical Chemistry B*, 107(3):668–677, 2003.

[109] W. Rechberger, A. Hohenau, A. Leitner, JR Krenn, B. Lamprecht, and F. R. Aussenegg. Optical properties of two interacting gold nanoparticles. *Optics Communications*, 220(1-3):137–141, 2003.

[110] A. Bek, R. Jansen, M. Ringler, S. Mayilo, T. A. Klar, and J. Feldmann. Fluorescence Enhancement in Hot Spots of AFM-Designed Gold Nanoparticle Sandwiches. *Nano Letters*, 8(2):485–490, 2008.

[111] A. J. Haes, S. Zou, G. C. Schatz, and R. P. Van Duyne. Nanoscale optical biosensor: short range distance dependence of the localized surface plasmon resonance of noble metal nanoparticles. *Journal of Physical Chemistry B*, 108(22):6961–6968, 2004.

[112] A. Kinkhabwala, Z. Yu, S. Fan, Y. Avlasevich, K. Müllen, and Moerner W. E. Large single-molecule fluorescence enhancements produced by a bowtie nanoantenna. *Nature Photonics*, 3(11):654–657, 2009.

[113] G. T. Boyd, T. Rasing, J. R. R. Leite, and Y. R. Shen. Local-field enhancement on rough surfaces of metals, semimetals, and semiconductors with the use of optical second-harmonic generation. *Physical Review B*, 30(2):519–526, 1984.

[114] K. S. Yee. Numerical solution of initial boundary value problems involving Maxwell's equations in isotropic media. *IEEE Trans. Antennas Propagat*, 14(3): 302–307, 1966.

[115] *FDTD Solutions* . Lumerical Solutions, Inc. URL `http://www.lumerical.com/fdtd.php`.

[116] R. Ruppin. Decay of an excited molecule near a small metal sphere. *Journal of Chemical Physics*, 76:1681, 1982.

[117] H. Chew. Transition rates of atoms near spherical surfaces. *Journal of Chemical Physics*, 87:1355, 1987.

[118] S. Kühn, U. Håkanson, L. Rogobete, and V. Sandoghdar. Enhancement of Single-Molecule Fluorescence Using a Gold Nanoparticle as an Optical Nanoantenna. *Physical Review Letters*, 97(1):17402, 2006.

[119] Robert H. Webb. Confocal optical microscopy. *Reports on Progress in Physics*, 59:427–471, 1996.

[120] J. B. Pawley and B. R. Masters. Handbook of biological confocal microscopy. *Journal of Biomedical Optics*, 13:029902, 2008.

[121] Felix Müller. Detektion und Manipulation nanoskopischer Partikel mittels Nahfeld- und Fluoreszenzmikroskopie. Diplomarbeit, Humboldt-Universität zu Berlin, Institut für Physik, AG Nano-Optik, 2003.

[122] R. Hanbury Brown and R. Q. Twiss. A test of a new type of stellar interferometer on Sirius. *Nature*, 178:1046, 1956.

[123] G. K. Liu and B. Jacquier. *Spectroscopic properties of rare earths in optical materials*. Springer Verlag, 2005.

[124] G. Binnig, H. Rohrer, C. Gerber, and E. Weibel. Tunneling through a controllable vacuum gap. *Applied Physics Letters*, 40:178, 1982.

[125] G. Binnig, C. F. Quate, and C. Gerber. Atomic Force Microscope. *Physical Review Letters*, 56(9):930–933, 1986.

[126] Wikipedia. Scanning probe microscopy — Wikipedia, The Free Encyclopedia. `http://en.wikipedia.org/w/index.php?title=Scanning_probe_microscopy&oldid=362980465`, 2010. [Online; accessed 24-May-2010].

[127] F. J. Giessibl. Advances in atomic force microscopy. *Reviews of modern physics*, 75(3):949–983, 2003.

[128] M. Radmacher, R. W. Tillamnn, M. Fritz, and H. E. Gaub. From molecules to cells: imaging soft samples with the atomic force microscope. *Science*, 257(5078): 1900, 1992.

[129] J. K. H. Horber and M. J. Miles. Scanning probe evolution in biology. *Science*, 302(5647):1002, 2003.

[130] D. M. Eigler and E. K. Schweizer. Positioning single atoms with a scanning tunnelling microscope. *Nature*, 344(6266):524–526, 1990.

[131] J. A. Stroscio and D. M. Eigler. Atomic and molecular manipulation with the scanning tunneling microscope. *Science*, 254(5036):1319, 1991.

[132] T. Junno, K. Deppert, L. Montelius, and L. Samuelson. Controlled manipulation of nanoparticles with an atomic force microscope. *Applied Physics Letters*, 66: 3627, 1995.

[133] R. D. Piner, J. Zhu, F. Xu, S. Hong, and C. A. Mirkin. "Dip-pen" nanolithography. *Science*, 283(5402):661, 1999.

[134] S. K. Kufer, E. M. Puchner, H. Gumpp, T. Liedl, and H. E. Gaub. Single-Molecule Cut-and-Paste Surface Assembly. *Science*, 319(5863):594, 2008.

[135] E. Betzig, P. L. Finn, and J. S. Weiner. Combined shear force and near-field scanning optical microscopy. *Applied Physics Letters*, 60:2484, 1992.

[136] N. G. Connelly et al. *Nomenclature of inorganic chemistry: IUPAC recommendations 2005*. Royal Society of Chemistry Publishing/IUPAC,., 2005.

[137] G. H. Dieke. *Spectra and Energy Levels of Rare Earth Ions in Crystals*. Interscience Publishers, New York, 1968.

[138] B. G. Wybourne. The fascination of the rare earths – then, now and in the future. *Journal of Alloys and Compounds*, 380(1-2):96–100, 2004.

[139] B. G. Wybourne. *Spectroscopic properties of rare earths*. Interscience Publishers, 1965.

[140] D. R. Lide. *CRC handbook of chemistry and physics: a ready-reference book of chemical and physical data*. CRC press, 2004.

[141] C.G. Mosander. Über die das Cerium begleitenden neuen Metalle Lanthanium und Didymium, so wie über die mit der Ytterede vorkommenden neuen Metalle Erbium und Terbium. *Annalen der Physik und Chemie*, 136(10), 1843.

[142] G. Urbain. Lutetium und Neoytterbium oder Cassiopeium und Aldebaranium. *Monatshefte für Chemie/Chemical Monthly*, 31(10), 1910.

[143] W. M. Yen, S. Shionoya, H. Yamamoto, P. Paillet, L. Demkowicz, R. James, P. S. Philippe, J. A. Felix, J. L. Autran, D. Henderson, et al. *Phosphor handbook*. Springer-Verlag, 2006.

[144] M. H. V. Werts. Making sense of lanthanide luminescence. *Science Progress*, 88 (2):101–131, 2005.

[145] J. H. van Vleck. The puzzle of rare-earth spectra in solids. *Journal of Physical Chemistry*, 41:67–80, 1937.

[146] B. R. Judd. Optical absorption intensities of rare-earth ions. *Physical Review*, 127 (3):750–761, 1962.

[147] G. S. Ofelt. Intensities of crystal spectra of rare-earth ions. *Journal of Chemical Physics*, 37(3):511–520, 1962.

[148] B. M. Walsh. Judd-Ofelt Theory: Principles and Practices. In B. di Bartolo and O. Forte, editors, *Advances in Spectroscopy for Lasers and Sensing*, chapter I. Springer London, 2006.

[149] L. Smentek. Theoretical Description of the Spectroscopic Properties of Rare Earth Ions in Crystals. *Physics Reports*, 297(4):155–237, 1998.

[150] M. J. Weber. Selective excitation and decay of Er^{3+} fluorescence in LaF_3. *Physical Review*, 156:231–241, 1967.

[151] W. D. Partlow and H. W. Moos. Multiphonon Relaxation in LaCl_3:Nd^{3+}. *Physical Review*, 157:252, 1967.

[152] M. J. Weber. Probabilities for radiative and nonradiative decay of Er^{3+} in LaF_3. *Physical Review*, 157(2):262–72, 1967.

[153] L. A. Riseberg and H. W. Moos. Multiphonon Orbit-Lattice Relaxation of Excited States of Rare-Earth Ions in Crystals. *Physical Review*, 174(2):429–438, 1968.

[154] M. F. H. Schuurmans and J. M. F. van Dijk. On radiative and non-radiative decay times in the weak coupling limit. *Physica, B+C*, 123(2):131–155, 1984.

[155] T. Miyakawa and D. L. Dexter. Phonon Sidebands, Multiphonon Relaxation of Excited States, and Phonon-Assisted Energy Transfer between Ions in Solids. *Physical Review B*, 1(7):2961–2969, 1970.

[156] K. K. Pukhov and V. P. Sakun. Theory of nonradiative multiphonon transitions in impurity centers with extremely weak electron-phonon coupling. *physica status solidi (b)*, 95(2), 1979.

[157] K. Huang and A. Rhys. Theory of light absorption and non-radiative transitions in F-centres. *Proceedings of the Royal Society of London. Series A, Mathematical and Physical Sciences*, pages 406–423, 1950.

[158] F. Auzel and Y. H. Chen. The effective frequency in multiphonon processes: Differences for energy transfers or side-bands and non-radiative decay. *Journal of Luminescence*, 66:224–227, 1996.

[159] F. Auzel and F. Pellé. Bottleneck in multiphonon nonradiative transitions. *Physical Review B*, 55(17):11006–11009, 1997.

[160] L. S. Menezes, G. S. Maciel, C. B. de Araújo, and Y. Messaddeq. Thermally enhanced frequency upconversion in Nd^{3+}-doped fluoroindate glass. *Journal of Applied Physics*, 90:4498, 2001.

[161] L. S. Menezes, G. S. Maciel, C. B. de Araújo, and Y. Messaddeq. Phonon-assisted cooperative energy transfer and frequency upconversion in a Yb^{3+}/Tb^{3+} codoped fluoroindate glass. *Journal of Applied Physics*, 94:863, 2003.

[162] F. Auzel and F. Pellé. Concentration and excitation effects in multiphonon nonradiative transitions of rare-earth ions. *Journal of Luminescence*, 69(5-6):249–255, 1996.

[163] F. Pellé, N. Gardant, F. Auzel, and G.O. des Terres Rares. Saturation effect on multiphonon relaxation rates. *Journal of Alloys and Compounds*, 275:430–434, 1998.

[164] F. Pellé and F. Auzel. Saturation of multiphonon relaxation rates of rare-earth ions in glasses and phonon localization in disordered structures. *Journal of Luminescence*, 87:598–600, 2000.

[165] E. Gutsche. Non-Condon Approximations and the Static Approach in the Theory of Non-Radiative Multiphonon Transitions. *physica status solidi (b)*, 109(2), 1982.

[166] R. Scheps. Upconversion laser processes. *Progress in Quantum Electronics*, 20(2): 271–358, 1996.

[167] F. Auzel. Upconversion and Anti-Stokes Processes with f and d Ions in Solids. *Chemical Reviews*, 104:139–173, 2004.

[168] J. Suijver. *Luminescence: from theory to applications*, chapter 6, pages 133–194. Wiley-VCH Weinheim, 2008.

[169] G. Yi, H. Lu, S. Zhao, Y. Ge, W. Yang, D. Chen, and L. H. Guo. Synthesis, Characterization, and Biological Application of Size-Controlled Nanocrystalline

$NaYF_4$: Yb, Er Infrared-to-Visible Up-Conversion Phosphors. *Nano Letters*, 4: 2191–2196, 2004.

[170] S. F. Lim, R. Riehn, W. S. Ryu, N. Khanarian, C. Tung, D. Tank, and R. H. Austin. In Vivo and Scanning Electron Microscopy Imaging of Upconverting Nanophosphors in Caenorhabditis. *Nano Letters*, 6(2):169–174, 2006.

[171] M. L. F. Phillips, M. P. Hehlen, K. Nguyen, J. M. Sheldon, and N. J. Cockroft. Upconversion phosphors: Recent advances and new applications. In *Physics and Chemistry of Luminescent Materials: Proceedings of the Eighth International Symposium*. Electrochemical Society, 2000.

[172] E. Downing, L. Hesselink, J. Ralston, and R. Macfarlane. A Three-Color, Solid-State, Three-Dimensional Display. *Science*, 273(5279):1185–1189, 1996.

[173] L. Aiguoy, G. Tessier, M. Mortier, and B. Charlot. Scanning thermal imaging of microelectronic circuits with a fluorescent nanoprobe. *Applied Physics Letters*, 87: 184105, 2005.

[174] M. F. Joubert. Photon avalanche upconversion in rare earth laser materials. *Optical Materials*, 11(2-3):181–203, 1999.

[175] S. Götzinger, L. S. Menezes, A. Mazzei, S. Kühn, V. Sandoghdar, and O. Benson. Controlled Photon Transfer between Two Individual Nanoemitters via Shared High-Q Modes of a Microsphere Resonator. *Nano Letters*, 6(6):1151–1154, 2006.

[176] T. Förster. Zwischenmolekulare Energiewanderung und Fluoreszenz. *Annalen der Physik*, 2:55, 1948.

[177] T. Franzl, T. A. Klar, S. Schietinger, A. L. Rogach, and J. Feldmann. Exciton recycling in graded gap nanocrystal structures. *Nano Letters*, 4(9):1599–1604, 2004.

[178] M. Achermann, M. A. Petruska, S. Kos, D. L. Smith, D. D. Koleske, and V. I. Klimov. Energy-transfer pumping of semiconductor nanocrystals using an epitaxial quantum well. *Nature*, 429:642–646, 2004.

[179] E. Nakazawa and S. Shionoya. Energy Transfer between Trivalent Rare-Earth Ions in Inorganic Solids. *Journal of Chemical Physics*, 47:3211, 1967.

[180] C. Eggeling, P. Kask, D. Winkler, and S. Jäger. Rapid analysis of Förster resonance energy transfer by two-color global fluorescence correlation spectroscopy: trypsin proteinase reaction. *Biophysical Journal*, 89(1):605–618, 2005.

[181] P. G. Wu and L. Brand. Resonance energy transfer: methods and applications. *Analytical Biochemistry*, 218(1):1–13, 1994.

[182] J. Michaelis, C. Hettich, J. Mlynek, and V. Sandoghdar. Optical microscopy using a single-molecule light source. *Nature*, 405(6784):325–328, 2000.

[183] F. Müller, S. Götzinger, N. Gaponik, H. Weller, J. Mlynek, and O. Benson. Investigation of Energy Transfer between CdTe Nanocrystals on Polystyrene Beads and Dye Molecules for FRET-SNOM Applications. *Journal of Physical Chemistry B*, 108:14527–14534, 2004.

[184] D. L. Dexter. A theory of sensitized luminescence in solids. *Journal of Chemical Physics*, 21:836, 1953.

[185] F. Auzel. Multiphonon-assisted anti-Stokes and Stokes fluorescence of triply ionized rare-earth ions. *Physical Review B*, 13(7):2809–2817, 1976.

[186] J. S. Chivian, W. E. Case, and D. D. Eden. The photon avalanche: A new phenomenon in Pr-based infrared quantum counters. *Applied Physics Letters*, 35: 124, 1979.

[187] F. Auzel. Compteur quantique par transfert d'energie de Yb^{3+} à Tm^{3+} dans un tungstate mixte et dans un verre germanate. *Comptes Rendus Hebdomadaires des Seances de l'Academie des Sciences*, 263b(14):819, 1966.

[188] M. Pollnau, D. R. Gamelin, S. R. Lüthi, H. U. Güdel, and M. P. Hehlen. Power dependence of upconversion luminescence in lanthanide and transition-metal-ion systems. *Physical Review B*, 61(5):3337–3346, 2000.

[189] J. H. Zeng, J. Su, Z. H. Li, R. X. Yan, and Y. D. Li. Synthesis and upconversion luminescence of hexagonal-phase $NaYF_4$: Yb, Er^{3+} phosphors of controlled size and morphology. *Advanced Materials*, 17(17):2119–2123, 2005.

[190] F. Wang, D. K. Chatterjee, Z. Li, Y. Zhang, X. Fan, and M. Wang. Synthesis of polyethylenimine/$NaYF4_4$ nanoparticles with upconversion fluorescence. *Nanotechnology*, 17(23):5786–5791, 2006.

[191] J. Shan, X. Qin, N. Yao, and Y. Ju. Synthesis of monodisperse hexagonal $NaYF_4$: Yb, Ln (Ln= Er, Ho and Tm) upconversion nanocrystals in TOPO. *Nanotechnology*, 18(44):445607, 2007.

[192] J. C. Boyer, F. Vetrone, L. A. Cuccia, and J. A. Capobianco. Synthesis of Colloidal Upconverting $NaYF_4$ Nanocrystals Doped with Er^{3+}, Yb^{3+} and Tm^{3+}, Yb^{3+} via Thermal Decomposition of Lanthanide Trifluoroacetate Precursors. *Journal of the American Chemical Society*, 128(23):7444–7445, 2006.

[193] J. C. Boyer, L. A. Cuccia, and J. A. Capobianco. Synthesis of Colloidal Upconverting $NaYF_4$: Er^{3+}/Yb^{3+} and Tm^{3+}/Yb^{3+} Monodisperse Nanocrystals. *Nano Letters*, 7(3):847–852, 2007.

[194] O. Ehlert, R. Thomann, M. Darbandi, and T. Nann. A Four-Color Colloidal Multiplexing Nanoparticle System. *ACS Nano*, 2(1):120–124, 2008.

[195] J. F. Suyver, J. Grimm, M. K. van Veen, D. Biner, K. W. Krämer, and H. U. Güdel. Upconversion spectroscopy and properties of $NaYF_4$ doped with Er^{3+}, Tm^{3+} and/or Yb^{3+}. *Journal of Luminescence*, 117(1):1–12, 2006.

[196] J. F. Suyver, A. Aebischer, D. Biner, P. Gerner, J. Grimm, S. Heer, K. W. Krämer, C. Reinhard, and H. U. Güdel. Novel materials doped with trivalent lanthanides and transition metal ions showing near-infrared to visible photon upconversion. *Optical Materials*, 27(6):1111–1130, 2005.

[197] J. F. Suyver, J.Grimm, K. W. Krämer, and H. U. Güdel. Highly effficient near-infrared to visible up-conversion process in $NaYF_4$:Er^{3+},Yb^{3+}. *Journal of Luminescence*, 114:53–59, 2005.

[198] Research group of Prof. Hans Ulrich Güdel. URL `http://www.dcb-server.unibe.ch/groups/guedel/start.html`.

[199] G. Chen, H. Liang, H. Liu, G. Somesfalean, and Z. Zhang. Near vacuum ultraviolet luminescence of Gd^{3+} and Er^{3+} ions generated by super saturation upconversion processes. *Optics Express*, 17:16366–16371, 2009.

[200] Dieter Bimberg, editor. *Semiconductor Nanostructures*, volume XXII. Springer Verlag, 2008. ISBN 3540778985.

[201] H. Schniepp and V. Sandoghdar. Spontaneous emission of europium ions embedded in dielectric nanospheres. *Physical Review Letters*, 89(25):257403, 2002.

[202] B. M. Tissue. Synthesis and Luminescence of Lanthanide Ions in Nanoscale Insulating Hosts. *Chemisty of Materials*, 10(10):2837–2845, 1998.

[203] W. Chen, J. O. Malm, V. Zwiller, R. Wallenberg, and J. O. Bovin. Size dependence of Eu^{2+} fluorescence in ZnS: Eu^{2+} nanoparticles. *Journal of Applied Physics*, 89: 2671, 2001.

[204] B. Mercier, C. Dujardin, G. Ledoux, C. Louis, O. Tillement, and P. Perriat. Observation of the gap blueshift on Gd_2O_3: Eu^{3+} nanoparticles. *Journal of Applied Physics*, 96:650, 2004.

[205] G. A. Hebbink, J. W. Stouwdam, D.N. Reinhoudt, and F. C. J. M. van Veggel. Lanthanide (III)-doped nanoparticles that emit in the near-infrared. *Advanced materials(Weinheim)*, 14(16), 2002.

[206] J. W. Stouwdam and F. Van Veggel. Improvement in the Luminescence properties and processability of LaF_3/Ln and $LaPO_4$/Ln Nanoparticles by surface modification. *Langmuir*, 20(26):11763–11771, 2004.

[207] Y. Wang, L. Tu, J. Zhao, Y. Sun, X. Kong, and H. Zhang. Upconversion Luminescence of β -$NaYF_4$: Yb^{3+}, Er^{3+}@β-$NaYF_4$ Core/Shell Nanoparticles: Excitation Power, Density and Surface Dependence. *Journal of Physical Chemistry C*, 113 (17):7164–7169, April 2009.

[208] M. Godlewski and D. Hommel. Eu^{2+} photocharge transfer processes in ZnS crystals determined by photo-ESR measurements. *physica status solidi (c)*, 95(1):261–268, 1986.

[209] G. K. Liu, H. Z. Zhuang, and X. Y. Chen. Restricted Phonon Relaxation and Anomalous Thermalization of Rare Earth Ions in Nanocrystals. *Nano Letters*, 2 (5):535–539, 2002.

[210] G. K. Liu, X. Y. Chen, H. Z. Zhuang, S. Li, and R. S. Niedbala. Confinement of electron-phonon interaction on luminescence dynamics in nanophosphors of Er^{3+}:Y_2O_2S. *Journal of Solid State Chemistry*, 171(1-2):123–132, 2003.

[211] L. Liu, E. Ma, R. Li, G. Liu, and X. Chen. Effects of phonon confinement on the luminescence dynamics of Eu^{3+} in Gd_2O_3 nanotubes. *Nanotechnology*, 18 (015403):015403, 2007.

[212] H. Song, B. Sun, T. Wang, S. Lu, L. Yang, B. Chen, X. Wang, and X. Kong. Three-photon upconversion luminescence phenomenon for the green levels in Er^{3+}/Yb^{3+} codoped cubic nanocrystalline yttria. *Solid State Communications*, 132(6):409–413, 2004.

[213] H. Richter, Z. P. Wang, and L. Ley. The One Phonon Raman Spectrum in Microcrystalline Silicon. *Solid State Communications*, 39(5):625–629, 1981.

[214] I. H. Campbell and P. M. Fauchet. The effects of microcrystal size and shape on the one phonon Raman spectra of crystalline semiconductors. *Solid State Communications*, 58(10):739–741, 1986.

[215] M. C. Klein, F. Hache, D. Ricard, and C. Flytzanis. Size dependence of electron-phonon coupling in semiconductor nanospheres: The case of CdSe. *Physical Review B*, 42(17):11123–11132, 1990.

[216] J. Zi, K. Zhang, and X. Xie. Comparison of models for Raman spectra of Si nanocrystals. *Physical Review B*, 55(15):9263–9266, 1997.

[217] F. Pellé and F. Auzel. Phonon bottleneck effect in multiphonon non-radiative transitions of rare-earth ions. *Journal of Luminescence*, 76:623–627, 1998.

[218] A. A. Balandin, E. P. Pokatilov, and D. L. Nika. Phonon Engineering in Hetero- and Nanostructures. *Journal of Nanoelectronics and Optoelectronics*, 2(2):140–170, 2007.

[219] T. Aisaka, M. Fujii, and S. Hayashi. Enhancement of upconversion luminescence of Er doped AlO films by Ag island films. *Applied Physics Letters*, 92:132105, 2008.

[220] L. R. P. Kassab, F. A. Bomfim, J. R. Martinelli, N.U. Wetter, J. J. Neto, and C. B. de Araújo. Energy transfer and frequency upconversion in Yb^{3+}–Er^{3+}-doped PbO-GeO_2 glass containing silver nanoparticles. *Applied Physics B: Lasers and Optics*, 94(2):239–242, 2009.

[221] V. K. Rai, L. S. Menezes, C. B. de Araújo, L. R. P. Kassab, D. M. da Silva, and R. A.Kobayashi. Surface-plasmon-enhanced frequency upconversion in Pr doped tellurium-oxide glasses containing silver nanoparticles. *Journal of Applied Physics*, 103:093526, 2008.

[222] E. Verhagen, L. Kuipers, and A. Polman. Enhanced nonlinear optical effects with a tapered plasmonic waveguide. *Nano Letters*, 7(2):334–337, 2007.

[223] E. Verhagen, L. Kuipers, and A. Polman. Field enhancement in metallic subwavelength aperture arrays probed by erbium upconversion luminescence. *Optics Express*, 17(17):14586–14598, 2009.

[224] R. Esteban, M. Laroche, and J. J. Greffet. Influence of metallic nanoparticles on upconversion processes. *Journal of Applied Physics*, 105(3):033107–033107, 2009.

[225] Research group of Prof. Thomas Nann,. URL `http://www.uea.ac.uk/che/people/faculty/nannt`.

[226] S. Schietinger, T. Aichele, H. Q. Wang, T. Nann, and O. Benson. Plasmon-Enhanced Upconversion in Single $NaYF_4$:Yb^{3+}/Er^{3+} Codoped Nanocrystals. *Nano Letters*, pages 271–358, 2010.

[227] A. Aebischer, M. Hostettler, J. Hauser, K. W. Krämer, T. Weber, H. U. Güdel, and H. B. Burgi. Structural and spectroscopic characterization of active sites in a family of light-emitting sodium lanthanide tetrafluorides. *Angewandte Chemie International Edition*, 45(17):2802–6, 2006.

[228] J. C. Maxwell. A dynamical theory of the electromagnetic field. *Philosophical Transactions of the Royal Society of London*, 155:459–512, 1865.

[229] M. Planck. Ueber das Gesetz der energieverteilung in Normalspectrum. *Annalen der Physik*, 4:553–563, 1901.

[230] A. Einstein. Über einen die Erzeugung und Verwandlung des Lichtes betreffenden heuristischen Gesichtspunkt. *Annalen der Physik*, 17(132):20, 1905.

[231] R. P. Feynman. The development of the space-time view of quantum electrodynamics. *Physics Today*, 19:31, 1966.

[232] C. H. Bennett, G. Brassard, et al. Quantum cryptography: Public key distribution and coin tossing. In *Proceedings of IEEE International Conference on Computers, Systems and Signal Processing*, volume 175, 1984.

[233] N. Gisin, G. Ribordy, W. Tittel, and H. Zbinden. Quantum cryptography. *Reviews of Modern Physics*, 74(1):145–195, 2002.

[234] E. Knill, R. Laflamme, and G. J. Milburn. A scheme for efficient quantum computation with linear optics. *Nature*, 409(6816):46–52, 2001.

[235] P. Walther, K. J. Resch, T. Rudolph, E. Schenck, H. Weinfurter, V. Vedral, M. Aspelmeyer, and A. Zeilinger. Experimental one-way quantum computing. *Nature*, 434(7030):169–176, 2005.

[236] M. Scholz. *New Light Sources for Quantum Information Processing* . PhD thesis, Humboldt-Universität zu Berlin, 2009.

[237] H. J. Kimble, M. Dagenais, and L. Mandel. Photon antibunching in resonance fluorescence. *Physical Review Letters*, 39(11):691–695, 1977.

[238] F. Diedrich and H. Walther. Nonclassical radiation of a single stored ion. *Physical Review Letters*, 58(3):203–206, 1987.

[239] P. Michler, A. Imamoğlu, M. D. Mason, P. J. Carson, G. F. Strouse, and S. K. Buratto. Quantum correlation between photons from a single quantum dot at room temperature. *Nature*, 406:968–970, 2000.

[240] C. Kurtsiefer, S. Mayer, P. Zarda, and H. Weinfurter. Stable Solid-State Source of Single Photons. *Physical Review Letters*, 85(2):290–293, 2000.

[241] A. M. Zaitsev. *Optical properties of diamond: a data handbook*. Springer Verlag, 2001.

[242] L. du Preez. *(unpublished)*. PhD thesis, University of Witwatersrand, 1965.

[243] G. Davies and M. F. Hamer. Optical studies of the 1.945 eV vibronic band in diamond. *Proceedings of the Royal Society of London. Series A, Mathematical and Physical Sciences*, 348(1653):285–298, 1976.

[244] J. Meijer, B. Burchard, M. Domhan, C. Wittmann, T. Gaebel, I. Popa, F. Jelezko, and J. Wrachtrup. Generation of single color centers by focused nitrogen implantation. *Applied Physics Letters*, 87:261909, 2005.

[245] F. M. Hossain, M. W. Doherty, H. F. Wilson, and L. C. L. Hollenberg. Ab Initio Electronic and Optical Properties of the NV^- Center in Diamond. *Physical Review Letters*, 101(22):226403, 2008.

[246] A. Gali and E. Kaxiras. Comment on "Ab Initio Electronic and Optical Properties of the NV^- Center in Diamond". *Physical Review Letters*, 102(14):149703, 2009.

[247] F. M. Hossain, M. W. Doherty, H. F. Wilson, and L. C. L. Hollenberg. Hossain et al. Reply. *Physical Review Letters*, 102(14):149704, 2009.

[248] T. Gaebel, M. Domhan, C. Wittmann, I. Popa, F. Jelezko, J. Rabeau, A. Greentree, S. Prawer, E. Trajkov, P. R. Hemmer, et al. Photochromism in single nitrogen-vacancy defect in diamond. *Applied Physics B: Lasers and Optics*, 82(2):243–246, 2006.

[249] C. D. Clark and C. A. Norris. Photoluminescence associated with the 1.673, 1.944 and 2.498 eV centres in diamond. *Journal of Physics C: Solid State Physics*, 4: 2223–2229, 1971.

[250] D. A. Redman, S. Brown, R. H. Sands, and S. C. Rand. Spin dynamics and electronic states of NV centers in diamond by EPR and four-wave-mixing spectroscopy. *Physical Review Letters*, 67(24):3420–3423, 1991.

[251] E. Van Oort, NB Manson, and M. Glasbeek. Optically detected spin coherence of the diamond NV centre in its triplet ground state. *Journal of Physics C: Solid State Physics*, 21:4385–4391, 1988.

[252] A. Gruber, A. Drabenstedt, C. Tietz, L. Fleury, J. Wrachtrup, and C. Borczyskowski. Scanning Confocal Optical Microscopy and Magnetic Resonance on Single Defect Centers. *Science*, 276(5321):2012, 1997.

[253] N. R. S. Reddy, N. B. Manson, and E. R. Krausz. Two-Laser Spectral Hole Burning in a Color Center in Diamond. *Journal of Luminescence*, 38(1-6):46–47, 1987.

[254] K. M. C. Fu, C. Santori, P. E. Barclay, L. J. Rogers, N. B. Manson, and R. G. Beausoleil. Observation of the dynamic Jahn-Teller effect in the excited states of nitrogen-vacancy centers in diamond. *Physical Review Letters*, 103(25):256404, 2009.

[255] P. Tamarat, N. B. Manson, J. P. Harrison, R. L. McMurtrie, A. Nizovtsev, C. Santori, R. G. Beausoleil, P. Neumann, T. Gaebel, F. Jelezko, P. R. Hemmer, and J. Wrachtrup. Spin-flip and spin-conserving optical transitions of the nitrogen-vacancy centre in diamond. *New Journal of Physics*, 10:045004, 2008.

[256] L. J. Rogers, S. Armstrong, M. J. Sellars, and N. B. Manson. Infrared emission of the NV centre in diamond: Zeeman and uniaxial stress studies. *New Journal of Physics*, 10(103024):103024, 2008.

[257] P. Delaney, J. C. Greer, and J. A. Larsson. Spin-Polarization Mechanisms of the Nitrogen-Vacancy Center in Diamond. *Nano Letters*, 2010. doi: 10.1021/nl903646p.

[258] P. Neumann, R. Kolesov, V. Jacques, J. Beck, J. Tisler, A. Batalov, L. Rogers, N. B. Manson, G. Balasubramanian, F. Jelezko, et al. Excited-state spectroscopy of single NV defect in diamond using optically detected magnetic resonance. *New Journal of Physics*, 11:013017, 2009.

[259] A. Beveratos, R. Brouri, T. Gacoin, J. P. Poizat, and P. Grangier. Nonclassical radiation from diamond nanocrystals. *Physical Review A*, 64(6):61802, 2001.

[260] A. Beveratos, R. Brouri, T. Gacoin, A. Villing, J. P. Poizat, and P. Grangier. Single photon quantum cryptography. *Physical Review Letters*, 89(18):187901, 2002.

[261] R. Alléaume, F. Treussart, G. Messin, Y. Dumeige, J. F. Roch, A. Beveratos, R. Brouri-Tualle, J. P. Poizat, and P. Grangier. Experimental open-air quantum key distribution with a single-photon source. *New Journal of Physics*, 6:92, 2004.

[262] Quantum Communications Victoria. URL `http://qcvictoria.com`.

[263] Microdiamant AG, . URL `http://www.microdiamant.com`.

[264] microParticles GmbH, . URL `http://www.microparticles.de`.

[265] V. M. Acosta, A. Jarmola, E. Bauch, and D. Budker. Optical properties of the nitrogen-vacancy singlet levels in diamond. *Physical Review B*, 82(20):201202, Nov 2010.

[266] R. J. Epstein, F. M. Mendoza, Y. K. Kato, and D. D. Awschalom. Anisotropic interactions of a single spin and dark-spin spectroscopy in diamond. *Nature Physics*, 1(2):94–98, 2005.

[267] A. Ashkin and J. M. Dziedzic. Observation of optical resonances of dielectric spheres by light scattering. *Applied Optics*, 20(1803):1814, 1981.

[268] P. Tamarat, T. Gaebel, J. R. Rabeau, M. Khan, A. D. Greentree, H. Wilson, L. C. L. Hollenberg, S. Prawer, P. R. Hemmer, F. Jelezko, et al. Stark Shift Control of Single Optical Centers in Diamond. *Physical Review Letters*, 97(8): 83002, 2006.

[269] S. Strauf, MT Rakher, I. Carmeli, K. Hennessy, C. Meier, A. Badolato, M. J. A. DeDood, P. M. Petroff, E. L. Hu, E. G. Gwinn, et al. Frequency control of photonic crystal membrane resonators by monolayer deposition. *Applied Physics Letters*, 88: 043116, 2006.

[270] W. Yang, Z. Xu, M. Feng, and J. Du. Entanglement of separate nitrogen-vacancy centers coupled to a whispering-gallery mode cavity. *New Journal of Physics*, 12: 113039, 2010.

[271] W. L. Yang, Z. Q. Yin, Z. Y. Xu, M. Feng, and J. F. Du. One-step implementation of multiqubit conditional phase gating with nitrogen-vacancy centers coupled to a high-Q silica microsphere cavity. *Applied Physics Letters*, 96(24):241113, 2010.

[272] A. T. Collins, M. F. Thomaz, and M. I. B. Jorge. Luminescence decay time of the 1.945 eV centre in type Ib diamond. *Journal of Physics C: Solid State Physics*, 16: 2177–2181, 1983.

[273] G. Nienhuis and C. T. J. Alkemade. Atomic radiative transition probabilities in a continuous medium. *Physica B+C*, 81(1):181–188, 1976.

[274] T. Flissikowski, A. Hundt, M. Lowisch, M. Rabe, and F. Henneberger. Photon beats from a single semiconductor quantum dot. *Physical Review Letters*, 86(14): 3172–3175, 2001.

[275] E. Dulkeith, T. Niedereichholz, T. A. Klar, J. Feldmann, G. von Plessen, D. I. Gittins, K. S. Mayya, and F. Caruso. Plasmon emission in photoexcited gold nanoparticles. *Physical Review B*, 70(20):205424, 2004.

[276] M. B.Mohamed, V. Volkov, S. Link, and M. A. El-Sayed. The 'lightning' gold nanorods: fluorescence enhancement of over a million compared to the gold metal. *Chemical Physics Letters*, 317(6):517–523, 2000.

[277] A. Beveratos, S. Kühn, R. Brouri, T. Gacoin, J. P. Poizat, and P. Grangier. Room temperature stable single-photon source. *The European Physical Journal D-Atomic, Molecular and Optical Physics*, 18(2):191–196, 2002.

[278] Y. Shen, T. M. Sweeney, and H. Wang. Zero-phonon linewidth of single nitrogen vacancy centers in diamond nanocrystals. *Physical Review B*, 77(3):33201, 2008.

[279] M. V. Gurudev Dutt, L. Childress, L. Jiang, E. Togan, J. Maze, F. Jelezko, A. S. Zibrov, P. R. Hemmer, and M. D. Lukin. Quantum Register Based on Individual

Electronic and Nuclear Spin Qubits in Diamond. *Science*, 316(5829):1312–1316, 2007.

[280] P. Neumann, J. Beck, M. Steiner, F. Rempp, H. Fedder, P. R. Hemmer, J. Wrachtrup, and F. Jelezko. Single-shot readout of a single nuclear spin. *Science*, 329(5991):542, 2010.

[281] C. H. Su, A. D. Greentree, and L. C. L. Hollenberg. Towards a picosecond transform-limited nitrogen-vacancy based single photon source. *Optics Express*, 16(9):6240–6250, 2008.

[282] T. H. Taminiau, F. D. Stefani, F. B. Segerink, and N. F. van Hulst. Optical antennas direct single-molecule emission. *Nature Photonics*, 2(4):234, 2008.

[283] J. Claudon, J. Bleuse, N. S. Malik, M. Bazin, P. Jaffrennou, N. Gregersen, C. Sauvan, P. Lalanne, and J. M. Gérard. A highly efficient single-photon source based on a quantum dot in a photonic nanowire. *Nature Photonics*, 2010.

[284] B. Henke, B. Ahrens, J. A. Johnson, P. T. Miclea, and S. Schweizer. Upconverted fluorescence in er-doped zblan glasses for high efficiency solar cells. In *Proceedings of SPIE*, volume 7411, page 74110E, 2009.

[285] G. N. Gol'tsman, O. Okunev, G. Chulkova, A. Lipatov, A. Semenov, K. Smirnov, B. Voronov, A. Dzardanov, C. Williams, and R. Sobolewski. Picosecond superconducting single-photon optical detector. *Applied Physics Letters*, 79:705, 2001.

[286] S. I. Bozhevolnyi, V. S. Volkov, E. Devaux, J. Y. Laluet, and T. W. Ebbesen. Channel plasmon subwavelength waveguide components including interferometers and ring resonators. *Nature*, 440(7083):508–511, 2006.

[287] G. Balasubramanian, I. Y. Chan, R. Kolesov, M. Al-Hmoud, J. Tisler, C. Shin, C. Kim, A. Wojcik, P. R. Hemmer, A. Krueger, T. Hanke, A. Leitenstorfer, R. Bratschitsch, F. Jelezko, and J. Wrachtrup. Nanoscale imaging magnetometry with diamond spins under ambient conditions. *Nature*, 455(7213):648–651, 2008.

[288] J. R. Maze, P. L. Stanwix, J. S. Hodges, S. Hong, J. M. Taylor, P. Cappellaro, L. Jiang, M. V. Gurudev Dutt, E. Togan, A. S. Zibrov, A. Yacoby, R. L. Walsworth, and M. D. Lukin. Nanoscale magnetic sensing with an individual electronic spin in diamond. *Nature*, 455(7213):644–647, 2008.

[289] A. W. Schell, G. Kewes, T. Hanke, A. Leitenstorfer, R. Bratschitsch, O. Benson, and T. Aichele. Single defect centers in diamond nanocrystals as quantum probes for plasmonic nanostructures. *Optics express*, 19(8):7914, 2011.

[290] K. Tanaka, E. Plum, J. Y. Ou, T. Uchino, and N. I. Zheludev. Multifold enhancement of quantum dot luminescence in plasmonic metamaterials. *Physical Review Letters*, 105(22):227403, Nov 2010. doi: 10.1103/PhysRevLett.105.227403.

[291] D. E. Chang, A. S. Sørensen, E. A. Demler, and M. D. Lukin. A single-photon transistor using nanoscale surface plasmons. *Nature Physics*, 3(11):807–812, 2007.

[292] P. Li and F. Li. Quantum information transfer with nitrogen-vacancy centers coupled to a whispering-gallery microresonator. *Arxiv preprint arXiv:1010.6138*, 2010.

[293] Thomas Aichele. *Detection and Generation of Non-classical Light States from Single Quantum Emitters* . PhD thesis, Humboldt-Universität zu Berlin, 2004.

Danksagung

Am Schluss dieser Arbeit möchte ich den Menschen danken, die mich während dieser Zeit unterstützt und begleitet haben. Da alles etwas länger dauerte, muss ich allen zunächst für ihre Geduld danken.

Die erste Person, der ich zu großem Dank verpflichtet bin, ist selbstverständlich Prof. Oliver Benson, der mir die Möglichkeit zu dieser Dissertation gab. Ich danke ihm vor allem für sein Vertrauen, auch in Zeiten, in denen sich Fortschritte sehr in Grenzen hielten. Ohne die gewährten Freiheiten wären viele Ergebnisse nicht zustande gekommen.

"Leo" Leonardo de Souza de Menezes hat mich auf Upconversion-Nanokristalle angesetzt, die sich zunächst als sehr widerspenstig erwiesen, aber dann umso spannendere Ergebnisse lieferten. Aber nicht nur als Wissenschaftler, sondern auch als Mensch habe ich ihn sehr zu schätzen gelernt.

Ob im Labor oder außerhalb immer unglaublich freundlich und hilfsbereit: Andrea Mazzei. Und obwohl oder vielleicht gerade weil man sich mit ihm wunderbar streiten kann, wurde er ein besonderer Freund, von dem ich viel gelernt habe.

Die Zeit mit Michael Barth im Labor war wohl die effektivste, und so hell haben Diamanten wohl noch nie geleuchtet. Mit Björn Lauritzen habe ich angefangen, "Hochkonversion" zu betreiben, wobei er nicht vollständig scheiterte, mir Jazz nahezubringen. Alexander Kuhlicke und Gesine Steudle, mit denen ich zusammen arbeiten durfte und das Büro geteilt habe, sind zu guten Freunden geworden, mit denen ich nicht nur eine Vorliebe für hochwertige, deutsche, sonntagabendliche Kriminalunterhaltung teile. Thomas Aichele kann (nach eigenem Bekunden) kein Hochdeutsch, aber alles andere, auf jeden Fall aber Kässpätzle.

Natürlich darf hier Diplom-Ingenieur Klaus Palis auf keinen Fall fehlen, der gute Geist der Gruppe und passionierter Saumagen-Esser. Bei allen Problemen war er stets mit Rat und Tat zur Stelle.

Alle andere Nanos, Rico, Markus G., Matthias L., Matthias S., Lars, David, Tim,

Andreas S., Andreas A. und Janik, machten die Zeit, erst am Hausvogteiplatz und dann in Adlershof, zu etwas Besonderem. Danke dafür! Aber auch die Qoms hatten daran ihren Anteil, vor allem Evgeny, Malte, Alex, Thilo, Sven und Katharina.

Meinen Eltern danke ich von ganzem Herzen, deren berechtigten Nachfragen ich mich zwar immer wieder –mehr oder weniger– erfolgreich entzogen habe, deren uneingeschränkte Unterstützung ich mir immer sicher sein kann, was sicherlich ein großes Glück ist.

Und wer hätte zu Beginn der Promotion gedacht, dass ich an deren Ende auch meiner eigenen kleinen Familie danken kann: meiner Frau Andrea, die mir so toll und so lange den Rücken frei gehalten hat und David, der ab jetzt endlich die volle Aufmerksamkeit an den Wochenenden bekommen wird! Und auch Fabian, der eigentlich schon zu diesr Familie gehört, hat seinen Anteil zu dieser Arbeit beigetragen. Nicht zuletzt dadurch, dass er mir Berlin schmackhaft gemacht hat.

Selbständigkeitserklärung

Hiermit erkläre ich, die vorliegende Arbeit selbständig verfasst und dazu nur die angegebenen Quellen und Hilfsmittel verwendet zu haben.

Ich habe mich anderweitig nicht um einen Doktorgrad beworben und besitze einen solchen auch nicht.

Die dem Verfahren zugrunde liegende Promotionsordnung der Mathematisch-Naturwissenschaftlichen Fakultät I der Humboldt Universität zu Berlin habe ich zur Kenntnis genommen.

Berlin, den 10. September 2011

Stefan Schietinger